Volume 71A
Number 4
July–Aug. 1967

Physics and Chemistry

U.S. DEPARTMENT OF COMMERCE

SECTION A

JOURNAL OF RESEARCH

NATIONAL BUREAU OF STANDARDS

Journal of Research

of the

National Bureau of Standards

A. Physics and Chemistry

July–Aug. • 1967

VOLUME • 71A

NUMBER • 4

Editor: C. W. Beckett

Associate Editors: D. D. Wagman
J. M. Richardson

Publication dates:
Feb. 1, Apr. 1, June 1, Aug. 1, Oct. 1, Dec. 1, 1967

JOURNAL OF RESEARCH

The National Bureau of Standards Journal of Research reports research and development in the fields of activity shown at right. Also included from time to time are survey articles on topics closely related to the Bureau's scientific and technical program.

The Journal is published in three separate sections as follows:

A. Physics and Chemistry

Contains papers of interest primarily to scientists working in these fields. Issued six times a year. Annual subscription: domestic, $5.00; foreign, $6.00. Single copy, $1.00.

B. Mathematics and Mathematical Physics

Presents studies and compilations designed mainly for the mathematician and the theoretical physicist. Issued quarterly. Annual subscription: domestic, $2.25; foreign, $2.75. Single copy, 75c.

C. Engineering and Instrumentation

Reports research and development results of interest chiefly to the engineer and the applied scientist. Issued quarterly. Annual subscription: domestic, $2.75; foreign, $3.50. Single copy, 75c.

The National Bureau of Standards is a principal focal point in the Federal Government for assuring maximum application of the physical and engineering sciences to the advancement of technology in industry and commerce. Its responsibilities include development and maintenance of the national standards of measurement, and the provision of means for making measurements consistent with those standards; determination of physical constants and properties of materials; development of methods for testing materials, mechanisms, and structures, and making such tests as may be necessary, particularly for government agencies; cooperation in the establishment of standard practices for incorporation in codes and specifications; advisory service to government agencies on scientific and technical problems; invention and development of devices to serve special needs of the Government; assistance to industry, business and consumers in the development and acceptance of commercial standards and simplified trade practice recommendations; administration of programs in cooperation with United States business groups and standards organizations for the development of international standards of practice; and maintenance of a clearinghouse for the collection and dissemination of scientific, technical and engineering information. The scope of the Bureau's activities is suggested in the following listing of its three Institutes and their organizational units.

Institute for Basic Standards. Applied Mathematics. Electricity. Metrology. Mechanics. Heat. Atomic Physics. Physical Chemistry. Laboratory Astrophysics.* Radiation Physics. Radio Standards Laboratory.* Radio Standards Physics & Radio Standards Engineering. Office of Standard Reference Data.

Institute for Materials Research. Analytical Chemistry. Polymers. Metallurgy. Inorganic Materials. Reactor Radiations. Cryogenics.* Materials Evaluation Laboratory. Office of Standard Reference Materials.

Institute for Applied Technology. Building Research. Information Technology. Performance Test Development. Electronic Instrumentation. Textile and Apparel Technology Center. Technical Analysis. Office of Weights and Measures. Office of Engineering Standards. Office of Invention and Innovation. Office of Technical Resources. Clearinghouse for Federal Scientific and Technical Information.**

*Located at Boulder, Colo. 80302.
**Located at 5285 Port Royal Road, Springfield, Va. 22151.

U.S. DEPARTMENT OF COMMERCE
Alexander B. Trowbridge, Secretary
NATIONAL BUREAU OF STANDARDS
A. V. Astin, Director

Order all publications from the Superintendent of Documents
U.S. Government Printing Office, Washington, D.C. 20402

Use of funds for printing this publication approved by the Director of the Bureau of the Budget (June 22, 1966).

JOURNAL OF RESEARCH of the National Bureau of Standards — A. Physics and Chemistry Vol. 71A, No. 4, July-August 1967

Kinetics of Crystallization in Multicomponent Systems: I. Binary Mixtures of n-Paraffins

John I. Lauritzen, Jr., Elio Passaglia, and E. A. DiMarzio

Institute for Materials Research, National Bureau of Standards, Washington, D. C. 20234

(April 19, 1967)

The kinetics of crystallization of a binary mixture of n-paraffins is treated using a theory for the rate of growth of chains in multicomponent systems. The kinetic chain is considered to be a strip of crystalline material composed of molecules of both components that is growing on a substrate of uniform thickness. This substrate is considered to be a close-packed surface step. Using the binary mixture of $C_{24}H_{50}$ and $C_{26}H_{54}$ as an example, the calculations are carried out by an iterative procedure so that the mean thickness of the strip equals that of the substrate. This procedure necessitates modification of the rate constants that would be used without this requirement. The rate of growth of the strips (total flux) is calculated as well as their composition over an appropriate range of temperature and a complete range of liquid compositions. The pair distribution in the strips is also determined. The substrate is assumed to be unkinked in the calculations, whereas the substrate is probably highly kinked in the actual system. For this reason the calculated total flux is probably not representative of the actual crystal growth rate in a binary mixture of $C_{24}H_{50}$ and $C_{26}H_{54}$. It is believed that the calculated compositions are reasonably accurate. For a binary mixture of longer n-paraffins (e.g., $C_{50}H_{102}$ $C_{52}H_{106}$) the substrate should have many fewer kinks, and the total flux calculated by this theory will be more closely related to actual crystal growth rate studies. However, no data exist for such systems.

Key Words: Crystal growth, multicomponent systems, kinetics, n-paraffins, phase diagrams, pair distributions.

1. Introduction

In a recent paper (subsequently abbreviated LDP) [1][1] we presented a theory by which the rate of growth and composition of a chain growing in a multicomponent system may be calculated. There are several kinetic problems which may be treated by the method developed in LDP. In particular the chain may be regarded as a layer (or strip) of atoms or molecules at a step on a growing crystal surface, the beginning and end of the chain, or strip, being kinks. The initiation and growth of such strips is one of the processes operative in crystal growth. In fact, in theories of polymer crystallization [2,3,4] it is generally considered that formation of such strips is the rate controlling step in the growth of polymer crystals, and hence the calculation of their rate of growth amounts to the calculation of the rate of growth of these crystals. In polymer crystals the growing step (or lamellar edge) is not expected to be very highly kinked, and this approach appears valid. We treat this problem in the following paper. In atomic systems, the situation is more complicated [5]. The rate-controlling step is almost certainly not the initiation and growth of these strips, since the step is highly kinked [5], and the problem of the calculation of the rate of growth of a crystal becomes essentially a diffusion problem. In systems of intermediate complexity, such as those treated here, the relevance of the kinetics of formation of these strips to the problem of crystal growth is somewhat harder to assess. However, in multicomponent systems, such as we are treating, it seems relatively clear that the elementary processes we treat in calculating the rate of growth and composition of these chains must be important in determining the composition of the crystal, for it must in large measure be the neighbor interaction energies that determine the composition. We thus present an application of the LDP theory to the problem of crystal growth of binary mixtures of n-paraffins. The pure normal paraffins are known to grow, at least from solution, by a screw-dislocation mechanism [6], and hence a surface step is present. It is expected that the composition of the chains calculated by this method will be a more accurate representation of the composition of the crystal than the calculated kinetics will be of the rate of crystal growth. However, it is expected that as the length of paraffin molecule increases, the calculated kinetics become a more adequate representation of the rate of crystal growth, for the growing step becomes less and less kinked.

[1] Figures in brackets indicate the literature references at the end of this paper.

Although concerned with a specific system, our aim will be less to account for the behavior of this specific system than to illustrate the general behavior of binary systems insofar as this can be done by the LDP theory. Considerable accurate data on the phase-diagrams of *n*-paraffin systems are available [7, 8] although, to our knowledge, no data are available on the kinetics of crystal growth in such mixtures. The homogeneous nucleation rate has been studied in pure *n*-paraffins [9], but not the crystal growth rate. However, many of the energy considerations relevant to crystal growth are well known [10]. The solid-phase behavior of the *n*-paraffins is also well known [10], and, since the LDP theory is applicable only to solid solutions, we will concentrate on a system in which solid-solutions are found at all concentrations. In particular, we will be concerned with the solidification to the hexagonal rotator phase in the system $C_{24}H_{50}-C_{26}H_{54}$, which meets these requirements. We will ignore any solid-solid phase transitions, and our task will be to calculate the rate of growth of the strips discussed above and their composition as a function of temperature and liquid composition. In what follows we use the words "chain" and "strip" interchangeably.

In order to describe the method of calculation, we will have to describe those aspects of the LDP theory necessary to make the subsequent exposition clear. The LDP theory begins by assuming only nearest neighbor interactions, with rate constants α^{ij} and β^{ij}, for, respectively, adding species j to a chain ending in species i, and removing species j from a chain whose terminal elements are originally i and j. These rate constants are assumed to be independent of the length of the chain. However, the rate constants for the initiation of the chain (i.e., the first step in the chain) are different, and are called α_0^j and β_1^j. That is, α_0^j gives the rate of initiation of new chains from the melt or solution, and β_1^j gives the rate of dissolution of this first step back to melt or solution.

Although there is no limit to the number of components or order of distribution which may be handled by the LDP theory, in this paper we will be concerned only with binary systems and pair distributions. Thus, we define N_ν^j and P_ν^{ij} as being, respectively, the number of chains in the system ν units long with species j in the νth position, and i and j in $(\nu-1)$th and νth positions. In this application, of course, i and j can take on only the values 1 and 2, with 1 representing $C_{26}H_{54}$ and 2 representing $C_{24}H_{50}$. Clearly, we must have

$$N_\nu^j=\sum_{i=1}^{2} P_\nu^{ij} \tag{1}$$

and

$$N_\nu^T=\sum_j N_\nu^j=\sum_{i,j} P_\nu^{ij}, \tag{2}$$

where N_ν^T is the total number of chains ν units long. We call these quantities, N_ν^j and P_ν^{ij}, "occupation numbers." Kinetic equations for the growth of chains may be formulated [1] in terms of these and more complex quantities. These may be solved at steady state under certain fairly broad conditions. For this purpose we define fluxes S_ν^j and S_ν^{ij} as being the net rate of growth of chains (at steady state) from $\nu-1$ to ν units by, respectively, adding species j to any chain, and to a chain whose terminal $(\nu-1)$th element is i. We obviously have

$$S_T=\sum_j S_\nu^j=\sum_{i,j} S_\nu^{ij}, \tag{3}$$

where S_T is the total flux. Thus, we may consider that the flux S_ν^j is associated with the occupation number N_ν^j, and the flux S_ν^{ij} with P_ν^{ij}.

Under certain and quite unrestrictive conditions on the rate constants, it is shown by LDP that the ratio of flux to its associated occupation number is independent of chain length (for sufficiently long chains) and dependent only on the terminal species in the chain. That is,

$$\frac{S_\nu^j}{N_\nu^j}=\frac{S_\nu^{ij}}{P_\nu^{ij}}=\lambda^j \quad , \tag{4}$$

where the ratio is denoted λ^j. This in turn is given by the equations

$$\lambda^j=\sum_i \frac{\alpha^{ij}\lambda^i}{\beta^{ij}+\lambda^i} \quad . \tag{5}$$

Moreover, it is also shown in LDP that

$$N_\nu^j=\sum_i \frac{\alpha^{ij}N_{\nu-1}^i}{\beta^{ij}+\lambda^j} \quad . \tag{6}$$

For sufficiently large ν, this recursion relation is shown to become [1]

$$N^j=\sum_i \frac{\alpha^{ij}N^i}{\beta^{ij}+\lambda^j} \quad . \tag{7}$$

Thus for sufficiently long chains, the occupation numbers become independent of chain length, and because of eq (4) the flux also does. "Sufficiently long" in this context is of the order of ten, and thus if the average number of lattice positions between kinks is of this order, this equation will be valid.

Equation (6) is a recursion relation for the N_ν. When combined with the equation for the first step in the chain

$$N_1^j=\frac{\alpha_0^j N_0^j}{\beta_1^j+\lambda^j} \tag{8}$$

it is entirely possible to build up the chain on a high-speed computer and thus get the initial ν-dependent

solution as well as the ν-independent limit. (In eq (8) $\alpha_0^j N_0^j$ is the rate of initiation of new chains from the melt or solution.)

Now, having the ν independent limit of N^j either by direct solution of eq (7) or iteration of eq (8), the flux is easily obtainable from eq (4):

$$S^j = \lambda^j N^j \tag{9}$$

and

$$S_T = \sum_j \lambda^j N^j \ . \tag{10}$$

It is shown by LDP that the total flux is conserved. Hence, we also have

$$S_T = \sum_j \lambda^j N_1^j = \sum_j \frac{\alpha_0^j N_0^j \lambda^j}{\beta_1^j + \lambda^j} \ . \tag{11}$$

In general we will not know the exact numerical value of $\alpha_0^j N_0^j$ or β_1^j and hence will not be able to predict the magnitude of the flux. We hope, however, to be able to predict correctly its dependence on temperature.

Now, the fraction of the jth species in the chain, f_j, is given by

$$f_j = \frac{S^j}{S_T} = \frac{\lambda^j N^j}{\sum_j \lambda^j N^j} \ , \tag{12}$$

and is thus easily obtained. The pair distributions are also easily obtained. It is shown by LDP that

$$P_{\nu+1}^{ij} = \frac{\alpha^{ij} N_\nu^i}{\beta^{ij} + \lambda^j} \tag{13}$$

and for chains that are sufficiently long that the occupation numbers become independent of ν,

$$P^{ij} = \frac{\alpha^{ij} N^i}{\beta^{ij} + \lambda^j} \ . \tag{14}$$

Now, clearly the fraction f_{ij} of i, j pairs in the chain is given by

$$f_{ij} = \frac{S^{ij}}{S_T} = \frac{\lambda^j P^{ij}}{S_T} = \frac{1}{S_T} \frac{\alpha^{ij} \lambda^j N^i}{\beta^{ij} + \lambda^j} \ . \tag{15}$$

The steps in the solution are as follows: (a) Having the rate constants α^{ij} and β^{ij}, compute the λ^j from eq (5). (b) Having the λ^j, compute the N_ν^j by iteration of eq (6) beginning with eq (8) until the N_ν^j arrive at a constant value N^j. (c) Compute S^j by eq (9), and S_T by eq (10). (d) Compute the composition of the chain by eq (12) and the pair distributions by eqs (14) and (15). The actual methods used for these computations will be discussed in greater detail below.

2. The Rate Constants

2.1. Preliminary Considerations

It is shown by LDP that the ratio of the rate constants is given by

$$\frac{\alpha^{ij}}{\beta^{ij}} = \exp\left[(\mu_j - e_{ij})/kT\right] \tag{16}$$

and

$$\frac{\alpha_0^j}{\beta_1^j} = \exp\left[(\mu_j - \epsilon_j^0)/kT\right] \tag{16a}$$

where μ_j is the chemical potential of the jth species, ϵ_{ij} is the change in free energy of the growing chain when j is added to a chain ending in species i, and ϵ_j^0 is the change in free energy for the initial element of the chain. There are two things to be noted about eq (16) and (16a). First, they were derived from consideration of an appropriate grand-canonical ensemble, under the principle of detailed balance and as a result kinetic factors such as interfacial transport terms do not appear. Secondly, eqs (16) and (16a) give only the ratio of the forward and backward rate constants in terms of the free energy changes involved in the process. Without more detailed knowledge of the details of the process we do not know how to apportion these free energy changes to the forward and backward rate constants. Rather than try to solve the problem of the detailed process, as has been attempted by Frank and Tosi for chain-folded polymer crystallization [3], we shall take a more empirical approach and solve the problem for various arbitrary apportionments. At equilibrium the results will, of course, be independent of this, and our hope is that this will also be the case under kinetic conditions. As will be seen, our hope is largely fulfilled.

2.2. Evaluation of μ_j and ϵ_{ij}

The quantity $(\mu_j - \epsilon_{ij})$ is the change in free energy of the system in removing species j from the liquid and placing it on the end of a chain whose terminal element is species i, and $(\mu_j - \epsilon_j^0)$ has the analogous interpretation. In order to do this we need both a model of the liquid and a model of the growing crystal. Our philosophy in this is to assume the simplest model possible for both; considering the adequacy of the theory and the state of our knowledge of the kinetics of crystallization in these systems, to assume more detailed models at this state would be presumptuous.

Accordingly, we assume that the liquid is an ideal solution of the two species. For the system considered here ($C_{24}H_{50}$ and $C_{26}H_{54}$) this is not a completely adequate description [11] but neither is it very far wrong. Indeed, for our purposes, it is completely sufficient. We may therefore write the free energy

$G^l(T,P)$ of a liquid mixture of N_1 molecules of $C_{26}H_{54}$ and N_2 molecules of $C_{24}H_{50}$ as

$$G^l(T,P)=N_1g_1^l+N_2g_2^l+N_1kT\ln x_1+N_2kT\ln x_2 \quad (17)$$

where g_1^l and g_2^l are the free energies per molecule of the pure liquid components at the same temperature and pressure, and x_1 and x_2 their mole fractions. We thus have immediately

$$\mu_1=g_1^l+kT\ln x_1$$

$$\mu_2=g_2^l+kT\ln x_2 \quad (18)$$

To obtain the ϵ_{ij} and ϵ_0^j we adopt a model illustrated schematically in figure 1. We assume a uniform substrate, or crystal flake, that has already grown with a thickness intermediate between the extended lengths of the molecules, l_1 and l_2. (Note that we do not allow any roughness in the substrate. This is discussed more fully below.) Since the solid phase has an hexagonal crystal structure, we assume for simplicity that each molecule in the chain is an hexagonal prism as shown. We now adopt a procedure similar to that used by Price [4] to calculate the energies. Each molecule may be considered to act as a rigid hexagonal prism with a surface free-energy σ per unit area. For the difference in length under consideration, this is not a bad assumption. Then, if g_j^c represents the average free energy per molecule in the pure crystal at the same temperature and pressure, we may write

$$\epsilon_{ij}=g_j^c+4a\sigma U(l_j-l_s)+2a\sigma U(l_j-l_i) \quad (19)$$

where

$$U(x)=x \qquad x\geq 0$$

$$=0 \qquad x\leq 0$$

and a is the length of the hexagon edge. Note that we have not included a term for the end-surface with free energy σ_e. This merely makes the melting point that of the macroscopic crystal rather than a single lamellar sheet and corresponds to the case of the substrate being a surface step. Hence we obtain for $\mu_j-\epsilon_{ij}$

$$\mu_j-\epsilon_{ij}=\Delta g_j-4a\sigma U(l_j-l_s)-2a\sigma U(l_j-l_i)+kT\ln x_j \quad (20)$$

where Δg_j is the free energy of fusion (considered as a positive quantity) for species j at the temperature in question. For the first step we obtain

$$\mu_j-\epsilon_j^0=\Delta g_j-4a\sigma U(l_j-l_s)-2a\sigma l_j+kT\ln x_j. \quad (20a)$$

Equation (20) indicates that if a molecule with length $l_j>l_s>l_i$ is added to a chain ending in species i, corrections to the free energy of fusion must be made because of the newly exposed surface area, but if $l_j<l_s<l_i$, no such corrections need be made. As usual for small supercoolings we assume

$$\Delta g_j=\frac{\Delta h_j\Delta T_j}{T_m^j}$$

where Δh_j is the heat of fusion and T_m^j is the melting point appropriate to the species in question and obtain finally

$$\mu_j-\epsilon_{ij}=\frac{\Delta h_j\Delta T_j}{T_m^j}-4a\sigma U(l_j-l_s)$$

$$-2a\sigma U(l_j-l_i)+kT\ln x_j \quad (21)$$

where $\Delta T_j=T_m^j-T$, with an analogous expression for the first element.

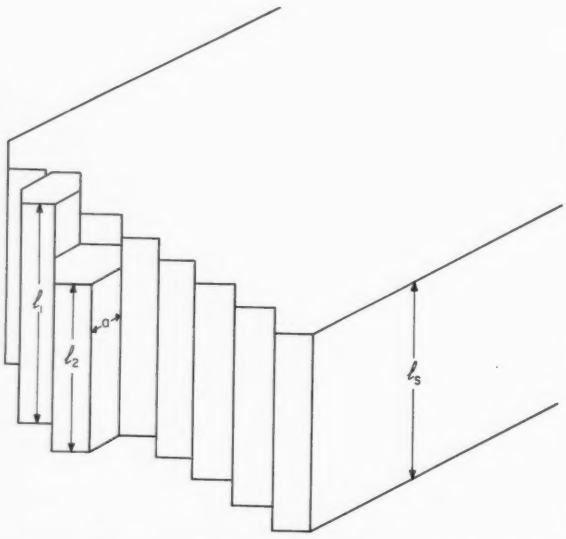

FIGURE 1. *Schematic diagram of a model for crystal growth of a binary mixture of* n-*paraffins.*

The growing strip is the kinetic chain of the LDP theory [1]. The lengths of the two paraffin components in extended configuration are l_1 and l_2. The cross section of the two components in the crystal are taken to be hexagonal since the solid solution is in the hexagonal rotator phase. The strip is growing on a substrate of uniform thickness, l_s.

2.3. The Effect of the Substrate and the Two-Dimensional Character of the Crystallization Problem

If we were interested in the strictly one-dimensional problem of the rate of growth and composition of a strip growing on a substrate of fixed length, then the free energies given by eq (20) and the ratios of rate constants calculated from them by eq (16) would be completely appropriate. It would be necessary only to carry out the computations as outlined at the end of the Introduction. This would lead to correct results

for a one-dimensional problem, for the LDP theory, within the limits of the assumptions, is rigorously correct.

Crystallization, however, presents a problem of a two-dimensional character. What is required as a minimum is that the strip have the same composition as the substrate. In this particular case, this is the same as requiring that the average thickness of the growing strip, defined as

$$\bar{l} = f_1 l_1 + f_2 l_2 \tag{22}$$

be the same as the average thickness of the substrate.

It would appear that this problem could easily be solved by this procedure: (a) Choose a substrate of some convenient thickness. (b) Calculate, by the methods outlined, the composition of a strip growing on this substrate. Its average thickness will in general be different from that of the substrate. (c) Use this strip as a substrate for another strip. (d) Continue this process until the average thickness of the grown strip is the same as that of the substrate. This procedure clearly gives a first and reasonable approximation to the true state of affairs in a growing crystal.

If this is done with the free-energies given by eq (20) and the rate constants calculated from them by eq (16), no matter how the energies are apportioned between the forward and backward reactions, results which are incorrect and aphysical are obtained. If, for example, a phase diagram is calculated by this formalism at equilibrium (total flux, $S_T = 0$), a minimum in the liquidus-composition curve occurs at a different composition from that in the solidus-composition curve. While such a situation could be conceived off equilibrium ($S_T > 0$) it is clearly impossible at equilibrium. This situation does not occur if the computations are carried out at fixed substrate thickness for all compositions of the liquid, but is caused by the varying thickness of the substrate and the resulting two dimensional character of the problem. We must, accordingly, modify the procedure in some manner.

One way of proceeding would be to construct a two-dimensional kinetic theory. This would obviously be a formidable problem, and rather than attack it with very small probability of success, we attempt a more tractable problem. We seek to modify the rate-constant ratio (eq 16) so that at least at equilibrium ($S_T = 0$) physical results are obtained. We then assume that the same form of this ratio will be appropriate under kinetic conditions ($S_T > 0$).

The method used for this is outlined here and developed more fully in the appendix. An ensemble of strips of various lengths and various average thicknesses growing on substrates of various thicknesses is considered. The system is considered to have molecules of two lengths, l_1 and l_2, with $l_1 > l_2$. The average thickness of the substrate is assumed to be

$$l_s = l_2 + f_s(l_1 - l_2) \tag{23}$$

where f_s is the fraction of species 1 in the substrate. Pair or higher order distributions are neglected in the substrate. The average free energy of a strip of length ν in this ensemble is given by

$$G_\nu = \sum_{j=1}^{2} q^j_{\nu,1}[\epsilon^0_j - \mu_j + kT \ln q^j_{\nu,1}] + \sum_{\eta=2}^{\nu}\sum_{i=1}^{2}\sum_{j=1}^{2} q^{ij}_{\nu,\eta}[\epsilon_{ij} - \mu_j + kT \ln p^{ij}_{\nu,\eta}] \tag{24}$$

where $q^j_{\nu,1}$ is the fraction of strips ν units long with species j in the first position, $q^{ij}_{\nu,\eta}$ is the fraction of strips ν units long with species j in the ηth position and species i in $(\eta-1)$th position, and $p^{ij}_{\nu,\eta}$ is the probability that if species i is in the $(\eta-1)$th position in a strip ν units long, then species j is in the ηth position. Denoting the number of chains in the ensemble by N_T, the total free energy is given by

$$G_T = \sum_{\nu=1}^{\nu_0} G_\nu N_\nu + kT \sum_{\nu=0}^{\nu_0} N \ln (N_\nu / N_T) \tag{25}$$

The fraction f of species 1 in the strip is clearly given by

$$f = \frac{\sum_{\nu=1}^{\nu_0} N_\nu \sum_{\eta=1}^{\nu} q^1{}_{\nu,\eta}}{\sum_{\nu=1}^{\nu_0} \nu N_\nu} \tag{26}$$

For given μ_j, ϵ^0_j, and ϵ_{ij}, the free energy given by eq (25) is a function of $q^j_{\nu,1}$, $q^{ij}_{\nu,\eta}$, N_ν, f_s and the fraction f of species 1 in the strip.

By variational methods using Lagrange multipliers, a minimum in this free-energy may be sought with respect to these variables, and this will give their values at equilibrium. This analysis is carried out in the appendix.

It is shown that the proper rate constant ratios to obtain the correct distribution at equilibrium are given by

$$\frac{\alpha^j_0}{\beta^j} = x_j \exp\left[\Delta h_j \Delta T_j / T^j_m kT - 2a\sigma l_j / kT - 2\zeta(1 - 2f_s + f_s\omega)\delta_{1,j} - 2\zeta f_s \omega \delta_{2,j}\right] \tag{27}$$

$$\frac{\alpha^{ij}}{\beta^{ij}} = x_j \exp\left[\Delta h_j \Delta T_j / T^j_m kT - \delta U(j-i) - 2\zeta(1 - 2f_s + f_s\omega)\delta_{1,j} - 2\zeta f_s \omega \delta_{2,j}\right] \tag{28}$$

where the quantities have the following meaning:

$$\zeta = 2a\sigma(l_1 - l_2)/kT$$

$$2\omega - 1 = \frac{\xi - x_2}{[(\xi - x_2)^2 + \xi x_2 \exp(-\zeta)]^{1/2}}$$

$$\xi = x_1 \exp[\Delta h_1 \Delta T_1 / T_m^1 kT$$

$$- \Delta h_2 \Delta T_2 / T_m^2 kT - 2\zeta(1 - 2f_s)]$$

and $\delta_{i,j}$ is the Kronecker delta.

At equilibrium we know that $f_s = f$. Moreover, as shown in the appendix, $f_s = \omega$, and under these conditions physical solutions to the problem are obtained. Hence, without further justification we choose the α^{ij}/β^{ij} given by eqs (27) and (28) to be the proper rate constant ratios.

2.4. The Apportionment of the Energy

As previously mentioned, without detailed knowledge of the microscopic processes involved, it is not possible to make a decision of how to apportion the free energy between the forward and backward reactions. Since we have no such knowledge we adopt a much more empirical approach and carry out calculations for various arbitrary apportionments. Thus, if we let the argument of the exponential in eq (28) be A, then we take

$$\alpha^{ij} = x_j \exp(\varphi A) \tag{29a}$$

$$\beta^{ij} = \exp[-(1 - \varphi)A] \tag{29b}$$

and carry out calculations for $\varphi = 0$, 1/2 and 1. It will be noticed that the concentration term x_j is placed only in the forward reaction. This seems proper in that the probability of adding species j to a growing chain ought to be proportional to the "availability" of that species in the liquid.

For the initial step, if we let the argument of the exponent in eq (27) be A', we take

$$\alpha_0^j = x_j \exp(A') \tag{30a}$$

$$\beta_1^j = 1. \tag{30b}$$

That is, for the initial step, we put all the energy into the forward reaction and take the backward reaction to be a constant. This affects only the magnitude of the flux, which, as previously mentioned, we cannot in any case expect to predict exactly.

2.5. The Transport Term

Equations (16), (27), and (28) for the rate constant ratios, being the result of equilibrium considerations, do not involve any transport (or diffusion) terms. The inclusion of such terms in eqs (29) and (30) poses difficult problems, for in general these terms are not known. If these transport terms depend upon both the species at the end of the chain and the species coming on or going off (i.e., depend upon both i and j) then their omission can lead to serious problems. Thus, if α'^{ij} and β'^{ij} are the rate constants including transport terms, the most general relation to the α^{ij} and β^{ij} are

$$\alpha'^{ij} = a^{ij}\alpha^{ij} \tag{31a}$$

and

$$\beta'^{ij} = b^{ij}\beta^{ij} \tag{31b}$$

where a^{ij} and b^{ij} represent the transport terms. At equilibrium, of course, we must have $a^{ij}/b^{ij} = 1$. These new rate constants determine new λ^j by eq (5) and hence new compositions and fluxes. These coefficients are, of course, unknown, and indeed in such theories as this are usually left as undetermined parameters.

In the present case however, the similarity of the two species in question is such that a reasonable approximation to the true state of affairs may be obtained with a much more restrictive condition than eq (31). In the particular case under consideration here we could adopt these relations

$$\alpha'^{ij} = a\alpha^{ij} \tag{32a}$$

$$\beta'^{ij} = b\beta^{ij}\,. \tag{32b}$$

Now, as long as $S_T = 0$, we know the ratio a/b is unity from eq (16), and we note that this statement is not restricted to the melting temperature. At the melting point, of course, $S_T = 0$, and $a = b$. For finite currents not too far below the melting point this latter equality is expected to be an excellent approximation, if not indeed a rigorous fact.

Thus, taking $a = b$, and calculating the λ'^i corresponding to α'^{ij} and β'^{ij} we have

$$\lambda'^i = \sum_j \frac{a\alpha^{ij}\lambda'^j}{a\beta^{ij} + \lambda'^j} \tag{33}$$

whence

$$\frac{\lambda'^i}{a} = \sum_j \frac{\alpha^{ij}\lambda'^j/a}{\beta^{ij} + \lambda'^j/a} \tag{34}$$

and

$$\lambda'^i = a\lambda^i.$$

Inspection of eq (6), (12), and (15) shows that the transport term as represented by the quantity a has

no effect on the occupation numbers and the composition, but inspection of eq (10) shows that the flux calculated without the transport term must be multiplied by the factor a to obtain the flux when the transport term is included. In the calculations carried out here we take a to be unity, for, as previously stated, we cannot expect to get the true magnitude of flux in any case. In addition, however, the temperature dependence of the flux we calculate will be slightly wrong, and should be multiplied by an Arrhenius type term. For the undercoolings involved in this work (at most several degrees) this causes a negligible error in the temperature dependence.

3. Method of Calculation

The energies and molecular lengths chosen for the calculation were taken from a paper by Broadhurst [10]. The lateral molecular dimensions were computed to give the cross-sectional area per molecule given by Vand [12]. The data and conditions are summarized in table 1. Of particular importance in the table are the values of surface free energy, σ, which were chosen to be 3, 4, and 8 ergs/cm^2. This is lower than the 8 − 12 ergs/cm^2 obtained from the data of Turnbull and Cormia [9]. Since we are considering the transition from liquid to hexagonal rotator phase we expect σ to be lower, and indeed, comparison with the data of Mazee [7] shows that it most probably is.

The calculations were carried out on an IBM 7094 computer as follows.

(a) For a given value of φ and a given concentration x_1 and $x_2(=1-x_1)$ in the liquid, a starting value of $f_s=x_1$ was chosen and rate constants calculated by eqs (29), (30), (27), and (28).

(b) From these rate constants, the λ were determined by eq (5). These were solved by an iteration procedure outlined in LDP. Starting with

$$B_0^j=\sum_j \alpha^{ij}/\beta^{ij} \tag{35}$$

we calculate successively

$$B_p^i=\sum_j \frac{\alpha^{ij}B_{p-1}^j}{\beta^{ij}+B_{p-1}^j}. \tag{36}$$

TABLE 1. *Data and conditions used for calculations*

Compound	Length, Å	$\Delta h_f/k$	T_m, °K	Concentration in liquid
$C_{24}H_{50}$	32.46	6590	323.8	0–1
$C_{26}H_{54}$	35.00	7150	329.5	0–1

$a=2.795$ Å
σ/k, Å$^{-2}=2.172, 2.896, 5.792$
$\varphi=0, 1/2, 1$
Temperature: 315 °K to melting point.

until convergence is obtained. It is shown by LDP that this series converges to λ^j. This is easier than solving eq (5) for the λ^j directly. Moreover, for $n>2$ such direct solution is usually impossible. Iteration was carried out until B_p^j was within 1 part in 10^7 of B_{p-1}^j. Convergence took only a few hundred steps except near the melting point ($\lambda^j=0$, $S_T=0$) where convergence was slow (10^4 steps). The series does not converge for T above the melting point for that particular composition ($\lambda<0$, $S_T<0$).

(c) Having the λ^j, the N_ν^j were obtained by successive iteration of eq (6) starting with eq (8) until convergence to 1 part in 10^7 was obtained. N_0^j was chosen to be 10^6.

(d) The quantities S_j, S_T, f_j, and f_{ij} were calculated by eqs (9), (10), (12), and (15), respectively.

(e) Having calculated f_j we of course have the composition of the grown strip. We now choose $f_s=f$ (the fraction of species 1 in the strip) and repeat the procedure, and continue this until the calculated f is equal to f_s to one part in 10^6.

The range of parameters given in table 1 takes about five minutes of computation time.

4. Results

What we wish to know from the computations are

(a) The rate of growth (total flux, S_T) as a function of temperature and liquid composition.

(b) The composition of the crystal, f, crystallizing from a liquid of composition x_1 as a function of x_1 and temperature.

(c) The pair distributions f_{11}, f_{12}, and f_{22}.

To achieve these aims, computations were carried out for the values of the parameters listed in table 1. Calculations were carried out at liquid compositions x_1 from 0 to 1 by increments of 0.1 For each composition calculations were carried out for all the integer values of temperature from 315 °K up to the closest integer value to the temperature at which $S_T=0$. For each of the quantities of interest we are particularly interested in determining the effect of σ and φ.

4.1. The Total Flux

Representative results for the total flux (S_T) are given in figure 2. We have illustrated its behavior with temperature by giving plots of it against temperature for $\sigma=4$ and 8 and $\varphi=0$ and 1. The curves for the other values of the parameters are very similar.

In all cases the total flux is essentially linear with temperature, but perhaps more striking is the fact that the slope of these curves is almost independent of composition. This means that the total flux is dependent essentially only on the undercooling appropriate to that composition. This is not a totally unexpected result, for the change in crystal free energy with composition (aside from entropy of mixing effects) is small considering the similarity of the

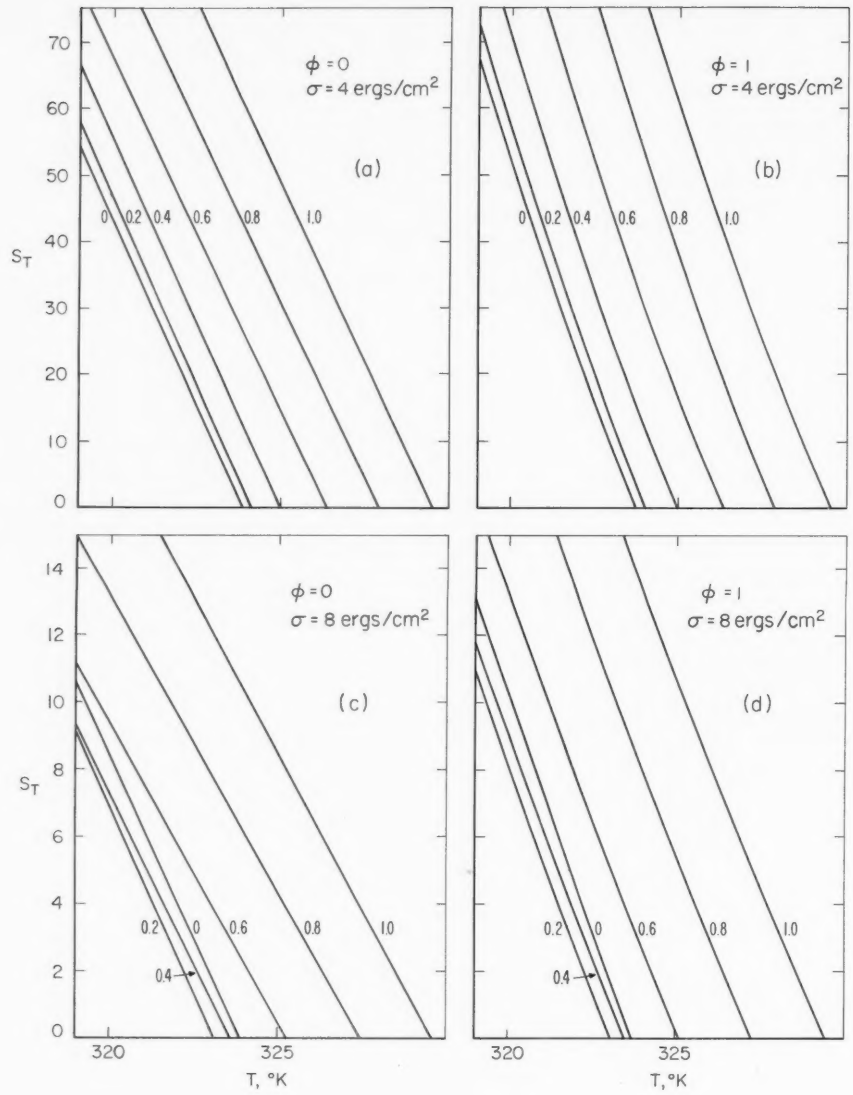

FIGURE 2. *Plots of total flux of crystallization versus temperature in binary mixtures of* $C_{24}H_{50}$ and $C_{26}H_{54}$.

Each of the four figures have plots for six values of liquid concentration of $C_{26}H_{54}$ ranging from 0 to 1. Figures 2(a) and 2(b) are calculated for $\sigma = 4$ ergs/cm^2 and for $\varphi = 0$ and $\varphi = 1$, respectively. Figures 2(c) and 2(d) are calculated for $\sigma = 8$ ergs/cm^2 and for $\varphi = 0$ and $\varphi = 1$, respectively. All plots are quite linear. When $\sigma = 4$ ergs/cm^2 the curves are displaced uniformly to higher temperatures with increasing liquid concentration of $C_{26}H_{54}$; when $\sigma = 8$ ergs/cm^2 the curves are first displaced to lower and then to higher temperatures with increasing liquid concentration of $C_{26}H_{54}$. This behavior results from the minimum that exists in the liquidus and solidus curves for the higher value of σ.

dimensions of the molecules. To the extent that these curves can be interpreted as rates of crystallization, they imply that this rate is dependent almost entirely on the undercooling appropriate to that composition.

A detailed analysis of these curves shows that their slopes are related systematically. If the average slope over the illustrated temperature interval is indicated by $m(\varphi,\sigma)$ then the following approximate relations hold:

$$\frac{m(\varphi, \sigma)}{m(0, \sigma)} = f(\varphi) \tag{37}$$

and

$$\frac{m(\varphi,\sigma)}{m(\varphi,\sigma_0)} = g(\sigma) \tag{38}$$

where $f(\varphi)$ and $g(\sigma)$ are functions only of φ and σ, respectively. This means that the variation of these slopes with φ for any given σ is independent of σ and the variation with σ for any given φ is independent of φ.

As previously discussed under the section on the transport terms, these slopes are not correct, for they do not contain the effect of this term. They should be multiplied by the factor a which is expected to be of the form

$$a = a_0 \exp\,[-\Delta H/kT]. \tag{39}$$

However, unless the preexponential factor a_0 and the activation energy ΔH are inordinately large, this will have only a negligible effect on the slopes over the eight degree range of undercoolings considered.

4.2. The Crystal Composition

The composition f of a strip crystallizing from a liquid with composition x_1 for various values of the parameter σ is shown in figures 3 and 4. Figure 3 is computed for $S_T = 0$ at all compositions and thus is a true phase diagram. The effect of the parameter φ is indistinguishable on the scale of these figures.

Figure 3 indicates that as the surface energy of the material is increased, a minimum in the phase diagram occurs, and the maximum separation between liquidus and solidus increases. Since σ is a measure of the interaction energy between the two species in the solid phase, this behavior is normal. Detailed calculations indicate that the liquidus and solidus curves approach the temperature axis horizontally for a σ value of 4.018 ergs/cm². The experimental curves given by Mazee [7] for this system indicate that the liquidus and solidus curves do not have such a horizontal portion, and we conclude that σ for the hexagonal rotator phase of the normal paraffins is somewhat less than 4 ergs/cm². This is to be compared with the value of about 12 ergs/cm² deduced from the data of Turnbull and Cormia [9] for the nonrotator phases.

Figure 4 looks superficially like the phase diagram, figure 3, but is not, for it is for kinetic conditions and hence the phase rule, which is derived for equilibrium, cannot be applied to it. This diagram gives the composition of the solid separating from a given liquid composition at constant total flux S_T and we call it a "kinetic phase-diagram," and even use the terms "liquidus" and "solidus," even though not entirely appropriately. The constant total flux was chosen by choosing the crystallization temperature for the pure x_2 case to be 321.0 °K (undercooling of 2.8 °C). The composition of crystal separating from a liquid of composition x_1 was then computed for this same flux, as well as the temperature at which this occurred. By the remarks made about the behavior of the total flux with temperature and composition, this gives *almost* a constant amount of undercooling throughout the diagram, but not quite, as is apparent from the $x_1 = 1$ end of the diagram.

The curves of figure 4 are superficially very similar to those of figure 3, and indeed it would take extremely careful experiments to be able to distinguish between the two. This indicates that even if conditions of exact equilibrium do not obtain when determining phase diagrams for this system, very little error will be made.

A more detailed analysis shows, however, that there are differences between these kinetic phase

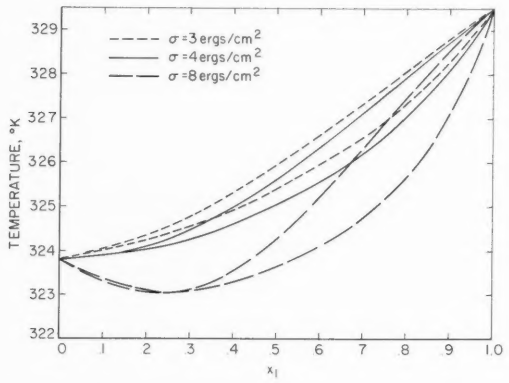

FIGURE 3. *Phase diagrams of the binary mixture of* $C_{24}H_{50}$ *and* $C_{26}H_{54}$ *for three values of* σ.

x_1 is the molar concentration of $C_{26}H_{54}$. This diagram represents the composition of the solid at equilibrium ($S_T = 0$) with a given liquid composition. The solidus curve falls below or touches the liquidus curve. As σ increases above 4.018 ergs/cm² a temperature minimum occurs in the phase diagram.

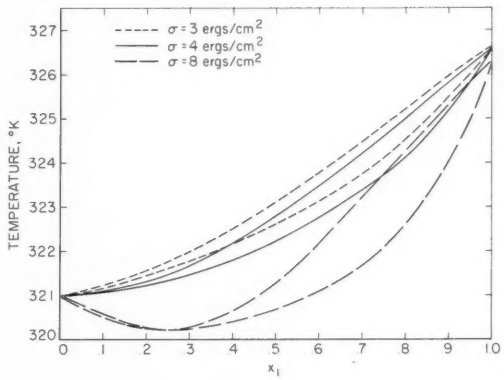

FIGURE 4. *A "Kinetic phase-diagram" of the binary mixture of* $C_{24}H_{50}$ *and* $C_{26}H_{54}$ *for three values of* σ.

x_1 is the molar concentration of $C_{26}H_{54}$. This diagram represents the composition of the solid separating from a given liquid concentration at constant total flux S_T. The total flux was chosen by choosing the crystallization temperature for the case $x_1 = 0$ to be 321.0 °K (undercooling of 2.8 °K). The composition of the crystal separating from a liquid of composition x_1 was computed for this same flux as well as the temperature at which this occurred. These curves have almost, but not quite, a constant amount of undercooling. The effect of the parameter φ is indistinguishable on the scale of this figure.

diagrams and the equilibrium phase diagram. The most striking difference is shown in figure 5 which is an enlargement of the region of the minimum for the curve calculated for $\varphi=1$ and $\sigma=8$ for the same total flux as in figure 4. This figure indicates that the minimum in the temperature-liquidus curve occurs at a different composition from that in the temperature-solidus curve. This could not, of course, occur in an equilibrium phase diagram, but there is nothing to preclude it happening in these kinetic diagrams. To the right of the vertical arrow the composition of the crystallizing solid is higher in species one than that of the liquid ($f>x_1$) while to the left it is lower ($f<x_1$). This is denoted by the horizontal arrows. At the point denoted by the vertical arrow the composition of the solid is the same as that of the liquid. This "equal-composition" point, which we denote by X_e, for an equilibrium phase diagram must, of course, occur at the minimum of the liquidus and solidus curves, but no such restriction occurs here.

It is to be noted that although the minimum in the liquidus and solidus curves occur at different compositions, the temperatures at the minima are the same. For this not to be true would require a double valuedness in the relation between f and x_1. But our α^{ij}, β^{ij}, and λ^j and the quantities calculated directly from them are continuous and single valued. Hence, this double-valuedness cannot exist, and the temperature at the minimum in both the solidus and liquidus curves must be the same. It is also clear on physical grounds, that any point on the liquidus curve must correspond to a point on the solidus curve, and vice versa. Thus the minimum in the two curves must be at the same temperature.

It is interesting to consider the effect of supercooling on the composition X_e. As the undercooling is increased, X_e decreases, and this is illustrated schematically in figure 6. In this figure we show the equilibrium phase diagram and one of the family of kinetic phase diagrams. On this figure there are shown three curves intersecting the kinetic phase diagram. These represent schematically the locus of $X_e(T)$, the locus of the minimum in the liquidus curve, $X_m(T)$, and the locus of points on the liquidus conjugate (i.e., at the same temperature) to X_e. This last locus we denote by X_e^c. The form of these curves is difficult to develop analytically. This much, however, can be said. The slope of $X_e(T)$ and $X_m(T)$ at the equilibrium diagram is negative. It does, however, depend upon φ and the σ involved, and this sign of the slope is not a general rule. The slope at the point where these curves cross the $x_1=0$ axis is positive, and also depends upon φ.

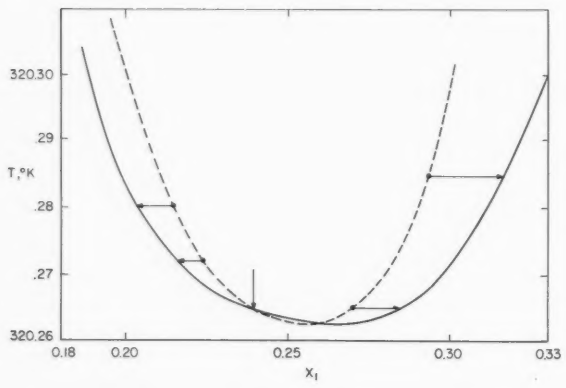

FIGURE 5. *An enlargement about the minimum of the "kinetic phase diagram" of figure 4 for $\sigma=8$ ergs/cm² and $\varphi=1$.*

Here the minima of the temperature-solidus (solid line) and the temperature-liquidus (dashed line) curves do not occur at the same composition. This could not occur in an equilibrium phase diagram. To the right of the vertical arrow the composition of the crystallizing solid is higher in $C_{30}H_{34}$ than that of the liquid, while to the left it is lower. This is indicated by the horizontal arrows. The vertical arrow indicates the "equal composition" point.

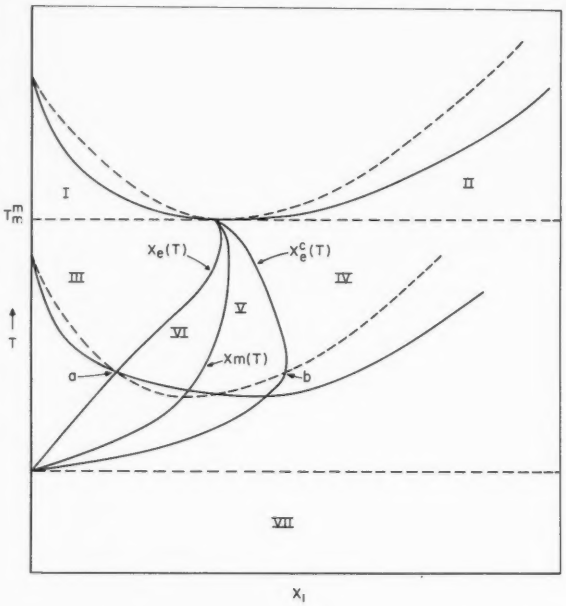

FIGURE 6. *Schematic presentation of the equilibrium phase diagram and one of the family of "kinetic phase diagrams" of a binary mixture of* n-*paraffins.*

Three curves intersect the "kinetic phase diagram." These curves represent schematically the locus of the equal composition point, $X_e(T)$, the locus of the minimum in the liquidus curve, $X_m(T)$, and the locus of the points conjugate to $X_e(T)$ (i.e., at the same temperature on the liquidus curve), $X_e^c(T)$. The temperature minimum of the equilibrium phase diagram is T_m^m. The supercooled area beneath the equilibrium phase diagram can be divided into 7 regions designated by Roman numerals and two points, a and b. In these 7 regions and at these two points the time dependence of the total flux are qualitatively different.

Moreover, the temperature $\overline{T}$ at which $X_e=0$ can be determined analytically. This can be shown to be

$$\overline{T}=\frac{\Delta h_1-\Delta h_2-6a\sigma(l_1-l_2)}{\Delta h_1/T_1-\Delta h_2/T_2}\,. \tag{40}$$

For the parameters for the curves in figures 4 and 5, $\overline{T}=232.5$ °K which is a completely unattainable under-

cooling. For $\sigma = 4.05$ ergs/cm² and all other parameters the same as for the above curves, $\overline{T} = 322.90$ which is an undercooling of only 0.9 deg, and hence in principle observable. However, in this case the minimum is very slight. For the system $C_{30}H_{62} - C_{35}H_{72}$, for which experimental data are available and a minimum exists, $\overline{T} = 191$ °K, and hence also completely unattainable. We thus conclude that the existence of $\overline{T}$ is a prediction of the LDP theory which is likely to remain academic.

The kinetic phase-diagrams in figures 4 and 5 give the composition of solid crystallizing at a given rate from a given composition of liquid. In other words, in a real system this gives the composition of the very first crystal formed. As time proceeds, however, the composition of the liquid changes, and it is interesting to deduce what happens to the total flux as time proceeds.

The most interesting case is that in which the phase diagram has a minimum, and the behavior in this case can be described with reference to figures 6 and 7. Figure 6 shows the equilibrium phase diagram and one of the family of constant flux kinetic phase diagrams. Those with smaller fluxes are above the illustrated kinetic phase diagram, and those with larger below. It is convenient to divide the temperature-composition space into seven areas, as shown, and two points, **a**, and **b**.

What happens to the total flux when a liquid of a given composition is brought to a temperature below the melting point and held at the temperature is shown for each of the seven regions and the two points in figure 7. The diagrams are almost self explanatory, but we will describe them briefly.

In regions I and II, as the liquid crystallizes, its composition changes such that the point describing it moves into areas where the crystallization rate is lower, finally reaching a point on the equilibrium liquidus curve at which time the flux drops to zero and crystallization ceases.

In regions IV and V, the flux initially decreases, but because the point representing the liquid composition crosses the curve, $X_m(T)$, the flux begins to increase again, eventually leveling off where the point reaches the $X_e(T)$ curve at, respectively, lower and higher values. If the initial liquid composition and temperatures are such that the initial liquidus point is on the $X_e^c(T)$ curve (point b), the flux first drops, but then increases back to its original value

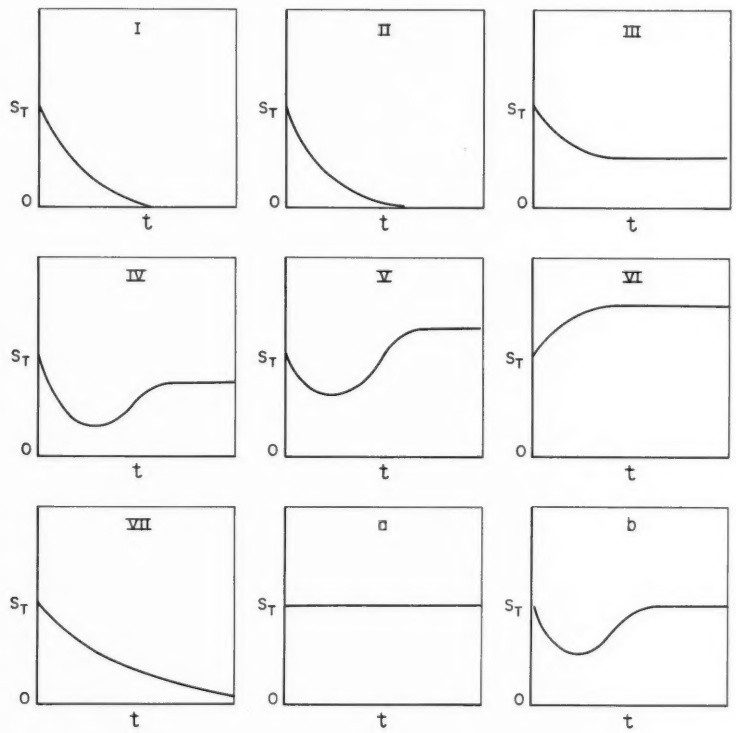

FIGURE 7. *Schematic plots of total flux, S_T, versus time for a binary mixture of n-paraffins that is represented in figure 6.*

Each plot represents schematically the time dependence of the total flux when crystallization begins in the indicated regions or at the indicated points of figure 6. In regions I and II crystallization does not proceed to completion.

when the liquid point reaches $X_e(T)$ and remains constant thereafter.

In region VI the flux increases monotonically since all points in this region are to the left of $X_m(T)$ eventually becoming constant when the liquid point reaches $X_e(T)$. In region III, the flux decreases monotonically until the liquidus point reaches $X_e(T)$ after which it becomes constant.

If the initial composition and temperature are such that the liquid point is on the curve $X_e(T)$ (point **a**), the composition and hence the flux are independent of time. This is clearly a generalization of the behavior at the minimum in the equilibrium curve.

In region VII (all points below $\overline{T}$) the flux decreases monotonically in time and reaches a constant value only when the species 1 is completely depleted from the liquid.

It should be pointed out again that although this behavior is a direct consequence of the LDP treatment, its experimental verification is likely to be very difficult, and its experimental importance relatively slight. In any real system the curves $X_e(T)$, $X_m(T)$ and $X_e^c(T)$ are almost certain to be practically coincident and vertical, and region VII will be unattainable. Thus, regions V, VI, and VII will practically disappear, and the behavior in all attainable regions will be such that the flux will decrease monotonically—to zero if the liquid point is above the minimum melting temperature but below the liquidus curve, and to a constant value if the liquid point is below the minimum melting temperature.

The last question we have to investigate is the occurrence of a eutectic. It is clear from what has been said about the continuous single-valued nature of our α^{ij}, β^{ij} and λ^j with respect to x_1 and f, that we will never obtain a eutectic unless we include its possibility in a more or less *ad hoc* manner. To do this it would be necessary to investigate the free-energy of the solid phase with respect to composition and determine if in some composition range the free energy of the solid is lower when expressed as a linear combination of two fixed solid compositions in standard ways [13]. For the values of the interaction parameter (σ) chosen here, this does not occur and no eutectic is formed. A simple calculation indicates that a value of σ greater than approximately 22 ergs/cm² is necessary before eutectic formation occurs at any reasonable undercooling. This is an unreasonably high value of surface energy for *n*-paraffins.

5. The Pair Distribution

As indicated in the introduction the pair distribution is easily calculated by the formalism of LDP. In order best to present typical results, in figure 8 we show plotted against composition f the difference between the observed f_{12} and the random mixing case, where f_{12} is given by $f(1-f)$. These are computed along the solidus line in figure 4 for $\sigma=4$ and 8 ergs/cm². This curve gives all the possible information about the pair distributions, for the following identities hold:

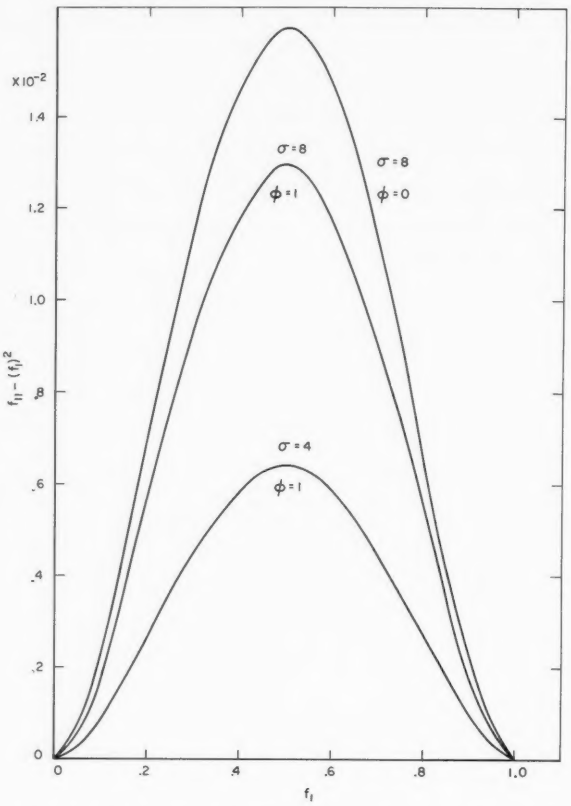

FIGURE 8. *Plot of the difference between the pair distribution* f_{11} *and the random mixing pair distribution* $(f_1)^2$ *versus the singlet distribution* f_1 *for various indicated values of* σ *and* φ.
These curves are calculated along the solidus curve in figure 4. The deviations from random mixing are very small.

$$f_{12}=f_{21}$$

$$f(1-f)-f_{12}=f_{11}-f^2$$

$$f_{11}-f^2=f_{22}-(1-f)^2.$$

First to be noticed in figure 8 is the small deviation of f_{12} from the random distribution. In the worst case this amounts to only about 6 percent at the $f=1/2$ point. This near equivalence is to be expected from the small magnitude of the interaction energy as expressed by $6a\sigma(l_1-l_2)$ in comparison to the entropy of mixing terms.

The effect of σ is such as to increase the deviation from randomness, as is to be expected, and the deviation is essentially proportional to σ for a given value of φ. The latter parameter causes a not inconsiderable effect, but we have no explanation for it.

The curves show an apparent symmetry about the point $f=0.5$. If this symmetry were indeed present,

it would mean that f_{12} is symmetric about $f=0.5$ since clearly the random case is. However, this symmetry is only apparent. Detailed investigation near $x=0$ and $x=1$ indicate that f_{12} is not symmetric about $f=0.5$. This is what would be expected considering the form of Equation 28, but the point is too recondite to pursue.

6. Conclusions

We have shown that by relatively routine calculations using the LDP method, it is possible to calculate the kinetics of growth and composition of new layers growing at a surface step on a growing crystal in a binary mixture when the solid phase forms a solid solution. This procedure is expected to be an adequate representation of one of the processes occurring in crystal growth when the average distance between kinks is of the order of ten or more lattice spacings. If this distance is very large then this calculation would give the kinetics of crystal growth, but it is expected that in the present application the results will be more accurate for the composition. If the calculations were made for a binary mixture of longer hydrocarbons (e.g., $C_{50}H_{102}-C_{52}H_{106}$) it may be expected that the distance between kinks would be large, and the flux calculated would have relevance to the crystal growth rates.

What it is necessary to know for the calculation in this paper are the rate constants for the addition and subtraction of a given species in the mixture to and from the growing strip. It is possible by equilibrium considerations to evaluate the free energy change in the system and relate this change to ratios of the rate constants for addition and subtraction, but it is not possible in general to evaluate the rate constants themselves. However, in this problem, various apportionments of this free energy change to the addition and subtraction rate constants have only minor effects on the results.

In the process of carrying out these calculations, specific account had to be taken of the two-dimensional nature of crystallization. This necessitated adapting the LDP theory, which is an exact theory for one-dimensional kinetic problems, to this two-dimensional problem. This was accomplished in an approximate, but in our view adequate, manner by appropriate modification of the rate constants.

Although these calculations were carried out on the rather simple binary system $C_{24}H_{50}$ and $C_{26}H_{54}$, there is in principle no reason why it could not be carried out on more complex mixtures, provided only that the interaction energy in the solid is not so great as to cause eutectic formation. Indeed, in the following paper we apply the LDP method to a system where as many as 50 components must be considered.

7. Appendix

In this appendix we derive expressions for (α^{ij}/β^{ij}) that are suitable for our model and our treatment. The physical model and the concepts are emphasized, while many mathematical steps are omitted.

We calculate these ratios from an ensemble that consists of a "mother liquor" formed by two hydrocarbon components that surrounds a large number of crystals. The crystals present N_T substrates to the "mother liquor" upon which strips can be formed. The length of a strip (the number of molecules crystallized from the "mother liquor") is designated by ν and ν can take on the values 0, 1, 2, . . ., ν_0.

We assume that all substrates have a uniform thickness, l_s. This uniform thickness is taken as the average thickness of the substrate, and is given by eq (23) of the text. The assumption of uniform thickness is necessary in order that we can apply our two component one-dimensional rate theory to the problem. This assumption is clearly an approximation, because the substrates will be of uneven rather than of uniform height. We shall see below that this assumption causes a modification of the rate constants.

The strips will be deposited upon the substrates in such a way that the free energy of the ensemble will be minimized. We shall determine the occupation numbers that characterize the strips such that the total free energy is minimized. These occupation numbers can be used to evaluate the ratio (α^{ij}/β^{ij}) by the principle of detailed balance. This is analogous to the method used in single component rate theory. In the present case this leads to [1]

$$\frac{\alpha^{ij}}{\beta^{ij}}=\left(\frac{P^{ij}_{\nu+1}}{N^i_\nu}\right)_e . \tag{1A}$$

In the present instance the ratio (α^{ij}/β^{ij}) is independent of ν, and we have anticipated this result in writing eq (1A). It should be noted that the occupation numbers on the right-hand side of eq (1A) are not the steady state occupation numbers obtained elsewhere in this paper. The total free energy of our ensemble is

$$G_T=\sum_{\nu=1}^{\nu_0} N_\nu G_\nu + kT\sum_{\nu=0}^{\nu_0} N_\nu \ln\frac{N_\nu}{N_T}. \tag{2A}$$

The reference state for this free energy expression is the state where no strips are deposited on the substrates. The average free energy of a strip of length ν is given by

$$G_\nu=\sum_{j=1}^{2} q^j_{\nu,1}[\epsilon^0_j-\mu_j+kT\ln q^j_{\nu,1}]$$

$$+\sum_{\eta=2}^{\nu}\sum_{i=1}^{2}\sum_{j=1}^{2} q^{ij}_{\nu,\eta}[\epsilon_{ij}-\mu_j+kT\ln p^{ij}_{\nu,\eta}]. \tag{3A}$$

The quantities appearing in eqs (2A) and (3A) have all been defined in the text. The quantities appearing

in these equations are not independent but must satisfy the following relations:

$$\sum_{\nu=0}^{\nu_0} N_\nu = N_T, \tag{4A}$$

$$\sum_{j=1}^{2} q^j_{\nu,1} = 1 \quad \sum_{i=1}^{2}\sum_{j=1}^{2} q^{ij}_{\nu,\eta} = 1, \tag{5A}$$

$$q^j_{\nu,1} = \sum_{i=1}^{2} q^{ji}_{\nu,2} \quad q^j_{\nu,\eta} = \sum_{i=1}^{2} q^{ji}_{\nu,\eta+1} = \sum_{i=1}^{2} q^{ij}_{\nu,\eta}. \tag{6A}$$

In addition the conditional probabilities in Equation (3A) satisfy the relations

$$q^{ij}_{\nu,\eta} = q^i_{\nu,\eta} p^{ij}_{\nu,\eta} \tag{7A}$$

$$\sum_{j=1}^{2} p^{ij}_{\nu,\eta} = 1. \tag{8A}$$

The fraction of component one in the strips is ω and is given by

$$\omega = \frac{\sum_{\nu=1}^{\nu_0} N_\nu \sum_{\eta=1}^{\nu} q^1_{\nu,\eta}}{\sum_{\nu=1}^{\nu_0} \nu N_\nu}. \tag{9A}$$

We discuss below the relationship between f_s and ω-the fractions of component one in the substrate and strips respectively.

We have written down the total free energy of the ensemble. In order to determine the occupation numbers that minimize this free energy, we calculate the variation of G_T, allowing the N_ν, $q^j_{\nu,1}$, $q^{ij}_{\nu,\eta}$, f_s, and ω to vary, and equate δG_T to zero. Since these quantities are not all independent, but instead are related by eq (4A), (5A), (6A), and (9A), we introduce Lagrange multipliers with these equations. Then the coefficients of δN_ν, $\delta q^j_{\nu,1}$, and $\delta q^{ij}_{\nu,\eta}$ are equated to zero.
This leads to quite complicated expressions, but the algebra is relatively straightforward.

The procedure followed here is similar to that employed by Mullins [14] for Markov chains, except that in our case the chains have finite lengths and the matrices involved are not symmetric. We shall not write down the equations involved but merely write down the solutions which are most easily expressed in matrix notation. Let us define the W matrix

$$(W)_{ij} = w_{ij} = x_j \exp\left\{\frac{\Delta g_j}{kT} - \frac{2a\sigma U(l_j - l_i)}{kT} - \frac{4a\sigma(l_1 - l_2)}{kT}\left[(1 - f_s - \Gamma)\delta^j_i + \Gamma\omega\right]\right\} \tag{10A}$$

The quantity Γ in this equation is a Lagrange multiplier associated with the variation of eq (9A).

We also define the row vector

$$w'_0 = (w^1_0, w^2_0) \tag{11A}$$

where

$$w^j_0 = x_j \exp\left\{\frac{\Delta g_j}{kT} - \frac{2a\sigma l_j}{kT} - \frac{4a\sigma(l_1 - l_2)}{kT}\left[(1 - f_s - \Gamma)\delta^j_i + \Gamma\omega\right]\right\} \tag{12A}$$

With these quantities we can write down our solutions as

$$q^{ij}_{\nu,\eta} = \frac{w'_0 (W)^{\mu-2}\begin{pmatrix}\delta^i_1\\ \delta^j_2\end{pmatrix} \omega_{ij}(\delta^i_1, \delta^j_2)(W)^{\nu-\eta}\begin{pmatrix}1\\1\end{pmatrix}}{w'_0 (W)^{\nu-1}\begin{pmatrix}1\\1\end{pmatrix}}, \tag{13A}$$

$$q^j_{\nu,\eta} = \frac{w'_0 (W)^{\eta-1}\begin{pmatrix}\delta^j_1\\ \delta^j_2\end{pmatrix} (\delta^j_1, \delta^j_2)(W)^{\nu-\eta}\begin{pmatrix}1\\1\end{pmatrix}}{w'_0 (W)^{\nu-1}\begin{pmatrix}1\\1\end{pmatrix}}, \tag{14A}$$

and

$$\frac{N_\nu}{N_0} = w'_0 (W)^{\nu-1}\begin{pmatrix}1\\1\end{pmatrix} \tag{15A}$$

These solutions allow us to evaluate the occupation numbers and evaluate the ratio of the rate constants.

$$\frac{\alpha^{ij}}{\beta^{ij}} = \left(\frac{P^{ij}_{\nu+1}}{N^i_\nu}\right)_e = \frac{N_{\nu+1} q^{ij}_{\nu+1,\nu+1}}{N_\nu q^i_{\nu,\nu}} = w_{ij} \tag{16A}$$

We therefore have an expression for the ratio of the rate constants.

Our solution is not complete, for the elements of the (W) matrix contain the quantities Γ and ω, which as yet have not been determined. We can obtain two further relationships. From eqs (9A), (14A), and (15A) it can be shown that for ν_0 very large

$$f = \frac{z - w_{22}}{2z - w_{11} - w_{22}} \tag{17A}$$

where z is the largest eigenvalue of the W matrix. This equation provides a relationship between ω and Γ.

A further relation is obtained by considering the variation of the ensemble total free energy. Using Equations (13A), (14A), and (15A) this becomes

$$\delta G_T = 4a\sigma\left(\sum_{\nu=1}^{\nu_0} \nu N_\nu\right)(\Gamma\delta\omega - \omega\delta f_s). \tag{18A}$$

This equation relates the variation of the total free

energy of the ensemble to the variation in the composition of the substrates and strips.

The two dimensional character of our problem must be kept in mind in our treatment of this equation. This can be illustrated by considering a truly one dimensional problem as an example: Let the mother liquor and strips be the two component system of hydrocarbons under consideration, but suppose the substrate consists of a third component, say still another hydrocarbon. Then we need consider no variation in f_s i.e., $\delta f_s = 0$. In this case in order that $\delta G_T = 0$, we set $\Gamma = 0$. The ratios of the rate constants become the usual Boltzmann factors that were derived in [1]. These rate constants are the proper ones for the one dimensional problem. However, if we follow this procedure in the present problem (i. e., set $\delta F_s = 0$, $\Gamma = 0$), the resulting rate constants are not the proper ones. This is most clearly seen when the equilibrium phase diagram has minima in the liquidus and solidus curves. These minima do not occur at the same value of the concentration, which would imply a region of concentrations where no stable equilibrium exists.

We must therefore treat eq (18A) more carefully. Suppose we have a particular liquid concentration at a particular temperature. There will exist a crystal concentration, $f_e(x_1,T)$, that is most stable. That is, if we vary the concentration of the crystal ($\delta f = \delta f_s$)

$$\delta G_T = 4a\sigma \left(\sum_{\nu=1}^{\nu=0} \nu N_\nu \right) (\Gamma - f_e)\delta f_s = 0$$

so that

$$\Gamma = f_e(x_1, T) = \omega = f_s. \tag{19A}$$

This property must hold at equilibrium (i.e., where x_1,T fall on the equilibrium liquidus curve), but it also will hold at other concentrations and temperatures. This result does not solve our problem, however, except at particular values. We wish a value of Γ that holds for any values of (x_1, T, f_s), while eq (19A) yields a value of Γ that holds for (x, T, $f_s = f_e$). When the kinetics of the crystallization process leads to values of $f_s \neq f_e$, it cannot be expected that δG_T vanishes.

A more critical analysis would be required to obtain values of Γ for general values of (x_1, T, f_s). Such an analysis does not seem worthwhile, because we have already introduced the approximation that the substrate height is uniform. Instead we shall assume

$$\Gamma = f_s. \tag{20A}$$

This assumption satisfies eq (19A) when $f_s = f_e$, and should be reasonably accurate at other values of f_s. At thermal equilibrium it satisfies our requirements.

We therefore have

$$\frac{\alpha^{ij}}{\beta^{ij}} = x_j \exp\left\{ \frac{\Delta g_j}{kT} - \frac{2a\sigma U(l_j - l_i)}{kT} - \frac{4a\sigma(l_1 - l_2)}{kT}[(1-2f_s)\delta_1^j + f_s\omega] \right\}. \tag{21A}$$

In this equation ω is the value that must satisfy eq (17A). This can be expressed as

$$2\omega - 1 = \frac{\xi - 1 + x_1}{\sqrt{(\xi - 1 + x_1)^2 + 4(1-x_1)\,\xi \exp\left\{\frac{2a\sigma(l_1 - l_2)}{kT}\right\}}} \tag{22A}$$

where

$$\xi = x_1 \exp\left\{ \frac{\Delta g_1}{kT} - \frac{\Delta g_2}{kT} - \frac{4a\sigma(l_1 - l_2)(1-2f_s)}{kT} \right\}. \tag{23A}$$

Then we see that for any values of (x_1, T, f_s) we can obtain ω from eqs (22A) and (23A). Then the ratios (α^{ij}/β^{ij}) are obtained from eq (21A). Equation (21A) is the same as eq (28) of the text.

8. References

[1] J. I. Lauritzen, Jr., E. A. DiMarzio and E. Passaglia, J. Chem. Phys. **45,** 4444 (1966).
[2] J. I. Lauritzen, Jr. and J. D. Hoffman, J. Res. NBS **64A** (Phys. and Chem.) No. 1, 73 (1960); J. D. Hoffman and J. I. Lauritzen, Jr., Ibid. **65A** (Phys. and Chem.) No. 2, 297 (1960).
[3] F. C. Frank and M. Tosi, Proc. Roy. Soc. **A263**, 323 (1961).
[4] F. P. Price, J. Chem. Phys. **35,** 1884 (1961).
[5] W. K. Burton, N. Cabrera and F. C. Frank, Phil. Trans. Roy Soc. (London) **A243,** 299 (1951).
[6] I. M. Dawson and V. Vand, Proc. Roy. Soc. **A206,** 555 (1951).
[7] W. M. Mazee, Anal. Chim. Acta **17,** 97 (1951).
[8] W. M. Mazee, Erdöl u. Kohle **13,** 88 (1960).
[9] D. Turnbull and R. L. Cormia, J. Chem. Phys. **34,** 820 (1961).
[10] M. G. Broadhurst, J. Research NBS **66A** (Phys. and Chem.) No. 3, 241 (1962).
[11] P. J. Flory, R. A. Orwall and A. Vriz, J. Phys. Chem. **86,** 3515 (1964).
[12] V. Vand, Acta. Cryst. **6,** 797 (1953).
[13] J. C. Slater, Introduction to Chemical Physics, (McGraw-Hill Book Co., New York, N.Y., 1939).
[14] W. W. Mullins, Phys. Rev. **114,** 389 (1959).

(Paper 71A4–457)

JOURNAL OF RESEARCH of the National Bureau of Standards—A. Physics and Chemistry Vol. 71A, No. 4, July-August 1967

Kinetics of Crystallization in Multicomponent Systems: II. Chain-Folded Polymer Crystals

John I. Lauritzen, Jr., and Elio Passaglia

Institute for Materials Research, National Bureau of Standards, Washington, D.C. 20234

(April 19, 1967)

Using polyethylene as an example, the kinetics of growth of chain-folded polymer crystals is treated using a theory for the kinetics of growth of chains in multicomponent systems. The kinetic chain is considered to be a chain-folded strip growing on the lateral face of a chain-folded lamella, and the various components are the possible lengths l_j the polymer chain may form on folding at the end of the growing strip. Thus, the number of components is in principle infinite, but it is sufficient to take a number of the order of 20–50 for the calculations. By an iteration procedure, the calculations are carried out so that the average thickness of the strip is the same as that of the chain-folded lamella on which it grows. This necessitates modification of the rate constants that would be used without this requirement. The rate of growth, average thickness and its standard deviation, and the pair distribution are calculated as a function of undercooling and other relevant parameters of the system. The results for the rate of growth and thickness are similar to those of simpler theories, provided that the constant end-surface free-energy of those theories is replaced by a temperature dependent "effective" surface free-energy. The standard-deviation of the thickness is larger than commonly believed, values of 8 to 14 Å being typical. Consequently, the crystals as grown may have quite rough fold surfaces, although the equilibrium roughness will be less.

Key Words: Chain-folded crystals, Crystal growth, kinetics, multicomponent systems, surface free-energy.

1. Introduction

In the preceding paper in this issue [1][1] (henceforth referred to as I) we demonstrated how a theory [2] (henceforth referred to as LDP) of the kinetics of growth of chains in multicomponent systems could be applied to the kinetics of crystallization in binary systems. The chain is considered to be a layer of molecules deposited at a growth step. The system chosen for study in I was that composed of the *n*-paraffins $C_{24}H_{50}$ and $C_{26}H_{54}$. It was shown in I that it is relatively easy using the LDP method to calculate the total flux, the composition of crystal growing from a given composition of liquid, and the pair distribution. Phase diagrams at equilibrium (total flux zero) and kinetic conditions (total flux greater than zero) were calculated, and the behavior of the flux with temperature deduced.

In I, there is some question about the relationship between the calculated flux and the crystal growth rate. In the present case a layer of chain-folded segments growing at the lateral surface of a chain-folded lamella forms the kinetic chain. This layer is expected to have only a very small number of kinks (if any) and hence the kinetics of growth of such a layer will quite accurately represent the rate of crystal growth. Indeed, this is the usual approach taken in theories of polymer crystallization [3, 4, 5].

It is our purpose, then, to apply the LDP theory to the problem of the kinetics of formation of chain folded polymer crystals. Several quite adequate theories for this problem are available [3, 4, 5], but they all have some deficiencies. These arise primarily from the methods of treating fluctuations in the lamellar thickness. In the theory of Hoffman and Lauritzen [3], fluctuation is not treated directly. Under given conditions, it is assumed that a uniform lamella (or, in the sense of I, a uniform strip) will grow. The growth rate as a function of the thickness is calculated, and this is maximized with respect to thickness. The thickness which gives the maximum rate is considered to be the thickness growing under those conditions, and its value is given by the well-known equation, derived for small undercoolings,

$$l_g^* = \frac{2\sigma_e T_m^0}{\Delta h \Delta T} + \frac{kT}{a\sigma} \tag{1}$$

where l_g^* is the thickness, σ_e the end surface free-energy, Δh the heat of fusion per unit volume of crystal, σ the lateral surface free-energy, a the lateral dimension of the unit cell, T_m^0 the melting point of the infinitely thick lamella, T the absolute temperature, ΔT the undercooling and k Boltzmann's constant. The distribution in thickness of these uniform strips

[1] Figures in brackets indicate the literature references at the end of this paper.

about this maximum rate thickness is also calculated and shown to be relatively small [3].

Clearly, this treatment is not completely adequate. Rather than *assuming* that a uniform strip grows, and consequently laying down segments of uniform length at the end of the growing strip, the deposited segment length should be permitted to vary, so that each deposited segment should have all possible lengths. This larger problem was attacked by Frank and Tosi [4] in their extension of the Hoffman-Lauritzen theory by permitting a single fluctuation in the segment length.

In addition to this, Frank and Tosi investigated the effect of change in substrate thickness, as discussed in I in the section on the effect of the two-dimensional character of crystallization, but again by allowing only a single fluctuation. This treatment led to the disquieting result that crystallization cannot occur at an undercooling less than

$$\Delta T = \sigma T_m^0 / a \Delta h. \tag{2}$$

The only complete attack on the problem was made by Price, who permitted all possible lengths for each segment deposited at the end of the growing strip. However, Price adapted a formalism developed by Mullins [6] for the distribution in Markov chains any step of which may go into any of n states, and this method is useful only when equilibrium obtains in the growing chain. (This equilibrium does not, of course, pertain to the whole lamella, for the equilibrium thickness implicitly assumed in all the kinetic theories is infinite.) It should thus be exactly applicable only when the crystallization rate is zero, although for very small undercoolings not too much error is likely to be made, as pointed out in I. For polymer crystallization, however, rather large undercoolings are easily attainable (indeed, they are the rule) and under these conditions significant differences between this equilibrium treatment and a truly kinetic theory may arise. Moreover, the equilibrium theory cannot, of course, say anything about the rate of crystallization.

In this paper we solve a problem which in our view is a more reasonable theoretical approximation to the true situation in polymer crystallization than any of the previously given treatments. The problem is best formulated with reference to figure 1. We have a substrate, which represents an already-grown chain folded lamella, of thickness l_s. On the edge of this lamella a new strip of chain folded material is initiated and grows. The thickness of the initial segment of the strip laid down is l^1; the molecule then folds and lays down a segment of thickness l^2; this in turn folds and lays down a segment of thickness l^3, etc. Each of the thicknesses l^1, l^2, l^3, etc. may have any value. We wish an answer to these questions: (a) What is the rate of growth (at steady state) of the strip as a function of the relevant parameters of the system? (b) What is the average thickness of the strip? (c) What is the width and nature of the distribution about this average? (d) What are the pair distributions, i.e., how much correlation is there between segments of various thicknesses?

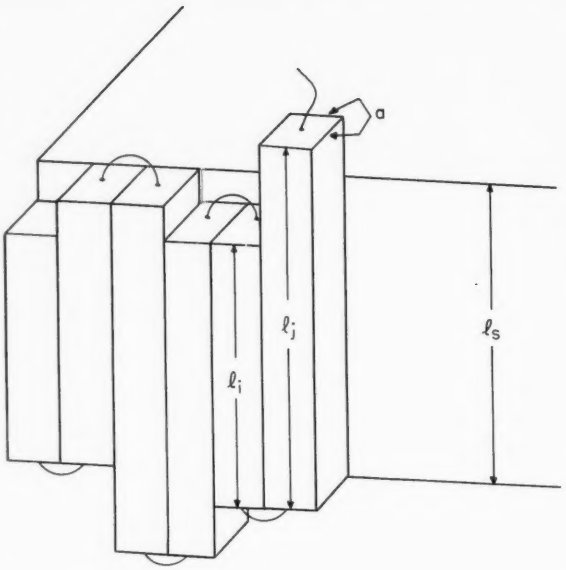

FIGURE 1. *Schematic diagram for the model of a chain folded strip growing on the lateral face of a chain-folded lamella of uniform thickness.*
The growing strip is the kinetic chain of the LDP theory [2], and the segment lengths (or thicknesses) l_i and l_j are the various components of the system.

It is clear that this problem is one that may be solved by the LDP theory. The "chain" in that theory is represented by the "strip" in this problem, and the components are the possible thicknesses l_j. These various thicknesses l_j are then considered as various "species" j, each species being one of the components of the system, and in what follows we will use the words "chain" and "strip," and "species j" and "thicknesses l_j" interchangeably. Considered in this sense, the "species" are evanescent things; they do not exist in the liquid phase and come into existence only when the random coil polymer chain in the liquid phase folds with the thickness l_j onto the lateral face of the growing crystal. Except for this character of the "species" this is, then, similar to the problem solved in I, but the number of components is, of course, larger than two. Indeed it is, in principle, infinitely large for an infinite molecular weight polymer. Since the LDP theory cannot easily be adapted to an infinite number of components, for the calculations a number of sufficient size must be taken so that the results are not affected by taking a larger number. This will be discussed more fully below.

An outline of the method by which these calculations may be made has already been given in I and in reference [2] and will not be repeated here. We will, however, give some pertinent equations which are necessary for the subsequent exposition. The LDP theory assumes only nearest neighbor interactions,

and assumes knowledge of the rate constants α_0^j, β_1^j, α^{ij} and β^{ij}, which are rate constants for the forward and backward processes for, respectively, the initial and subsequent steps in the chain. The kinetic equations for chain growth at steady state are solved in terms of quantities λ^j defined by

$$\lambda^j = \sum_{i=1}^{n} \frac{\alpha^{ji}\lambda^i}{\beta^{ji} + \lambda^i} \tag{3}$$

where n is the number of components in the system. The total flux is given by

$$S_T = \sum_{j=1}^{n} \frac{\alpha_0^j N_0 \lambda^j}{\beta_1^j + \lambda^j} \tag{4}$$

where N_0 is simply a scaling factor. The fraction f_i of species i in the grown chain is given by

$$f_i = \frac{\lambda^i N^i}{S_T} \tag{5}$$

and the N^i in turn are obtained from the recursion relation

$$N_\nu^i = \sum_{j=1}^{n} \frac{\alpha^{ji} N_{\nu-1}^j}{\beta^{ji} + \lambda^i} \tag{6}$$

with N_1^i given by

$$N_1^i = \frac{\alpha_0^i N_0}{\beta_1^i + \lambda^i}. \tag{7}$$

For large ν, eq (6) becomes independent of ν and becomes the matrix equation

$$N^i = \sum_{j=1}^{n} \frac{\alpha^{ji} N^j}{\beta^{ji} + \lambda^i}. \tag{8}$$

The pair distribution function, f_{ij}, which gives the fraction of i, j pairs in the system is given by

$$f_{ij} = \frac{\lambda^j \alpha^{ij} N^i}{\beta^{ij} + \lambda^j} \cdot \frac{1}{S_T}. \tag{9}$$

With these equations, and knowing the rate constants, the complete problem may be solved, and the description of the method of calculation will be given in a subsequent section.

There are two processes conceptually possible in the chain fold problem that are not considered by the LDP theory, and one of which is not possible in I. These are processes by which a given species at a given position in the chain may be replaced by another species. In the LDP theory, the only way in which a certain species j (thickness l_j) at a given position ν in the chain (position in the strip) can change to species i is by removal of all species from positions ν, $(\nu+1)$, etc. (i.e., "melting" of the strip back to position $(\nu-1)$) and then replacing species j at position ν with species i at that position. In the present problem, however, it would seem relatively easy to change species at a given location by readjustment in the lengths of segments between folds, provided only that the contour length of the deposited polymer chain remain unaltered. (In I such a change of species would require an actual interchange of molecules.) This process, which is not considered in this treatment, may, as will be discussed below, have important consequences in the experimental correlation of values of surface energies obtained from crystallization experiments with those obtained from melting point experiments. In the second process, the change of species j to species i at position ν can be accomplished by only *incomplete* removal of species j and subsequent refolding to the length appropriate to species i. The importance of this process is difficult to assess without a detailed theory in which it is incorporated.

Of these two processes the first clearly is not part of the sequential growth process of the strip, and arises from rearrangements after the strip has grown. Its effect in the present treatment will not change the growth rate, insofar as this can be considered as determined by the sequential deposition of segments at the lateral face of the growing lamella. Nor, in fact, will it change the average thickness of the strip, for the contour length of the polymer chain must be preserved. But it may have an important bearing on the ultimate *distribution* of thicknesses in the strip and will affect the pair and higher distributions. We will return to this point later; for the present it should be borne in mind that the distributions we compute are those determined by the kinetic process of growth and not necessarily those obtaining after rearrangements occur.

For the calculations we use parameters appropriate to polyethylene, since the crystallization behavior of this polymer is better understood than that of any other. Unlike the approach in I, our aim in this paper is an intensive study of this well-known system. The results are illustrative of what happens in polymer crystallization in general.

2. The Rate Constants

2.1. Preliminary Considerations

In order to apply the LDP theory we need to know the rate constants α_0^j, β_1^j, α^{ij} and β^{ij}, which are, respectively, the rate of initiation of new strips by depositing from the melt or solution the species l_j on a fresh substrate; the rate of dissolution of this back to melt or solution; the rate of adding species j to a strip whose

terminal element is species i; and the rate of removal of species j from a strip whose terminal elements are i and j. Under kinetic conditions, these rate constants are impossible to deduce without knowing the exact details of the elementary processes involved in adding and subtracting species from the chain. However, it is shown in LDP that at equilibrium (total flux or rate of crystallization zero) the ratios of α_0^j/β_1^i and α^{ij}/β^{ij} are given by

$$\frac{\alpha_0^j}{\beta_1^j} = \exp\left[(\mu_j - \epsilon_j^0)/kT\right] \tag{10a}$$

$$\frac{\alpha^{ij}}{\beta^{ij}} = \exp\left[(\mu_j - \epsilon_{ij})/kT\right] \tag{10b}$$

where μ_j is the chemical potential of species j in the liquid phase, and ϵ_j^0 and ϵ_{ij} are, respectively, the free energies of initiating a chain and of adding species j to a chain terminating in species i. Clearly, the arguments of these exponentials are the changes in free energy of the system which result from removing the species j from solution or melt and placing it on the substrate, divided by kT.

These equations give only the ratio of the rate constants; without more knowledge we do not know how to apportion this free energy change between the forward and backward rate-constants. Frank and Tosi [4] considered the problem of apportionment and came to the conclusion that it was reasonable to assign all the free energy change to the energetically more unfavorable step. As in I, we, however, adopt a somewhat more empirical approach. We first *assume* that under kinetic conditions, the rate-constant ratio is still given by eqs (3). Then we carry out calculations for various arbitrary assignments of the free energy change.

The calculation of this free energy change is easily carried out by a method similar to that used by Price [5] and outlined in I. More elaborate and more accurate methods could doubtless be used. In particular, for crystallization from solution, the Flory-Huggins theory [7] of polymer solutions could be used to evaluate μ_j, but to enter into this much detail at this stage of our knowledge of polymer crystallization adds a detail which is unnecessary for the understanding of the elements of the problem. In the method used by Price each species added to the growing strip is considered to be a rectangular parallelepiped. We assumed it to have a square cross-section with an area one half the area of the (001) cross section of the polyethylene unit cell. This parallelepiped is considered to have a surface free energy σ per unit lateral area and σ_e per unit end area. Then, if the strip grows on a substrate of thickness l_s, and with reference to figure 1, we may write

$$\mu_j - \epsilon_j^0 = a^2 l_j \frac{\Delta h \Delta T}{T_m^0} - 2al_j\sigma - 2a\sigma U(l_j - l_s) + kT \ln \Delta l/\delta \tag{11a}$$

$$\mu_j - \epsilon_{ij} = a^2 l_j \frac{\Delta h \Delta T}{T_m^0} - 2a^2\sigma_e - 2a\sigma U(l_j - l_i) - 2a\sigma U(l_j - l_s) + kT \ln \Delta l/\delta \tag{11b}$$

where Δh is the heat of fusion per unit volume of crystal, T_m^0 is the melting point of the infinitely thick lamella, $\Delta T = T_m^0 - T$, and $U(x)$ is the function

$$U(x) = x \qquad x \geq 0$$

$$U(x) = 0 \qquad x \leq 0.$$

Except for the term $kT \ln \Delta l/\delta$ (which is discussed below) these are the same energies used by Price, although he symmetrized the matrix composed of them because of the requirements of the Mullins treatment, and which in any case is the correct procedure at equilibrium. In our own case it will be noticed that the $\mu_j - \epsilon_{ij}$ matrix is not symmetric.

It will be noticed that in eq (11a) we do not have a term involving the end surface energy. This is not an omission. In our view, the first segment attached to the substrate has a length of dangling polymer chain on each end. One end (or possibly both) will subsequently fold, but we take the energy necessary for this into account in the energy for the next step (eq llb, and see below under Apportionment of Free Energy). The first step, as we count them, does not involve folding. What *should* be added is a term involving the localization of the chain, but such a term is difficult to calculate. Moreover, the initial rate constant is important primarily in determining the temperature dependence of the total flux, and such terms as this would add negligibly to this temperature dependence. We also note that if the end of the polymer chain is considered to lie flush with the edge of the substrate (in our view a highly unlikely event) then this would involve a surface energy more like σ than σ_e.

The term $kT \ln \Delta l/\delta$ does not arise from fundamental causes but only because of computational limitations. In this term δ represents the minimum length difference between unlike species (generally the length of one unit cell c dimension) and Δl represents the difference in length between two adjacent species chosen for the computation, i.e., $\Delta l = l_{j+1} - l_j$. For very broad distributions, as are found in this problem as will be discussed fully under Results, it is necessary to have a very wide range of lengths. Now, the number of components in the system is this range of lengths divided by the difference in length between adjacent species. This length difference should be the "natural" length δ, but this makes the number of components greater than the capacity of the computer (on the order of 50 components). Hence, it is necessary to use a larger length, Δl. This in turn causes an underestimation of the free-energy change on crystallization because each "species" chosen for the calculation represents $\Delta l/\delta$ "natural" species, resulting in an incorrect estimation of the entropy of

$k \ln \Delta l/\delta$. When comparing calculations carried out for various Δl it is important to include this term.

The rigid-rod approximation for the species used in calculating these free energies is expected to be only a crude approximation to the true energies involved. This approximation will be worse the larger the length of species j is compared to the substrate. For large differences (what might be called large "overhangs") the portion of the chain extending above the substrate will doubtless be some type of random loop, and the use of the rigid-rod approximation should not be taken to imply that this is our view of the true physical state of these overhanging chains. The rigid-rod approximation is in our view, however, a good approximation for those chains shorter than the substrate and those only slightly longer. We use it for all lengths because it is difficult to know exactly at what lengths to begin treating the overhanging chains as random coils, and because such treatment would in itself be subject to considerabe uncertainty. All that we can say with certainty about these greatly overhanging chains is that their free energy is higher than that of the same chains in the crystalline state and the rigid-rod approximation adequately takes this into account. Moreover, to treat properly large loops of random coils on the surface would involve more than nearest neighbor interactions, and a thorough treatment of the problem would become quickly intractable.

As have previous authors, we neglect those (presumably rare) occasions where l_j may be less than l_s but still protrude beyond the substrate.

2.2. The Effect of the Two-Dimensional Nature of the Problem

As already discussed in I, the process of crystallization has a two-dimensional character that makes it difficult to treat by the one-dimensional LDP theory. Thus, when the composition of the growing strip is calculated by the LDP theory, there is no assurance that its average thickness, defined as

$$\bar{l} = \sum_j f_j l_j \tag{12}$$

where f_j is the fraction of species j in the grown strip, is the same as that of the substrate. Clearly, if our calculations are to represent a real physical process of crystallization, this is a minimum requirement. It would appear that this physical process could easily be represented by choosing a substrate thickness l_s, growing a strip on it, using this strip as a substrate for a subsequent strip and continuing the process until $l_s = \bar{l}$. This is essentially the procedure used by Price. This would meet the requirement that the thickness of the growing crystal would be constant, but would not assure us that the pair and higher distributions in the strip and the substrate would be the same; but it would be a first and reasonable approximation to the true physical situation.

If this process is carried out with the rate constants calculated by eqs (10) using the energies in eqs (11), it is found that crystallization does not proceed at temperatures above by some finite undercooling, essentially as was found by Frank and Tosi. Above these temperatures the thickness converges to a value below that stable for that undercooling and the flux drops to zero. This does *not* occur if the thickness of the substrate is not allowed to vary.

In this problem, as also in I, when rate constants appropriate to a one-dimensional problem are used for a two-dimensional one, difficulties are encountered. In particular, we would expect our theory to predict crystallization at temperatures near the melting point for it is at these temperatures that the steady-state conditions assumed would be most likely to obtain. Thus, the result that crystallization does not proceed at a temperature *above* a relatively large undercooling (about 33 degrees) seems to us to be the result of an incorrect treatment of an essentially two-dimensional problem by a one-dimensional theory, and results as an artifact of the treatment. However, it should be noted at this time, that in the process of correcting this difficulty we trade it for another, but perhaps more explicable one. This is discussed fully in the section on the Total Flux.

The only proper way to overcome this difficulty would be to construct a truly two-dimensional theory. This would be a truly formidable task. As in I, we adopt a more realistic course of action and ask if there is some way of modifying the rate constants so that physical results will be obtained over the entire temperature range.

In order to answer this question, the same type of variational analysis carried out in the appendix to I may be carried out for this problem. That is, an ensemble consisting of crystals of various thicknesses each with strips of various thicknesses and lengths growing on them is considered. The free energy of this system is expressed in terms of the number of strips and their lengths, compositions, thickness and substrate thicknesses. This free energy is minimized with respect to these variables. Then, using the principle of detailed balance it may be shown that the rate constant ratio that minimizes this free energy *at equilibrium* (total flux zero, but not necessarily at the melting point) is given by

$$\frac{\alpha_b^i}{\beta_i^i} = \exp \frac{1}{kT}\left[a^2 l_j \frac{\Delta h \Delta T}{T_m^0} - 2a\sigma l_j - a\sigma|l_j - l_s|\right] \tag{13a}$$

$$\frac{\alpha^{ij}}{\beta^{ij}} = \exp \frac{1}{kT}\left[a^2 l_j \frac{\Delta h \Delta T}{T_m^0} - 2a^2\sigma_e - 2a\sigma U(l_j - l_i) - a\sigma|l_j - l_s|\right]. \tag{13b}$$

During this derivation it was necessary to assume that the distribution of species in the strip was symmetric. This will not necessarily be the case under kinetic conditions.

These rate constants are very similar to those in eqs (11), the only difference being the replacement of the term $2a\sigma U(l_j - l_s)$ with $a\sigma|l_j - l_s|$. The term $2a\sigma U(l_j - l_s)$ arose because we had a very definite process in mind of placing species of thickness l_j on a substrate of thickness l_s. It is in just this step that the two-dimensional character of the problem becomes apparent, and, as already pointed out, we cannot take this two-dimensional character exactly into account. Now, if instead of considering the *formation* of a crystal in the dimension normal to the growing strip we were asked to calculate the free-energy of an already grown crystal, we should use a term just like $a\sigma|l_j - l_s|$. This makes the appearance of this term somewhat more plausible.

In a somewhat more empirical vein, it should be noted that, in the ratio of α^{ij}/β^{ij} in eqs (11) (which determines the composition of the growing strip) either of the U functions may be replaced by an absolute value function. Of the four possibilities only that expressed by eqs (13) leads to the result that crystallization proceeds continuously to T_m^0, whatever the distribution of free-energy to forward and backward rate constants. Moreover, symmetrizing the rate constants as was done by Price also leads to a cessation of crystallization at all temperatures above a finite undercooling. In short, the rate constants given by eqs (13) are the only ones that do not lead to a cessation of cyrstallization above a finite temperature below T_m^0.

Without further discussion, then, we take the same approach as in I and *assume* that these rate-constant ratios, which are derived for equilibrium, will also hold under kinetic conditions. We then have left the problems of the apportionment of the free-energies and the treatment of interfacial transport terms.

2.3. The Apportionment of the Free Energies

As previously discussed, without a detailed model of the processes involved in the deposition of species on the growing strip, it is not possible to know how the free-energy changes in crystallization are to be apportioned to the forward and backward rate constants. Rather than assume such a model, or try to derive it, we adopt a more empirical approach and carry out calculations for various arbitrary apportionments.

First, we have the problem of apportioning the free-energy to the rate constants for the initial step in the chain, viz. α_0^j and β_1^j. These rate constants do not affect the composition of the chain, but they do strongly affect the total flux. We cannot hope to predict this accurately in any case, and all we can do is try to predict its dependence on temperature.

There are two extreme cases to be considered: (a) All the free energy in the forward reaction rate constant and (b) all in the backward rate constant. In the former case, β_1^j in unity: in the latter, α_0^j is unity, and it is easy to derive the relationship between the total flux in the two cases. If we let S_7^a and S_7^b represent the fluxes in the two cases we may write from eqs (4) for the total flux in each case

$$S_7^a = \sum_j \frac{N_0 \alpha_0^j \lambda^j}{1 + \lambda^j}$$

$$S_7^b = \sum_j \frac{N_0 \lambda^j}{\beta_1^j + \lambda^j}.$$

Now, for the second case, β_1^j is $(\alpha_0^j)^{-1}$ for the first case. Hence we may write

$$S_7^b = \sum_j \frac{N_0 \alpha_0^j \lambda^j}{1 + \alpha_0^j \lambda^j}.$$

Now, if both λ^j and α_0^j are much less than unity, both fluxes are approximately the same. Near T_m^0, $\lambda^j \ll 1$, and α_0^j is always much less than unity. At rather large undercoolings λ^j is no longer small, and may be as high as 0.2. Nevertheless, we only carry out calculations in which all the energy is assigned to the forward rate constant and take $\beta_1^j = 1$. In a sense this is physically reasonable, since it makes the free energy a "barrier" to be overcome in the initial step of the chain, and is the apportionment that Frank and Tosi derived as being correct.

For the subsequent steps in the chain we envision the following process. When a polymer chain has laid a segment on the growing strip, before it can lay down another segment on the strip it must form a fold. This requires an energy approximately of the amount $2a^2\sigma_e$ which therefore acts as a "barrier" to subsequent growth of the strip. We thus put this term in the α^{ij}. The remainder of the energy we apportion in arbitrary ways, as was done in I. If we let E_{ij} be the argument of the exponentials in eq (13b) then we take

$$\alpha^{ij} = \exp[-2a^2\sigma_e/kT] \exp[\varphi(E_{ij} + 2a^2\sigma_e)/kT] \qquad (14a)$$

$$\beta^{ij} = \exp[(\varphi - 1)(E_{ij} + 2a^2\sigma_e)/kT] \qquad (14b)$$

where φ is an arbitrary parameter the value of which can range from zero to unity. We shall see that the value of φ has a significant effect on the results, particularly at high undercoolings.

2.4. The Effect of the Interfacial Transport Term

The rate constant ratios expressed by eqs (13) were derived at equilibrium (total flux zero) and as a result do not contain terms expressing the rate of transport or diffusion of species from the melt or solution to the growing interface. If this diffusion or transport depends upon both the diffusing species (j) and the species at the end of the chain (i), then the rate constants given by eqs (12) should be multiplied by factors a_{ij} and b_{ij}, as already pointed out in I. Unfortunately, it seems almost impossible at this time to decide what these factors ought to be.

A simpler but less correct approach is to assume that a_{ij} and b_{ij} are independent of i and j. If this is done, then, as discussed in I, the composition and

distribution in the chain is not affected. The only result is that the total flux as calculated by the LDP theory should be multiplied by a transport term. Because this term will have an Arrhenius or WLF [8] temperature dependence, the temperature dependence of the total flux calculated here will be somewhat in error, and this error will become greater the greater the undercooling and the closer to the glass-transition temperature the conditions become. However, as will be seen below, other effects intervene at such large undercoolings. Nevertheless, it will be understood that where we discuss the temperature dependence of the total flux we do not include this transport term.

3. Method of Calculation

The constants, parameters and the variables and their ranges used in the computations are given in table 1. The equilibrium melting point, heat of fusion and lateral dimension are those of polyethylene. The parallelepiped shown in figure 1 was assumed to have a square cross section, but this is expected to have no significant effect on the calculations. Three different values of the end and lateral surface energies were used, although most of the calculations were carried out with the values $\sigma_e = 60$ ergs/cm^2 and $\sigma = 10$ ergs/cm^2. The values of σ_e given in the literature cover a wide spectrum, with the value 60 ergs/cm^2 being on the low side [4, 5, 9, 10, 11]. As we will see, however, the actual value of this constant is less important than the value of a parameter derived from it. The value of 10 ergs/cm^2 is a normal value from several different sources [9, 12]. The number of components was usually taken to be 21, although often the calculations were repeated with 50 components, particularly under those conditions where the deposited layer had a broad distribution of lengths. With the value of Δl shown, these numbers of components gave ranges of lengths of 105, 250, 210, and 500 Å. Usually the combinations $n = 21$, $\Delta l = 5$, or $n = 50$, $\Delta l = 5$ were used.

TABLE 1. *Value and range of parameters for calculation*

Temperature	360–415.2 °K
$\Delta h/k$	21.2 °K/Å^3
T_m^0	415.2 °K
Δl	5[a], 10Å
Number of Components	21, 50
σ_e	82.8, 60, 41.4 ergs/cm^2
σ	5, 10[a], 20 ergs/cm^2
φ	0, 1/2, 1
a	4.285 Å

[a] Most commonly used values.

The calculations were carried out as follows. First, for the temperature in question, a substrate thickness l_s close to the final expected layer thickness was chosen. The lengths l_j were chosen so that the shortest length was given by $l_s - \left(\frac{n-1}{2}\right)\Delta l$ for n odd, and $l_s - \frac{n}{2}\Delta l$ for n even. If this minimum length was less than zero, the value 5 Å was chosen. With this value of substrate thickness, lengths l_j, and the other relevant parameters, α_0^j, β_i^j, α^{ij} and β^{ij} were calculated from eqs (14). From these, the values of λ^j defined by eq (3) were calculated by the iteration procedure outlined in I and LDP until covergence to one part in 10^7 was obtained. From these λ^j, the N_ν^j were calculated by the recursion formula eq (6) until again convergence to one part in 10^7 was obtained, and then the f_i were calculated by eq (5). From these last quantities the average thickness $\overline{l}$ of the grown strip was computed by eq (12). This was now compared to l_s. If the difference was greater than one part in 10^7, the whole procedure was repeated using $\overline{l}$ as the new l_s. A new set of lengths l_j was chosen by the procedure already outlined, which had the advantage in most cases of having one of the l_j equal to $\overline{l}$ when convergence between $\overline{l}$ and l_s was obtained. When $\overline{l}$ was the same as l_s within one part in 10^7, the iteration was discontinued and S_T and the f_i computed by eqs (4) and (5) respectively. For those computations with $n = 21$, f_{ij} (eq (9)) were also computed. In addition to these, two other quantities of interest were calculated. The first, which we denote by s_l, is the standard deviation in l, and is defined by

$$s_l = \left(\sum_i f_i (l_i - \overline{l})^2\right)^{1/2}.$$

This gives a measure of the spread in the distribution. The second, which we denote by $\overline{g}$, is the average free energy per segment in the strip, and is given by

$$\overline{g} = \overline{l}a^2 \frac{\Delta h \Delta T}{T_m^0} + kT \sum_j f_j \ln f_j - kT \sum_{i,j} f_{ij} \ln f_{ij} - a\sigma \sum_j f_j |l_j - l_s| - a\sigma \sum_{i,j} f_{ij} |f_i - f_j| - 2a^2\sigma_e + kT \ln \Delta l/\delta. \quad (16)$$

We will now discuss in some detail the behavior of the various quantities calculated. We are particularly interested in the total flux, S_T; the average length, $\overline{l}$; and the composition of the chain, f_i and f_{ij}.

4. Results

4.1. The Average Thickness and Its Standard Deviation

A plot of $\overline{l}$ against the reciprocal of the undercooling is given in figure 2 for $\sigma = 10$ ergs/cm^2, $\sigma_e = 60$ ergs/cm^2, and for the three values of φ.

The curves are similar to those already presented by Price and Frank and Tosi. They have a linear portion at low undercooling, fall to a minimum value at an undercooling of 20 to 25 degrees, and then rise rapidly to very large values. We will henceforth denote the temperature at which the thickness diverges by T_d. The behavior in this region depends markedly on

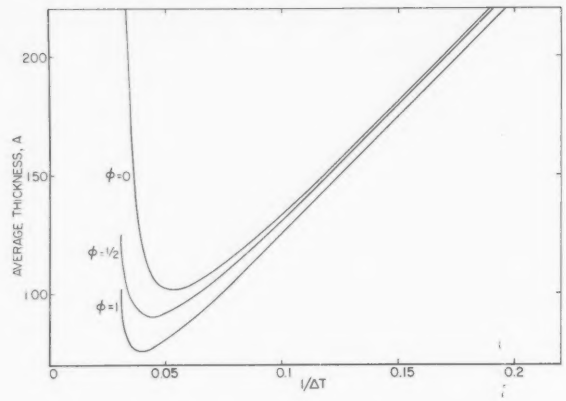

FIGURE 2. *Plots of average thickness of chain folded crystals against reciprocal of the undercooling for* $\sigma = 10$ *ergs/cm*^{2}, $\sigma_e = 60$ *ergs/cm*^{2}, *and for three values of* φ.

The almost linear portion at low undercoolings extends to the melting point.

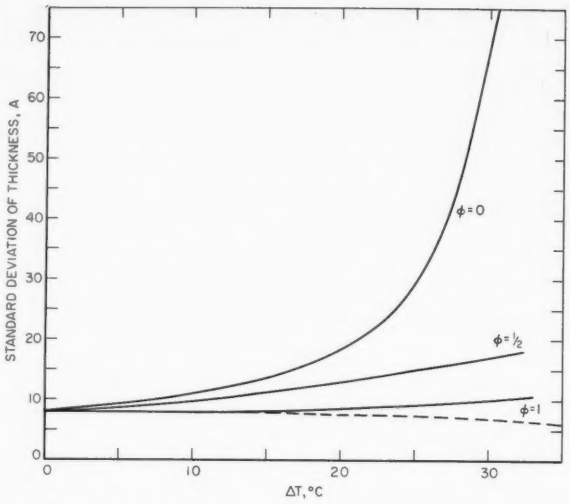

FIGURE 3. *Plots of standard deviation of thickness (eq 15 of the text) of chain folded crystals against undercooling for* $\sigma = 10$ *ergs/cm*^{2} *and for three values of* φ.

The standard deviation of the thickness is essentially independent of σ_e for reasonable values of thickness. The dashed curve represents the value of s_l that minimizes the free energy of a chain folded crystal when the mean thickness of the crystal is maintained constant.

the value of φ, but discussion of these curves will be postponed until we have presented the results for s_l.

The results for s_l against undercooling are given in figure 3 for $\sigma_e = 60$ ergs/cm^2 and $\sigma = 10$ ergs/cm^2 for the three values of the parameter φ. It will become clear from the subsequent discussion in this section that s_l is independent of σ_e (over any reasonable range of values), the experimental value of which has considerable uncertainty, but is strongly dependent on σ, which fortunately is somewhat better known. The behavior of s_l varies considerably with φ. In all cases, the value of s_l approaches 8.133 Å at T_m^0, but below this temperature the curves diverge considerably. For $\varphi = 1$ and $\varphi = 1/2$, the change of s_l with temperature is not very great, but for $\varphi = 0$, s_l becomes very large as the temperature at which $\bar{l}$ goes to infinity is approached (figure 2). In fact, detailed investigation in this region indicates that not only does $\bar{l}$ approach infinity, but, for $\varphi = 0$, the *width* of the distribution f_j also approaches infinity, with a consequent divergence of s_l at this temperature.

It is interesting to compare our results for the value of "surface roughness" as expressed by figure 3 with those of Price. On the figure there is indicated the equilibrium[2] value of s_l, which is closest to the curve for $\varphi = 1$, but in any case this is considerably larger than the 1 to 2 Å roughness quoted by Price. Indeed, the minimum values of 8 to 10 Å obtained here for $\varphi = 1/2$ and $\varphi = 1$ are relatively large for crystals of ordinary thickness (125 to 150 Å), to say nothing of the case for $\varphi = 0$, which would predict very furry crystals indeed at large undercoolings. However, for experimental purposes, the differences in these curves may be less important, for at the normally attainable undercoolings (for polyethylene) of 10 to 15 °C, s_l varies only from 8.5 to 14 Å for the various values of φ.

We now return to a discussion of the curves in figure 2. The linear portion of the curves makes it tempting to analyze their behavior by an equation analogous to eq (1). We accordingly define two parameters σ_{eff} and δl, and express the average thickness at any temperature T by the equation

$$\bar{l} = \frac{2T_m^0 \sigma_{\text{eff}}(T)}{\Delta h \Delta T} + \delta l(T). \tag{17}$$

This is of the same form as eq (1), with $\delta l(T)$ replacing $kT/a\sigma$, and with σ_e replaced by a temperature dependent σ_{eff}. The parameter σ_{eff} is amenable to nonarbitrary definition; hence the form of eq (17). That is, $\sigma_{\text{eff}}(T)$ may be defined, in analogy to the theory of Lauritzen and Hoffman, by

$$2a^2\sigma_{\text{eff}} = \frac{a^2 \bar{l} \Delta h \Delta T}{T_m^0} - \bar{g} \tag{18}$$

where $\bar{g}$ is defined by eq (16). From this equation it will be seen that σ_{eff} is given by

$$2a^2\sigma_{\text{eff}} = 2a^2\sigma_e - kT \sum_j f_j \ln f_j + kT \sum_{i,j} f_{ij} \ln f_{ij} + a\sigma \sum_j f_j |l_j - l_s| + a\sigma \sum_{i,j} f_{ij} |f_i - f_j| - kT \ln \Delta l/\delta. \tag{19}$$

[2] The "equilibrium" value of s_l is the value of s_l that minimizes the free energy of a chain folded crystal when the thickness of the crystal is maintained constant. The method of calculation will be presented in a subsequent publication.

In the theory of Lauritzen and Hoffman, σ_e is of course essentially temperature independent, and in the present work it is interesting to compare σ_e and σ_{eff}.

Accordingly, in figure 4 we show a plot of $\sigma_e - \sigma_{eff}$ for several different values of the *lateral* surface energy σ, and for several different values of the parameter φ. First, it will be noticed that since σ_e is a constant, σ_{eff} is rather strongly temperature-dependent. Secondly, it will be noticed from the curves for $\sigma = 10$ that there is a strong dependence on φ, which, however, becomes progressively smaller as ΔT approaches zero, and disappears entirely at T_m^0. Thirdly, it will be noticed that the difference between σ_e and σ_{eff} is dependent upon σ, and is a significant fraction of σ_e. From the definition of σ_{eff}, it is clear that if f_i and f_{ij} are independent of σ_e, then $\sigma_e - \sigma_{eff}$ will also be independent of it. But from the definition of the rate constants, the term in $\bar{l}2a^2\sigma_e/kT$ is simply a multiplicative factor independent of i and j and hence does not influence the distribution. We have the result, then, that $\sigma_{eff} - \sigma_e$ is a measure of the width of the distribution, which is strongly influenced by σ, as is evident from the expressions for the rate constants. Thus, $\sigma_{eff} - \sigma_e$, measures, so to speak, the same thing s_l does, but is somewhat more basic, for, as will be discussed in the section on the total flux, σ_{eff} controls this quantity.

There is a rather simple physical explanation for the behavior of $\sigma_e - \sigma_{eff}$. For a rough surface, a great deal of extra lateral surface is exposed, and this would tend to make the effective surface free-energy greater than the surface energy of the smooth surface, σ_e. This is expressed by the terms $a\sigma \sum_i f_i |l_i - l_s|$ and $a\sigma \sum_{i,j} f_{ij} |f_i - f_j|$ in the definition of σ_{eff}. These terms would tend to raise the free energy of the solid phase compared to the (higher) free-energy of the liquid phase. But the introduction of this rough surface introduces a "mixing entropy" expressed by the terms $kT\Sigma f_i \ln f_i$ and $kT\Sigma f_{ij} \ln f_{ij}$. The mixing entropy arises from the various configurations a polymer in the crystal may adopt. These terms tend to lower the free-energy of the solid as compared to the liquid. At the equilibrium these latter terms must win out and override the effect of the lateral surface terms, for if they did not there would be no mixing. Thus, at the melting point $\sigma_e - \sigma_{eff}$ is positive, rather than negative as might be expected from considerations of surface energy alone. However, for highly nonequilibrium distributions, such as occur with $\varphi = 0$ near the divergence temperature T_d (see fig. 3), the lateral surface terms win out and $\sigma_e - \sigma_{eff}$ is negative, and hence $\sigma_{eff} > \sigma_e$. Note that σ_{eff} can be equal to σ_e under two conditions. The first and obvious one is when all the species are of the same length and the distribution is therefore a delta function. This is the Hoffman and Lauritzen case. The second, and less obvious, is when for kinetic reasons sufficient lateral surface is exposed that the terms relating to those in eq (19) just balance the mixing terms. This, as explained above, cannot happen at equilibrium.

The value of δl calculated from eq. (17) at each temperature is shown in figure 5 plotted against undercooling for the same values of the parameters as figures 2 and 3. The values for $\varphi = 0$ and 1/2 are about the same up to undercoolings of approximately 20 degrees and then the $\varphi = 0$ curve rapidly increases, as would be expected from the behavior of the curves of figure 2. The curve for $\varphi = 1$ is somewhat lower over the whole range, but also diverges at T_d.

It is interesting to compare the values of δl in the range of 0 to 20 degrees undercooling with the term $kT/a\sigma$ in eq (1). The values of δl in this range of ΔT vary from about 18 to 35 Å, whereas $kT/a\sigma$ in this range by comparison is constant and equal to 12.9 Å.

The undercooling at which $\bar{l}$ approaches infinity is given by $\sigma T_m^0/a\Delta h$ for all values of φ, although this is

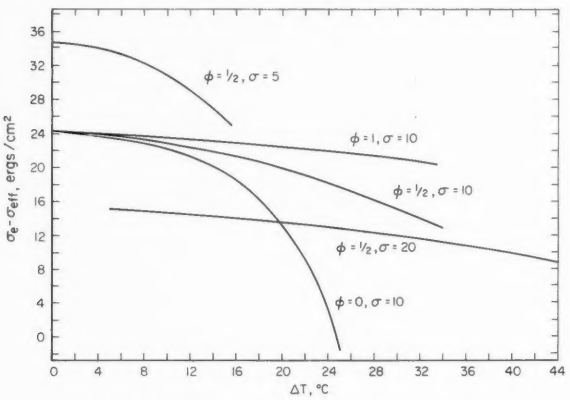

FIGURE 4. *Plots of* $(\sigma_e - \sigma_{eff})$ *(eq 19 of the text) versus undercooling for various values of* σ *and* φ.

The quantity $(\sigma_e - \sigma_{eff})$ is not appreciably dependent on σ_e unless σ_e is very small.

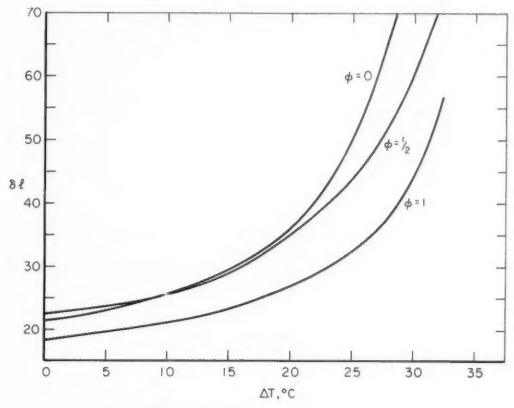

FIGURE 5. *Plots of* δl *(eq 17 of the text) versus supercooling for* $\sigma = 10$ *ergs/cm², and for three values of* φ.

These plots are independent of σ_e unless σ_e becomes too small. The curves for $\varphi = 0$ and $\varphi = 1/2$ do not actually cross one another, the $\varphi = 0$ curve being above the $\varphi = 1/2$ curve throughout the whole range.

difficult to prove analytically except for $\varphi = 1$, and is as much a deduction as a proof. It is interesting to note in this regard, however, that this is the same undercooling at which Price found such a divergence, but is *half* the undercooling at which Frank and Tosi found it. The existence of this divergence is not the result of a fluctuation treatment of the problem, for it is also found in an extension of the Hoffman-Lauritzen treatment [13]. In that treatment as in that of Frank and Tosi it occurs at twice the undercooling found here. For $\sigma = 10$ ergs/cm^2, the undercooling at which the divergence occurs in our work is 33.14 °C.

This is a rather high undercooling which is very difficult or perhaps impossible to achieve experimentally in crystallization from the melt, but can be achieved in crystallization from solution. Nevertheless at such high undercoolings it may be that the steady-state conditions required by the theoretical treatment are never attained. We return to this point when discussing the behavior of the total flux.

We will not attempt at this time to fit experimental results with our theoretical treatment. This rather long and involved task will be reported in a subsequent publication. It will be shown there that in order to fit the known experimental results (with any theory, not necessarily our own) it is necessary to invoke a small temperature dependence for σ as well as the temperature dependence for σ_{eff} and δl found here.

As a result of this analysis we can say that over most of the range of interest, the variation of lamellar thickness with temperature may be represented by an equation of the form of eq (1), namely eq (17). However, the parameters σ_e and δl must be considered temperature dependent, the exact amout of this dependence depending on the value of φ appropriate to the problem.

4.2. The Total Flux

The behavior of the total flux, S_T, which, except for transport terms, is representative of the rate of crystallization, is best analyzed by an equation analogous to that derived by Frank and Tosi. In our notation this may be written

$$S_T = S_T^{\varphi}(\varphi, T)\left[\exp\left(\frac{a\Delta h\Delta T}{\sigma T_m^0}\right) - 1\right]\exp\left(\frac{-4a\sigma\sigma_e T_m^0}{\Delta h \Delta T k T}\right). \tag{20}$$

In this expression the preexponential term $S_T^{\varphi}(\varphi, T)$ is expected to have only a slight temperature dependence as compared to the exponential terms, as it should if this representation is to be of value. Moreover, it is expected that the dominant term is

$$\exp\left(-4a\sigma\sigma_e T_m^0/\Delta h \Delta T k T\right),$$

the other having only a minor effect. We anticipate that σ_e in eq (20) should be replaced by σ_{eff}.

A plot of $\Delta T \log S_T$ against ΔT is given in figure 6 for the same value of the parameters as in figures 2 and 3. For low to moderate undercoolings, the curves are very nearly linear with an average slope that depends on φ. This near linearity indicates that in this range the terms $S_T^{\varphi}[\exp(a\Delta h\Delta T/\sigma T_m^0) - 1]$ are indeed of negligible variation compared to the other term in eq (20). However, near T_d the curves have a maximum. For the $\varphi = 0$ curve, this maximum is caused in fact by the very large values of σ_{eff}, but in the other curves it is caused by a fall-off of the S_T^{φ} term. It is to be noted that this maximum exists *without* a transport term and is not occasioned, as usually accepted, by the activation energy for transport becoming the dominant factor in the nucleation process. The flux falls to zero at an undercooling of $\sigma T_m^0/a\Delta h$, and we will return to this important point at the end of this section.

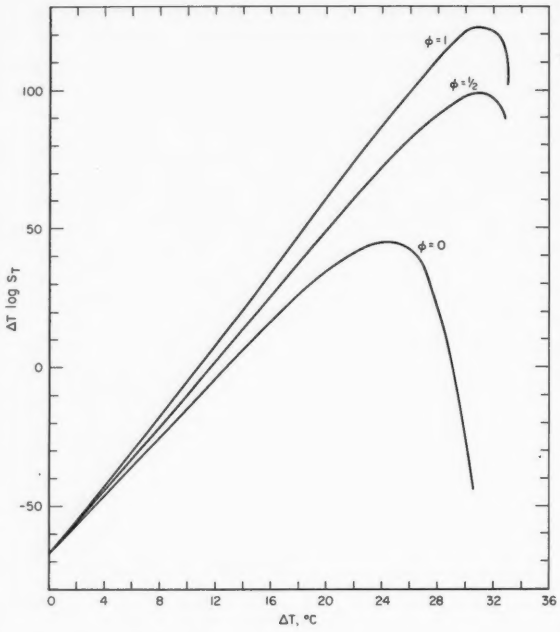

FIGURE 6. *Plots of* $\Delta T \log S_T$ *versus undercooling for* $\sigma = 10$ *ergs/cm*^{2}, $\sigma_e = 60$ *ergs/cm*^{2}, *and for three values of* φ.
The curves are very nearly linear at low undercoolings.

In spite of this maximum in the total flux, over a large range of undercooling the curves are approximately linear, which indicates that over this range $S_T^{\varphi}(\varphi, T)$ is indeed approximately constant. To illustrate this, in figure 7 we show the value of $\log S_T^{\varphi}(\varphi, T)$ plotted against undercooling for a range of ΔT of 30 °C. (The temperature T_d corresponds to a ΔT of 33.14 °C.) Over this range $S_T^{\varphi}(0, T)$ shows a variation of about one order of magnitude, while $S_T^{\varphi}(1/2, T)$ and $S_T^{\varphi}(1, T)$ show a variation of about one half order of magnitude. Compared to the variation in the exponential factors, this variation is completely negligible. In fact, over the range of undercoolings considered, the variation of

$$(\exp[a\Delta h\Delta T/\sigma T_m^0] - 1),$$

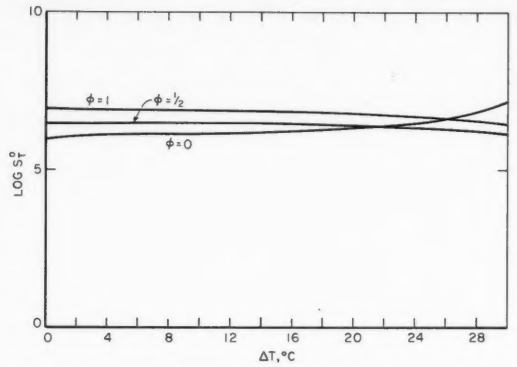

FIGURE 7. *Plots of* log S_T° *(eq 20 of the text) versus undercooling for* $\sigma = 10$ *ergs/cm*^{2}, $\sigma_e = 60$ *ergs/cm*^{2}, *and for three values of* φ.

is also negligible, as is indeed the variation with φ. Thus we conclude that the total flux, for an undercooling of as much as 30 °C is given with more accuracy than is usually necessary for the interpretation of growth rate data by the expression

$$S_T = S_T^\circ \frac{a\Delta h \Delta T}{\sigma T_m^\circ} \exp\left(\frac{-4a\sigma\sigma_{\text{eff}} T_m^\circ}{\Delta h \Delta T k T}\right) \qquad (21)$$

where S_T° is a constant.

Now, eq (21) has an important consequence for the interpretation of growth rate data, for it indicates that to the extent that this theory is representative of the processes involved in the growth of chain folded polymer crystals, $\sigma\sigma_{\text{eff}}$ is the parameter that controls the temperature dependence of the growth rate, and not $\sigma\sigma_e$. As we have seen, for low undercoolings, σ_{eff} may be quite small compared to σ_e and independent of φ.

With this interpretation, there is no reason to expect the value of the end surface free-energy computed from crystal growth data to be the same as the value of the end surface free-energy obtained from, for example, experiments on melting point against lamellar thickness. The reason for this is as follows: the parameter σ_{eff} is a measure of both the free energy of making a fold and of the irregularity of the folded surface, as is evident from eq (19). If the surface is perfectly regularly folded, σ_{eff} is equal to σ_e, but for surfaces that are not perfectly regular, the value of σ_{eff} is dependent upon the particular distribution of fold lengths. For the values of σ_{eff} quoted here this distribution is *determined by the kinetics of the growth process.* Now, it is quite possible that although when a lamella is freshly grown it may have this kinetic distribution of fold lengths, upon subsequent storage, and particularly upon heating to the melting point, this distribution will very likely change and approach some other distribution, even though $\bar{l}$ may remain unchanged. If the distribution approaches a perfectly sharp distribution, then the surface energy measured will indeed be σ_e. However, it is much more likely that the distribution would approach the *equilibrium* distribution characteristic of the particular temperature in question, and the end surface energy would be the value characteristic of that distribution. In short, kinetic experiments such as growth-rate measurements, lead to a value of σ_{eff} characteristic of a *kinetic* distribution, while "equilibrium" type experiments lead to a value characteristic of an *equilibrium* distribution.

The difference between the two types of experiments should not, however, be overemphasized. In particular, in the worst case, namely $\varphi = 0$, for $\sigma_e = 60$ ergs/cm^2 the value of σ_{eff} varies from about 36 ergs/cm^2 at very low undercoolings to about 46 ergs/cm^2 at an undercooling of 20 deg. The value characteristic of the equilibrium distribution over this whole temperature range is approximately 36 ergs/cm^2. As may be seen from figure 4, the variation for $\varphi = 1/2$ and $\varphi = 1$ is somewhat less.

We now turn to a discussion of the maximum in S_T, and the decrease of S_T to zero at an undercooling of $\sigma T_m^\circ / a\Delta h$. This, of course, is the same undercooling at which Frank and Tosi found a cessation of crystallization, but there is one important difference between our results and theirs. In our case, crystallization proceeds relatively normally above this temperature, whereas in theirs crystallization proceeds only below it. Moreover, at this temperature our thickness diverges, while theirs is regular. Nevertheless, by our choice of rate constants, we have traded the disquieting result that crystallization does not proceed *above* a certain undercooling for the equally disquieting result that crystallization does not proceed below it. Of the two possibilities we prefer the latter, although it would seem to be contrary to experience. After all, we know from experiments on homogeneous nucleation that crystal growth can occur at undercoolings greater than $\sigma T_m^\circ / a\Delta h$. The reason for our preference is that these theories of crystallization presume that steady-state exists. Now, it is much more likely that steady-state can be obtained near the melting point where processes are slow, than at large undercoolings where processes are rapid and more complex. While we are by no means certain that this is the proper explanation of the difference between our results and observed behavior, we can suggest that at undercoolings approaching our divergence temperature, steady state never obtains in the real physical case, and our treatment (and any other) becomes inapplicable. To see how this rationalizes the results, we note first that if the thickness of the growing layer is finite, the total flux is not zero, as will be evident from our expressions for α_0^j/β_1^j and α^{ij}/β^{ij}. If we now imagine a strip nucleating on a substrate formed, for example, from a homogeneous nucleus, it may start with some finite thickness, and begin to increase to the thickness determined by the steady state equations, which may be infinite. If it could achieve this, its rate of growth would drop to zero (eq. (13a)), but it is entirely likely that before it reaches this thickness it might encounter another strip growing in the same manner on the same substrate and hence never approaches this steady-state

thickness. Clearly, to solve this problem correctly (in one dimension), one would have to solve the full time dependent equations given in LDP. We know of no way to do this, and the only conclusion we can come to is that the reason our treatment does not reproduce reality in the range of undercoolings of T_d and below is that steady state is never attained.

We note also that the inclusion of transport terms to slow down the overall rate will not necessarily help matters any. It is not the absolute magnitude of the flux which is important, but the relative rates of initiation and growth of strips (in our notation, essentially the relative magnitudes of α_0^j/β_j^i and α^{ij}/β^{ij}). Thus, unless the transport terms affect initiation and growth in significantly different ways (which we consider unlikely) the retardation of the whole process by transport will not change the achievement of steady state materially.

4.3. The Distribution

Having discussed the effect of the distribution as exemplified, e.g., by s_l and σ_{eff}, we now give some detailed examples of it.

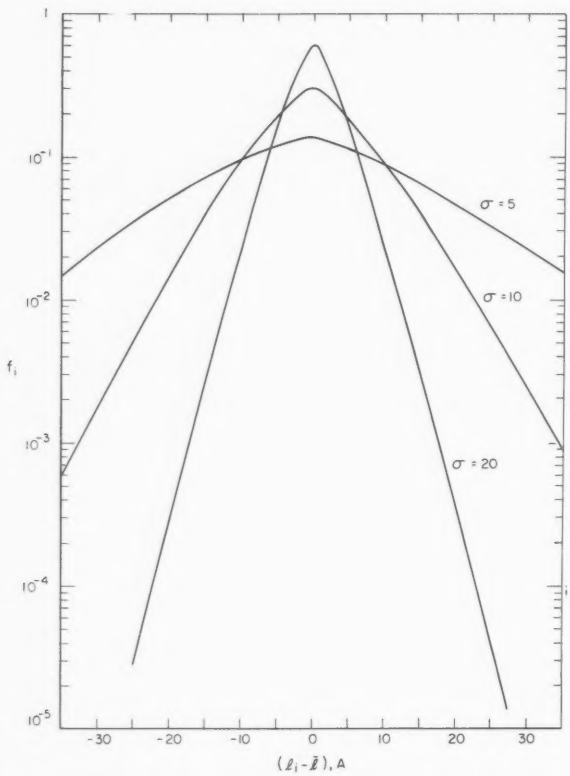

FIGURE 8. *Plots of* f_i, *the fraction of species* i (*eq 5 of the text*), *versus the deviation of* l_i *from its mean value for* $\Delta T = 3$, $\varphi = 1/2$, *and three values of* σ.

This plot is essentially independent of the value of σ_e, except that $\bar{l}$ is different for the different values of σ_e. At higher undercoolings the curves are similar but broader.

Figure 8 gives a plot of f_j against $l_j - \bar{l}$ at an undercooling of 3 degrees for three different values of the lateral surface energy term σ and for $\varphi = 1/2$. The curves have a peak at the value of $l_j = \bar{l}$, and fall off on both sides of this value at a rate which is dependent on the value of the lateral surface energy σ. These curves are very similar to those already presented by Price. The curves are not affected by the value of σ_e, although $\bar{l}$ of course is strongly dependent on it. The higher the value of lateral surface energy the sharper the distribution, as would be expected, for the higher the value of σ, the more energetically unfavorable is the exposure of lateral surface, and this results in a smoother surface. The values of s_l, which is characteristic of the distribution, are 3.745, 8.548, and 18.519 Å respectively, for $\sigma = 20$, 10, and 5 ergs/cm^2.

Figure 9 gives an example of the pair distribution function, f_{ij}. This is plotted from the results for $\varphi = 1/2$, $\Delta T = 15$ °C, $\sigma_e = 60$ ergs/cm^2, $\sigma = 10$ ergs/cm^2. The plot is made so that the origin is at $l_j = l_i = \bar{l}$. At this point, as is expected, f_{ij} is a maximum and falls off monotonically in all directions.

Not too much can be said about the figure, but some things should be pointed out. First, in any plane l_j = constant, or l_i = constant, the maximum value of f_{ij} occurs at the value of l_i or l_j equal to $\bar{l}$. This indicates that correlation with the substrate thickness is the most important factor in determining f_{ij}. Second, a shoulder is noticeable in the region $l_i > \bar{l}$, $\bar{l} \leq l_j \leq l_i$. (The same shoulder appears opposite the origin,

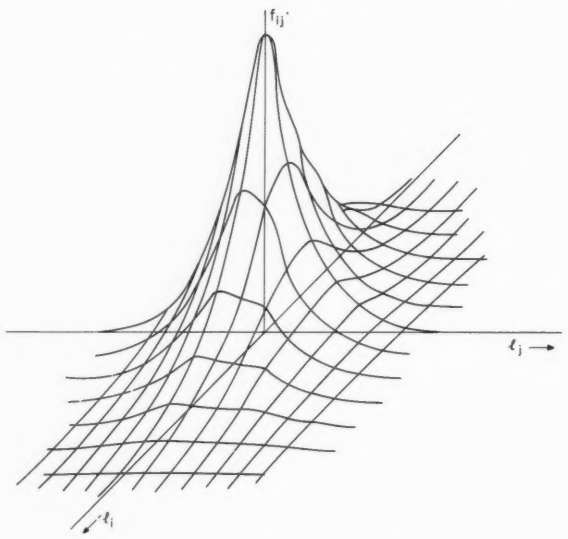

FIGURE 9. *Plot of* f_{ij}, *the pair distribution* (*eq 9 of the text*) *versus* l_i *and* l_j *for* $\Delta T = 15$, $\varphi = 1/2$, *and* $\sigma = 10$ *ergs/cm*^{2}.

This plot was calculated for $\sigma_e = 60$ ergs/cm^2, and is essentially independent of σ_e provided the origin is at $l_i = l_j = \bar{l}$. The peak in the plot is at the origin, and is more pronounced at lower undercoolings.

i.e., where $l_i < \bar{l}$, $\bar{l} \geq l_j \geq l_i$.) This indicates that correlation occurs with $\bar{l}$ and all lengths between l_j and $\bar{l}$, but falls off very rapidly for $l_j > l_i$. Similarly, f_{ij} falls off very rapidly with l_j as l_j becomes smaller than $\bar{l}$ for $l_i \leq \bar{l}$. All these remarks have their counterparts for $l_i < l$.

This behavior is what would be expected on physical grounds. Imagine a segment $l_i > l_s = \bar{l}$ deposited at the end of the growing strip. The next segment to be deposited, l_j, will be energetically most favored if it is the same thickness as $\bar{l}$. For any thickness less than $\bar{l}$, not only is the bulk free-energy term $\alpha^2 l_j \Delta h \Delta T / T_m^0$ in eq (13b) less than if $l_j = \bar{l}$, but the term $\alpha\sigma|l_j - l_s|$ further reduces it. If $l_j > l_s$ but less than l_i, the bulk free energy term $\alpha^2 l_j \Delta h \Delta T / T_m^0$ tends to favor accretion as compared to $l_j = l_s$, but the term $a\sigma|l_j - l_s|$ more than compensates for it except near T_a. Finally, for $l_j > l_i$, the term $2a\sigma U(l_j - l_i)$ is added to the term $a\sigma|l_j - l_s|$ and the probability of accretion falls off rapidly with increasing l_j. The same remarks, with proper changes, apply when $l_i < l_s$.

We may compare f_{ij} with the pair-distribution that would occur for random mixing, as was done in I. For the random case we have,

$$f_{ij}^r = f_i f_j = f_{ji}^r$$

where f_{ij}^r is the (symmetric) pair distribution when random mixing occurs. From this we may construct the difference

$$\delta f_{ij} = f_{ij} - f_{ij}^r = f_{ij} - f_i f_j .$$

The results for this difference are difficult to present graphically. However, in the difference matrix the following behavior is observed at low undercoolings (3 °C). The maximum occurs at f_{ii} where $l_i = \bar{l}$, as is to be expected. Now, if for the purposes of discussion a cartesian coordinate system is laid on the matrix with origin at $f_{\bar{l}\bar{l}}$, and the x axis along the direction of increasing j, then for small ΔT the first and third quadrants are negative and the second and fourth positive, and the coordinate axes are positive. Said less graphically but more precisely

$$\delta f_{ij} > 0,\ l_i \geq \bar{l},\ l_j \geq \bar{l}$$

$$\delta f_{ij} > 0,\ l_i \leq \bar{l},\ l_j \leq \bar{l}$$

$$\delta f_{ij} < 0,\ l_i > \bar{l},\ l_j < \bar{l}$$

$$\delta f_{ij} < 0,\ l_i < \bar{l},\ l_j > \bar{l}.$$

For ΔT somewhat larger (15 deg) these quadrants are *predominantly* of the same signs as for lower ΔT, but deviations occur for l_j or l_i considerably larger or smaller than $\bar{l}$, i.e., away from the origin but near the coordinate axes. The δf_{ij} matrix is almost symmetrical but definitely not so, and thus the f_{ij} matrix is also not. This is as expected from the matrix of the α_{ij} and β_{ij}.

4.4. The Approach to the Steady-State Thickness

It will be recalled that in the section on the method of calculation, we described that beginning with a substrate of thickness $\bar{l}_s$ we grow on it at a given temperature a strip the thickness of $\bar{l}$ which in general will be different from l_s. This is then used as a substrate for a subsequent strip, and the process continued until $\bar{l} = l_s$. This amounts to a theoretical analog of the well-known experiment in which a crystal growing at a given temperature is cooled to another temperature and growth permitted to proceed with the formation of a step. Our procedure gives a profile of this step. This type of information has already been given by Price, and although we have not pursued this matter thoroughly, preferring to replace the above iteration scheme with a considerably more efficient one mathematically, we will present one result both because it is different from what Price has already presented and because it may be of some experimental interest. Accordingly, we show in figure 10 the approach to the final thickness when a substrate 133.1 Å thick is used as a substrate for growth at a temperature at which the final thickness is 113.8 Å. This corresponds to having grown a crystal at 405.2 °K and continuing growth on it at 402.2 °K. It will be noticed that the decrease in thickness is monotonic, arriving smoothly at the final result. After 24 steps the thickness is within 1 Å of the final result, but it takes 81 steps to arrive at within one part in 10^7 of the final thickness. It is interesting to note that some recent results of Bassett, Blundell, and Keller [14] obtained by gold deposition on surfaces, show a different behavior of the gold in a region approximately 100 Å wide near a step than in other regions. Twenty-four layers corresponds to 103 Å; however, before more can be said, detailed calculations for the particular conditions in question would have to be carried out, and a knowledge of just what this gold deposition technique measures in the region of the step would have to be known.

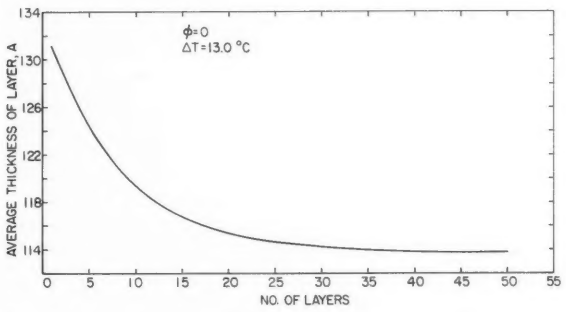

FIGURE 10. *Plot of average layer thickness versus the number of layers as the layer thickness approaches its final steady state value.*

This calculation was made for $\sigma = 10$ ergs/cm², $\sigma_r = 60$ ergs/cm², $\varphi = 0$, $\Delta\bar{T} = 13$. The original substrate thickness was 133.1 Å and corresponds to an undercooling of 10 deg.

5. Conclusions

We have shown that the LDP theory for the kinetics of the growth of chains in multicomponent systems may successfully be applied to the problem of the growth of chain-folded polymer crystals. In this problem each of the possible folded segment lengths deposited at the end of the growing strip is considered a component and the strip itself is the chain. Over most of the temperature range of interest, it is necessary to take the number of components so defined to be of the order of 50.

The most difficult aspect of this application of the LDP theory is its adaptation to the two-dimensional character of crystal growth, but it should be pointed out that this same problem arises in all previous theories of polymer crystallization. In the present instance, this adaptation was accomplished by appropriate modification of the rate constants, using as a criterion the fact that crystallization, given some type of nucleus, should occur at small undercoolings.

The problem of the apportionment to forward and backward rate constants of the free energy changes occurring in the process of accretion of elements at the end of the growing strip has not been solved. Instead, calculations were carried out for various arbitrary apportionments, with significant differences in the results. In our views, this is an outstanding theoretical problem in the treatment, but is not one likely to be solved without detailed knowledge (or at best a detailed model, which is a different thing) of the microscopic process by which a polymer chain adds to the growing crystal.

Perhaps the most intriguing result of this treatment is the roughness of the crystal surface as grown. This produces a standard deviation in the thickness of some 8 Å at the melting point and increases to more than ten angstroms at normal undercoolings, the exact amount depending strongly on the exact apportionment of the free energy changes. There are some experiments, notably density [15] and heat of fusion measurements [16], which have as one interpretation such a rough surface, but it should be borne in mind that the roughness calculated here is that occurring during the kinetic processes of growth and not necessarily the equilibrium roughness appropriate to the temperature in question. Nevertheless, unless a smooth surface is energetically favored over a rough surface (which could be theoretically accomplished, for example, by incorporating into the theory what might be called a "lock-in" energy, that is, an energy that would favor adjacent segments in the growing layer being of the same thickness and the same thickness as the substrate) such smooth crystallographic surfaces as are seen in isolated polyethylene lozenges [17] are likely to remain inexplicable on the basis of this theory, and probably any other statistical mechanical theory.

Over the range of undercoolings of usual experimental interest, the thickness grown as a function of temperature and the total rate of crystallization (neglecting transport or diffusion terms) can be analyzed by equations previously derived by others (eqs (1) and (18) of the text) provided that the end-surface free energy σ_e in those theories is replaced by an "effective" end surface free energy σ_{eff}. This latter quantity is intimately related to the roughness of the surface, and is temperature dependent, the exact amount of this dependence depending on the apportionment of the free energy to forward and backward rate-constants. Near the melting point, where the results are independent of this apportionment, the difference between σ_e and σ_{eff} is about 24 ergs/cm² for $\sigma = 10$ ergs/cm² and independent of σ_e, with σ_{eff} being smaller. This difference becomes smaller as undercooling is increased, and varies with the value of σ.

At undercoolings approaching $\sigma T_m^0/a\Delta h$, the grown length approaches a minimum and then becomes infinite at this undercooling. For all the free-energy in the backward rate constants ($\varphi = 0$ in eqs (14)) the distribution also becomes infinitely broad, while for all the energy in the forward or equally divided between forward and backward rate constants the distribution remains finite, and the approach to the infinite length is logarithmic, as was found also by Frank and Tosi, although at twice the undercooling. The distribution for $\varphi = 0$ is thus very different from the equilibrium distribution and in a sense represents a very inefficient mode of crystallization. Indeed, for crystals with such very rough surfaces, the use of the LDP theory can be questioned, for nonnearest-neighbor interaction should most likely be taken into account.

At the same temperatures where the grown thickness reaches a minimum, the growth rate, or total flux, reaches a maximum and then falls off, even in the absence of transport terms. Again this effect is most pronounced for $\varphi = 0$, and again the relevance of these results to reality in this region may be questioned for under conditions of such rapid growth, steady state may never be reached. The same criticism, however, applies to all other theories and this situation is likely to remain, for to solve the kinetic equation under nonsteady-state conditions is a truly formidable task.

We wish to thank most of our colleagues at the National Bureau of Standards for the large amount of time they spent discussing with us the various aspects of this problem and these results. Particular thanks are due to E. A. DiMarzio and John D. Hoffman in this respect. But most of all we wish to thank F. L. McCrackin, for it was only through his help in the computer programming that we were able to carry out this work.

6. References

[1] J. I. Lauritzen, Jr., E. Passaglia and E. A. DiMarzio, J. Res. NBS **71A**-457, 245 (July-Aug. 1967).

[2] J. I. Lauritzen, Jr., E. A. DiMarzio and E. Passaglia, J. Chem. Phys. **45**, 4444 (1966).

[3] J. I. Lauritzen, Jr., and J. D. Hoffman, J. Res. NBS **64A** (Phys. and Chem.) No. 1, 73 (1960); J. D. Hoffman and J. I. Lauritzen, Jr., J. Res. NBS **65A** (Phys. and Chem.) No. 2, 297 (1961).
[4] F. C. Frank and M. Tosi, Proc. Roy. Soc. **A263,** 323 (1961).
[5] F. P. Price, J. Chem. Phys. **35,** 1884 (1961).
[6] W. W. Mullins, Phys. Rev. **114,** 389 (1959).
[7] P. J. Flory, Principles of Polymer Chemistry (Cornell Univ. Press, Ithaca, N.Y., 1953).
[8] M. L. Williams, R. F. Landel and J. D. Ferry, J. Am. Chem. Soc. **77,** 3201 (1955).
[9] J. D. Hoffman, SPE Transactions, P. 327 ff (1964).
[10] R. G. Brown and R. K. Eby, J. Appl. Phys. **35,** 1156 (1964).
[11] B. Wunderlich and A. Arakawa, J. Polymer Sci. A, **2,** 3697 (1964).
[12] D. Turnbull and R. L. Cormia, J. Chem. Phys. **34,** 820 (1961).
[13] F. Gornick and J. D. Hoffman, Ind. Eng. Chem. **58,** 41 (1966).
[14] G. A. Bassett, J. D. Blundell, and A. Keller, J. Macromol. Sci. (Physics), in press.
[15] G. M. Martin and E. Passaglia, J. Res. NBS **70A** (Phys. and Chem.) No. 3, 221 (1966).
[16] H. Hendus and K. H. Illers, Kunststoffe, to be published.
[17] D. C. Bassett and A. Keller, Phil. Mag. **8,** 345 (1961).

(Paper 71A4–458)

JOURNAL OF RESEARCH of the National Bureau of Standards—A. Physics and Chemistry Vol. 71A, No. 4, July-August 1967

Infrared Absorption Spectra of 2-Oxo-1,3-bis-(phenylhydrazono) Derivatives and Related Bis- and Tris-phenylhydrazones

Alexander J. Fatiadi

Institute for Materials Research, National Bureau of Standards, Washington, D.C. 20234

(April 19, 1967)

The infrared absorption spectra of six 2-oxo-1,3-bis(phenylhydrazones), four tris(phenylhydrazones), and six related mono- and bis-(phenylhydrazono) derivatives are presented. For comparison, partial spectra of ten selected aromatic azo compounds are also given and discussed.

The important features of the absorption bands arising from the N = N (1579 to 1558 cm^{-1} and 1447 to 1408 cm^{-1}), N–H (bending) (1557 to 1515 cm^{-1}), and Ph–N (1163 to 1123 cm^{-1}) groups are presented and discussed.

Key Words: Absorption spectra, infrared spectra, mono-, bis-, and tris-(phenylhydrazones), phenylazo compounds

1. Purpose and Scope of the Study

The main objective of the present study was to record the infrared absorption spectra of selected, characteristic members of a group of 2-oxo-1,3-bis(phenylhydrazono) derivatives. These compounds have attracted interest because of their unique structure, in which an electrophilic oxo group is in proximity to two phenylhydrazono groups. Interaction of these groups can give rise to tautomeric phenylhydrazono–phenylazo structures, and the expected N=N vibration frequencies in the compound formed are of particular interest. As is known [1,2],[1] the N=N vibration frequencies of aromatic and aliphatic azo compounds are difficult to recognize, and therefore they have been the least studied. In this report, complete spectra are recorded for six 2-oxo-1, 3-bis(phenylhydrazono) derivatives; also spectra of ten selected aromatic azo compounds are presented.

2. Compounds Investigated

Table 1 lists the compounds studied, their melting points, pertinent references, and an index to the spectrograms; the serial number of a compound is the same as the number of its spectrogram.

Spectra were measured in the region of 4000 to 667 cm^{-1} for compounds I–XVI, and in the region of 400 to 1300 cm^{-1} for compounds XVII–XXVI. The spectrograms of compounds I–XVI, XVIII, and XXI are given in figures 1 and 2, respectively.

3. Structure of 2-Oxo-1,3-bis(phenylhydrazono) Derivatives and Related Mono-, Bis-, and Tris-(phenylhydrazones)

The structures of the 2-oxo-1,3-bis(phenylhydrazono) derivatives, compounds I to VI, have recently been established [3] [4]. A typical new representation of the structure of compound I, as shown elsewhere [3], is depicted in formula Ia. The conventional structure I, having a free C=O group, has been found to exist as the resonance-stabilized, enolic phenylhydrazono–phenylazo structure Ia. Although, for simplicity of representation, conventional carboxyl structures are shown with spectrograms 1–6,

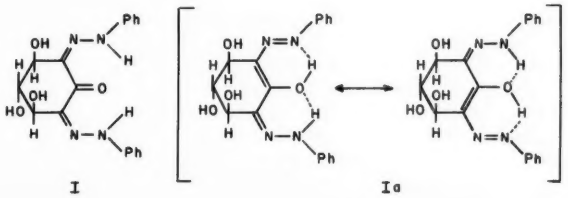

I Ia

[1] Figures in brackets indicate the literature references at the end of this paper. The references for table 1 are given at the end of the table.

the enolic structures, corresponding to Ia, should actually be considered for all of these compounds.

The structures of the tris(phenylhydrazones) (compounds VII to X) and the related bis(phenylhydrazones), compounds XII and XIV, have been examined recently [4]; also, study of compounds X and XIV has recently been reported [5]. The n.m.r. spectra of these compounds show bands characteristic of hydrogen bonding, thus indicating the presence of chelate-ring structures.

As pointed out elsewhere [4], the infrared spectra of compounds I to VI are in full agreement with the structures determined by other spectroscopic means. Examination of the spectra of compounds I to VI (see fig. 1) does not reveal the absorption typical of a free C=O group, but N=N and N−H (bending) bands are observed; this will be discussed in section 4; compound III, however, shows a C=O band at about 1720 cm^{-1} as it should, because of the carboxyl group.

4. Discussion of the Spectra

Discussion of the infrared absorption spectra of solid phenylhydrazono–phenylazo derivatives (compounds I to XVI and XVII to XXVI) will be limited to the important features of the absorption bands arising from the N=N, N−H (bending), and Ph−N groups. As pointed out by Bellamy [2], there is difficulty in assigning frequencies to such groups as N=N, C=N, and C=C when two or more occur in a single structure, because all of these groups absorb near 1600 cm^{-1}. The same can be said about phenylhydrazono–phenylazo structures, in which N=N and N−H (bending) bands must be incorporated into a relatively narrow region between two bands (due to the phenyl ring at 1590 cm^{-1} and at 1490 cm^{-1}). A relatively weak N=N band or even a moderately strong N−H (bending) band can easily be masked, either by the phenyl ring absorptions or by mutual overlapping.

4.1. The N=N Group

The N=N stretching vibration frequency has not been thoroughly characterized [1,6]; this is particularly true in early work on the frequency assignments for aromatic azo compounds [7, 8, 9]. It was noted [1, 2] that the N=N frequency is not observed for tetrazoles or certain other symmetrical diazo derivatives.

Structurally, the N=N group is iso-π-electronic with the C=C group [10], but the absorption intensity of the former group is much lower in comparison to that of the olefinic group [11]. Le Fevre and co-workers [12, 13, 14, 15] have studied a series of 43 aromatic diazo compounds and assigned the absorption bands at 1577 ± 8 cm^{-1} and at 1406 ± 14 cm^{-1} to the N=N group; the same authors also assigned the region at 1576 to 1565 cm^{-1} to the aliphatic azo group. Interest in the infrared absorption spectra of azo compounds continues. McGreen and co-workers [16] and van Aiken and Rinehart [17] observed the N=N band in the region of 1548 to 1540 cm^{-1}. Overberger and co-workers [18] and Church and co-workers [19] assigned to the N=N group the regions at 1555 to 1545 cm^{-1} and 1583 to 1575 cm^{-1}. Gale and co-workers [20] observed an N=N band at 1570 cm^{-1}; Gills and Hagarty [21] assigned the region near 1500 cm^{-1} to a conjugated N=N band; and certain pyridazyl bis(phenylhydrazones) showed a band at 1584 to 1569 cm^{-1} supposedly associated with the N=N

TABLE 1. *Compounds measured and index to spectrograms*

Number	Compound	mp(°C)	References	Spectrogram
	2-Oxo-1,3-bis(phenylhydrazono) derivatives			
I	*xylo*-4,5,6-Trihydroxy-2-oxo-1,3-bis-(phenylhydrazono)cyclohexane	185–187	1,2	1
II	2-Oxo-1,3-bis(phenylhydrazono)-cyclohexane	132–133	3	2
III	1-Carboxy-3-oxo-2,4-bis(phenylhydrazono)cyclohexane	222–223	4	3
IV	2-Oxo-1,3-bis(phenylhydrazono)-cyclopentane	247–249	5	4
V	2-Oxo-1,3-bis(phenylhydrazono)indane	207–209	6	5
VI	2-Oxo-1,3-bis(phenylhydrazono)propane	174–175	7,8	6
	Tris(phenylhydrazones)			
VII	1,2,3-Tris(phenylhydrazono)-cyclohexane	185–186	3	7
VIII	1-Carboxy-2,3,4-tris(phenylhydrazono)-cyclohexane	232–234	4	8
IX	1,2,3-Tris(phenylhydrazono)-cyclopentane	206–208	5	9
X	1,2,3-Tris(phenylhydrazono)propane	166	7,9,10	10
	C. Mono- and bis-(phenylhydrazono) derivatives			
XI	2,2-Dihydroxy-1,3-bis(phenylhydrazono)-cyclohexane	137	11	11
XII	D-*myo*-Inosose-1 phenylosazone	207–209	12	12
XIII	*myo*-Inosose-2 phenylhydrazone	174–176	13	13
XIV	2,3-Bis(phenylhydrazono)-1-propane-carboxaldehyde	196–198	9,10	14
XV	1,2-Bis(phenylazo)ethylene	149–150	14,15	15
XVI	D-Mannose *N,N*-diphenylformazan	174–175	16	16

References for Table 1

1 A. J. Fatiadi and H. S. Isbell, J. Res. NBS **68A** (Phys. and Chem.) No. 31, 287 (1964).
2 H. S. Isbell and A. J. Fatiadi, Carbohyd. Res. **2**, 204 (1966).
3 B. Pecherer, L. M. Jampolsky, and H. M. Wüest, J. Am. Chem. Soc. **70**, 2587 (1948).
4 W. Mayer, R. Bachmann, and F. Kraus, Chem Ber. **88**, 316 (1955).
5 T. Reichstein and R. Oppenauer, Helv. Chim. Acta **16**, 988 (1933); **17**, 390 (1934).
6 S. Ruhemann, J. Chem. Soc. **97**, 1438 (1910).
7 H. Pechmann and K. Jenisch, Ber. **24**, 3255 (1891).
8 W. Hahn, R. Bartnik, and J. Epsztajn, Roczniki Chem. **36**, 1645 (1962).
9 E. Chargaff and B. Magasanik, J. Am. Chem. Soc. **69**, 1459 (1947).
10 H. El Khadem and M. M. A. Abdel Rahman, Carbohyd. Res. **3**, 25 (1966).
11 A. J. Fatiadi and H. S. Isbell (to be publiched).
12 B. Magasanik and E. Chargaff, J. Biol. Chem. **174**, 173 (1948).
13 T. Posternak, Biochem. Prepn. **2**, 57 (1952).
14 H. Pechmann, Ber. **21**, 2751 (1888).
15 H. El Khadem and Z. M. El-Shafei, J. Chem. Soc. (1958) 3117.
16 L. Mester and A. Major, J. Am. Chem. Soc. **78**, 1403 (1956).

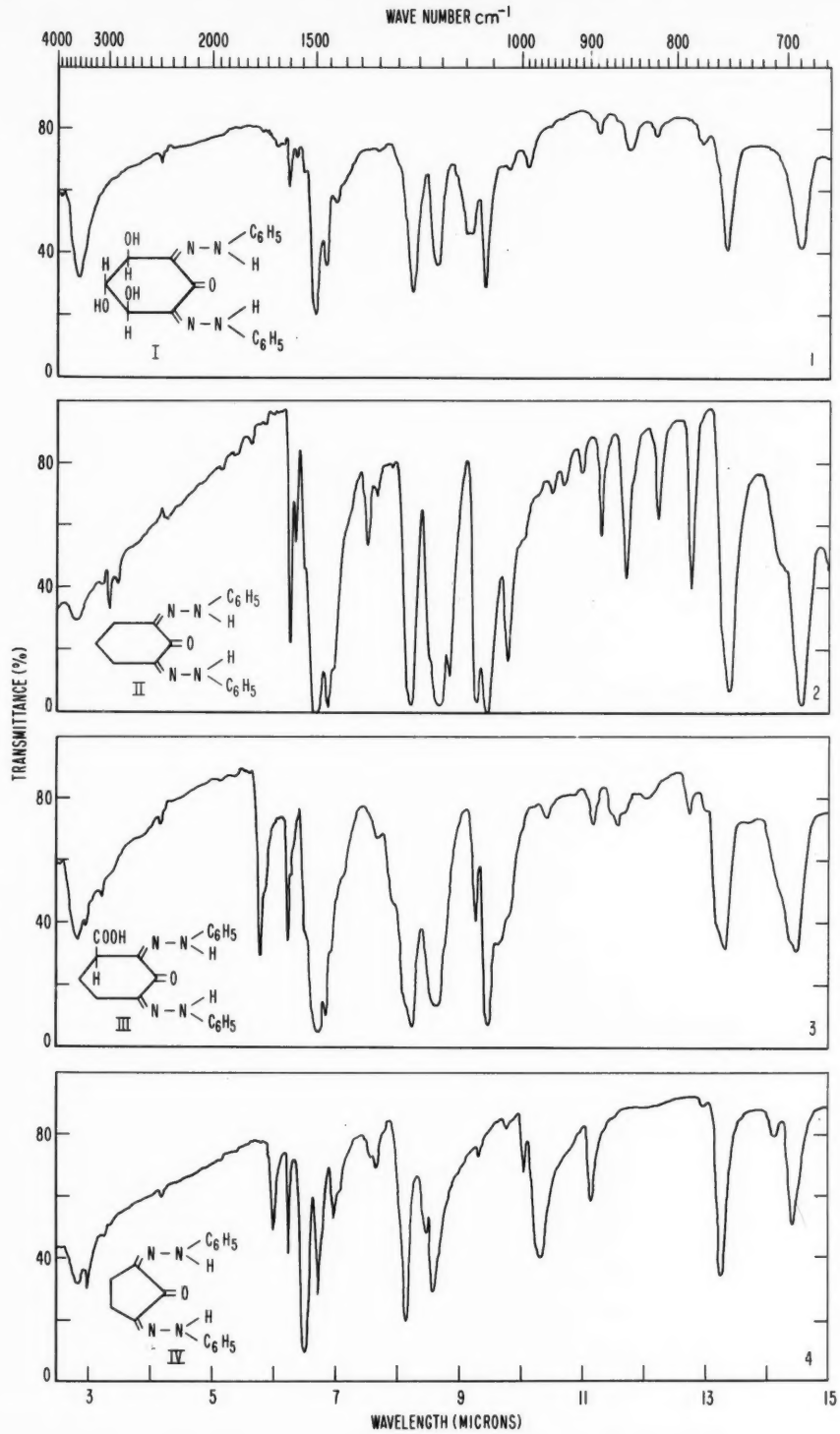

FIGURE 1. *Spectrograms of compounds in potassium chloride pellets.*

I, *xylo*-4,5,6-Trihydroxy-2-oxo-1,3-bis(phenylhydrazono)cyclohexane; II, 2-oxo-1,3-bis(phenylhydrazono)cyclohexane; III, 1-carboxy-1,3-bis(phenylhydrazono)cyclohexane; IV, 2-oxo-1,3-bis(phenylhydrazono)cyclopentane.

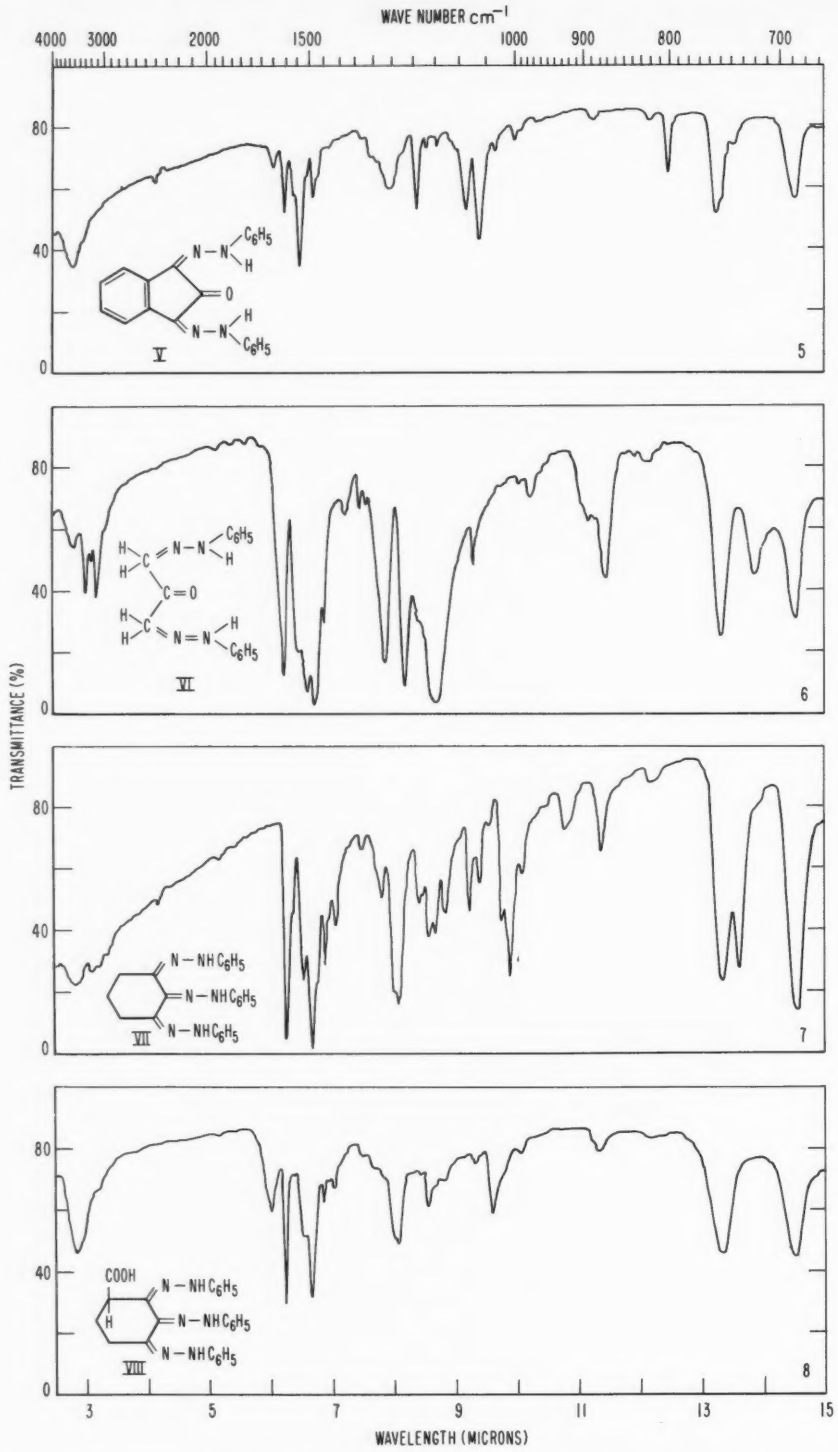

FIGURE 1. *Spectrograms of compounds in potassium chloride pellets.*—Continued

V. 2-oxo-1,3-bis(phenylhydrazono)indane: VI. 2-oxo-1,3-bis(phenylhydrazono)propane: VII. 1,2,3-tris(phenylhydrazono)cyclohexane: VIII. 1-carboxy-2,3,4-tris(phenylhydrazono)cyclohexane.

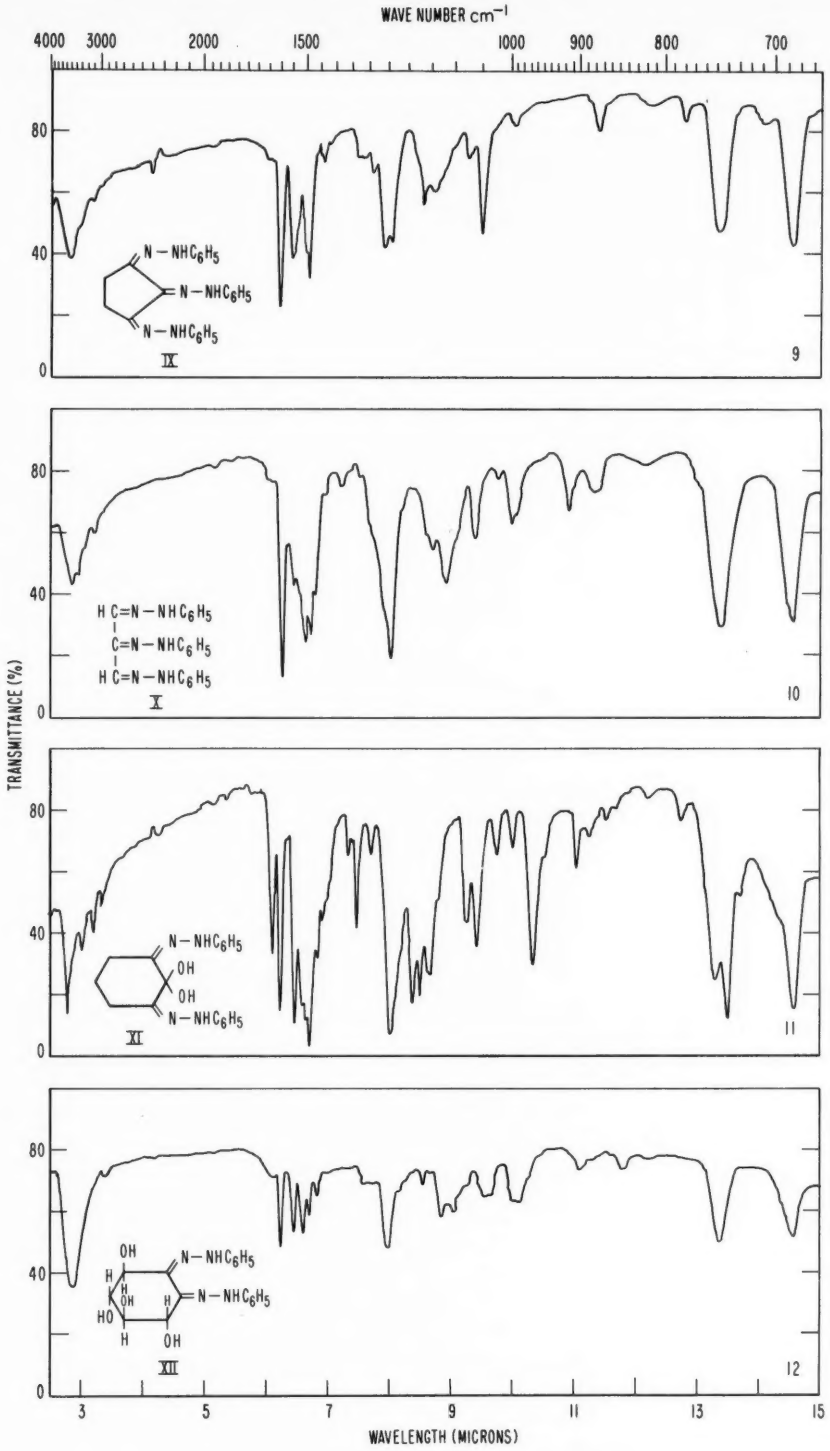

FIGURE 1. *Spectrograms of compounds in potassium chloride pellets.*—Continued

IX. 1,2,3-tris(phenylhydrazono)cyclopentane; X. 1,2,3-tris(phenylhydrazono)propane; XI. 2,2-dihydroxy-1,3-bis(phenylhydrazono)cyclohexane; XII. D-*myo*-inosose 1-phenylosazone.

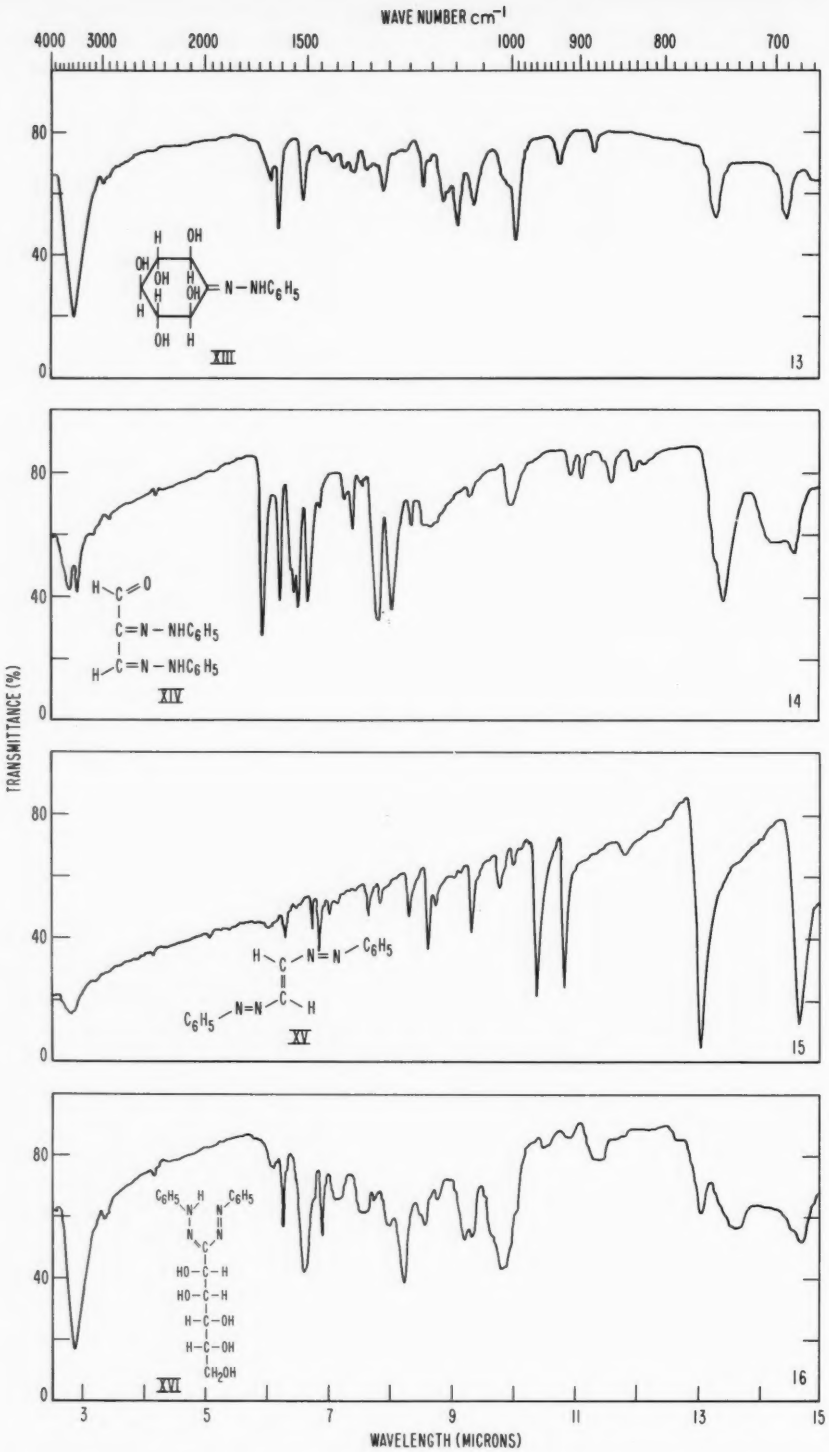

FIGURE 1. *Spectrograms of compounds in potassium chloride pellets.*—Continued

XIII. *myo*-inosose 2-phenylhydrazone; XIV. 2,3-bis(phenylhydrazono)-1-propanecarboxaldehyde; XV. 1,2-bis(phenylazo)ethylene; XVI. D-mannose *N,N*-diphenylformazan.

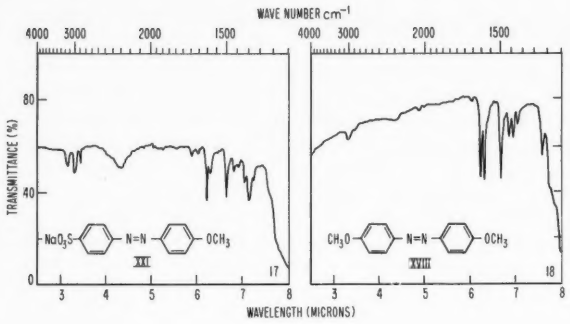

FIGURE 2. *Spectrograms of compounds in Fluorolube mulls.*
XXI, Sodium *p*-(*p*-methoxyphenylazo)benzenesulfonate; XVIII, *p*-phenylazoanisole.

linkage [3]. From a recent comprehensive study of the infrared absorption spectra of 110 aromatic azo compounds, Bassignana and Cogrossi [22] assigned two bands to the N=N group, namely near 1580 cm^{-1} (actually, 1558 to 1582 cm^{-1}) and at 1410 ± 30 cm^{-1}; it was cautiously stated by the authors [22] that the band at 1580 cm^{-1} must be regarded as the azo band in conjugation with the phenyl ring. The authors [22] also observed an important absorption band at 1145 ± 15 cm^{-1} which they assigned to the C−N= group; the band is actually the Ph–N stretching vibration [23, 24].

From study of the above results, it may be concluded that the absorption due to the N=N group should appear in two regions, namely at 1580 to 1560 cm^{-1} (here called Region A) and at 1450 to 1400 cm^{-1} (Region B). Thus, the appearance of the azo bands in Regions A and B may depend on: (1) how strongly they are superimposed on a band due to either the C−H bending vibration at 1468 to 1452 cm^{-1} or at 1500 to 1450 cm^{-1}; (2) a possible overlap of the N=N band with the N−H (bending) band in the region of 1600 to 1500 cm^{-1}; and (3) whether or not the molecule is symmetrical [1, 2, 6].

Examination of the infrared spectra of 2-oxo-1,3-bis(phenylhydrazono) compounds I to V reveals that the N=N band for this group shows a stronger absorption in Region A (1580 to 1560 cm^{-1}) than in Region B (1450 to 1400 cm^{-1}), except for compound IV which shows no N=N band in Region A. Perhaps, the resonating enolic structure of these compounds, as depicted in Ia, may influence the phenyl-ring absorption at 1590 cm^{-1}, to give a sharper separation of the N=N band; for the same reason, the phenyl absorption around 1480 cm^{-1} may overlap the azo band in Region B.

It is also observed that all of the 2-oxo-1, 3-bis(phenylhydrazones), compounds I to V, show the stronger absorption bands in Region A; compound VI, an open-chain 2-oxo derivative, showed medium absorption for the N=N group in Region B (1447 cm^{-1}) and a weak absorption in Region A.

It is also found that recording of the N=N absorption bands for pressed KCl or KBr pellets is useful as a supplement to the spectra measured in Fluorolube or Nujol; sometimes, the azo band recorded for pellets had poor resolution. For example, the N=N band of compound III showed good separation from phenyl-ring absorption in Nujol mull, but not in a KCl pellet (Region A); compound VI in Nujol showed a definite azo absorption in Region A, whereas in a KCl pellet, the N=N band was almost submerged with the phenyl-ring absorption; possibly, the spectral differences with KCl pellets indicate chemical change due to the pressure.

All of the outstanding features in the infrared absorption spectra of 2-oxo-1,3-bis(phenylhydrazono) derivatives are reported in table 2.

TABLE 2. *Bands*[a] *(cm^{-1}) in infrared spectra of compounds I to VI*

Compound No.	N=N band		N−H (bending)	Ph−N
	Region A 1577–1558	Region B 1447–1420	1543–1519	1163–1131
I	1577(w)	1428(w)	1543(w)	1163(s)
II	1567(m)	1432(vw)	1538(vw)	1149(s) 1131(m)
III	[b] 1577(w)	1420(vw)	1536(vw)	1156(s)
IV		1432(m)	1538(s)	1163(s)
V	1562(vw)	1428(w)	1536(s)	1165(m) 1149(m)
VI	[b] 1558(w)	1447(m)	1519(s)	1149(s)

[a] Key: m, medium; s, strong; v, very; w, weak.
[b] In Nujol.

To obtain better information about the absorption of the N=N group, the spectra of several selected phenylazo compounds in Fluorolube mull were recorded. Compounds XVII–XXVI showed a weak to moderate absorption for the N=N group in either Region A or Region B; especially, a sharp N=N band (Region A) was given by compounds XVIII and XXI (figure 2). Compounds XX and XXII–XXV, containing one or more hydroxyl groups on the aromatic ring either *ortho* or *para* to the azo group, showed, in addition to N=N absorption, a weak to moderate absorption at 1634 to 1618 cm^{-1} (conjugated C=O, and C=N) and at 1527 to 1515 cm^{-1} (N−H bending), indicative of the hydrazono structure; this observation is in agreement with the observed tautomerism of *ortho*-hydroxyazo and some *para*-hydroxyazo compounds [22, 25, 26, 27]. The important absorption features of the infrared spectra of compounds XVII to XXVI are reported in table 3.

4.2. Ph–N Stretching Band

In characterizing the phenylhydrazono–phenylazo derivatives, the absorption due to the Ph–N stretching band was found especially useful; fortunately, this band appears well inside the finger-print region and is, compared to N=N or N−H (bending) bands, relatively free from interference by bands of functional

TABLE 3. *Bands (cm^{-1}) in the infrared spectra of compounds XVII to XXVI*

Compound No.	Compound	N=N band		Conj. C=O, C=N	N−H (bending)
		Region A 1579–1562	Region B 1424–1408		
XVII	Phenol, 4,4'-azodi-	1562(vw)	1420(w)		
XVIII	Anisole, 4,4'-azodi-	1577(m)	1416(w)		
XIX	Phenol, *p*-phenylazo-	1567(vw)	1412(m)		
XX	Benzenesulfonate, sodium *m*-(*p*-hydroxyphenylazo)-		1410(w)	1613(m)	1515(m)
XXI	Benzenesulfonate, sodium *p*-(*p*-methoxyphenylazo)-	1579(m)	1408(w)		
XXII	Phenol, *o*-phenylazo-		1414(m)	1615(m)	
XXIII	Phenol, 3,5-dimethyl-6-phenylazo-		1422(m)	1534(m) 1613(w)	
XXIV	Benzenesulfonic acid, *m*-(2,4,6-trihydroxyphenylazo)-	1575(w)	1424(m)	1618(w)	1519(w)
XXV	Azoresorcin Yellow [a]	1562(vw)	1416(w)	1634(w)	
XXVI	6-Phenylazo-*trans*-5-hexene-D-*lyxo*-1,2,3,4-tetrol tetraacetate [b]		1420(w)		

[a] Commercial name.
[b] This compound was prepared as described by M. L. Wolfrom, A. Thompson, and D. R. Lineback, J. Org. Chem. **27**, 2563 (1962); they named it D-*arabino*-3,4,5,6-tetraacetoxy-1-phenylazo-*trans*-1-hexene.

groups. Only a few reports have appeared describing the absorption of the Ph–N group. Kübler and co-workers [23] and Rosenthal and Weir [24] assigned to the Ph−N group an absorption band in the region of 1149 to 1132 cm^{-1}; Bassignana and Cogrossi [22] assigned to this group a band at 1145 ± 15 cm^{-1}.

Inspection of the spectra of compounds I–XVI reveals the presence of a medium to strong absorption in the region of 1163 to 1123 cm^{-1}; the band sometimes appears as a sharp peak or a strong doublet. The above region appears to be characteristic of the Ph–N group; this group is always found in compounds having the phenylhydrazono–phenylazo structure. Interfering bands could arise from a C−O stretching frequency or a tertiary alcohol (1140 to 1124 cm^{-1}), esters of α,β-unsaturated acids and esters of aromatic acids (1200 to 1100 cm^{-1}), lactones (1370 to 1200 cm^{-1}), and C−H in-plane deformation of a monosubstituted benzene ring (1175 to 1125 cm^{-1}). This paper is concerned with nonsubstituted phenylhydrazono–phenylazo derivatives only.

4.3. N–H (Bending or Deformation) Band

All secondary amides, when examined in the solid state, display a sharp N−H (bending) band at 1570 to 1515 cm^{-1} (Amide II) [28, 29]; all primary and secondary amines exhibit the N−H (bending) absorption at 1650 to 1560 cm^{-1} [30, 31, 32]; amino acids show a strong N−H (bending) absorption at 1550 to 1485 cm^{-1} [31]. In a study of the infrared spectra of aminoquinones, Wallenfels and Draber [33] assigned a medium to strong band at 1509 to 1491 cm^{-1} to N−H (bending). Bell and co-workers [34], in a structural study of amidoximes in solution, recognized a NH_2 (bending) absorption at 1620 to 1575 cm^{-1}; the bands disappeared on deuteration. Dudek and Volpp [35], in a study of the structure of β-keto amides and β,β-diketo amides, observed N−H (deformation) absorption at 1642 and 1563 cm^{-1}; deuteration shifted the 1563 cm^{-1} band to 1458 cm^{-1}, indicative of chelated coupling; the authors [35] assigned the band at 1492 to 1458 cm^{-1} to N−D (deformation).

Examination of the infrared spectra of the phenylhydrazono–phenylazo derivatives, compounds I–X, XIV, and XV, reveals the presence of a medium to strong absorption at 1557 to 1510 cm^{-1} which may be attributed to N−H (bending); the absorption in this region is particularly characteristic for mono-, bis-, or tris-(phenylhydrazono) structures; as expected, the sharpness and intensity of this band is influenced by the proximity of the phenyl-ring absorption. The characteristic features in the infrared absorption spectra of the tris(phenylhydrazones) (compounds VII–X) and other mono- and bis-(phenylhydrazones), are reported in table 4.

In conclusion, a structural feature of compounds XI and XIV should be mentioned. The conversion of XI into II will be discussed elsewhere [4], and so only spectral changes pertinent to this paper will be mentioned.

The yellow compound XI has a typical bis(phenylhydrazono) structure, resembling those of sugar phenylosazones [36], and shows a strong N−H (bending) band at 1543 cm^{-1}. Slight warming of a solution of compound XI in absolute ethyl alcohol causes a dramatic, structural change to occur; this is accompanied by complete disappearance of the strong band at 1543 cm^{-1} (N−H bending) and appearance of a sharp new band (medium intensity) at 1572 cm^{-1}, attributed to the formation of a N=N group; only the infrared spectra recorded for the solid form proved successful for following the structural

TABLE 4. *Bands (cm^{-1}) in the infrared spectra of compounds VII to XVI*

Compound No.	N=N band		N−H (bending)	Ph−N
	Region A	Region B	1557–1515	1157–1123
VII			1531(m)	1126(m)
VIII			1527(w)	1134(w)
IX			1553(s)	1147(m)
X			1557(w)	1123(s)
XI			1543(s)	1152(s)
XII			1548(s)	1156(m)
XIII			1515(s)	1123(m)
XIV			1543(m) 1534(s)	1149(m)
XV	[a] 1562(vw)	1422(m)		1157(s) 1138(s)
XVI			1515(s)	1139(s)

[a] In Nujol.

change from XI to II; the red color of II arises from its new enolic structure, similar to that depicted in Ia.

Interconversion of compound XI produced spectroscopically pure tautomer II; the other members of the 2-oxo-1,3-bis(phenylhydrazones) studied, compounds I and III to VI, deviate somewhat from the pure enolic structure, analogous to Ia, and show (in addition to the N=N band) a minute absorption due the hydrazono structure [C=N and N−H (bending) absorption]. Compound XIV shows a normal carbonyl absorption at 1686 cm^{-1}; a displacement of normal carbonyl absorption (1700 to 1650 cm^{-1}) to a lower frequency (1584 cm^{-1}) is generally associated with a chelated C=O group [35]; hence, the infrared finding is in agreement with the n.m.r. spectrum of XIV, which shows the presence of one chelate ring between two phenylhydrazono groups [4, 5].

5. Experimental Procedures

5.1. Preparation and Purification of the Compounds

The compounds listed in table 1 were prepared by the methods given in the references cited. The compounds listed in table 3 were commercial preparations, except for compound XXVI. Each compound was purified by column chromatography (silica gel with acetic acid, or acetic acid–ethyl acetate–benzene as the mobile phase) and the purity was checked by thin-layer chromatography [silica gel G on microscope slides with 2:1(v/v) ethyl acetate–benzene as the solvent].

5.2. Measurement of Infrared Absorption

The spectrograms were recorded with a Perkin-Elmer Model 137 spectrophotometer [2] which was calibrated against a polystyrene standard (found value and deviation in parentheses): 3030 (3096; +66), 2924 (2976; +52), 2849 (2865; +16), 1946 (1953; +7), 1802 (1808 to 1805; +6 to +3), 1603 (1605 to 1600; +2 to −3), 1495 (1495 to 1493; 0 to −2), 1155 (1155 to 1153; 0 to −2), 1029 (1029 to 1028; 0 to −1). The spectrograms for compounds I to XVI were recorded for potassium chloride pellets; recording for each spectrum was repeated with a Nujol mull. The spectrograms for compounds XVII to XXVI were recorded in Fluorolube. In this study, the bands in the range of 4000 to 1800 cm^{-1} were of little interest; the bands in the range of 1800 to 1000 cm^{-1} were corrected by reference to the above calibration (polystyrene absorption at 1603 cm^{-1}) or to the Nujol band at 2861 cm^{-1}. The intensities recorded next to each band are classified on an arbitrary scale (in percent absorption): 2–10, vw (very weak); 10–20, w (weak); 20–70, m (medium); 70–90, s (strong); 90–100, vs (very strong).

[2] Certain commercial instruments are identified in this paper in order to specify adequately the experimental procedure. In no case does such identification imply recommendation or endorsement by the National Bureau of Standards, nor does it imply that the equipment identified is necessarily the best available for the purpose.

The author thanks Robert Schaffer for his encouragement, Horace S. Isbell for his interest, and R. Stuart Tipson for his counsel.

6. References

[1] C. N. R. Rao, Chemical Applications of Infrared Spectroscopy p. 267 (Academic Press Inc., New York, N.Y., 1963).
[2] L. J. Bellamy, The Infra-red Spectra of Complex Molecules, p. 271 (John Wiley & Sons, Inc., New York, N.Y., 1958).
[3] H. S. Isbell and A. J. Fatiadi, Carbohyd. Res. **2,** 204 (1966).
[4] A. J. Fatiadi and H. S. Isbell (to be published).
[5] H. El Khadem and M. M. A. Abdel Rahman, Carbohyd. Res. **3,** 25 (1966).
[6] R. M. Silverstein and G. C. Bassler, Spectrometric Identification of Organic Compounds, p. 68 (John Wiley & Sons, Inc., New York, N.Y., 1963).
[7] H. Zollinger, Azo and Diazo Chemistry of Aliphatic and Aromatic Compounds, p. 322 (Interscience Publishers, Inc., New York, N.Y., 1961).
[8] W. Otting and F. Drawert, Chem. Ber. **88,** 1469 (1955).
[9] E. Lieber, C. N. R. Rao, T. S. Chai, and H. Rubenstein, Can. J. Chem. **36,** 1441 (1958).
[10] H. H. Jaffe and M. Orchin, Theory and Applications of Ultraviolet Spectroscopy, p. 185 (John Wiley & Sons, Inc., New York, N.Y., 1962).
[11] R. N. Jones and C. Sandorfy, in Technique of Organic Chemistry, Vol. IX, W. West, ed. (Interscience Publishers, Inc., New York, N.Y., 1956).
[12] R. S. W. Le Fevre, M. F. O'Dwyer, and R. L. Werner, Chem. Ind. (London) 378 (1953).
[13] R. S. W. Le Fevre, M. F. O'Dwyer, and R. L. Werner, Australian J. Chem. **6,** 341 (1953).
[14] R. S. W. Le Fevre and J. B. Sousa, Australian J. Chem. **9,** 151 (1956).
[15] R. S. W. Le Fevre and R. L. Werner, Australian J. Chem. **10,** 26 (1957).
[16] D. E. McGreen, W. Wai, and G. Carmichael, Can. J. Chem. **38,** 2400 (1960).
[17] T. V. van Auken and K. L. Rinehart, Jr., J. Am. Chem. Soc. **84,** 3736 (1962).
[18] C. G. Overberger, N. Weinshenker, and J. P. Anselme, J. Am. Chem. Soc. **86,** 5364 (1964).
[19] R. F. R. Church, A. S. Kende, and M. J. Weis, J. Am. Chem. Soc. **87,** 2665 (1965).
[20] D. M. Gale, M. J. Middleton, and C. G. Krespan, J. Am. Chem. Soc. **87,** 657 (1965).
[21] B. T. Gills and J. D. Hagarty, J. Am. Chem. Soc. **87,** 4576 (1965).
[22] P. Bassignana and C. Cogrossi, Tetrahedron **20,** 2361 (1964).
[23] R. Kübler, W. Lüttke, and S. Weckberlin, Z. Elektrochem. **64,** 650 (1960).
[24] A. Rosenthal and M. R. S. Weir, J. Org. Chem. **28,** 3025 (1963).
[25] Ref. [7], pp. 322–327.
[26] M. Dolinsky and J. H. Jones, J. Assoc. Offic. Agr. Chemists **37,** 197 (1954).
[27] D. Hadzi, J. Chem. Soc. (1956) 2143.
[28] Ref. [2] pp. 205–219.
[29] Ref. [6] p. 66.
[30] Ref. [2] p. 249.
[31] Ref. [6] p. 67.
[32] Ref. [11] p. 520.
[33] K. Wallenfels and W. Draber, Tetrahedron **20,** 1889 (1964).
[34] C. L. Bell, C. N. V. Nambury, and L. Bauer, J. Org. Chem. **29,** 2873 (1964).
[35] G. O. Dudek and G. P. Volpp, J. Org. Chem. **30,** 50 (1965).
[36] W. Otting, Ann. **640,** 44 (1961).

(Paper 71A4–459)

JOURNAL OF RESEARCH of the National Bureau of Standards—A. Physics and Chemistry Vol. 71A, No. 4, July-August 1967

Dielectric Constant of N-Hexane as a Function of Temperature, Pressure, and Density

Frederick I. Mopsik

Institute for Materials Research, National Bureau of Standards, Washington, D.C. 20234

(April 17, 1967)

A description is given of apparatus employing a cell that is both a bellows dilatometer and a three-terminal electrode set for measuring simultaneously the density and dielectric properties of liquids as functions of temperature and pressure. Measurements are possible at temperatures from 120 °K to over 300 °K and pressures from 1 to 2000 atm with an uncertainty of 0.03 percent. The density, dielectric constant, and Clausius-Mossotti function of *n*-hexane have been measured for temperatures from 223 to 298 °K (−50 to 25 °C) and at pressures from 1 to 2000 atm. There is a linear decrease in the Clausius-Mossotti function with density and a decrease with temperature corresponding to an effective dipole moment of 0.085 debye.

Key Words: Clausius-Mossotti, density, dielectric constant, dilatometer, function, high pressure, *n*-hexane, pressure, three-terminal electrode set.

1. Introduction

The dielectric properties of liquids have usually been measured as a function of temperature only. Any attempt to relate these properties to a molecular model requires that the density changes that accompany any temperature changes be taken into account explicitly. However, the models may not be adequate for such a purpose. Moreover, they usually use certain parameters that are assumed to be independent of the density but need not be, notably the polarizability. It would be a great aid to understanding dielectric behavior if density effects could be separated from temperature effects with good accuracy.

Since a liquid is relatively incompressible, high pressures are required to cause significant density changes apart from those due to temperature alone. While the dielectric constants of several liquids have been measured as a function of pressure [1, 2],[1] the temperature range was restricted and the accuracy not too high. This was partly because only a two-terminal capacitance cell was used.

Therefore, apparatus was assembled with the aim of making accurate dielectric measurements on liquids with a three-terminal electrode set over a wide range of pressure and temperature. At the same time, provisions were made for a means of monitoring the density simultaneously. This latter provision eliminates the reliance on previous density measurements. Furthermore, pressure gauge calibrations and sample variations are removed as sources of error when the dielectric constant is studied as a function of density.

[1] Figures in brackets indicate the literature references at the end of this paper.

2. Apparatus

2.1. Cell

The measuring cell was a bellows dilatometer in which a three-terminal electrode set was suspended. The cell, shown in figure 1, was made entirely of AISI 316 stainless steel.

a. Electrodes

The dielectric measurements were made by the electrode set, F, G, H, whose leads were brought out of the endplate, K, by alumina ceramic feedthroughs. The gold plated electrodes were self-shielded, three-terminal, coaxial cylinders. Alumina ceramic disks were used as the insulating spacers. The assembly was held together by screws in an axially symmetric manner to minimize shifts in alinement for large changes in temperature. The end alumina disks were perforated for liquid passage and the guard electrodes, G, had small oblique holes for the same purpose. The lead from the guarded central electrode, F, was shielded by a small piece of tubing at the top of the electrodes and a projecting collar on the endplate that completely shielded the feedthrough for this lead. This eliminated any measurable stray capacitance and the electrodes could be used for absolute measurements. The guard electrodes were brought out by a separate feedthrough and grounded externally. The outer electrode, H, was brought out through a third feedthrough. Electrical contact with the bellows, which was grounded, was prevented by a small ring, L, of heat-shrinkable fluorinated ethylene-propylene copolymer. This ring had a

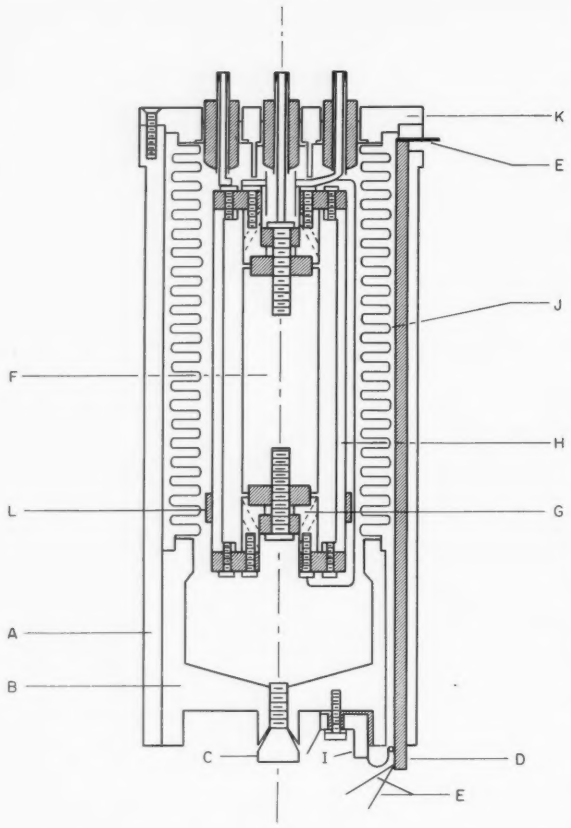

FIGURE 1. *Cross section of combined dilatometer and dielectric cell.*
A, sleeve; B, piston; C, filling plug; D, fused silica rod; E, electrical leads; F, guarded inner electrode; G, guard ring; H, outer electrode; I, sliding contact assembly; J, bellows; K, endplate; L, insulating spacer.

volume small enough so that its volume changes with temperature and pressure were negligible. The geometric capacitance of the assembly was 4.1158 $\pm$0.0005 pF.[2]

b. Dilatometer

The dilatometer was formed with a seamless bellows, J, soldered at one end to an end plate, K, and at the other to a piston, B. The piston moved in a close fitting sleeve, A, that was attached to the endplate. Because of this constraint, the motion of the bellows assembly was purely axial. To provide access for filling, a screw plug with a tapered head, C, seated against a similar taper in the piston. A silver gasket acted as a seal that could be made or unmade with moderate torques.

The extension of the bellows was monitored by a potentiometric method. A fused silica rod, D, had a resistive stripe of Liquid Bright Platinum[3] applied to it. The rod was mounted in a groove in the outer sleeve by a small amount of epoxy cement at the end close to the endplate. This end also was soldered to a fine copper wire, E, and to the sleeve. The other end of the rod had soldered to it two more fine copper wires, E. The piston carried a sliding contact assembly, I, consisting of a mounting block, a light beryllium copper spring and a small piece of platinum wire which served as the actual contact. By use of the cell mounting as a current return and one of the two wires at the piston end of the rod as a current source, it was then possible to use a four-terminal method for determining the voltage across the resistance stripe proper.

c. Calibration

The ratio of the voltage at the slide contact to the total voltage across the silica rod was calibrated as a function of length by deflecting the bellows and measuring the deflection on a dial gauge calibrated with gauge blocks to 1 μ. The corresponding voltage ratio was measured by means of an ordinary laboratory potentiometer. It was possible to resolve a deflection of 1 μ for a total deflection of 1.2 cm with a reproducibility of ± 5 μ. A similar fused silica rod which had a very fine wire contact soldered to it showed no change in voltage ratio when placed in dry ice, so it was assumed that a given voltage ratio corresponded to the same position on the rod under all experimental conditions.

The constants needed to convert voltage ratios into density changes were obtained from calibrations using distilled water. The complete cell was weighed with and without water, the temperature and voltage ratio being taken prior to the weighing with water. Also, the filled cell was connected to a calibrated glass capillary and the bellows deflected. These data were sufficient to give both the total volume of the cell, 26.999 $\pm$0.005 cm^3 and the change in volume per unit length of bellows deflection, 4.915 $\pm$ 0.004 cm^3/cm.

d. Corrections

The cell constants were corrected for temperature and pressure. For the dilatometer, this was facilitated by having the inner diameter of the piston very nearly equal to the effective diameter of the bellows. Excluding the volume of the electrodes, the dilatometer will then display the temperature and pressure coefficients of fused silica in length and AISI 316 stainless steel in cross-sectional area. The electrodes consisted of 7.6 ml of steel and 1.1 ml of alumina and their change in volume was computed separately. For the electrodes, the geometric capacitance was corrected for the linear coefficients of AISI 316 stainless steel.

The thermal expansion factors for the fused silica and AISI 316 stainless steel were taken from NBS Monograph No. 29 [3]. The compressibility of the fused silica was taken as 28.09×10^{-7} atm^{-1} [4] while that of steel was taken as 5.84×10^{-7} atm^{-1} [5]. For alumina, the thermal expansion and compressibility were derived from data of Coors Porcelain Co. [6];

[2] All error limits, unless indicated otherwise, are estimates of maximum uncertainty.
[3] Certain commercial products are mentioned in this paper to completely specify the experimental procedure. In no case does such identification imply a recommendation or endorsement by the National Bureau of Standards.

the thermal expansion was taken as 1/5 that of steel, the compressibility 7.5×10^{-7} atm^{-1}. It is believed that these factors are sufficiently accurate to introduce no appreciable systematic error.

As a check on the corrections for capacitance and on the design of the electrodes, the electrode assembly was cooled in both liquid nitrogen and dry ice and its capacitance measured. The change in capacitance agreed with that predicted from the thermal expansion factors in the Monograph and the room temperature capacitance was recovered on warming. Similarly, repeated measurements on the geometric capacitance after both pressure and temperature cycling always gave the same results within limits of measurement.

2.2. Pressure System

The cell was suspended in a cylindrical stainless steel pressure vessel, sealed on both ends by plugs with composite copper polytetrafluorethylene gaskets. The bottom plug had a standard high pressure fitting. The top plug had six electrical leads through it, two of which were coaxially shielded. The top plug also had a thermocouple well in it that extended into the working volume. The working volume was about 5 cm in diameter by 12 cm in length. The vessel was suspended from a metal plate by three thin walled stainless steel tubes to minimize thermal conduction to the vessel.

Pressures were generated by means of an air-driven differential piston pump. For the measurements reported in this paper, isopentane was used as the hydraulic fluid. A special needle valve capable of very low flow rates was placed at the output of the pump so that the pressure inside the pressure vessel could be changed slowly. Pressure was measured by an 18 in Heise pressure gauge having a full scale range of 2000 atm.[4]

2.3. Temperature Control

Temperature was maintained by immersion in a large glass Dewar filled with stirred heptane as the bath fluid. Since the leads from the pressure vessel were surrounded by the bath fluid, a hydrocarbon was chosen because of its low conductivity. An immersed heater and a large copper cooling coil were used for control. The coolant was gas from evaporating liquid nitrogen or, for rapid cooling to a desired temperature, liquid nitrogen itself.

For temperature regulation a copper-constantan thermocouple was immersed in the bath. The output was fed into a potentiometer set to the emf corresponding to the desired temperature. The error signal was detected by a chopper-stabilized D.C. amplifier (4×10^7 gain). This controlled a servo motor which in turn drove a cam-operated switch for relays supplying power from variable autotransformers to either the heater in the bath or another heater in a Dewar containing liquid nitrogen. A vacuum-jacketed transfer tube connected the Dewar to the cooling coil of the bath. Just above the liquid nitrogen the tube had a vent plug that could be operated from outside the Dewar. In this way, either evaporating gas or liquid could be driven by the heater into the cooling coil. With this system, it was possible to stabilize the bath temperature to better than the equivalent of 1 μV of thermocouple output or approximately 0.03 °C at temperatures from 120 °K to over 300 °K.

2.4. Temperature Measurement

Temperature was measured by a copper-constantan thermocouple in the well in the top cap of the pressure vessel. The thermocouple was calibrated to ± 0.1 °C. Because of the large mass of the pressure vessel and the poor thermal conductivity of stainless steel, pressure changes of 100 to 200 atm required a wait of about ½ hour before the temperature of the thermocouple returned to equilibrium. This final temperature was constant to 0.006 °C, the resolution of the potentiometer, with no apparent fluctuations or drift. Furthermore, there did not seem to be an appreciable thermal lag between the thermocouple and the cell as indicated by volume changes. Temperature uniformity could not be checked but it should have been excellent since the working volume was the relatively small interior of the vessel which was well immersed in the bath.

2.5. Electrical Measurements

The electrical measurements of capacitance and equivalent parallel conductance were made with a bridge of the Cole-Gross Type [7]. The bridge used a transformer from a General Radio Type 1605 Impedance Comparator (see footnote 3). A General Radio Type 1422CC variable capacitor fitted with a vernier that could be read to 0.001 pF over a range of 5 to 110 pF served as the standard capacitor. The conductance network used a Vogue Instrument 10-turn potentiometer that had very low stray and distributed impedances and was linear to 0.01 percent. The standard conductances were metal film resistors, two in series for each range. This arrangement greatly reduced their equivalent shunt capacitance; when needed, a wire connected to ground was wrapped around their junction to reduce the capacitance further. It was possible to keep the shunt capacitance below 0.05 pF quite easily. By careful shielding of the bridge to reduce capacitance to ground, balancing the capacitance to ground of the 1422CC capacitor across the transformer and carefully choosing the ground points in the wiring, the bridge was usable from 40 Hz to 400 kHz with an accuracy of 0.001 pF for parallel capacitance, at least 0.1 percent for parallel conductance over full scale ranges of 0.1 to 100 μmho, and a minimum tan δ of 0.0001 for a cell with a geometric capacitance of 4 pF.

[4] Pressures are expressed in normal atmospheres each equivalent to 1.01325 bars, 1.01325×10^6 dyne cm^{-2}, or 1.01325×10^5 N m^{-2}.

3. Measurements

The *n*-hexane used in this study was reagent grade material stated to be 98+ percent pure. It was fractionally distilled through a packed 25 cm column. The initial fraction, which amounted to 10 percent of the total, was discarded and the remainder, which had a constant boiling point of 68.7 °C at 760 mm Hg, was collected. The density as measured in the dilatometer was 0.6547 ± 0.0002 g/cm³ at 25 °C. The refractive index of a separate sample of *n*-hexane was measured to be 1.37407 ± 0.00005 at 22 °C for the sodium D line. Literature values [8] for the boiling point, density and refractive index are 68.74 °C, 0.65483 g/cm³ and 1.37382 respectively.

The *n*-hexane was freed from dissolved air by boiling under reduced pressure produced by a mechanical vacuum pump with a trap. It was then run into the cell, which had been evacuated to about 10^{-5} torr. No air bubbles were formed inside the cell and there was never any indication of voids during the measurements. Voids would have manifested themselves by an abnormally high initial compressibility or a failure of the volume to return to its original value at atmospheric pressure after a pressure cycle.

The measurements were run at 25, 0, −25, and −50 °C for gauge pressures of 0 to 2000 atm except at −50 °C where a maximum pressure of 1500 atm was used. Measurements were taken for both increasing and decreasing pressure, and no systematic difference was found. The dielectric constant was measured at 10 kHz and no measurable loss was ever observed. The measured values of the dielectric constant and density are given in table 1. These values are averages of two measurements, one for increasing, and one for decreasing pressure. The variation of density with pressure and temperature is shown in figure 2, the variation of the dielectric constant in figure 3.

TABLE 1. *Density, dielectric constant, and* CM *of* n-*hexane*

	25°			0°			−25°			−50°		
P	ρ	ϵ	$\frac{\epsilon-1}{\epsilon+2}\frac{M}{\rho}$	ρ	ϵ	$\frac{\epsilon-1}{\epsilon+2}\frac{M}{\rho}$	ρ	ϵ	$\frac{\epsilon-1}{\epsilon+2}\frac{M}{\rho}$	ρ	ϵ	$\frac{\epsilon-1}{\epsilon+2}\frac{M}{\rho}$
(atm)	(g/cm³)		(cm³/mol)	(g/cm³)		(cm³/mol)	(g/cm³)		(cm³/mol)	(g/cm³)		(cm³/mol)
1	0.6547	1.8799	29.854	0.6769	1.9178	29.827	0.6987	1.9540	29.760	0.7193	1.9908	29.745
101	.6647	1.8972	29.846	.6856	1.9320	29.796	.7054	1.9658	29.754	.7261	2.0015	29.708
201	.6737	1.9123	29.828	.6937	1.9449	29.758	.7120	1.9778	29.751	.7320	2.0112	29.679
401	.6898	1.9379	29.759	.7067	1.9679	29.752	.7245	1.9979	29.690	.7422	2.0294	29.664
601	.7022	1.9599	29.752	.7183	1.9874	29.710	.7348	2.0158	29.667	.7513	2.0449	29.635
801	.7133	1.9789	29.723	.7286	2.0045	29.668	.7441	2.0319	29.644	.7595	2.0596	29.618
1001	.7240	1.9955	29.657	.7380	2.0204	29.636	.7523	2.0462	29.619	.7672	2.0732	29.598
1251	.7350	2.0148	29.637	.7482	2.0380	29.609	.7619	2.0626	29.587	.7761	2.0881	29.557
1501	.7450	2.0317	29.602	.7578	2.0541	29.569	.7703	2.0780	29.575	.7841	2.1021	29.530
1751	.7540	2.0478	29.592	.7660	2.0690	29.557	.7786	2.0195	29.526			
2001	.7627	2.0620	29.544	.7738	2.0828	29.537	.7858	2.1045	29.511			

4. Discussion

4.1. Treatment of Data

For a nonpolar liquid, such as *n*-hexane is normally assumed to be, the theory of the static dielectric constant [9] predicts that

$$\frac{\epsilon-1}{\epsilon+2}\frac{M}{\rho}=\frac{4\pi}{3}N\alpha,$$

where N is Avogadro's number, M is the molecular weight, ρ is the density, ϵ is the static dielectric constant and α is the molecular polarizability. The left-hand side of the equation, commonly called the Clausius-Mossotti function, or CM, is therefore, predicted to be a constant if α remains constant.

To check for this constancy, the CM was calculated for each measured point. The results are given in table 1 and a plot of the CM as a function of density is given in figure 4. It should be noted that the CM for a given temperature and pressure was computed for each measurement and averaged separately from the density and dielectric constant. This procedure was followed to reduce the effect of any lack of reproducibility in temperature or pressure on the CM. It can be easily seen that the CM is not a constant.

At constant temperature, the experimental CM is found to decrease linearly with density to within the experimental uncertainty, 0.03 percent. While this is at variance with the analysis of earlier data [10] which found linearity in a plot of the reciprocal of the CM, the difference between the two plots is less than experimental error. Moreover, since least squares reduction of the data showed a slightly better fit for the plot of the CM than that of its reciprocal, the simpler linear function was used here to fit the data. Similarly, the CM is seen to decrease with increasing temperature at constant density. For this case the change is much smaller so that no attempt was made to determine the functional form of the behavior.

The constants obtained by the least squares fit of the CM at each temperature as a linear function of density are given in table 2. The corresponding lines are indicated in figure 4. Also, the last column

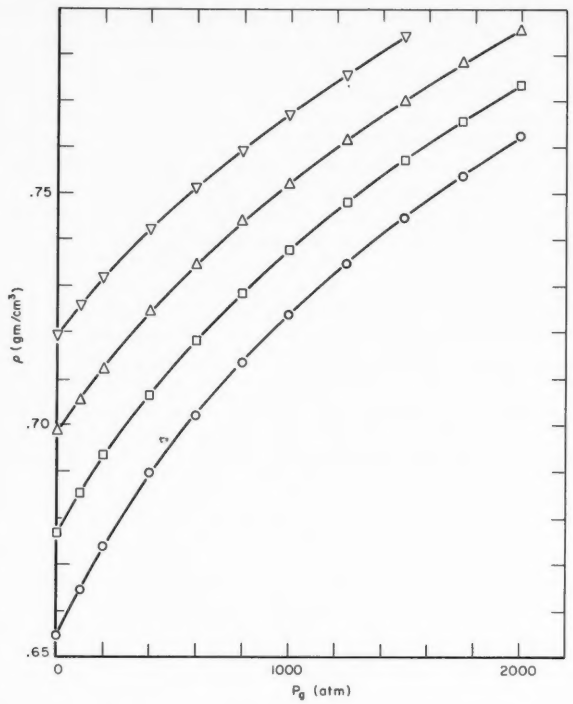

FIGURE 2. *Density of* n-*hexane as a function of pressure.*
0, 25 °C; □, 0 °C; △, −25 °C, ▽, −50 °C.

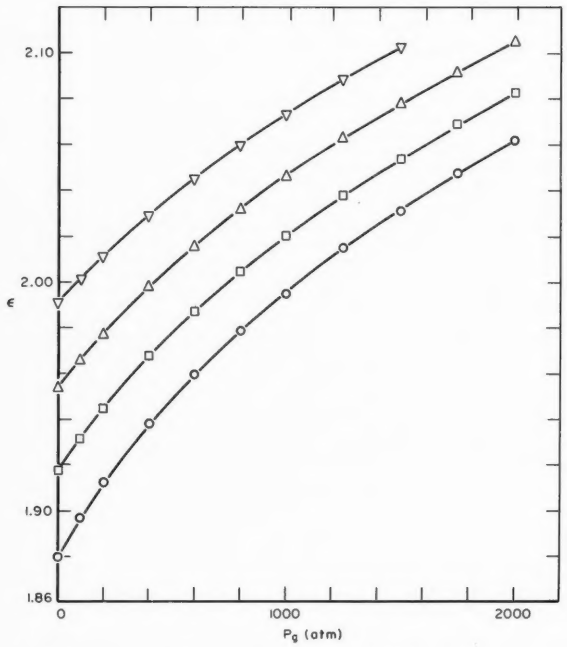

FIGURE 3. *Dielectric constant of* n-*hexane as a function of pressure.*
0, 25 °C; □, 0 °C; △, −25 °C, ▽, −50 °C.

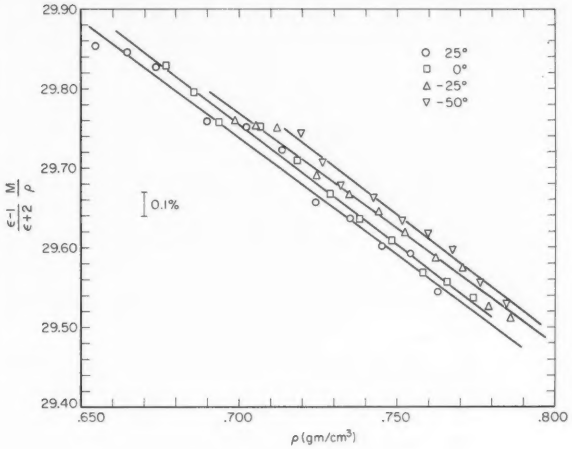

FIGURE 4. *CM of* n-*hexane as a function of density.*
0, 25 °C; □, 0 °C; △, −25 °C; ▽, −50 °C.
The drawn lines are the least squares fit of the data for each temperature to a straight line of the form $CM = m\rho + b$.

TABLE 2. *Least squares fit of CM to form* $CM = m\rho + b$
(see footnote 5)

T	m	b	CM for $\rho = 0.7300$
	$\left(\frac{cm^6}{g\ mol}\right)$	(cm³/mol)	(cm³/mol)
25°	−2.950 ± 0.092	31.804 ± 0.065	29.650 ± 0.004
0°	−3.028 ± .078	31.873 ± .057	29.663 ± .003
−25°	−2.903 ± .088	31.801 ± .065	29.681 ± .002
−50°	−3.019 ± .108	31.904 ± .081	29.700 ± .003

of table 2 gives the CM calculated from the fitted equation at a density of 0.7300 g/cm³, a value well within the range of values for each temperature. This is a much better indication of the variation with temperature than the intercept b, which involves a long extrapolation.

4.2. Comparison of Data

Some comparisons with published work on *n*-hexane are possible. The values of the dielectric constant and at 25 and −50°C are 1.882 and 1.990, respectively, at atmospheric pressure according to NBS Circular 514 [11]. These compare quite favorably with the values reported here of 1.8799 and 1.9908. Data as a function of pressure have also been reported [2] and the comparison given in table 3. The two sets of data are parallel to each other, but the earlier data seem to contain a significant systematic error, perhaps because the capacitance was measured using a two-terminal cell which is relatively less accurate than the three-terminal cell used in the present work.

Somewhat better comparisons can be made for the density. The density at atmospheric pressure at

TABLE 3. *Comparison of results*

p	ϵ(25 °C)		ρ(20 °C)		ρ(0 °C)	
	This work	Chang [a]	This work	Eduljee [b]	This work	Eduljee [b]
0	1.8799	1.896	0.6547	0.6550	0.6769	0.6769
101	1.8972	1.911	.6647		.6856	
501	1.9489	1.962	.6960	.6958	.7125	.7125
1001	1.9955	2.002	.7240	.7235	.7380	.7378
1501	2.0317		.7450	.7448	.7578	.7577
2001	2.0620	2.077	.7627	.7623	.7738	.7743

[a] Data of Chang [2] adjusted from pressures reported in kg/cm² and a temperature of 30 °C using coefficients derived from this work.
[b] Data of Eduljee [13] reported in volume relative to 0 °C and 1 atm pressure. The data have been made to coincide with the data reported here at 1 atm pressure and 0 °C.

25° is reported to be 0.65483 g/cm³ [8] while at 0° 0.6769 g/cm³ [12]. The measured values are 0.6547 and 0.6769 g/cm³. Some quite good density measurements have been made as a function of pressure [13] and the comparison is given in table 3. The agreement is excellent and easily within the combined experimental uncertainties. As with all comparisons that could be made, this one supports the claimed uncertainties of 0.02 percent for ϵ, 0.02 percent for ρ, and 0.03 percent for CM.

4.3. Interpretation

The observed density dependence of the CM is consistent with the results of the earlier work. Since the equations normally used for the liquid state, such as Onsager's, predict a constant CM, they are clearly inadequate and offer no guide as to the form of the density dependence. It should be noted, however, that the zero density extrapolation of the CM to 31.8 cm³/mol is considerably higher than the reported gas value of 30.0 [14]. This is possibly due to the use of an erroneous form for the density dependence. However, the use of the reciprocal of CM would lead to a still higher value.

The variation of CM with temperature at constant density is also of interest. Within experimental error, the variation seems to be independent of density. One possibility is that *n*-hexane in the liquid state is polar. This is reasonable since any conformation other than the straight chain could have a permanent moment. If the observed difference of 0.050 ± 0.007 cm³/mol in the CM between -50 and 25 °C is considered to result from a $\mu^2/3kT$ term [17], an effective dipole moment of 0.085 ± 0.006 D (1 debye $= 10^{-12}$ cgs units)[5] is calculated. This is comparable to moments observed in other hydrocarbons [15]. It is doubtful that it is due to impurities, especially water, since it is believed that the hexane used is quite dry. Even if it is assumed to be saturated with water, (0.053 mole percent [16]) the water contribution would only be 0.02 D. It is believed that the hexane used was drier than this; consequently, impurities are not a likely cause for the temperature variation observed. Also, if the dipolar contribution to the dielectric constant is subtracted out, this would lead to a dielectric constant of 1.8742 at 25 °C and 1 atm which seems too low. Therefore, the temperature dependence of the CM for *n*-hexane seems to be a property of the pure liquid. Caution should be exercised, however, in interpreting the temperature dependence of the CM as due to a dipole moment. In particular, since the CM is density dependent and this cannot be accounted for by a dipole moment, there could well be a temperature dependence even if there were no dipole moment. This matter will require clarification by further measurements on liquids having known dipole moments.

[5] The error indicated is the computed standard deviation.

Much of the initial work in constructing the apparatus was done by Norman L. Brown.

5. References

[1] W. E. Danforth, Jr., Phys. Rev. **38,** 1224 (1931).
[2] Z. T. Chang, Chinese J. Phys. **1,** 1 (1924).
[3] R. J. Corruccini and J. J. Gniewek, Thermal expansion of technical solids at low temperatures, NBS Mono. 29 (1961).
[4] L. H. Adams and R. E. Gibson, J. Washington Acad. Sci. **21,** 381 (1931).
[5] P. W. Bridgman, Proc. Amer. Acad. Arts Sci. **74,** 11 (1940).
[6] Data Sheet 0001, Revised August 1964, Coors Porcelain Co., Golden, Colo.
[7] R. H. Cole and P. M. Gross, Jr., Rev. Sci. Instr. **20,** 252 (1949).
[8] F. D. Rossini et al., Selected Values of Physical and Thermodynamic Properties of Hydrocarbons and Related Compounds (Carnegie Press, Pittsburgh, 1953).
[9] L. Onsager, J. Am. Chem. Soc. **58,** 1486 (1936).
[10] J. S. Rosen, J. Chem. Phys. **17,** 1192 (1949).
[11] A. A. Maryott and E. R. Smith, Table of dielectric constants of pure liquids, NBS Circ. 514, (1951).
[12] J. Timmermans, Physico-Chemical Constants of Pure Organic Compounds (Elsevier Publishing Co., Inc., New York, 1950).
[13] H. E. Eduljee, D. M. Newitt, and K. E. Weale, J. Chem. Soc. **1951,** 3086.
[14] A. A. Maryott and F. Buckley, Table of dielectric constants and electric dipole moments of substances in the gaseous state, NBS Circ. 537 (1953).
[15] D. R. Lide, Jr., J. Chem. Phys. **33,** 1514 (1960).
[16] J. H. Hildebrand and R. L. Scott, The Solubility of Nonelectrolytes, 3d ed. (Reinhold Publishing Corp., New York, 1950).
[17] P. Debye, Polar Molecules (Dover, New York, 1947).

(Paper 71A4–460)

JOURNAL OF RESEARCH of the National Bureau of Standards—A. Physics and Chemistry Vol. 71A. No. 4, July-August 1967

Heat Capacities and Related Thermal Data for Diethyl Phthalate Crystal, Glass, and Liquid to 360 °K

S. S. Chang, J. A. Horman,* and A. B. Bestul

Institute for Materials Research, National Bureau of Standards, Washington, D.C. 20234

(March 28, 1967)

Experimentally determined heat capacity values, precise to within 0.1 percent, and related thermal data are reported for quenched and annealed diethyl phthalate glasses from 10 °K to the glass transformation temperature, T_g (around 180 °K), for the liquid from T_g to 360 °K, and for the crystal from 10 °K to the melting temperature (269.9 °K). The mole fraction of liquid-soluble, solid-insoluble impurity in the sample as determined by fractional melting was 0.0012. Common thermodynamic properties calculable from the experimental data are reported. The heat capacities of the two glasses differ by more than the uncertainty of the measurements, and both lie below that of the crystal in the range from 30 to 75 °K. At low temperatures, just above 10 °K, the heat capacities of the glasses rise as much as 8 percent above that of the crystal.

Key Words: Annealed glass, crystal, diethyl phthalate, glass transformation, heat capacity calorimetry, molecular configurational state, normal and supercooled liquid, quenched glass, residual (configurational) entropy, thermodynamic properties.

1. Introduction

The crystallization process in diethyl phthalate is conveniently controllable. Crystallization can easily be avoided and the liquid cooled to the glass by convenient procedures. By different convenient procedures the crystal can easily be formed. This controllability makes diethyl phthalate a convenient substance on which to perform studies in the crystalline, liquid, and vitreous conditions. The relations between the properties in these three conditions are important especially to progress in understanding the glassy condition.

This paper reports precision heat capacity and related thermal measurements on diethyl phthalate glasses from 10 °K to the glass transformation temperature, T_g (around 180 °K) on the liquid from T_g to 360 °K, and on the crystal from 10 °K to the melting point (269.9 °K). The results provide suggestive, explanatory, or confirmatory information on several questions concerning thermodynamic relations for glasses.

2. Experimental Detail

2.1. Calorimetry

The measurements reported here were performed in the low-temperature adiabatic precision calorimeter described in reference [1].[1]

At temperatures below 12 °K, however, the NBS–1955 provisional temperature scale cited in reference [1] was not used. Rather a temperature scale (hereafter referred to as the 2–5 scale) was used which was based partly on the observed resistance of the calorimeter's resistance thermometer at the boiling temperature of helium. An equation of the form $R = C_0 + C_2T^2 + C_5T^5$, where R is resistance, T is temperature, and the C's are constant coefficients, was fitted to this observed resistance at the helium boiling temperature and to the resistance and temperature derivative of resistance given for 12 °K by the NBS–1955 provisional temperature scale calibration of the resistance thermometer. The 2–5 scale was used rather than the NBS–1955 scale at temperatures below 12 °K because the lowest temperature of calibration of the resistance thermometer against the NBS–1955 scale was 11.42 °K, and the extrapolation of this calibration to lower temperatures showed an inconsistency with the observed resistance (considered correct) of the thermometer at the boiling temperature of helium. The establishment of the 2–5 scale will be described more fully in a subsequent publication on the heat capacities of arsenious oxide. The heat capacities used in the present paper for the empty calorimeter at temperatures below 12 °K were also recalculated on the basis of this 2–5 scale.

Calculations of heat capacity values from measurements on the glass in the glass transformation range of temperature (where the molecular configuration changes with time) were performed in the manner

*Present address: 4506 Andes Court, Fairfax, Va. 22039.

[1] Figures in brackets indicate the literature references at the end of this paper.

described below. This procedure was directed at yielding the heat capacity of the glass in a definite state in which the molecular configuration is fixed at that existing at the midtime of the calorimetric heat input. To do this the extrapolation of calorimetrically observed temperatures to the midtime of a heat input is based on observed temperature drifts which include observable contributions from configurational change (configurational drift) as well as from heat transfer between the calorimeter and its environment.

This procedure is distinctly different from an alternative one often used. According to this alternative procedure the drift of temperature of the calorimeter between heat inputs is observed for a period of time sufficiently long so that the configurational contribution decreases to a level below the limit of observability. Then the extrapolation to the midtime of a heat input is based on drift rates which presumably arise only from heat transfer between the calorimeter and its environment.

Initial and final temperatures obtained in this alternative manner for a given heat capacity determination apply to different configurational states of the experimental substance. However, these states are still not the equilibrium supercooled liquid states. If they were, the resulting heat capacity value would apply unequivocally to the equilibrium supercooled liquid. In the transformation region, where no equilibrium configuration is attained however, so-called heat capacity values determined according to this alternative procedure do not apply to any definite state of substance.

In the transformation region the heat capacity values reported in this paper for successive temperatures in a given measurement series should apply to glasses of progressively different, but definite configurations.

In principle our procedure has the disadvantage that once the experimental data are reduced to a heat capacity versus temperature relationship, the temperature integral of the heat capacity may not give accurate values of the enthalpy change through the glass transformation region. This is because, for reasons explained below, the glass transformation temperature (T_g) value indicated by the heat capacity curve is not necessarily characteristic of the glass that existed at temperatures well below the transformation region and to which the main body of heat capacity data apply.

The T_g value indicated by the heat capacity curve is usually taken as that of the midpoint of the heat capacity rise from the value for the glass to that for the liquid. This value is characteristic of the glass that exists at that time, when the configurational relaxation times for the existing glass become short enough to allow configurational equilibration within the experimental time scale. However, the molecular configurations in the glass also change slowly but incompletely during passage through the lower temperature part of the transformation range. Therefore, the configurational state corresponding to the indicated T_g value is different from that of the glass that existed at temperatures well below the transformation region. This means that the heat capacities used in the enthalpy integration may change from the (lower) values for the glass to the (higher) values for the liquid at a temperature other than that which yields the correct enthalpy difference between the liquid and the glass that existed well below the transformation region. The indicated T_g can be either too low or too high depending on whether, and to what extent, the glass is either quenched or annealed.

The same displacement of T_g is equally possible when heat capacities are calculated according to the alternative method mentioned above. However, in this case the temperature integral of heat capacity yields a correct enthalpy difference. This is because each heat capacity value includes the heat effect which accompanies the configurational change that occurs during the determination, even though the initial and final configurations may be unspecified. It is this inclusion that prevents these heat capacity values from representing any definite configurational state.

We have chosen to present heat capacity values which represent definite configurational states, but whose integral may not yield valid enthalpy changes rather than values whose integral yields valid enthalpy changes, but which do not represent definite configurational states. This choice is important in situations involving quantitative use of ΔC_p, the difference in heat capacity between the glass and the liquid. Valid enthalpy changes are obtained here by summing over the entire transformation range the energy inputs for all the heat capacity determinations made in the range in a given series, assuming perfect adiabaticity in calorimetric conditions. These enthalpy changes are checked by comparing results from different series containing different numbers of determinations, and from continuous heating through the entire transformation range.

Calorimeter temperature drifts including configurational contributions are sometimes nonlinear. The functional relation of configurational drift rate to temperature, time, configurational state and deviation from equilibrium has not yet been established in an analytical fashion. Therefore in our heat capacity calculations we have performed the necessary extrapolation of nonlinear drifts by graphical methods. The uncertainty introduced by this procedure cannot always be evaluated.

Such uncertainty is not necessarily responsible for the high points to be observed in the heat capacity curve for the annealed glass at the highest temperatures in the transformation region. Such high points can occur with formally valid extrapolations for one special point in each measurement series. This occurs when the initial temperature of a determination is still in the transformation region, but the final temperature is in the equilibrium supercooled liquid region. In this case the resulting peak point does not represent either fixed molecular config-

urations or equilibrium molecular configurations, but is a kind of hybrid.

Once a valid enthalpy-temperature plot has been established for a given glass, this can be used to obtain a T_g value that is characteristic of the configurations fixed in the glass at temperatures well below the glass transformation range.

Measurements were made of heat of fusion by fractional melting, and by continuous melting. The fractional melting data also yield values for melting point and for liquid-soluble, solid-insoluble impurity.

2.2. Preparation of Sample

Commercial diethyl phthalate was purified[2] by fractional distillation at a pressure of 20 mm Hg in a spinning-vane type column having a theoretical plate number around 100. The distillate was collected at a rate of about 2.5 ml/hr with a reflux ratio of 1:30.

Gas chromatograms obtained with a silicone oil absorption column and a flame ionization detector for the middle fractions from the distillation often indicated a small initial shoulder on the main peak with a ratio of peak heights on the order of 1:2,000. The original material however showed only a much earlier separate peak.

Chemical analysis indicated a composition of 65.0 percent C and 6.4 percent H (theoretical values of $C_{12}H_{14}O_4$ are C:64.85 percent and H:6.35 percent). Determination of water content by the Karl Fisher method indicated 0.005 percent.

Fractional melting data from the calorimetric measurements indicated the presence of 0.0012 mole fraction of solid-insoluble, liquid-soluble impurities.

The calorimetric sample weighed 112.575 g. Using a molecular weight of 222.243, this corresponds to 0.506540 moles. The above weight was obtained as the difference between the weight of the loaded and of the empty calorimeter measurement cell. During these weighings the cell was disconnected from the calorimeter assembly, the cell top was soldered in place, and the filling tube was open. The weighings were performed by double weighing in a kilogram capacity analytical balance designated as NBS 3245. The total weight of the loaded cell was about 390 g. Class S–2 calibrated weights designated NBS 3246 were used. The sample weight was adjusted for air buoyancy using 1.123 g/cm^3 as the density of diethyl phthalate, 8.40 g/cm^3 as the density of the brass weights, and 0.00120 g/cm^3 as the density of air.

2.3. Physical States of Sample

An important feature of the results reported in this paper is the comparison of the data for diethyl phthalate in the different physical forms. Therefore, we give here some description of the procedures by which these forms were established for the reported measurements.

a. Liquid

At reported temperatures above the melting point the liquid exists as the unique form (the vapor pressure being negligibly small), so measurements at these temperatures are unequivocally on the liquid form. At temperatures below the melting point and above the glass transformation temperature, T_g, measurements can be made on the (equilibrium supercooled) liquid form only if crystallization is completely avoided. This can be accomplished for diethyl phthalate by using two different procedures for two sections into which this temperature range must be divided. If the liquid is heated to a temperature well above the melting point, say to 360 °K, and then cooled to a temperature below the melting point but not below 220 °K, it may be reheated to the melting point without the occurrence of crystallization. Measurements on the supercooled liquid in the range from 220 °K to the melting point are made in this manner. If the liquid is cooled to or below T_g and then reheated, crystallization will commence around 210–220 °K, but not below this temperature. Measurements on the supercooled liquid in the range from T_g to 220 °K are made in this manner.

The classical interpretation of this behavior is that homogeneous crystal nuclei form in the liquid only at temperatures below 220 °K. Therefore, if existing nuclei are destroyed by heating well above the melting point, crystallization will not occur if the temperature is maintanied above 220 °K. However, crystal growth upon existing nuclei apparently does not occur at temperatures below 210 °K. Therefore, if the liquid is held at temperatures below 210 °K crystallization will not occur even if nuclei are present. This interpretation applies to crystallization based on homogeneous nucleation. That fact that crystal growth does not occur in the well-melted liquid unless it has been previously cooled below 220 °K suggests that heterogeneous nuclei were not present to an effective extent in the sample concerned here.

The absence of crystals from the equilibrium super-cooled liquid on which measurements are reported here is demonstrated by the heat capacity results for the liquid in the vicinity of the melting point. No heat capacity peak associated with the melting of any crystals is observed. We may cite an exaggerated experimental uncertainty of 0.1 percent in the heat capacity value around 355 joule per degree and mole for the liquid near the melting point; a heat of fusion around 18,000 joule per mole and a melting range around 10°. These figures lead to a value of 0.02 percent as the upper limit on the fraction of crystal which could be present in the supercooled liquid without being detected by the effect of the heat evolved in its melting upon the heat capacities of the liquid near the melting point.

b. Crystal

To crystallize the sample the liquid is cooled below 220 °K and then rewarmed to that point, around which

[2] This purification was performed by R. Leslie of the NBS Analysis and Purification Section

crystallization commences. Under adiabatic conditions the latent heat of fusion evolved warms the crystallizing sample further, with maximum crystallization rate (as indicated by rate of temperature rise) being reached around 245 °K. Complete crystallization raises the temperature to about 260 °K. The major part of the crystallization, occurring between 225 and 260 °K, requires less than an hour: however, the sample is allowed several hours after this for the completion of the last traces of crystallization. The completeness of crystallization in the samples for which crystal heat capacities are reported here is demonstrated by the heat capacity results for the crystal in the vicinity of T_g. No heat capacity shift corresponding to the transformation of any glass is observed. The heat capacity of the crystal near T_g is around 200 joule per degree and mole with a claimed experimental uncertainty of 0.1 percent. The change in heat capacity in going from pure glass to pure liquid is 115 joule per degree and mole. Assuming a simple additivity, these figures lead to a value of 0.2 percent as the upper limit on the fraction of uncrystallized material which could be present in the crystal without being detected by the effect of its heat capacity shift at T_g on the measured heat capacity.

c. Glasses

Glassy conditions are produced by three different kinds of procedures: (i) quenching, i.e., fast cooling: (ii) rate annealing, i.e., slow cooling: and (iii) soak annealing, i.e., thermostatting for an extended time at a temperature in the glass transformation range.

Quenched glasses were produced starting with the liquid sample in the calorimeter cell at about 350 °K and insulated thermally by the cryostat vacuum from solid nitrogen at about 50 °K in the refrigerant Dewar. Thermal conduction was then established between the sample and the solid nitrogen by breaking the cryostat vacuum with helium gas and cooling of the sample commenced. The temperature of the sample was thus lowered to about 50 °K in a few hours. The rate of cooling of the sample in the glass transformation region (just below 180 °K) was at least 2.5° per minute.

Rate annealed glasses were produced starting with the liquid sample in the calorimeter cell thermostatted by the controlled adiabatic shields at about 200 °K inside the evacuated cryostat can surround by liquid nitrogen. The heat supply to the adiabatic shields was cut off and unavoidable heat loss through the insulating cryostat vacuum and electrical supply wires slowly cooled the shields and subsequently the cell and sample. In this manner the temperature of the sample was lowered to around 170 °K overnight. The rate of cooling in the glass transformation range was around 1° per hour. Subsequent cooling below the glass transformation temperature range was done by breaking the insulating cryostat vacuum with helium gas, and proceeded at rates on the order of degrees per minute.

Soak annealed glasses were produced starting with either quenched or rate annealed glasses. These initial glasses are then maintained for extended periods of time at fixed temperatures in the glass transformation range. For this purpose the calorimeter cell containing the sample under treatment is thermostatted using the controlled adiabatic shields inside the evacuated cryostat can surrounded by liquid nitrogen. The specific temperatures and times for which samples used in particular determinations were held are given in table 1. The series identification of the samples will be explained in section 3.

TABLE 1. *Soak annealing schedules*

Series	Soaking temperature, °K	Soaking time
XX	181	2.5 hr
XXX	162	2 weeks
XXXI	(XXX +) 169	6 days
XXXII, XXXIII	(XXXI +) 173	3 days
XLI	170	16 hr
XLIV	160 +170	2 days 1 day

3. Results

The heat capacity results are listed in table 2 and their overall graphical presentation is shown in figure 1. In table 2 the heat capacities are grouped first according to the different physical forms for which data are reported. For each physical form the data are grouped in numbered series of successive measurements. These series are numbered according to their chronology in the entire set of measurements on diethyl phthalate, irrespective of physical form. The chronology of the entire set of measurements can therefore be followed, if desired, by following the numbers of these series. If a series covers a transformation from one physical form to another, parts of the series appear under each of the two physical forms. For each physical form, the series are ordered in table 2 in increasing temperature of the first member.

The vapor pressure of diethyl phthalate at 360 °K is less than 0.2 mm Hg [2]. The corresponding correction from C_{obs} to C_p (p = 1 atm) is about 0.002 percent of the value, and thus is disregarded.

The absence of crystals from the glass samples on which measurements are reported here can be demonstrated directly only for samples for which heat capacities were measured around the melting point for the liquid formed by heating the sample through the glass transformation range. Since the crystalline content of a sample can increase but not decrease at equilibrium supercooled liquid temperatures, the possible crystallinity thus allowed for the liquid sample serves as an upper limit for that of the glass sample from which the liquid sample was formed. This value is around 0.02 percent as explained earlier. For glass samples for which the above type of data is not obtained, limits on the crystallinity can be obtained by comparison of heat capacity results with samples for which such data are available. These comparisons

TABLE 2. *Heat capacity data for diethyl phthalate*
(Units in °K. joule and mole)

CRYSTAL

T	C_p	T	C_p	T	C_p
Series XXVI		Series X		Series XXXV	
10.26	6.28	87.58	124.11	228.09	240.45
11.32	7.95	95.58	132.10	Series XXIII	
12.66	10.14	104.54	140.50		
14.11	12.56	113.61	148.67	243.23	253.23
15.65	15.47	122.72	156.64	253.95	262.57
17.40	18.82	132.15	164.54	Series XXVIII	
19.30	22.48	141.77	172.36		
Series XXVII		151.49	179.98	247.56	257.09
		Series XI		257.23 Fusion	266.49
17.36	18.52	133.74	165.74	Series V	
18.91	21.68	Series XII			
20.70	25.24			251.01	259.03
22.82	29.51	154.26	182.05	259.77 Fusion	269.61
25.09	34.11	164.42	190.00	Series XIII	
27.64	39.18	174.36	197.91		
30.52	44.82	184.01	205.31	258.37 Fusion	267.98
33.62	50.81	193.64	212.76	Series XV	
37.11	57.19	203.39	220.41		
40.98	63.74	213.11	228.13	260.50	270.74
45.15	70.46	Series IX		Series XXXVI	
49.69	77.43			Fusion	
54.70	84.49	208.64	224.50		
60.11	91.81	218.93	232.95		
Series XXII		229.24	241.38		
		239.56	250.36		
56.38	86.74	249.59	259.17		
61.96	94.30	259.32	271.75		
68.37	102.07	265.80	317.92		
75.11	110.01				
82.05	118.14				
89.22	125.79				

LIQUID

T	C_p	T	C_p	T	C_p
Series XX		Series XXXIV		Series XXXVII	
184.81	331.16	192.74	331.57	260.22	349.22
190.48	331.84	Series VIII		267.90	352.67
Series XXI				272.98	354.43
		198.31	332.44	280.55	357.54
185.65	330.78	208.37	334.04	290.55	362.39
192.52	331.38	Series XVIII		300.57	367.02
Series IV				310.58	372.15
		214.79	335.41	Series XVI	
187.33	331.01	Series XIX			
195.77	332.07			262.05	350.17
205.72	333.60	223.54	337.60	266.38	351.99
Series XXXIII		Series XVII		269.78	353.80
				273.17	354.86
187.52	331.27	229.49	339.15	279.39	357.82
Series XLI		Series XIV		288.40	362.03
				Series XXIX	
189.23	331.03	237.54	341.68		
199.07	332.66	247.87	344.89	273.23	354.61
Series XL		258.11	348.43	275.08	355.88
		268.22	353.05	Series XXXVI	
190.67	331.11	278.21	357.00		
Series XLIV				274.12	354.88
				Series XIII	
192.58	331.02			276.92	356.57

TABLE 2. *Heat capacity data for diethyl phthalate*—Continued
(Units in °K. joule and mole)

LIQUID—Continued

T	C_p	T	C_p	T	C_p
Series VI		Series XXXVIII		Series VII	
283.41	359.30	320.36	377.02	343.78	389.11
295.97	365.24	330.36	382.26	353.42	394.56
306.34	370.35	340.27	387.30		
316.44	375.61	350.06	392.62		
326.36	380.14				
336.14	385.41				

QUENCHED GLASS

T	C_p	T	C_p	T	C_p
Series XXV		Series I		Series III	
11.02	8.11	52.25	80.80	135.18	171.25
11.62	9.37	54.84	84.40	145.36	180.76
12.86	11.61	60.97	92.76	155.10	190.61
14.60	14.60			Series XL	
16.53	18.22	Series XXXIX			
18.51	21.88			150.79	185.54
20.68	26.07	58.57	89.48	161.24	195.72
22.92	30.46	64.59	97.36	Glass Transformation	
Series XXIV		Series II		Series XXI	
20.27	25.30			152.92	187.75
21.11	26.80	67.11	100.70	163.87	199.74
22.91	30.53	74.39	109.28	172.03	207.85
25.38	35.21	81.56	117.87	177.33	224.09
28.07	40.38	88.64	125.81	181.86	315.29
31.03	45.95	96.05	133.43	Series IV	
34.29	52.02	104.36	141.78		
37.68	57.94	113.21	150.61	159.61	194.71
41.44	64.17	122.47	159.26	169.85	207.43
45.70	71.04	132.11	168.27	179.43	252.67
50.29	78.06				
55.28	84.97				

ANNEALED GLASS

T	G_p	T	C_p	T	C_p
Series XLII		Series XLIII		Series XXX	
18.41	21.58	120.23	156.76	165.40	198.62
25.56	35.46	130.95	166.67	Series XLIV	
27.97	40.07	141.12	175.90		
30.70	45.18			167.67	201.15
33.76	50.88	Series XXXIII		Glass Transformation	
37.11	56.84			Series XX	
40.88	63.13	125.07	161.25		
44.96	69.65	134.31	169.85	168.84	202.60
49.47	76.73	143.63	177.99	171.95	207.72
54.45	83.64	153.07	186.92	175.16	215.12
59.88	91.09	162.64	195.77	178.45	243.96
Series XXXII		172.08	205.64	181.31	341.57
		178.96	269.99	Series XXXI	
59.17	90.43	183.08	393.95		
65.39	98.27	Series XLI		171.22	204.81
72.33	106.57			Series XXXIV	
79.62	115.28	141.27	176.06		
87.45	124.16	151.70	185.43	Glass Transformation	
96.35	133.34	161.57	194.61		
105.98	142.81	171.07	204.55		
115.65	152.10	180.12	316.54		

may be made preferably for the corresponding liquids above the glass transformation range, or if these are not investigated, for the glass samples themselves. The results of several such comparisons will be cited

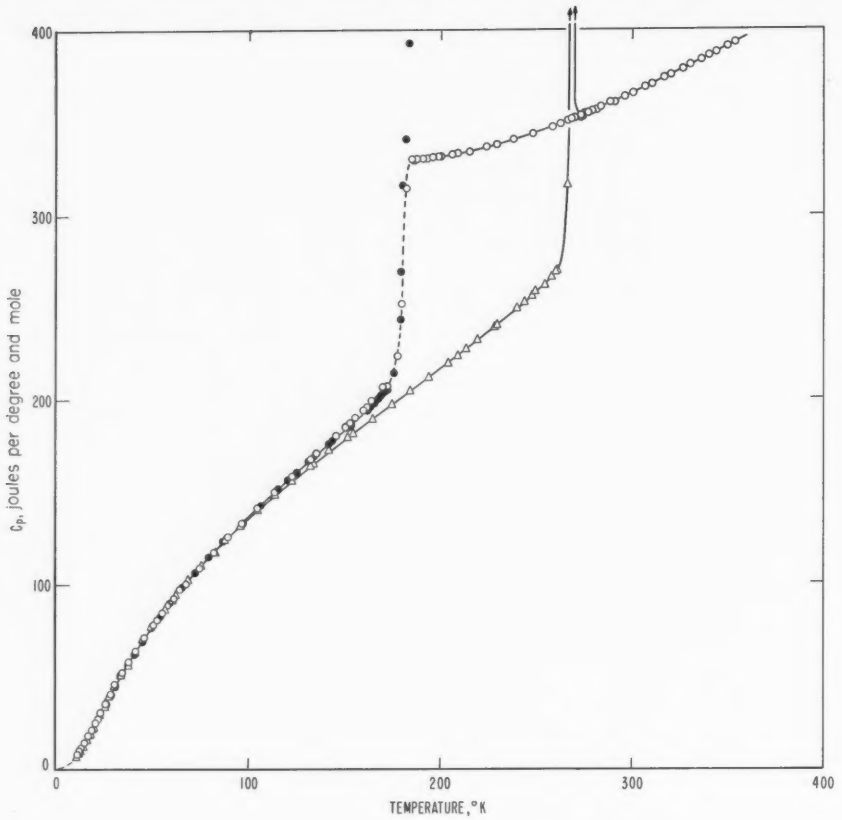

FIGURE 1. *Molar heat capacity of diethyl phthalate versus temperature.*
Triangles represent crystal, open circles represent liquid and quenched glass, filled circles represent annealed glass.

later in this paper when they become specifically pertinent.

To provide more nearly complete information on the thermal history of the diethyl phthalate investigated, several entries that are not heat capacity data are included in table 2. They indicate only that a fusion or a glass-to-liquid transformation was performed at the indicated point in the course of the measurements. For the glass transformation these indications usually designate heat inputs large enough to encompass most of the transformation process. The results of such determinations are not appropriately represented as heat capacities because the temperature changes concerned are too large to make reliable curvature corrections. Other measurements were made on the glass-to-liquid transformation in which the transformation process was encompassed by a number of smaller energy increments. These are represented as heat capacity data in table 2. Tables 3 and 4 give the results of all the above determinations for enthalpy and entropy changes over temperature intervals encompassing the glass transformation and the fusion processes respectively.

TABLE 3. *Glass transformation of diethyl phthalate*
(Units in °K, joule and mole)

Series	No. of runs	$T_{initial}$	T_{final}	$H^c_{190} - H^c_{160}$	$S^c_{190} - S^c_{160}$
QUENCHED GLASSES					
IV	3	164.81	190.90	7214.	40.94
XXI	5	158.55	187.51	7182.	40.71
XL	2	156.05	186.50	7141.	40.60
ANNEALED GLASSES					
XX	6	167.28	186.93	7585.	43.08
XXXIII	5	157.82	190.06	7791.	44.11
XXXIV	1	169.95	188.94	7669.	43.59
XLI	4	156.73	193.91	7779.	44.08
XLIV	2	162.47	188.92	7641.	43.36

The results of a fractional melting of diethyl phthalate are given in table 5. The data at temperatures approaching complete melting were treated by simple melting point depression theory. From the slope of the plot of melting point versus the reciprocal ($1/F$) of the fraction of the heat of fusion supplied and the approximate heat of fusion, the mole fraction. N_2,

TABLE 4. *Fusion of diethyl phthalate*
(Units in °K, joule and mole)

Series	No. of runs	$T_{initial}$	T_{final}	$H^{l}_{275}-H^{c}_{250}$	ΔH_f
V	6	246.56	276.83	25128.	17982.
XIII	2	254.24	274.21	25126.	17981.
XXVIII	2	251.73	272.42	25134.	17989.
XXXVI	1	260.16	271.71	25130.	17985.
Average				25130. ± 3.[a]	17984. ± 3.[a]

$\Delta S_f = 66.64$ J per degree and mole

[a] These represent only the r.m.s. deviations.

of liquid-soluble, solid-insoluble impurity in the sample investigated is determined as 0.0012. By the device of extrapolating $1/F$ to zero the melting point of the pure substance is determined as 269.92 ± 0.02 °K.

The heat of fusion is obtained from the enthalpy change through the melting region by subtracting the heat capacity integral over this region. This requires the correction of some observed crystal heat capacities for the heat absorbed by fusion (premelting) at the lower temperatures in the melting range. Attempts to do this using simple melting point depression theory over the entire melting range with the above result (and other trial values) for N_2 gave unacceptable results, suggesting that the simple theory is not adequate over the entire range. The base line for heat capacity in the premelting region was therefore established arbitrarily. The resulting value for the heat of fusion of the calorimetric sample at the above temperature is $17{,}984 \pm 3$ joules per mole. In view of the uncertainties involved the accuracy of this value is estimated as ± 0.1 percent of the value.

TABLE 5. *Fractional melting of diethyl phthalate*

T °K	$\frac{1}{F}$
269.386	13.393
269.810	2.652
269.872	1.276
Triple point of sample = 269.88	1.000
Triple point of pure diethyl phthalate = 269.92	0.000
Mole fraction of impurities = 0.0012	

If we assume that the molecular weight of the impurity in the sample is the same as that of diethyl phthalate, the above value is corrected to 18,006 joules per mole as the heat of fusion of pure diethyl phthalate at its melting point. Since the molecular weight of the impurity is unknown, we arbitrarily assign to this correction an uncertainty equal to the value of the correction (22 joules per mole). This corresponds to assuming that the molecular weight of the impurity lies between zero and twice the value of that of diethyl phthalate.

With the intention of obtaining quantitative information about enthalpy changes, the behavior of the calorimeter was followed during several instances of crystallization processes, namely at the end of run series IV, VIII, XVIII, and XLI. The rate of spontaneous temperature rise increases progressively after the commencement of crystallization around 210–220 °K, and then remains at a maximum rate of 4 to 5 °K per minute from 235 °K until a final temperature of 260 to 265 °K. As a result of failure of the adiabatic shield to follow closely to the temperature of the calorimeter during the crest of crystallization process, a certain amount of heat released by the sample was lost to the shield. Depending upon the different degrees of deviation from adiabaticity for the individual cases, the values of heat of fusion calculated from crystallization processes vary from 0.15 to 0.75 percent higher than that from actual fusion processes.

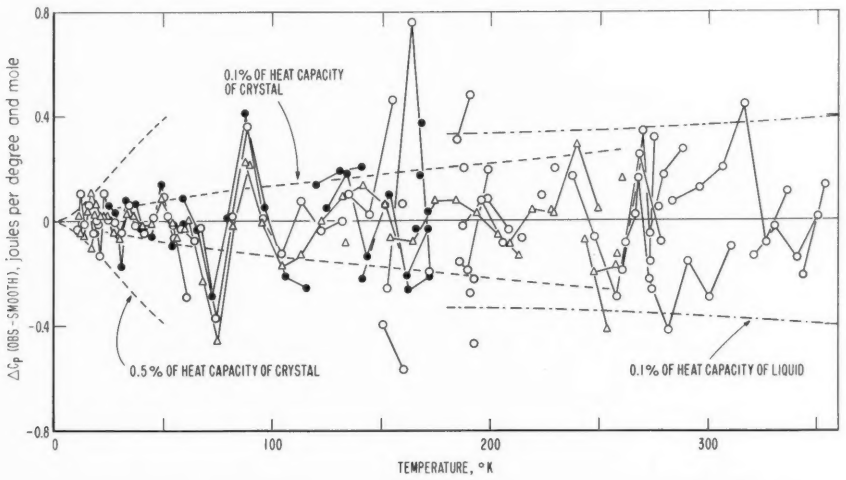

FIGURE 2. *Deviation of individual heat capacity points from smoothed values for diethyl phthalate.*
Triangles represent crystal, open circles represent liquid and quenched glass, filled circles represent annealed glass.

4. Analysis of Data

4.1. Representation and Precision of Heat Capacities

Figure 2 shows the deviations of the individual heat capacity points from the smooth values for the physical forms concerned. The smoothed values were obtained by fitting the individual values with three to six degree polynomials in temperature using an IBM 7094 digital computer and Fortran programming. The crystal data were fitted in three segments and the data for the glasses in two segments. Adjacent segments overlapped by 10° to 30° in temperature. Individual data points for the crystal near its melting point were omitted from the curve fitting if their final temperature was above 264 °K because some of the energy represented by them may have been latent heat of fusion rather than thermal energy. Individual data points for the glasses near the glass transformation temperatures were omitted from the curve fitting if their final temperature was above 175 °K for the quenched glass or above 180 °K for the annealed glass because of uncertainty in the correction for configurational change during individual determinations.

The root mean square percentage deviations of the heat capacities from the polynomials at temperatures above 25 °K are less than 0.1 percent (usually about 0.07%). As temperatures decrease below 25 °K, the root mean square deviation increases, reaching about 0.5 percent around 10 °K.

The smoothed heat capacity values are listed in table 6. These values together with the data from tables 3 and 4 result in the values listed in table 6 for the usually stated thermodynamic functions for diethyl phthalate crystal, liquid, and glass. For the crystal and for the liquid above the melting temperature these functions were calculated by integrating the appropriate integrand from absolute zero temperature to the temperature concerned. For the supercooled liquid and the glass, the calculations proceeded from the values (obtained as above) for the liquid at the melting temperature. From these were subtracted the integrals of the appropriate integrands for the glass and the supercooled liquid from the temperature concerned to the melting temperature.

The integrals between absolute zero temperature and the lowest temperature of measurement (around 10 °K) were obtained by extrapolation assuming heat capacity proportional to T^3 at these temperatures. The resulting values for the integrals differ from values for the same integrals obtained by graphical extrapolation by less than the uncertainty of the experimentally determined integrals between 10 and 35 °K.

The minimum and maximum in the heat capacity deviations between 70 and 100 °K are attributed to a peculiarity in the temperature scale used. This peculiarity has been discussed previously by Furukawa and Reilly [3] and by Roder [4].

Figure 2 also suggests a small peak within the 0.1 percent uncertainty limits around 270 °K. This may be associated with some suspected minute aqueous inclusion in the empty calorimeter which may have an irreproducible freezing behavior. This matter is currently under further investigation.

4.2. Glass Versus Crystal

The relative behavior of heat capacity as a function of temperature for the crystal and the quenched and annealed glasses can be discussed conveniently with reference to figure 3. This shows plots as functions of temperature of the differences between the heat capacities of the crystal and of the two different glasses. The immediately noticeable general feature is that, contrary to widely held belief [5], the heat capacity of the glass differs from that of the

TABLE 6. *Thermodynamic functions of diethyl phthalate*
(Units in °K, joule and mole. Reference state = crystal)

T	C_p	$H-H_0^\circ$	$(H-H_0^\circ)/T$	S	$-(G-H_0^\circ)/T$	$-(G-H_0^\circ)$
			CRYSTAL			
10	5.91	14.8	1.48	1.97	0.49	4.9
15	14.23	64.4	4.29	5.88	1.59	23.8
20	23.84	159.2	7.96	11.27	3.31	66.1
25	33.91	303.5	12.14	17.67	5.53	138.1
30	43.86	498.1	16.60	24.73	8.13	243.9
35	53.32	741.3	21.18	32.21	11.03	386.2
40	62.12	1030.2	25.75	39.91	14.16	566.4
45	70.27	1361.4	30.25	47.71	17.45	785.4
50	77.81	1731.9	34.64	55.51	20.87	1043.5
60	91.64	2580.1	43.00	70.93	27.93	1675.9
70	104.25	3560.5	50.86	86.02	35.16	2461.0
80	115.80	4661.6	58.27	100.71	42.44	3395.0
90	126.43	5873.4	65.26	114.97	49.71	4473.8
100	136.31	7187.7	71.88	128.81	56.93	5693.0
110	145.58	8597.6	78.16	142.24	64.08	7048.5
120	154.35	10098.	84.15	155.28	71.14	8536.5
130	162.74	11683.	89.87	167.97	78.10	10153.
140	170.86	13352.	95.37	180.33	84.96	11895.
150	178.79	15100.	100.67	192.39	91.72	13759.
160	186.61	16927.	105.79	204.18	98.39	15742.
170	194.38	18832.	110.78	215.73	104.95	17841.
180	202.14	20815.	115.64	227.06	111.42	20056.
190	209.94	22875.	120.39	238.19	117.80	22382.
200	217.75	25014.	125.07	249.16	124.09	24819.
210	225.57	27230.	129.66	259.97	130.31	27365.
220	233.80	29526.	134.21	270.66	136.44	30018.
230	242.16	31906.	138.72	281.23	142.51	32777.
240	250.52	34369.	143.21	291.71	148.51	35642.
250	259.31	36918.	147.67	302.12	154.45	38612.
260	269.93	39561.	152.16	312.48	160.32	41684.
			LIQUID			
190	331.31	33051.	173.95	270.07	96.11	18261.
200	332.59	36370.	181.85	287.09	105.24	21048.
210	334.37	39705.	189.07	303.36	114.29	24000.
220	336.60	43059.	195.72	318.96	123.24	27113.
230	339.25	46438.	201.90	333.98	132.08	30378.
240	342.30	49845.	207.69	348.48	140.79	33790.
250	345.71	53285.	213.14	362.52	149.38	37346.
260	349.44	56761.	218.31	376.15	157.84	41040.
270	353.48	60275.	223.24	389.42	166.18	44868.
280	357.78	63831.	227.97	402.35	174.38	48827.
290	362.31	67431.	232.52	414.98	182.46	52914.
300	367.04	71078.	236.93	427.35	190.42	57125.
310	371.94	74773.	241.20	439.46	198.26	61460.
320	376.97	78517.	245.37	451.35	205.98	65914.
330	382.11	82312.	249.43	463.03	213.59	70486.
340	387.33	86160.	253.41	474.51	221.10	75174.
350	392.58	90059.	257.31	485.81	228.50	79976.
360	397.84	94011.	261.14	496.95	235.80	84890.
273.15	354.80	61391.	224.75	393.53	168.78	46101.
298.15	366.15	70340.	236.12	425.08	188.96	56337.

TABLE 6. *Thermodynamic functions of diethyl phthalate*—Continued

(Units in °K, joule and mole. Reference state = crystal)

T	C_p	$H-H_0^\circ$	$(H-H_0^\circ)/T$	S	$-(G-H_0^\circ)/T$	$-(G-H_0^\circ)$
QUENCHED GLASS						
10	6.44	8737.	873.69	24.57	−849.12	−8491.
15	15.39	8791.	586.08	28.85	−557.23	−8358.
20	24.80	8892.	444.58	34.56	−410.02	−8200.
25	34.43	9040.	361.58	41.13	−320.46	−8011.
30	43.99	9236.	307.86	48.25	−259.61	−7788.
35	53.23	9479.	270.83	55.73	−215.09	−7528.
40	61.95	9767.	244.18	63.42	−180.76	−7231.
45	70.03	10097.	224.39	71.19	−153.20	−6894.
50	77.47	10467.	209.33	78.96	−130.37	−6519.
60	91.44	11312.	188.53	94.33	−94.20	−5652.
70	104.29	12291.	175.59	109.41	−66.19	−4633.
80	116.13	13394.	167.43	124.11	−43.31	−3465.
90	127.14	14611.	162.35	138.44	−23.91	−2152.
100	137.49	15935.	159.35	152.37	−6.98	−698.
110	147.34	17359.	157.81	165.94	8.13	894.
120	156.86	18880.	157.34	179.17	21.83	2620.
130	166.24	20496.	157.66	192.10	34.44	4477.
140	175.62	22205.	158.61	204.76	46.15	6461.
150	185.20	24009.	160.06	217.20	57.14	8571.
160	195.13	25910.	161.94	229.47	67.53	10804.
170	205.82	27915.	164.21	241.62	77.41	13160.
ANNEALED GLASS						
15	15.05	8205.	547.03	26.05	−520.98	−7815.
20	24.66	8305.	415.23	31.69	−383.54	−7671.
25	34.37	8452.	338.09	38.23	−299.85	−7496.
30	43.91	8648.	288.27	45.35	−242.92	−7288.
35	53.07	8891.	254.02	52.81	−201.21	−7042.
40	61.72	9178.	229.45	60.47	−168.98	−6759.
45	69.81	9507.	211.26	68.21	−143.05	−6437.
50	77.36	9875.	197.50	75.96	−121.54	−6077.
60	91.23	10719.	178.65	91.31	−87.34	−5240.
70	104.00	11696.	167.08	106.34	−60.74	−4252.
80	115.80	12796.	159.95	121.01	−38.94	−3115.
90	126.79	14009.	155.66	135.29	−20.37	−1833.
100	137.11	15329.	153.29	149.19	−4.10	−410.
110	146.92	16750.	152.27	162.72	10.45	1149.
120	156.37	18266.	152.22	175.91	23.69	2843.
130	165.60	19876.	152.90	188.79	35.90	4667.
140	174.78	21578.	154.13	201.40	47.27	6618.
150	184.03	23372.	155.82	213.77	57.96	8694.
160	193.53	25260.	157.87	225.95	68.08	10893.
170	203.42	27245.	160.26	237.98	77.72	13212.

crystal in a more complicated way than by a slight increase due to a lowering of all vibrational force constants resulting from the greater specific volume of the glass. The deviation of the heat capacity of the glass from that of the crystal is not uniform over their entire common temperature range. It is qualitatively different in different segments of the temperature range.

The commonly expected relationship of glass heat capacity exceeding crystal heat capacity does apply for diethyl phthalate at temperatures immediately below T_g, even at temperatures low enough (say below 170 °K) so that the molecular configurations in the glass may be presumed to remain fixed so that no glass transformation effects occur. However, the increment decreases rapidly with decreasing temperature (even in a relative sense) until at temperatures somewhat below 100 °K the heat capacity of the glass falls below that of the crystal.

In the temperature range about from 30 to 75 °K the heat capacities of both diethyl phthalate glasses investigated are lower than that of the crystal. The values for the annealed glass are as much as 0.6 percent below the values for the crystal, and the maximum difference for the quenched glass is about 0.3 percent. Thus the difference is definitely greater than the experimental uncertainty of the values, though of the same order of magnitude.

For several other substances the heat capacity of the glass has also been reported as lower than that of the crystal over some temperature range [6–10]. These are summarized in table 7.

However, reliable data exist for a number of other substances for which it is clear that the heat capacities of the glass are unequivocally higher than those for the crystal at all temperatures between the lowest temperature of measurement (which are near or below 10 °K in many cases) and the glass transformation temperature. It follows that no universally applicable conclusion can be made as to the

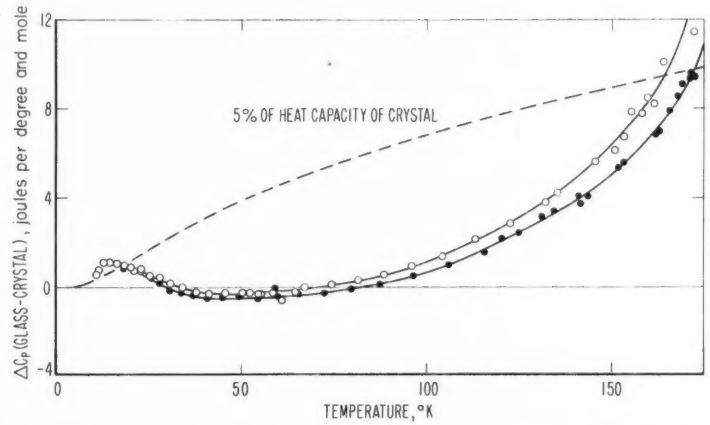

FIGURE 3. *Difference between heat capacities of diethyl phthalate glass and crystal.*

Open circles represent quenched glass, filled circles represent annealed glass.

TABLE 7. *Glasses having lower heat capacities than their crystals*

Substance	Reference	Temperature range °K	Maximum difference	Experimental uncertainty
			%	%
Diethyl Phthalate	This work	30–75	0.6	0.1
d,l- Lactic Acid	[6]	< 90–170	3	0.3
Selenium	[7]	~ 100– ~ 200	1	1
Sodium Tetraborate	[8]	35– > 350	3	0.1
Boron Trioxide	[8]	300–(?)		
Silicon Dioxide	[9]	~ 200– > 300	1	0.1
Pyroxane	[10]	300–800	0.3	0.3
Anorthite	[10]	300–400	0.9	0.3

relative magnitude of the heat capacities of the glassy and the crystalline forms of a substance. This fact is in no way disconcerting. It simply indicates that the molecular motions in the glass and in the crystal differ in a more complicated way than corresponds to any universal type shift in their heat capacity function. It appears inappropriate to view the equations of molecular motion for a glass as only minor variations of those of the crystal of the same substance. What appears necessary eventually is to investigate the equations of molecular motion of glasses in their own right.

4.3. Low Temperature Heat Capacity of Glass

At the lowest temperatures of measurement, just above 10 °K, the heat capacity values for diethyl phthalate glass rise as much as 8 percent higher than those for the crystal. This feature is reminiscent of, though possibly distinct from, observations which have been made on other glasses in recent years. These observations all involve a glass at sufficiently low temperatures having higher heat capacity values than would be expected according to some kind of conventional considerations usually based at least implicitly on concepts strictly applicable to crystals.

For vitreous silica the ratio of measured heat capacity to temperature cubed (C/T^3), extrapolated to absolute zero temperature, is about twice the value calculated from measured elastic constants [11]. Flubacher, Leadbetter, Morrison, and Stoicheff [12] as well as Rosenstock [13] have discussed proposed explanations of this discrepancy in terms of optical modes of molecular motion having unusually low frequencies. The former authors [12] have also reported contributions corresponding to such frequencies (on the order of 1–100 cm^{-1}) in the Raman and Brillouin spectra of vitreous silica.

It has been suggested to apply the same proposition to vitreous glycerol, for which the plot of C/T^3 versus T^2 shows a minimum slightly above 2 °K and *increases* with further decreasing temperature down to the lowest temperature of measurement (around 1.5 °K) [14]. Similar minima have been observed for several alkali-silicate glasses around 6 to 7 °K, with the measurements extending down to slightly above 5 °K [15]. Such minima are, however, a distinctly different type of observation from that mentioned above for vitreous silica, though the same type of explanation can be applied to both. The explanation of the minima requires a much more drastic effect than does that of the C/T^3 discrepancy. The minima are also more susceptible to scepticism about experimental finality than is the C/T^3 discrepancy, since the minima could result spuriously from relatively simple distortions of the temperature scale, whereas the C/T^3 discrepancy could not. Very careful measurements on vitreous silica [12] reveal no suggestion of any minimum in the C/T^3 versus T^2 plot in the low temperature region extending down to slightly below 2.5 °K.

Simon and Lange [16] reported that the heat capacity of amorphous glycerol rises markedly above that of the crystal as temperature decreases below about 70 °K, becoming about 80 percent higher at 10 °K.

For vitreous polyethylene the limit at absolute zero temperature of calorimetric values for C/T^3 is about three times the value for the crystal [17]. This comparison is strictly different than that between the calorimetric and the mechanical values for the C/T^3 limit. However, in a rough way it is suggestive of the same kind of discrepancy, if one assumes that the mechanical value for the glass is not too far above the calorimetric value for the crystal. This is the case for silica, for instance: the mechanical value for the glass is less than twice the calorimetric value for the crystalline form quartz [18]. The same type of differences between calorimetric and mechanical results have been claimed for amorphous polystyrene and polymethyl methacrylate on the basis of sound velocity results extrapolated from 140 °K to absolute zero temperature [19].

The heat capacity values reported in the present paper for diethyl phthalate are at too high temperatures (above 10 °K) to extrapolate to a limiting value of C/T^3. The effects of the classical equipartition limit are still apparent. The relatively high heat capacity values for the glass between 10 and 30 °K are however still amenable to the same type of explanation as discussed in the preceeding paragraphs; namely, unusually low frequencies of molecular motion. In this case however, the possibility of low acoustical frequencies is not eliminated. To determine whether any unusually low frequencies present were acoustical would require heat capacity measurements at still lower temperatures (say about 4 °K, or preferably around 2 °K), as well as low temperature acoustical measurements on vitreous diethyl phthalate.

The idea of the general existence of unusually low frequencies of optical modes of molecular motion in glasses is one which may be related to their amorphous nature. Rosenstock [13] discusses them in terms of physical regions of "localized" low-frequency molecular oscillations. Anderson [11] argues that in vitreous silica these are more likely to be associated with small intermolecular force constants than with large molecular masses oscillating as rigid units.

Such regions have also been mentioned as possibly instrumental in several types of physical phenomena other than heat capacities. Such regions might be

identified with the "defects" of the defect-diffusion model discussed by Glarum [20] and by Hunt and Powles [21] to explain dielectric relaxation in liquid and vitreous isobutyl bromide, and nuclear spin relaxation, dielectric relaxation and indirectly ultrasonic absorption in liquid and vitreous glycerol. At relatively low temperatures, near and below the glass transformation, Hunt and Powles find the defect-diffusion mechanism in itself sufficient to reproduce observed molecular relaxation phenomena, though at higher temperatures an additional mechanism is necessary both in Hunt and Powles' and in Glarum's treatments. Klemens' [22] treatment of the temperature dependence of low temperature thermal conductivity of vitreous silica can be interpreted in terms of such regions, and he has proposed an explanation [23] of the temperature dependence of the spin-lattice relaxation of vitreous silica in terms of defects with low frequency mechanical resonances (around 20 cm^{-1}).

In view of the repeated emergence of this idea in connection with diverse physical properties, definitive evidence about its generality is especially important. This requires further direct structural investigations.

4.4. Comparison of Annealed and Quenched Glasses

According to current understanding of the glass transformation process, the principal difference in thermal properties between a quenched and an annealed glass arises because the annealed loses more enthalpy on cooling through the glass transformation region than does the quenched. This is illustrated in figure 4, which shows the enthalpy increment below the equilibrium supercooled liquid at 190 °K for both the quenched and the annealed glasses. There is a corresponding difference in the entropies. The curves in figure 4 represent respectively the most drastically quenched glass and the most thoroughly annealed glass investigated. For these glasses at 160 °K, just below the glass transformation region, the entropy of the quenched glass is 3.5 joule per degree and mole higher than that of the annealed, which is in turn 22 joule per degree and mole higher than that of the crystal. At absolute zero temperature the entropy of the quenched glass is 2.9 joule per degree and mole higher than that of the annealed, which is in turn 20 joule per degree and mole higher than that of the crystal.

The residual entropy at absolute zero temperature is therefore 20 joule per degree and mole for the annealed glass and 23 joule per degree and mole for the quenched glass. Certain implications of the residual entropies of glasses were discussed in more detail in reference [24].

The glass transformation temperatures specified for the annealed and the quenched glasses respectively by the intersections of the (extrapolated) enthalpy versus temperature plots for the equilibrium supercooled liquid and the configurationally fixed glasses are 176.5 °K and 180.8 °K.

The decrease in the entropy difference between the two glasses as temperature decreases from just below

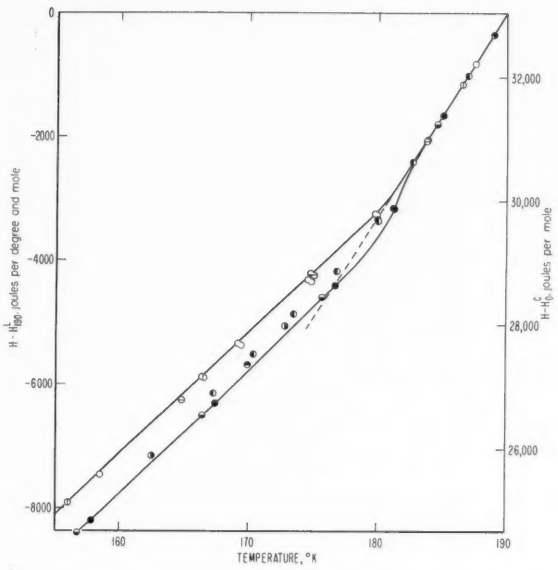

FIGURE 4. *Enthalpy plot for amorphous diethyl phthalate near glass transformation temperature region.*

Open and barred circles represent quenched glasses. Shaded circles represent annealed glasses.

the glass transformation region to absolute zero is due to the difference in the heat capacities of the two glasses. At the precision of the present measurements, this difference is observable, as illustrated in figure 3. Even well below the glass transformation region the heat capacity of the annealed glass is lower than that of the quenched by more than the uncertainty of the measurements. As low as 30 °K the annealed is 0.5 percent lower than the quenched, with an uncertainty of measurement less than 0.1 percent. It may be noted however that although the different quenched glasses respectively, as well as the different annealed glasses, show differences in the enthalpy change through the glass transformation, no heat capacity differences beyond the limits of uncertainty of the present measurements are detectable between any of the quenched glasses or between any of the annealed glasses investigated.

The possibility of this heat capacity difference arising spuriously from partial crystallization of the annealed glass can be eliminated by the fact that no difference is observed between the heat capacities for the equilibrium supercooled liquids resulting from heating the annealed and the quenched glasses respectively through the glass transformation region, as anticipated in subsection 2.3. At 190 °K the heat capacity of the equilibrium supercooled liquid decreases from about 335 to 210 joule per degree and mole on crystallization. At 160 °K the heat capacity of the quenched glass decreases from about 195 to 186 joule per degree and mole on crystallization. Therefore, any relative difference between the heat capacities of

the two glasses due to partial crystallization of one of them would be magnified by a factor near ten in compering the corresponding equilibrium supercooled liquids. Comparison of the results for heat capacity Series IX, XX, and XXXIX with those for Series XIX, XXXII, XXXIII, XL, and XLIII shows that the heat capacities are the same within the calorimetric limits of uncertainty for the equilibrium supercooled liquids corresponding to the quenched and the annealed glasses respectively. Therefore the observed difference between the heat capacities of the two glasses has no measurable contribution due to partial crystallization of either of them.

The uniformly lower heat capacities of the annealed glass, as compared with the quenched, is consistent with the proposition that the intermolecular force constants in the annealed glass are greater as indicated by the decrease in specific volume generally associated with annealing.

The fact that the difference between the entropies of the annealed and the quenched glasses at temperatures just below the glass transformation region varies only slightly from the difference between their residual entropies at absolute zero temperature is consistent with approximating the (fixed) configurational entropy of a glass by its residual entropy at absolute zero temperature. This approximation and the consequences of its application are discussed in more detail in reference [24].

Reference [24] also dwells at some length on the fact that an annealed glass maintains its fixed molecular configurations at temperatures much closer to the glass transformation proper than does quenched glass. A clear concrete demonstration of this fact for diethyl phthalate is provided in figure 5, which is presented specifically for this purpose. It shows the (configurational) drifts of calorimeter temperature between individual calorimetric energy inputs for the annealed and the quenched glasses respectively at temperatures approaching the glass transformation. (Warm) drifts set in for the quenched glass when the temperature rises above 145 °K. This shows that the molecular configurations are starting to change at such temperatures. However, for the annealed glass, the temperature must rise above 170 °K before (cold) drifts set in. Therefore the molecular configurations fixed in the annealed glass are maintained fixed up to this temperature. For the annealed glass, as compared with the quenched, one gains an additional 25° of temperature range over which the measurement results are characteristic of the fixed molecular configurations existing well below the glass transformation.

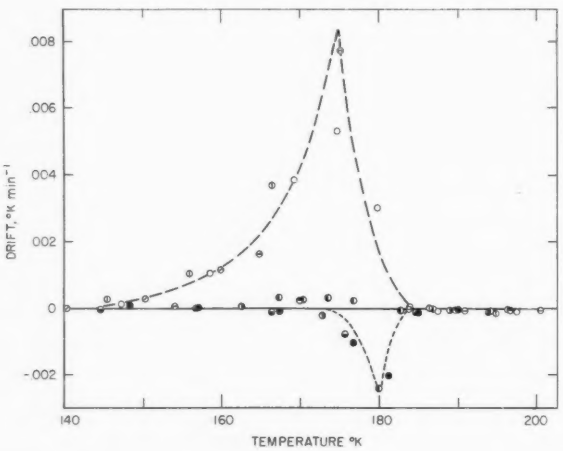

FIGURE 5. *Calorimeter drifts for diethyl phthalate glasses in glass transformation temperature region.*

Open and barred circles represent quenched glasses. Shaded circles represent annealed glasses.

4.5. Δc_p

The difference, Δc_p, between the heat capacities of the glass and of the equilibrium supercooled liquid, both extrapolated to an arbitrarily specified glass transformation temperature, is utilized in certain considerations of the glass transformation process [25]. The precise specification of the heat capacity of the glass to be used in obtaining this difference is discussed in reference [24]. Wunderlich [26] has shown that for most glass-forming substances Δc_p has a value of 11.3 ± 2.1 joule per degree per specifically defined material unit designated as a "bead." In using Δc_p it is usually assumed as a first approximation that the quantity is independent of temperature, though this is well recognized as a crude approximation.

From the present work, Δc_p for diethyl phthalate is evaluated as 115 ± 3 joule per degree and mole at 180 °K. Usual criteria suggest seven beads per molecule for diethyl phthalate. On this basis Δc_p would be 16.4 ± 0.4 joule per degree and mole. To bring the value within the limits mentioned above, it would be necessary to assume at least nine beads per molecular for diethyl phthalate. The higher value could be rationalized by assuming that the phthalyl group is not made completely rigid by conjugation resonance effects. The observed temperature derivative of Δc_p for diethyl phthalate at 180 °K is 1.0 joule per degree, degree and mole, or about 1 percent of the value itself. This indicates the level of validity of the temperature independence approximation.

5. References

[1] K. F. Sterrett, D. H. Blackburn, A. B. Bestul, S. S. Chang, and J. Horman, J. Res. NBS **69C** (Engr. and Instr.) No. 1, 19 (1965).

[2] P. A. Small, K. W. Small, and P. Cowley, Trans. Faraday Soc. **44**, 810 (1948).

[3] G. T. Furukawa and M. Reilly, J. Res. NBS **69A** (Phys. and Chem.) No. 1, 5 (1965).

[4] H. M. Roder, J. Res. NBS **69A** (Phys. and Chem.) No. 6, 527 (1965).

[5] cf., e.g., G. O. Jones, Glass, p. 49 (John Wiley & Sons, Inc., New York, N.Y., 1956).

[6] G. S. Parks, S. B. Thomas, and D. W. Light, J. Chem. Phys. **4**, 64 (1936).

[7] C. T. Anderson, J. Am. Chem. Soc. **59**, 1036 (1937).

[8] E. F. Westrum, Jr. and G. Grenier, J. Am. Chem. Soc. **79,** 1799 (1957).
[9] E. F. Westrum, Jr., V International Congress on Glass, Paris, 1956, VII–6.
[10] W. P. White, Am. J. Sci. **47,** 1 (1919).
[11] O. L. Anderson, J. Phys. Chem. Solids **12,** 41 (1959).
[12] P. Flubacher, A. J. Leadbetter, J. A. Morrison, and B. P. Stoicheff, J. Phys. Chem. Solids **12,** 53 (1959).
[13] H. B. Rosenstock, J. Phys. Chem. Solids **23,** 659 (1962).
[14] R. S. Craig, C. W. Massena and R. M. Mallya, J. Appl. Phys. **36,** 108 (1965).
[15] E. F. Westrum, Jr., unpublished data.
[16] F. Simon and F. Lange, Z. Physik **38,** 227 (1926).
[17] W. Reese and J. E. Tucker, Bull. Am. Phys. Soc. **10,** 323 (1965).
[18] O. L. Anderson and G. J. Dienes, in Non-Crystalline Solids, p. 453, V. D. Frechette, ed. (John Wiley & Sons, Inc., New York, N.Y., 1960).
[19] W. Reese, J. Appl. Phys. **37,** 3959 (1966).
[20] S. H. Glarum, J. Chem. Phys. **33,** 639 (1960).
[21] B. I. Hunt and J. G. Powles, Proc. Phys. Soc. **88,** 513 (1966).
[22] P. G. Klemens, in Non-Crystalline Solids, p. 508, V. D. Frechette, ed. (John Wiley & Sons, Inc., New York, N.Y., 1960).
[23] P. G. Klemens, J. G. Castle and D. W. Feldman, Phys. Chem. Glass **5,** 104 (1964).
[24] S. S. Chang, A. B. Bestul, and J. A. Horman, Proc. VII International Congress on Glass, Brussels, 1965, Gordon and Breach (New York) 1966, p. 26–1.3.1.
[25] cf., e.g., R. O. Davies and G. O. Jones, Proc. Roy Soc. **A217,** 26 (1953).
[26] B. Wunderlich, J. Phys. Chem. **64,** 1052 (1960).

(Paper 71A4–461)

JOURNAL OF RESEARCH of the National Bureau of Standards—A. Physics and Chemistry Vol. 71A, No. 4, July-August 1967

Heats of Formation of Aluminum Diboride and α-Aluminum Dodecaboride[1]

Eugene S. Domalski and George T. Armstrong

Institute for Basic Standards, National Bureau of Standards, Washington, D.C. 20234

(April 24, 1967)

The energies of combustion of AlB_2 and α-AlB_{12} were measured in a bomb calorimeter using fluorine as the oxidant. Major problems of this investigation were the assessment of the state and distribution of impurities in the samples and the establishment of the stoichiometry of the aluminum boride phase. We obtain -16 ± 3 kcal mol^{-1} and -48 ± 10 kcal mol^{-1} for the heats of formation of AlB_2 and α-AlB_{12}, respectively. The uncertainties cited are the overall experimental errors. Their magnitudes are chiefly due to uncertainties in the impurity correction applied and the uncertainties in the heats of formation of the combustion products.

Key Words: Aluminum diboride, α-aluminum dodecaboride, aluminum fluoride, bomb calorimeter, boron trifluoride, fluorine, heat of combustion, heat of formation, Teflon.

1. Introduction

Thermodynamic data on the aluminum borides are not plentiful. There exist essentially no data from which the heats of formation can be calculated. Van Arkel [1][2] estimated the heat of formation of aluminum diboride to be -80 kcal mol^{-1} by a method that he did not describe. The vapor pressure of AlB_{12} was measured by Bolgar, Verkhoglyadova, and Samsonov [2] between 1100 and 2000 °C. They observed aluminum in the vapor, but do not state whether any other species were present in the vapor. It is, therefore, not clear what relationship exists between their calculated heat of vaporization, and the heat of formation of AlB_{12}(c). Interpretation of their work is further complicated by the discrepancy of about an order of magnitude in the heats of vaporization of titanium diboride and zirconium diboride as reported by the above authors and as reported by Schissel and Trulson [3] and by Leitnaker, Bowman, and Gilles [4].

Because no calorimetric study had been made to determine the heats of formation of any of the borides of aluminum, we undertook this task using fluorine bomb calorimetry. Combustion of the aluminum borides in oxygen presumably forms two solid oxides as products, Al_2O_3 and B_2O_3, which may interact with one another, and may retain unburned starting material mixed with them. The amount of reaction is very difficult to determine in this kind of process. On the other hand, when an aluminum boride is burned in fluorine one of the products is gaseous and the difficulties in obtaining a more complete reaction and of measuring the degree of completeness are correspondingly decreased.

A previous study of the combustion of aluminum [5, 6] in fluorine in our laboratory provided a directly applicable technique for carrying out the reaction process in the calorimeter, and in addition, provided some of the essential auxiliary data necessary to calculate the heat of formation of the aluminum borides from their heats of combustion in fluorine. Concurrently with this work a study of the combustion of boron in fluorine was carried out, and is reported elsewhere [7]. The determination of the heats of combustion of aluminum and boron in fluorine using the same calorimetric system and the same preparative technique for the samples was considered important in order to minimize systematic errors because relatively small heats of formation for the aluminum borides are to be deduced from large heats of combustion.

At the time this work was undertaken, no studies had been made of refractory borides using the fluorine bomb technique and a large fraction of our interest was in the establishment of techniques and in the formation of an appraisal of the ultimate usefulness of the technique chosen for refractory compounds. However, the lack of data on the aluminum borides in particular, and metallic borides in general, can also be linked to difficulties met in preparing and characterizing single phase materials having a definite stoichiometry and a high state of purity. Although the samples used were as good in quality as we considered to be obtainable at the time, we found that interpreting

[1] This research was sponsored by the Air Force Aero Propulsion Laboratory, Research and Development Division, Air Force Systems Command, Wright-Patterson Air Force Base, Ohio, under USAF Delivery Order No. 33(615)64-1003 and by the Air Force Office of Scientific Research under Order No. OAR ISSA 65-8.

[2] Figures in brackets indicate the references at the end of this paper.

the type and distribution of impurities, normalizing the sample composition, and deciding upon the stoichiometry of the boride phase were more difficult than performing the heat measurements.

Calorimetric measurements were performed on samples of AlB_2, α-AlB_{12}, and γ-AlB_{12}. The measurements on α-AlB_{12} were amenable to interpretation in terms of stoichiometry although the total observed analysis was found to be in excess of 100 percent. The measurements on AlB_2 were more difficult to interpret because of the deviation of the apparent formula from stoichiometry, and greater deviation of the total observed analysis from 100 percent. We found it impossible to obtain a reasonable interpretation of the measurements on γ-AlB_{12} for the following reasons: the sample contained about 10 percent of the α-phase syntactically intergrown, the apparent formula was calculated to be $AlB_{12.57}$, the total observed analysis was only 97.2 percent, and only two calorimetric measurements were made. Therefore, only the measurements on AlB_2 and α-AlB_{12} are reported here.

2. Materials

The aluminum borides were prepared for us by the Carborundum Company and are similar to materials described by Matkovich, Economy and Giese [8]. The elemental analysis for the aluminum borides is given in table 1. Unless otherwise indicated analyses were performed by the NBS Analysis and Purification Section. Analyses for aluminum, boron and metallic impurities did not differ significantly from those obtained by the supplier. Crystallographic examinations by x-ray diffraction were made by the NBS Crystallography Section.

The aluminum diboride sample consisted of extremely thin black crystalline platelets with areas up to several mm^2, having a metallic luster. Inspection of table 1 shows the boron content of the AlB_2 sample to be in excess of the theoretical value. The observed boron to aluminum atomic ratio is 2.215 which is ascribed by the supplier to lattice vacancies and/or boron atoms in aluminum positions. The x-ray pattern showed the aluminum diboride sample to be hexagonal. The lattice constants found were, $a = 3.005$ Å, and, $c = 3.250$ Å, in good agreement with previously reported constants for this phase ($a = 3.009$ Å and $c = 3.262$ Å [9]).

The α-AlB_{12} sample was obtained as a reddish-brown powder having a maximum particle size of about 75 μ. The boron and aluminum analyses on this sample gave a boron to aluminum atomic ratio which was essentially stoichiometric, 12.03. X-ray analysis showed the unit cell to be tetragonal with the lattice constants, $a = 10.162$ Å and $c = 14.26$ Å (previously reported: $a = 10.161$ Å and $c = 14.283$ Å [10]).

The samples were analyzed for boron, aluminum, and metallic impurities using appropriate wet chemical and instrumental methods. Nitrogen in the samples was determined by the Kjeldahl method. Carbon was determined gravimetrically by oxygen combustion of the sample and measurement of the CO_2 formed. The oxygen content of the aluminum borides was determined by neutron activation and inert-gas fusion techniques. The oxygen analysis by inert-gas fusion is preferred over the analysis by neutron activation because of suspected interference of isotopic species produced from irradiation of the boron in the sample [11].

TABLE 1. *Elemental analysis of the aluminum borides (weight percent)*

Aluminum Boride	AlB_2	α-AlB_{12}
Al theoretical	55.51	17.22
B theoretical	44.49	82.78
Al found	53.00	16.98
B found	47.04	81.85
Cu	0.075	.....
Fe	.025	.....
Si	.026	0.05
Mg	.024	.15
Ca	.013	.018
Mn	.010	.....
O	[a](1.0), [b]0.89	[a](1.3), [b]1.44
N	.30	0.27
C	.08	.11
Total	101.483	100.868

[a] Neutron activation analysis (General Atomic).
[b] Inert-gas fusion analysis (Ledoux and Co.).
(The inert-gas fusion results for oxygen were used in forming the totals.)

The Teflon (polytetrafluoroethylene) film and the Teflon powder ("Teflon 5") used in preparing pelleted mixtures, and the fluorine used in the heat measurements were the same as described in an earlier paper [6]. Neither the Teflon film nor powder was modified or treated in any special way prior to use. The energy of combustion, $\triangle E^\circ_{303}$, of "Teflon 5" was $-10{,}371.7$ Jg^{-1}. The fluorine was analyzed using the mercury absorption technique [12] and found to be 99.79 percent F_2.

3. Treatment of the Analytical Data

Because of the large departure of the total elemental analysis of the aluminum borides from 100 percent, it has been a difficult task to decide upon how much of the aluminum boride was present and in what state the impurities occurred. The difficulty was aggravated by the nonstoichiometry evident in AlB_2. Whether AlB_2 is nonstoichiometric as implied by the boron to aluminum ratio, or whether interaction of the impurities with boron and aluminum merely gives this impression, remains unsolved. Chemical analyses for constituent elements have shown that both AlB_2 and α-AlB_{12} samples possess total compositions of 101.5 and 100.9 percent, respectively. A gross error in the analysis of one or more elements is required in order to account for the discrepancy, but has not been found.

Summaries of the treatments of the impurities in aluminum diboride and α-aluminum dodecaboride are shown in tables 2 and 3 in which five treatments are presented. In all cases we have assumed the metallic

TABLE 2. *Treatment of Impurities in* AlB_2

Treatment	1	2	3	4	5
Normalization mode	Entire composition	Entire composition	Entire composition	Impurities only	AlB_2 content only
AlB_2	90.848	94.078			
$AlB_{2.215}$			97.409	98.854	97.371
Al					
B	5.937	3.593			
Cu	0.074	0.074	0.074	0.033	0.075
Fe	.025	.025	.025	.011	.025
Si	.026	.026	.026	.011	.026
Mg	.024	.024	.024	.010	.024
Ca	.013	.013	.013	.006	.013
Mn	.010	.010	.010	.004	.010
Al_2O_3	1.863		.579	.256	.588
B_2O_3		1.272	.876	.388	.889
AlN	0.866		.269	.119	.273
BN		0.524	.361	.160	.366
Al_4C_3	.315		.181	.080	.184
B_4C		.363	.154	.068	.156
Total	100.001	100.002	100.001	100.000	100.000

TABLE 3. *Treatment of impurities in* α-AlB_{12}

Treatment	1	2	3	4	5
Normalization mode	Entire composition	Entire composition	Entire composition	Impurities only	α-AlB_{12} content only
α-AlB_{12}	83.564	96.521			
α-$AlB_{12.03}$			96.653	97.492	96.624
Al		0.216			
B	11.969				
Mg	0.149	.149	0.149	0.111	0.150
Si	.050	.050	.050	.037	.050
Cu	.018	.018	.018	.013	.018
Al_2O_3	3.033		.233	.175	.235
B_2O_3		2.071	1.911	1.432	1.928
AlN	0.783		0.060	.045	.061
BN		0.474	.437	.328	.441
Al_4C_3	.435		.087	.065	.088
B_4C		.502	.402	.301	.405
Total	100.001	100.001	100.000	99.999	100.000

impurities in AlB_2 and α-AlB_{12} to be present as the elements. When one considers the possible distribution of nonmetallic impurities, two possibilities present themselves. First, the aluminum boride can be considered as stoichiometric and the nonmetals as combined entirely with one element or the other. Some excess of elemental aluminum or boron will also be present. This gives two extreme cases which are shown in tables 2 and 3 in treatments marked (1) and (2). In treatment (1) the nonmetals are combined entirely with aluminum, leaving an excess of elemental boron, and in treatment (2) they are combined entirely with boron, leaving an excess of elemental aluminum. Second, the aluminum boride samples can be considered as nonstoichiometric and the nonmetallic impurities as distributed between boron and aluminum in proportion to the relative number of moles of boron and aluminum. This latter possibility appears to us to represent a more probable situation in the absence of specific information about the distribution of the elements.

In either case, since the total elemental analysis of AlB_2 and α-AlB_{12} deviates from 100 percent, we must normalize the composition in order to attain a proper mass balance. The mode of normalization used in treatments 1, 2, and 3 of tables 2 and 3 is that involving the entire composition. Inherent in this procedure is the assumption that the error in a particular analysis for an element is proportional to the amount of that element present in the sample. This assumption introduces a large adjustment in the case of the boron analysis in our α-AlB_{12} sample since it is the element present in the greatest amount and also because the deviation of the total composition from 100 percent is large. Treatments (4) and (5) of tables 2 and 3 illustrate the effects of normalization in such ways as to throw the error completely into the boride phase, or into the impurities, and thus allow calculation of the extreme effects that the manner of treating the analysis can have on the calculated heat of formation. Under treatment (4) the amount of the impurities is adjusted retaining the original amounts of AlB_2 and α-AlB_{12} as found from the analysis after the nonmetallic impurity distribution had been taken into account. Treatment (5) results from retaining the original amounts of impurities and adjusting the amount of the boride phase.

It is evident that an indefinite number of distributions other than the ones suggested are possible. Because of the manner of assigning the compositions used in the various treatments, we feel that the heats of formation derived for AlB_2 and α-AlB_{12} using these treatments represent both the extreme and the more likely values, and envelop values that could result from most other selections of the sample composition. Treatment (1) of table 3 in which all the nonmetallic impurities are assumed to be combined entirely with aluminum is not a likely situation for the α-AlB_{12} sample, although it depicts a limit to an impurity state and distribution. Since boron comprises over 80 percent of the sample, it seems improbable that the non-metals would not interact with the boron. A smaller error may result from use of treatment (2) in which all of the nonmetals are assumed to combine with boron. In the case of the AlB_2 sample, treatments (1) and (2) seem more nearly equally likely since the weight percent of boron and aluminum is almost the same.

Several studies have shown that boron has a tendency to form interstitial compounds with certain light (low atomic weight) elements [13, 14]. These findings might possibly question certain choices for the distribution of nonmetals present in our samples between aluminum and boron. For example, when oxygen is present only in small proportions the oxygen combination with boron is likely to resemble B_60 [14, 15] more than B_2O_3, however, no thermodynamic data are available on B_60 to permit calculation with it as a possible impurity. In the absence of data on the binding of oxygen in a large excess of boron, we are forced to assume that the binding energy per oxygen atom is similar to that in B_2O_3. Interestingly enough, α-AlB_{12} may be considered an interstitial compound of aluminum in boron in view of recent work on the structure of β-rhombohedral boron [16, 17].

Treatment (3) of tables 2 and 3 is the most likely state and distribution for the impurities in that it

not only includes the interaction of the nonmetals with boron, but does not exclude such interaction with aluminum. Treatment (4) of tables 2 and 3 is not a likely representation of the sample composition because a range of values greater than 0.5 percent has been found in the determination of boron in the aluminum borides we have submitted for analysis, hence, giving the determination a high uncertainty. There is a striking similarity between treatments (3) and (5) which illustrates that our choice of the most likely distribution leans heavily upon the accuracy of the analyses of the impurities. It is also in keeping with our suspicions about the accuracy of boron analysis in refractory boron compounds. The effects of the impurity distribution and normalization made upon the calculation of the heats of formation of AlB_2 and α-AlB_{12} will be discussed in section 9.2.

4. Preparation of Sample Pellets

Attempts to prepare suitable pellets of the aluminum borides under study, without the aid of an auxiliary substance, were not successful because of their hardness and resistance to compression, or their reaction with fluorine in the combustion bomb prior to the desired time of ignition. Three methods of sample preparation were used in preparing the samples for combustion in fluorine, which have already been described in detail earlier [5, 6]. In brief, one method (Method A) consisted of weighing the sample powder and Teflon powder in a sealable Teflon bag, mixing the powder to obtain homogeneity, and pressing the mixture into pellet form. Another method (Method B) was used for samples which reacted with fluorine upon contact. An additional coating of Teflon was provided to prevent reaction from occurring. In a third technique (Method C), the sample powder and Teflon powder were weighed in a small beaker, mixed to obtain homogeneity and transferred to a pellet die for pressing. This latter method, which was the first method developed, was found to be not suitable for samples that reacted spontaneously with fluorine and was less satisfactory than Method A with respect to the accounting for weight losses. We assumed that the total loss of mixture took place in proportion to the amounts of sample and Teflon present in the pellet.

In table 4, we present a brief summary of the average quantities of sample and Teflon powder which comprise a prepared pellet of a given aluminum boride. Also included are the method used to prepare a pellet, the number of the experiment using a particular method, and losses encountered in preparing a pellet. Samples were weighed to the nearest 0.01 mg. The densities of the substances, used in making buoyancy corrections were as follows in g cm^{-3}: "Teflon 5", 2.23; Teflon film, 2.15; AlB_2, 2.955 [8]; α-AlB_{12}, 2.557 [10].

TABLE 4. *Summary of the preparative technique used in the fluorine combustion of the aluminum borides*

Sample in pellet	Method of preparation and experiment number using a given method	Mass Teflon bag	Mass sample in mixture	Mass Teflon in mixture	Mass Teflon coating	Loss Teflon in sealing bag (Methods A and B)	Mass mixture adhering to breaker (Method C)	Loss of mixture in pelleting	Total loss
		Grams	*Grams*	*Grams*	*Grams*	*mg*	*mg*	*mg*	*mg*
AlB_2	B 1–6	0.3	0.238	1.84	0.8	0.04	.....	0.22	0.26
	C 1–9	.....	0.312	1.77	.....	.....	0.33	0.26	0.59
α-AlB_{12}	A 10	0.3	0.238	2.28	.....	0.16	.....	0.15	0.31
	B 11	0.3	0.200	1.70	0.8	0.02	.....	0.37	0.39

5. Calorimetric System

No major changes had been made in the bomb calorimeter, heat measurement station or combustion bomb since our earlier work [6, 7] which was carried out in the same apparatus. The apparatus will be discussed here only briefly.

An isothermal-jacket, stirred-water calorimeter was used in making the heat measurements. The jacket was maintained at a constant temperature near 30 °C to within 0.002 °C. Temperature changes were measured to 0.0001 °C with a G-2 Mueller Bridge in conjunction with a platinum resistance thermometer. Reactions were carried out in an "A"-nickel combustion bomb (volume, 360 cm^3) designed for service with fluorine.

The quantities of the sample and Teflon powder in the pellet were adjusted to provide a temperature rise of three degrees (27 to 30 °C). Two aluminum electrodes, each suspended from the bomb head by a Monel rod, held a tungsten fuse. Depending upon the diameter of the fuse an energy of either 20 J or 50 J was produced as a result of ignition and reaction of the fuse with fluorine. The electrical energy from the ignition process was assumed to be negligible. For procedures dealing with the loading and emptying of the combustion bomb, and for details of the design and construction of the fluorine manifold, our earlier work should be consulted [5].

6. Products of Combustion

The white powder present in the combustion bomb as a result of burning the aluminum borides in fluorine was identified by its x-ray diffraction pattern as aluminum trifluoride. Previous work [5, 6] has estab-

lished that Teflon burns in 15 to 20 atm of fluorine to carbon tetrafluoride as the only major product. Higher fluorocarbons were not detected in amounts greater than 0.02 mole percent. Product gases from the combustion of the aluminum borides in fluorine were analyzed in a mass spectrometer after absorption of the excess fluorine in mercury. Mass spectra comparable to those found in our earlier work [6, 7] were obtained. As in our work on the combustion of boron in fluorine, we found no sign of BF_3 as a result of examination in a mass spectrometer. An interaction of some kind on the part of BF_3 with the mercury fluoride formed during the absorption of fluorine is suspected.

Boron trifluoride was identified as a combustion product in an infrared spectrometer. Samples from aluminum boride-Teflon combusion experiments were examined in the region 400 to 600 cm^{-1}, and the BF_3 band at 481 cm^{-1} was observed. Also present in the spectra was the CF_4 band at 630 cm^{-1}. Spectra of the evacuated cell and of BF_3 alone were taken in this region in order to substantiate the identification. The cell used was 8 cm long and had polyethylene windows 0.0625 in thick.

7. Calibration Experiments

Twenty calibration experiments were performed in which benzoic acid (Standard Sample 39i) was burned in 30 atm of oxygen and with one ml of distilled water in the nickel combustion bomb. Their consistency and reproducibility have been discussed in our earlier paper [6]. The average energy equivalent was calculated to be 14,803.27 $\pm$0.99 J deg^{-1}. The uncertainty cited is the standard deviation of the mean. The energy equivalent is that of the standard initial oxygen calorimeter which included the nickel combustion bomb with 30 atm of oxygen, a platinum crucible and fuse support wires, platinum fuse (2 cm long, 0.01 cm diam), a type 304 stainless-steel liner, Monel pellet holder, and no sample. Fastened to the bomb was a heater and ignition leads. The mass of the calorimeter vessel and water was 3750.0 g. The calorimetric data obtained in the calibration experiments were programmed for the IBM 7094 computer according to the procedures outlined by Shomate [18].

Using the appropriate heat capacity data, the energy equivalent of the standard oxygen calorimeter was adjusted to the proper value for the fluorine experiments. This involved allowing for the heat capacities of 30 atm of oxygen, 1 ml of distilled water, the platinum ware, 21 atm of fluorine and two aluminum electrodes. The application of these corrections gave 14,805.17 J deg^{-1} for the energy equivalent of the standard initial fluorine calorimeter for the temperature range used.

8. Fluorine Combustion Experiments

The heat measurements on the aluminum borides were made contemporaneously with ten experiments, previously reported in detail [6], in which "Teflon 5" was burned in 21 atm of fluorine. The value listed in section 2 for the energy of combustion, $\triangle E^\circ_{303}$, was determined in these ten experiments.

Preliminary experiments on AlB_2 in which Method C was used to prepare pelleted mixtures showed a slow reaction with fluorine in the fore-period of the experiment, i.e., prior to the time of ignition. Six heat measurements, shown in table 5, were performed in which AlB_2-Teflon pellets prepared by Method B were burned in 21 atm of fluorine. Normal values for the fore-period drift rates and the apparent heat transfer coefficients were observed, indicating the absence of a premature reaction.

Eleven heat measurements shown in table 6, were made in which α-AlB_{12}-Teflon pellets were burned in fluorine. In the first nine experiments a pressure of 16 atm of fluorine was used for combustion of a pelleted mixture prepared using Method C, which was the only method that had been developed in the early stages of this work. In the last two experiments on α-AlB_{12}, which were made near the end of the work, a pressure of 21 atm of fluorine was used and the pellets were prepared by Methods A and B, respectively. No significant difference was observed in the heat measurements as a result of using different preparative techniques for the samples.

No sign of premature reaction was observed in experiments on α-AlB_{12} as a result of inspecting the

TABLE 5. *Aluminum diboride-Teflon combustion experiments*

Experiment No.		1	2	3	4	5	6
(1a)	$m(AlB_2$ sample)....gram...	0.267374	0.253674	0.220437	0.222195	0.226260	0.234477
(1b)	m(Teflon)....gram...	2.999471	2.846011	2.897229	2.957633	2.875395	2.933704
(2)	$P(F_2)$....atm...	21.9	21.8	21.5	21.6	21.5	21.7
(3)	(ϵ)....J deg^{-1}...	14,805.63	14,805.88	14,803.19	14,803.25	14,803.30	14,801.49
(4)	Δt_c....deg...	3.48196	3.29846	3.16402	3.21878	3.18094	3.26692
(5)	$(\epsilon)(-\Delta t_c)$....J...	−51,552.6	−48,830.0	−46,837.6	−47,648.4	−47,088.4	−48,355.3
(6)	ΔE fuse....J...	20.4	20.4	20.4	20.4	20.4	20.4
(7)	ΔE gas....J...	11.8	11.0	11.4	11.5	11.2	11.5
(8)	ΔE° (Teflon)....J...	31,109.6	29,518.0	30,049.2	30,675.7	29,822.7	30,427.5
(9)	$\Delta E^\circ_{303}(AlB_2$ sample)....J g^{-1}...	−76,338.0	−76,005.4	−76,015.4	−76,242.9	−76,169.5	−76,322.6

(10) ΔE°_{303} (AlB_2 sample) = −76,182.3 J g^{-1}.
(11) Standard Deviation of the Mean = 59.7 J g^{-1} = 0.73 kcal mol^{-1}.
(12) $\Delta E^\circ_{298} - \Delta E^\circ_{303} = -0.7$ J g^{-1}.
(13) ΔE°_{298} (AlB_2 sample) = −76,183.0 J g^{-1}.

TABLE 6. *α-Aluminum dodecaboride-Teflon combustion experiments*

Experiment No.	1	2	3	4	5	6	7	8	9	10	11
(1a) $m(\alpha\text{-AlB}_{12}$ sample)....g	0.313053	0.319321	0.306651	0.311374	0.286230	0.305196	0.305665	0.345568	0.318994	0.200065	0.237862
(1b) m(Teflon)....g	1.762627	1.759965	1.754308	1.763376	1.770452	1.771312	1.769831	1.784548	1.781811	2.724602	2.575942
(2) $P(F_2)$....atm	16.6	16.4	16.7	16.8	16.9	16.9	16.8	16.6	16.8	21.6	21.5
(3) (ϵ)....J deg^{-1}	14,804.37	14,804.41	14,804.21	14,804.29	14,805.19	14,804.42	14,804.42	14,803.41	14,804.11	14,799.95	14,803.61
(4) Δt_c....deg	3.20119	3.24529	3.15950	3.19296	3.04124	3.16284	3.16234	3.42228	3.25155	3.16372	3.29831
(5) $(\epsilon)(-\Delta t_c)$....J	−47,391.6	−48,044.6	−46,773.9	−47,269.5	−45,026.1	−46,824.0	−46,816.6	−50,661.4	−48,136.3	−46,822.9	−48,826.9
(6) ΔE fuse....J	41.7	37.4	37.5	36.9	36.2	31.8	42.1	42.0	42.5	20.4	20.4
(7) ΔE gas....J	6.5	6.4	6.4	6.5	6.6	6.6	6.3	6.6	6.6	12.6	11.9
(8) $\Delta E°$ (Teflon)....J	18,281.4	18,253.8	18,195.2	18,289.2	18,362.6	18,371.5	18,356.2	18,508.8	18,480.4	28,258.8	26,716.9
(9) $\Delta E°_{303}(\alpha\text{-AlB}_{12}$ sample)....J g^{-1}	−92,834.1	−93,157.0	−93,053.0	−92,932.9	−93,004.6	−93,101.2	−92,951.4	−92,902.1	−92,813.0	−92,625.4	−92,817.3

(10) $\Delta E°_{303}(\alpha\text{-AlB}_{12}$ sample)$= -92{,}926.5$ j g^{-1}.
(11) Standard deviation of the mean $= 45.8$ J g$^{-1} = 1.7$ kcal mol^{-1}.
(12) $\Delta E°_{298} - \Delta E°_{303} = +0.9$ J g^{-1}.
(13) $\Delta E°_{298}(\alpha\text{-AlB}_{12}$ sample)$= -92{,}925.6$ J g^{-1}.

fore-period drift rates and apparent heat transfer coefficients.

In each experiment the pelleted mixture was placed in the recess of a monel or "A"-nickel plate, the bomb was attached to the fluorine manifold and filled to the desired pressure. All bomb parts (bomb body, bomb head assembly and electrodes, liner and support plate) were weighed before the first experiment and after each experiment. Each part was washed with water and dried before the weighings were made.

The numbered entries in the tables are as follow:

(1a) Mass of the sample mixed with Teflon in the pellet corrected for weight loss in preparation and for recovery of unburned sample.

(1b) Mass of Teflon mixed with sample in the pellet corrected for weight loss.

(2) Pressure of fluorine introduced into the bomb prior to combustion corrected to 30 °C.

(3) Energy equivalent of the calorimeter for a given experiment.

(4) Temperature change of the calorimeter thermometer corrected for heat of stirring and heat transfer.

(5) Total energy change in the bomb process.

(6) Energy liberated by the tungsten fuse assuming the fuse burns according to the reaction:

$$W(c) + 3F_2(g) = WF_6(g).$$

From the heat of formation of WF_6 [19], we calculated 9.44 J mg^{-1} for the energy of combustion of the fuse.

(7) Net energy correction for the hypothetical compression and decompression of bomb gases.

$$\Delta E \text{ gas} = \Delta E^i(\text{gas})]_0^{P_{i(\text{gas})}} + \Delta E^f(\text{gas})]^0_{P_{f(\text{gas})}}.$$

(8) Standard energy of combustion per gram of Teflon at 30 °C multiplied by the corrected mass of Teflon in the pellet.

(9) Standard energy of combustion per gram of the sample.

(10) Average standard energy of combustion per gram of the sample.

(11) Standard deviation of the mean of the average cited in (10).

(12) Heat capacity correction converting the reference temperature to 298 °K.

(13) Standard energy of combustion of the sample at 298 °K not corrected for impurities.

The heat capacities at constant pressure, Cp, used in the calculation of entries (3) and (12) are as follows in cal deg^{-1} g^{-1} at 25 °C: aluminum, 0.216 [20]; boron, 0.245 [21]; Teflon, 0.28 [22]; AlB_2, 0.23; α-AlB_{12}, 0.24; aluminum fluoride, 0.213 [20]. The heat capacities of AlB_2, and α-AlB_{12} were estimated by assuming the molar heat capacities of the compounds to be the sums of the atomic heat capacities of the elements. The heat capacities at constant volume, C_V, used in the calculation of entries (3) and (12) were 5.52 [23], 12.62 [24] and 10.04 [21] cal deg^{-1} mol^{-1}, respectively for fluorine, carbon tetrafluoride and boron trifluoride at 30 °C.

Washburn corrections, entry (7), were calculated following the procedure outlined by Hubbard [25] for experiments in which fluorine is used as the oxidant. The coefficients $[\partial E/\partial P]_T = -T[dB/dT]$ were found in tables based on a Lennard-Jones 6–12 potential function as compiled by Hirschfelder, Curtiss, and Bird [26] using the appropriate force constants. The force constants used for fluorine, carbon tetrafluoride, and boron trifluoride were those determined by White, Hu, and Johnston [27], Douslin [28], and Brooks and Raw [29], respectively.

In calculating the corrections for the combustion of impurities in the AlB_2 and α-AlB_{12} samples, the following values, in kcal mol^{-1}, were used for the heats of formation of other compounds: Al_2O_3, −400.4 [30]; B_2O_3, −304.20 [31]; Al_4C_3, −49.7 [32]; AlN, −76.0 [20]; BN, −60.8 [31]; MgF_2, −268.7 [33]; CaF_2, −290.3 [34]; SiF_4, −385.98 [35]; FeF_3, −235 [36]; CuF_2, −126.5 [34]; MnF_3, −238 [36]. In calculating the correction for the B_4C impurity in our samples, we have chosen $\Delta E°_{298} = -97.84$ k Jg^{-1} for the reaction: $B_4C(c) + 8F_2(g) = 4BF_3(g) + CF_4(g)$ based upon heat measurements performed in our laboratory which will be reported in more detail in a future publication.

The combustion experiments were programmed for calculation in the same way as the calibration experi-

ments, however, the only valid data calculated by the computer were the corrected temperature rises, Δt_c, because the program used had not been modified to accommodate the use of fluorine as the oxidant.

Atomic weights were taken from the 1961 table of atomic weights based on $C^{12}=12$ and adopted by the International Union of Pure and Applied Chemistry [37]. The unit of energy is the joule, and one calorie was defined as 4.1840 J.

9. Discussion and Results

9.1. Analysis of Combustion Residues

A residue assumed to be unburned Teflon and/or carbon was observed in heat measurements involving Teflon alone. No correction was applied to any experiment for this residue, and we assumed that the formation of the residue took place in all experiments approximately in proportion to the amount of Teflon initially present. The heat of combustion per gram of Teflon would, hence, be constant and the error due to residue formation would be eliminated when the energy due to the combustion of Teflon was subtracted from the total energy released in the combustion.

Aluminum fluoride residues resulting from the burning α-AlB_{12}-Teflon pellets prepared using Method C were analyzed for boron content in order to determine the amount of unreacted aluminum boride. In the analysis, the AlF_3 residue underwent carbonate fusion, followed by solution with acid and extraction of the aqueous phase with an organic solvent. The boron in the organic phase was determined spectrophotometrically with carminic acid [38]. The recovery of unburned α-AlB_{12} ranged from 0.01 to 0.04 mg.

Aluminum fluoride residues obtained from the combustion of AlB_2-Teflon, and α-AlB_{12}-Teflon mixtures, in which Methods A and B were used for sample preparation were analyzed in the same way as the α-AlB_{12}-Teflon mixtures prepared by Method C except for the following differences. After fusion and acid solution, the boron in the aqueous phase was determined spectrophotometrically with methylene blue. The recovery ranged from 0.07 to 0.16 mg for AlB_2 and 0.34 to 0.41 mg for α-AlB_{12}.

A noncalorimetric experiment was performed in which an α-AlB_{12}-Teflon pellet was burned in 21 atm of fluorine and the AlF_3 residue was analyzed for carbon. Results of the analysis showed 0.17 mg of carbon present. A similar experiment was performed on an AlB_2-Teflon pellet resulting in the detection of 0.33 mg of carbon in the AlF_3 residue. Both results are somewhat above the values found for carbon when Teflon burns alone in fluorine (0.05 to 0.15 mg [6]), however, no correction has been applied to the data for them.

9.2. The Heats of Formation of Aluminum Diboride and α-Aluminum Dodecaboride

Tables 7 and 8 show a range of calculated values for the heats of combustion and formation of our aluminum diboride and α-aluminum dodecaboride samples and the dependence of these values upon the type of impurity correction applied. The datum in row 4 of these tables is the uncorrected energy of combustion obtained from the heat measurements shown in entry (13) of tables 5 and 6. The corrected energy of combustion is given in row 7 of the tables and is obtained by subtracting the energy contribution of the impurities (row 5) from row 4 and dividing by the fraction of the sample calculated to be the pure aluminum boride phase for a given treatment (row 6). The ΔnRT term (row 8) allows for the calculation of the heats of combustion in Jg^{-1} (row 9) and kcal $(gfw)^{-1}$ (row 10). The heat of formation per gram-formula-weight of the formula in row 2 for each treatment is calculated in row 11 by taking the difference between the sum of the heat of formation of the products (row 12) and the corresponding heat of combustion in row 10. The values used for the heats of formation of AlF_3(c) and BF_3(g) are -361.0 ± 1.6 and -271.03 ± 0.51 kcal mol^{-1}, respectively, as determined from our earlier work [5, 6, 7]. The uncertainties cited are the overall experimental errors of the respective studies.

For the sake of consistency, the treatments shown in row 1 of tables 7 and 8 correspond with the respective treatments in tables 2 and 3 of section 3.

As mentioned earlier in section 3, the treatment of the impurities which seem most likely to be relevant appears in tables 7 and 8 as treatment 3. In this treatment the assumption is made that the non-

TABLE 7. *The dependence of the heat data upon the treatment of the impurities in* AlB_2

1	Treatment	1	2	3	4	5
2	Stoichiometry	AlB_2	AlB_2	$AlB_{2.215}$	$AlB_{2.215}$	$AlB_{2.215}$
3	Assumptions regarding the state and distribution of the impurities	Nonmetals combined entirely with aluminum; free boron present	Nonmetals combined entirely with boron; free aluminum present	Nonmetals distributed between aluminum and boron in proportion to the amount of aluminum and boron present in the sample.		
4	Energy of combustion, uncorrected for impurities (from table 5), $J\,g^{-1}$	−76,183.0	−76,183.0	−76,183.0	−76,183.0	−76,183.0
5	Energy of combustion of impurities, $J\,g^{-1}$	−6,948.0	−4,529.9	−708.8	−312.7	−718.5
6	Fraction of sample calculated to be pure AlB_2 (or $AlB_{2.215}$)	0.90848	0.94078	0.97409	0.98854	0.97371
7	Energy of combustion, corrected, ΔE°_{298}, $J\,g^{-1}$	−76,209.7	−76,163.5	−77,481.8	−76,749.9	−77,502.0
8	ΔnRT term, $J\,g^{-1}$	−127.5	−127.5	−137.4	−137.4	−137.4
9	Heat of combustion, ΔH°_{298}, $J\,g^{-1}$	−76,337.2	−76,291.0	−77,619.2	−76,887.3	−77,639.3
10	Heat of combustion, ΔH°_{298}, kcal $(gfw)^{-1}$	−886.77	−886.24	−944.78	−935.88	−945.03
11	Heat of formation, ΔH°_{f298}, kcal $(gfw)^{-1}$	−16.29	−16.82	−16.55	−25.45	−16.30
12	Sum of the heats of formation of the products, kcal $(gfw)^{-1}$	−903.06	−903.06	−961.33	−961.33	−961.33

TABLE 8. *The dependence of the heat data upon the treatment of the impurities in* α-AlB_{12}

1	Treatment	1	2	3	4	5
2	Stoichiometry	α-AlB_{12}	α-AlB_{12}	α-$AlB_{12.03}$	α-$AlB_{12.03}$	α-$AlB_{12.03}$
3	Assumptions regarding the state and distribution of the impurities	Nonmetals combined entirely with aluminum; free boron present	Nonmetals combined entirely with boron; free aluminum present	Nonmetals distributed between aluminum and boron in proportion to the amount of aluminum and boron present in the sample.		
4	Energy of combustion, uncorrected for impurities (from table 6), J g^{-1}	−92,925.6	−92,925.6	−92,925.6	−92,925.6	−92,925.6
5	Energy of combustion of impurities, J g^{-1}	−13,530.4	−1,178.8	−1,024.5	−767.4	−1,029.9
6	Fraction of sample calculated to be pure α-AlB_{12} (or α-$AlB_{12.03}$)	0.83564	0.96521	0.96653	0.97492	0.96624
7	Energy of combustion, corrected, ΔE°_{298}, J g^{-1}	−95,012.3	−95,054.7	−95,084.5	−94,529.9	−95,104.3
8	ΔnRT term, J g^{-1}	−118.6	−118.6	−118.4	−118.4	−118.4
9	Heat of combustion, ΔH°_{298}, J g^{-1}	−95,130.9	−95,172.3	−95,202.9	−94,648.3	−95,222.7
10	Heat of combustion, ΔH°_{298}, kcal (gfw)$^{-1}$	−3563.2	−3564.7	−3573.2	−3552.4	−3574.0
11	Heat of formation, ΔH°_{f298}, kcal (gfw)$^{-1}$	−50.2	−48.7	−48.3	−69.1	−47.5
12	Sum of the heats of formation of the products, kcal (gfw)$^{-1}$	−3613.4	−3613.4	−3621.5	−3621.5	−3621.5

metals are distributed between aluminum and boron in proportion to the amount of aluminum and boron present in the sample. Also reasonably probable is treatment 5, in which the total amount of impurities is assumed to be correct and the normalization of the composition is made entirely by adjusting the amount of the aluminum boride phase.

Treatment (2) represents a probable situation for both AlB_2 and α-AlB_{12} while treatment (4) does not: treatment (1) represents a probable situation for AlB_2 but not for α-AlB_{12}. In treatments (3), (4), and (5), the heat of formation is calculated assuming the boride phase to be nonstoichiometric, however, an equivalent result is obtained if we assume the aluminum boride to be stoichiometric but accompanied by an excess of elemental boron. With the application of a correction for this excess, the calculation of the heats of formation of the stoichiometric and nonstoichiometric formulas become identical. Although certain treatments depict unlikely situations, they have been presented to show possible extremes in the calculations and to be used in estimating errors.

We have selected −16 kcal mol^{-1} as the best value for the heat of formation of stoichiometric AlB_2. This value is the average of the calculated heats of formation found in treatments (1), (2), (3), and (5) of table 7. It will be noted that the calculation in treatments (1) and (2) gives results for the heat of formation of the stoichiometric formula, AlB_2, which shows little difference numerically from the calculation in treatments (3) and (5) for the heat of formation of the nonstoichiometric formula, $AlB_{2.215}$. Thus the value −16 kcal mol^{-1}, could as readily be selected for the heat of formation of $AlB_{2.215}$.

In a similar manner, we have chosen −48 kcal mol^{-1} as the best value for the heat of formation of stoichiometric α-AlB_{12}. This value is the average treatments (2), (3), and (5) in table 8. Here again, these treatments give almost the same heat of formation regardless of the stoichiometry. In this case, the stoichiometric and nonstoichiometric formulas are close enough together to be of little concern.

In making these selections, the factors of stoichiometry, manner of normalization of the composition, and distribution of the nonmetallic impurities have been considered. It is of interest to note that those methods of treatment which on an a priori basis appear to us to represent the more probable situations give values for the heats of formation which lie rather close together.

Assuming the borides to be stoichiometric, eqs (1) and (2) illustrate the combustion processes for AlB_2 and α-AlB_{12}:

$$AlB_2(c) + 9/2F_2(g) = AlF_3(c) + 2BF_3(g) \quad (1)$$

$$\alpha\text{-}AlB_{12}(c) + 39/2F_2(g) = AlF_3(c) + 12BF_3(g). \quad (2)$$

We calculate the heats of combustion in fluorine of AlB_2 and α-AlB_{12} to be −887 and −3565 kcal mol^{-1}, respectively, on the basis of the selected values for the heats of formation of these borides.

9.3. Sources of Error

The error incurred as a result of deciding upon the appropriate impurity distribution, which in turn defines the amount of AlB_2 in the sample, was 2.2 kcal mol^{-1}. We calculated this value by taking the difference between the corrected and uncorrected energies of combustion (rows 7 and 4 of table 7) and finding the average deviation of the differences. Using a similar approach, we calculated the error due to the choice of the appropriate impurity distribution for α-AlB_{12} to be 6.8 kcal mol^{-1}. The errors introduced by the uncertainties in the heats of formation of AlF_3(c), 1.6 kcal mol^{-1}, and BF_3(g), 0.51 kcal mol^{-1}, were calculated to be 1.9 and 6.3 kcal mol^{-1} for the AlB_2 and α-AlB_{12} data, respectively. These values were obtained by taking the square root of the sum of the squares of the terms, $(x)(1.6)$ and $(y)(0.51)$, in which x and y corresponding to the moles of AlF_3(c) and BF_3(g) formed in the combustion reaction. We estimate that the error introduced by the uncertainties in the heats of formation of the products is an upper limit because the measurements made on the heats of formation of AlF_3 and BF_3, as well as the heat of combustion of α-AlB_{12} in fluorine were performed using the same calorimetric system and were subject to the same preparative procedure for the samples. Hopefully, because of these features, certain systematic errors would tend to cancel. Errors incurred as a result of

performing the heat measurements, such as the error from calibration or combustion experiments, losses in sample preparation, analysis for the amount of unburned α-AlB_{12}, incomplete fuse combustion, etc., are adequately covered by using two times the standard deviation of the mean, (entry 11, tables 5 and 6). Finally, by taking the square root of the sum of the squares of the three main sources of error, we obtain 3 and 10 kcal mol^{-1} for the estimated error of the heats of formation of AlB_2 and α-AlB_{12}, respectively.

10. References

[1] A. Van Arkel, Alloys as Solid Rocket Fuels, National Research Corp., Cambridge, Mass., October 7, 1960.

[2] A. S. Bolgar, T. S. Verkhoglyadova and G. V. Samsonov, Izv. Akad. Nauk SSSR Otd. Tekhn. Nauk, Met. i Toplivo, No. 1, 142–4 (1961).

[3] P. O. Schissel and O. C. Trulson, J. Phys. Chem. **66,** 1492–6 (1962).

[4] J. M. Leitnaker, M. G. Bowman, and P. W. Gilles, J. Chem. Phys. **36,** 350–8 (1962).

[5] E. S. Domalski and G. T. Armstrong, J. Res. NBS **69A** (Phys. and Chem.) No. 2, 137–147 (1965).

[6] E. S. Domalski and G. T. Armstrong, J. Res. NBS **71A** (Phys. and Chem.) No. 2, 105–118 (1967).

[7] E. S. Domalski and G. T. Armstrong, J. Res. NBS **71A** (Phys. and Chem.) No. 3, 195–202 (1967).

[8] V. I. Matkovich, J. Economy and R. F. Giese, Jr., J. Am. Chem. Soc. **86,** 2337–2340 (1964).

[9] E. J. Felten, J. Am. Chem. Soc. **78,** 5977–8 (1956).

[10] J. A. Kohn and D. W. Eckart, Anal. Chem. **32,** 296–8 (1960).

[11] (a) G. H. Andersen, General Atomic, San Diego, California, private communication, March, 1966. (b) Kaman Nuclear, Technical Note (TN–105), 10 June 1965.

[12] G. T. Armstrong and R. S. Jessup, J. Res. NBS **64A** (Phys. and Chem.) No. 1, 49–59 (1960).

[13] V. I. Matkovich, J. Am. Chem. Soc. **83,** 1804–6 (1961).

[14] J. Economy, V. I. Matkovich, and R. F. Giese, Jr., Z. Krist. **122,** 248–258 (1965).

[15] H. F. Rizzo, W. C. Simmons, and H. O. Bielstein, J. Electrochem. Soc. **109,** 1079–1082 (1962).

[16] R. E. Hughes, C. H. L. Kennard, D. B. Sullenger, H. A. Weakliem, D. E. Sands, and J. L. Hoard, J. Am. Chem. Soc. **85,** 361–2 (1963).

[17] V. I. Matkovich, R. F. Giese, Jr., and J. Economy, Z. Krist. **122,** 116–130 (1965).

[18] C. H. Shomate, Computer Calculations of Combustion Bomb Calorimetric Data, Technical Progress Report 327, NOTS 3288, U.S. Naval Ordnance Test Station, China Lake, California (Aug. 1963).

[19] O. E. Myers and A. P. Brady, J. Phys. Chem. **64,** 491–4 (1960).

[20] G. T. Furukawa, M. L. Reilly, and J. Henning Piccirelli, NBS, private communication, July 1, 1960.

[21] W. H. Evans, NBS, private communication, January 1, 1961.

[22] W. D. Good, D. W. Scott, and G. Waddington, J. Phys. Chem. **60,** 1080–9 (1956).

[23] W. H. Evans, J. Hilsenrath, and H. W. Woolley, NBS, private communication, July 1, 1960.

[24] Dow Chemical Company, JANAF Thermochemical Tables, PB 168 370. (Clearinghouse for Federal Scientific and Technical Information, Springfield, Virginia, 1965.)

[25] W. N. Hubbard, Fluorine Bomb Calorimetry, Chapter 6, Experimental Thermochemistry, Vol. **II,** H. A. Skinner, editor (Interscience Publishers, Inc., New York, 1962).

[26] J. O. Hirschfelder, C. F. Curtiss, and R. B. Bird, Molecular Theory of Gases and Liquids (John Wiley & Sons, Inc., New York, N.Y., 1954, Second Printing 1964).

[27] D. White, H. Hu, and H. L. Johnston, J. Chem. Phys. **24,** 1149–52 (1953).

[28] D. R. Douslin, paper No. 11, pp. 135–46, PVT Relations and Intermolecular Potentials for Methane and Carbon Tetrafluoride, in Progress in International Research on Thermodynamics and Transport Properties, J. F. Masi and D. H. Tsai, Editors (Academic Press, New York, 1962).

[29] G. L. Brooks and C. J. G. Raw, Trans. Faraday Soc. **54,** 972–4 (1958).

[30] A. D. Mah, J. Phys. Chem. **61,** 1572–3 (1957).

[31] D. D. Wagman, W. H. Evans, I. Halow, V. B. Parker, S. M. Bailey, and R. H. Schumm, NBS Technical Note 270–2 May 6, 1966.

[32] R. C. King and G. T. Armstrong, J. Research NBS **68A,** 661–7 (1964).

[33] E. Rudzitis, H. M. Feder, and W. N. Hubbard, J. Phys. Chem. **68,** 2978–81 (1964).

[34] F. D. Rossini, D. D. Wagman, W. H. Evans, S. Levine, and I. Jaffe, Selected values of chemical thermodynamic properties, NBS Circ. 500 (U.S. Government Printing Office, Washington, D.C., 1952).

[35] S. S. Wise, J. L. Margrave, H. M. Feder, and W. H. Hubbard, J. Phys. Chem. **67,** 815–21 (1963).

[36] L. Brewer, L. A. Bromley, P. W. Gilles, and N. Lofgren, The Thermodynamic Properties of the Halides, paper 6, Chemistry and Metallurgy of Miscellaneous Materials: Thermodynamics, L. L. Quill, editor (McGraw-Hill Book Company, Inc., New York, 1950).

[37] A. E. Cameron and E. Wichers, J. Am. Chem. Soc. **84,** 4175–97 (1962).

[38] W. J. Ross, A. S. Meyer, Jr., and J. C. White, U.S.A.E.C. Report, ORNL–2135 (1956).

(Paper 71A4–462)

JOURNAL OF RESEARCH of the National Bureau of Standards—A. Physics and Chemistry Vol. 71A, No. 4, July-August 1967

Effect of Environment Upon the Melting Point of Al_2O_3

S. J. Schneider and C. L. McDaniel

Institute for Materials Research, National Bureau of Standards, Washington, D.C. 20234

(April 24, 1967)

The melting point of Al_2O_3 has been determined in vacuum, air, argon, and helium utilizing iridium or tungsten containers. All melting point experiments were conducted in induction furnaces capable of heating small samples under blackbody conditions to 3000 °C in vacuum, 2600 °C in inert atmospheres, and 2400 °C in air. Temperatures were continuously monitored with a recording photoelectric pyrometer which has a sensitivity of ±0.2° at 1063 °C and ±1° at 2000 °C. Melting points were determined on specimens having a purity in excess of 99.9 percent. The data indicated that the melting point of Al_2O_3 determined in vacuum (~6.5×10^{-5} torr) is 2051 °C (IPTS). The overall maximum uncertainty was estimated to be ±6 °C. The measurements themselves were precise within ±1.5 °C. Vacuum treatment had least detrimental effect upon the Al_2O_3 specimens. Each of the gaseous atmospheres including air yielded lower melting points for Al_2O_3, presumably due to a premelting phenomenon.

Key Words: Al_2O_3, dissociation, environmental effects, melting point, premelting.

1. Introduction

The International Practical Temperature Scale of 1948 (IPTS) [1][1] represents an experimental approach to the ideal thermodynamic temperature scale. Six points define the practical scale between the lowest assigned value, the oxygen point (−182.97 °C) and the highest, the gold point (1063 °C)[2]. Above the gold point, temperatures are based entirely upon the Planck relationship:

$$\frac{J_t}{J_{Au}} = \frac{\exp\left[\frac{C_2}{\lambda(t_{Au}+T_0)}\right]-1}{\exp\left[\frac{C_2}{\lambda(t+T_0)}\right]-1}$$

where,

J_{Au} and J_t = radiant energies per unit wavelength emitted by unit area of a blackbody at temperature t and the gold point t_{Au} (1063 °C)
λ = wavelength
C_2 = second radiation constant (1.438 cm deg)
T_0 = 273.15 deg.

The utilization of the Planck expression to realize the scale above the gold point presents an ideal situation on one hand and a dilemma on the other. Once the gold point and the second radiation constant are defined and the wavelength established, no other material property need be considered. In practice, however, an estimate must be made on how well a temperature measuring system reproduces the IPTS. Generally, this estimate is obtained through calibration against well-defined transformations similar to the fixed points listed for the low and moderate temperature portions of IPTS. The need for additional references is partly met by IPTS which recommends certain secondary points useful for calibration purposes. Table 1 lists the available secondary reference points for temperatures above 1063 °C. Unfortunately, the materials included in the table are few in number and generally not well-suited to a wide variety of applications. All are metals and susceptible to varying degrees of oxidation. Each is specified as applicable to equilibrium conditions under a pressure of one standard atmosphere even though the original data may have been obtained in different environmental situations. The melting points of nickel [2] and rhodium [3] for instance, were determined in a vacuum of 0.01 to 0.001 mm Hg while both platinum [4] and iridium [5] were investigated in air. Small variations in pressure generally have inconsequential effect upon a melting point. The chemical nature of the pressure medium, however, cannot be overlooked. Reaction between the environmental gas and the metal standard and container materials could alter the determined melting point significantly.

The lack of recognized high temperature reference materials necessarily has forced the use of pseudo-

[1] Figures in brackets indicate the literature references at the end of this paper.
[2] It is anticipated that the numerical value of some of these fixed points and defining constants will be changed in the near future.

TABLE 1. *Secondary reference points of the International Practical Temperature Scale* [1]

Material	Temperature [a]
	°C, IPTS
Copper	[b] 1083
Nickel	1453
Cobalt	1492
Palladium	1552
Platinum	1769
Rhodium	1960
Iridium	2443
Tungsten	3380

[a] The temperature indicates the melting point at one standard atmosphere.
[b] A reducing atmosphere is required.

standards which often are of nebulous or unknown quality. The metal oxides and their compounds have been utilized extensively for this purpose. At one time or another materials including Al_2O_3, Cr_2O_3, MgO, NiO, $CaMgSi_2O_6$ (diopside), 15 percent CaO:85 percent SiO_2 and $CaSiO_3$ [6] all have been employed although there is no common consensus as to their exact melting points. Such a myriad of oxide melting point values have been perpetuated through the literature that present day knowledge regarding these pseudostandards is in a state of utter confusion.

In order to help clarify the situation, the National Bureau of Standards has undertaken a program to completely characterize and elucidate more fully the melting behavior of the metal oxides. The initial effort, since published [6], consisted of a complete literature survey of oxide melting points coupled with a critical analysis and general evaluation of individual investigations. The second part of the program involves the experimental determination of the melting points of a number of the more important oxides with sufficient accuracy and precision to justify their use as reliable reference points.

Numerous metal oxides warrant consideration as reference materials, and foremost among these α Al_2O_3 (corundum) appears to be one of the more promising substances. In fact, its melting point was included as one of the secondary reference points on practical temperature scales used by many [7] prior to the adoption of the International Temperature Scale of 1927. Even today, Al_2O_3 still is employed widely for calibration purposes, and for this reason, it was selected for the first detailed study. The present work reports results obtained in an investigation of the melting characteristics of Al_2O_3 in environments of either vacuum,[3] argon, helium, or air utilizing tungsten or iridium containers. In this study emphasis was placed on two major problem areas of equal importance. First, every effort was made to insure precise temperature measurements of the highest obtainable accuracy compatible with the actual melting point determination. It is one thing to measure temperatures per se and quite another to determine the temperature at which a transformation occurs. The second area receiving detailed attention was the material aspect of the problem. Strictly speaking the melting point of any material will remain constant for a given confining pressure. However, if the oxide changes in any manner, whether it be by partial dissociation, chemical reaction, or others, its melting point must change. Knowledge of these changes must be obtained before any credibility can be placed in the determined melting point.

[3] Preliminary results on the melting point of Al_2O_3 in vacuum have been published [8]. Since that time, the work has been expanded in scope and for completeness of data and unity of thought, portions of the earlier study are included here.

2. Previous Investigations

Since 1911 there have been at least 24 separate determinations of the melting point of Al_2O_3. Some are of only historical interest, others merit consideration as worthwhile. Table 2 summarizes the important details of each study. With few exceptions each investigation employed optical pyrometry to measure temperatures. Curiously enough, none made any serious attempt to study the effect of environmental conditions.

The melting point preferred by many today is that determined by Kanolt in 1914 [9]. The original value, 2050 °C, is employed time and time again as a reference point even though changes in temperature scales require an adjustment in the original to about 2072 °C (IPTS) [10]. In light of some of the more recent work it would appear that the suggested correction is somewhat too high and there is no longer any justification in giving reference to Kanolt because of the inherent uncertainties in the adjusted temperature.

3. Apparatus

3.1. Induction Equipment

a. Vacuum Furnace

Figure 1 illustrates the essential components of the vacuum induction furnace and associated equipment. The furnace is capable of attaining about 3000 °C at reduced pressures. Power for induction heating was supplied to the furnace by a 20 kW, 450 kHz radio frequency electronic tube generator used in conjunction with a saturable reactor, magnetic amplifier and an adjustable current controlling device. The power control mechanism provided for both manual and automatic operation. In the manual mode, two ten-turn high precision potentiometers allowed current adjustment in small enough increments to produce temperature changes of less then 2 °C. A filter network of 0.1 μF capacitors were used to prevent extraneous emf from interfering with the control circuit or temperature measurement.

The primary load coil, attached to the rf generator by flexible water-cooled leads, was mounted external to the system around a Pyrex glass bell jar. The induction field from the load coil was concentrated in the region of the susceptor by means of a hollow water-cooled copper load coil concentrator. The concentrator was doughnut-shaped, having a vertical bore diameter of 0.875 in, an outer diameter of 2.8 in, a length of 3.0 in and a 0.01 in wide longitudinal slot.

The bell jar, approximately 7.5 in high and 3.75 in maximum diameter enclosed the concentrator and

TABLE 2. *Compilation of the melting points of* Al_2O_3[a]

Date	Investigator	Purity	Furnace type	Temperature measurement	Method	Environment	Original temp.[b] scale	Melting points[c]	
								Original °C	Int. 1948 °C
1911	Ruff & Goecke [33]	Not stated	Resistance, graphite element	Optical pyrometer	Observation of specimen during heating	Nitrogen	(C_2 = 1.48 cm deg) Au point = 1071 °C	2020	2044
1913	Ruff [34]	Pure	Resistance, graphite element	Optical pyrometer	Observation of specimen during heating	Not stated	C_2 = 1.46 cm deg Pt point = 1755 °C	2010	2035
1914	Kanolt [9]	Fe – 0.001% SiO_2 – 0.001% Chloride – 0.005% Sulfate – 0.001%	Resistance, graphite element	Optical pyrometer	Thermal analysis, heating curves	(A) Vacuum at 2 mm Hg (B) Hydrogen	Not stated[d]	2050	2072
1914	Tiede & Birnbrauer [35]	Not stated	Arc	Optical pyrometer	Observation of specimen during heating	Vacuum	Not stated	1890	.....
1916	Ruff & Lauschke [36]	Pure	Resistance, graphite element	Optical pyrometer	Observation of specimen during heating	(A) Air at 7.5 mm Hg	C_2 = 1.437 cm deg Au point = 1062.4 °C	(A) 2005	2005
						(B) Air at 7.7 mm Hg		(B) 2008	2008
1928	v. Wartenberg et al. [43]	Pure	Flame, oil-oxygen	Optical pyrometer	Observation of specimen during heating	Air	Int. 1927	2055	2049
1931	Bunting [38]	99.95%	Induction, Ir alloy susceptor	Optical pyrometer	Examination of specimen after heating	(Air)	Int. 1927	2045	2038
1931	Weigel & Kaysser [39]	Not stated Two samples A and B	Resistance, graphite element	Optical pyrometer	Observation of specimen during heating	(A1) One atm. nitrogen (A2) Air (B1) Reducing (B2) Air	C_2 = 1.44 cm deg Au point = 1063 °C	(A1) 2007 (A2) 2010 (B1) 2001 (B2) 2005–2010	2009 2012 2003 2007–2012
1943	Geller & Bunting [40]	99.98%	Resistance	Optical pyrometer	Observation of specimen during heating	Air	Int. 1927	2035	2029
1945	Geller & Yavorsky [41]	Three samples: (A) 0.05% soda (B) 0.01% impurities (C) < .07% impurities	Resistance, ThO_2-CeO_2 elements	Optical pyrometer	Observation of specimen during heating	(Air)	Int. 1927	2000–2030	1994–2024
1952	Lambertson & Gunzel [42]	99.9%	Resistance, W element	Optical pyrometer	Examination of specimen after heating	Helium	(Int. 1948)	2034	2034
1956	Lang et al. [43]	99.9%	Resistance, graphite element	Optical pyrometer	Observation of specimen during heating	Argon	Int. 1948	2049	2049
1959	Aldred & White [44]	High purity	Arc-image	Radiation pyrometer	Thermal analysis, heating curves	(Air)	(Int. 1948)	2060	2060
1959	Mark [45]	Not stated	Resistance, graphite element	Optical pyrometer	Observation of specimen during heating	Neutral	(Int. 1948)	2020	2020
1960	Diamond & Schneider [46]	99.9%	Solar	Optical pyrometer	Observation of specimen during cooling	Air	Int. 1948	2025	2025
1961	McNally et al. [47]	Not stated	Induction, graphite susceptor	Optical pyrometer	Observation of specimen during heating	Air, argon, nitrogen	Int. 1948	2043	2043
1963	Chekhovskoi & Petrov [48]	0.1–0.2% impurities	Resistance, W element	Optical pyrometer	Thermal analysis, heating and cooling curves	Argon	Int. 1948	2044	2044
1964	Gutt [49]	Not stated	Hot wire, Ir–Ir alloy element	100Ir–60Ir:40Rh thermocouple	Not stated	Argon	(Int. 1927)	2070	2063
1964	Riley [50]	Not stated	Resistance, graphite element	Optical pyrometer	Observation of specimen during heating	Argon	Int. 1948	(A) 2045 (B) 2050 (C) 2050	2045 2050 2050
1965	Foex [51]	99.97%	Solar	Optical pyrometer	Thermal analysis, cooling curves	Air	Int. 1948	2042	2042
1965	Gitlesen & Motzfeldt [29]	> 99.7%	Resistance, graphite element	Optical pyrometer	Thermal analysis, heating curves. Also, by observation of molten specimen from orifice	Argon at 400 torr	Int. 1948	2041	2041
1966	Kantor et al., [52]	99.99%	Resistance, graphite element	Optical pyrometer	Thermal analysis, heating and cooling curves	Vacuum[e]	Int. 1948	2049.7	2049.7
1966	Sata [53]	Pure	Resistance, graphite element	100W–74W:26Re thermocouple	Thermal analysis	Argon at 30 mm Hg	Int. 1948	2037	2037
1966	Urbain & Rouannet [54]	Two samples: A) < .3% impurities B) < .02% impurities	Resistance, graphite element	Optical pyrometer	Thermal analysis	Argon	Int. 1948	2047	2047

[a] All phases, numbers, etc. enclosed in parentheses indicate that these items are not directly expressed in quoted reference. Based on information contained in the report the enclosed terms are assumed valid.

[b] Int 1927 = The International Temperature Scale [55]: Int 1948 = The International Practical Temperature Scale of 1948 [1]: C_2 = Second radiation constant.

[c] Method of conversion of original values to IPTS of 1948 given by Schneider [6].

[d] Kanolt did not employ a defined scale. A complete discussion of his work is reported by Schneider [10].

[e] Chemical Abstracts [56] erroneously reports the environment as argon.

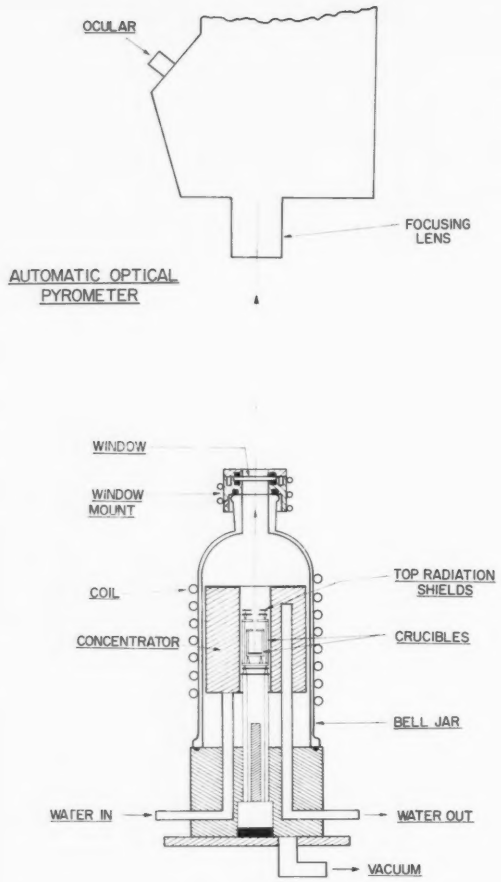

FIGURE 1. *Schematic drawing of vacuum induction furnace and related apparatus.*

susceptor. The base of the bell jar was located on a brass flange which in turn rested on a brass base plate connected to the vacuum system. A clear 1.125 in diam, 0.125 in thick fused silica window mounted in a water cooled brass holder attached to the top of the bell jar, provided a means to view the interior of the furnace.

High temperature O-rings were employed as vacuum seals between the base plate, flange, bell jar, window mount and window. The vacuum system consisted of a mechanical pump, a 4-in oil diffusion pump and a liquid nitrogen cold trap located between the pumps and the furnace. Pressures were monitored with thermocouple and ion gauges. After degassing, the ultimate obtainable pressure was 1×10^{-6} torr. However, at 2000 °C the normal operating pressure of the system was nominally 6.5×10^{-5} torr.

b. Atmosphere Furnace

Figure 2 indicates the primary features of the equipment used for all work requiring a helium or argon environment. The atmosphere furnace is suitable for use at temperatures up to 2600 °C at positive pressures of 0 to 50 in H_2O. The environmental setup utilized the same rf generator and control system described for the vacuum furnace. In addition, it was found necessary to incorporate a 12:1 load coil transformer between the generator and the coil. This in essence reduced the potential and increased the amperage of the load coil a sufficient amount to permit heating without apparent ionization of either argon or helium.

The load coil and susceptor were mounted inside a 11 in high, 7 in maximum diameter Pyrex glass bell jar. A plastic retaining collar clamped the bell jar in place and provided a gas tight seal between the aluminum base plate, O-ring and bell jar. The base plate in turn was connected through a valve arrangement to both a mechanical pump and to a gas vent glycerol bubbler. Cold traps were located intermediate between the furnace and the bubbler as well as between the pump and the remainder of the system.

A 1.125 in diam, 0.125 in thick fused silica viewing window mounted in a water-cooled brass holder was attached to the top of the bell jar. Environmental gas was admitted to the system through a 0.125 in diam port located directly below the window. The position of the entrance port aided greatly in preventing severe deposits of condensed vapors from accumulating on the window.

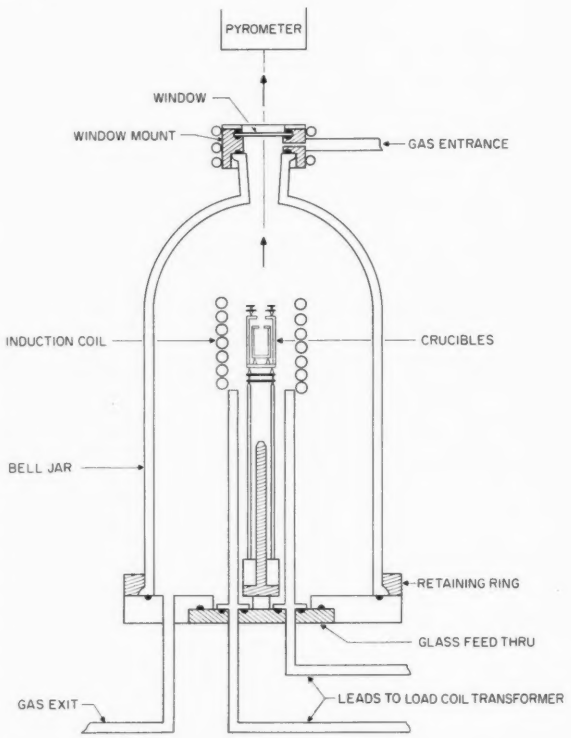

FIGURE 2. *Schematic drawing of atmosphere furnace and related apparatus.*

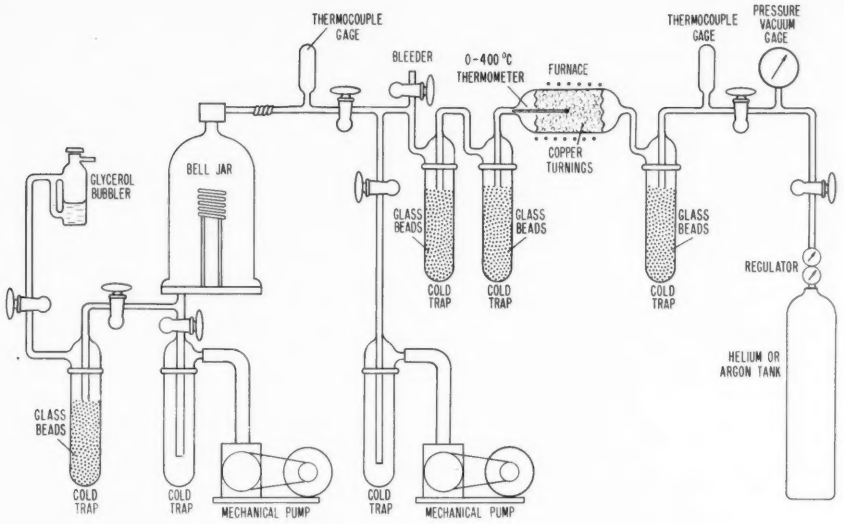

FIGURE 3. *Schematic drawing of gas purification train.*

Figure 3 shows a schematic diagram of the gas purification train. With the exception of nitrogen, the train regularly can deliver gas to the system having impurity levels less than 10 ppm for helium and 72 ppm for argon.[4] Gas from the bottled tank passed first through a cold trap, then over hot copper turnings (395 to 400 °C) and finally through two more cold traps. All three cold traps were filled with glass beads to disperse the flowing gas and promote more efficient trapping of impurities. Liquid nitrogen and an alcohol-dry ice mixture were used as the trap coolants for helium and argon, respectively.

All tubing and connections between the various components of the train were either glass or metal. High diffusion rates through natural or synthetic rubber, plastic or even nylon tubing caused the impurity content of the environmental gas to raise to a sufficiently high level to produce oxidation of the tungsten components of the furnace.

A mechanical pump was used to evacuate the train to facilitate the gas flushing process. Flexible heating tapes aided in degassing the system prior to admitting the environmental gas. Once put into operation the train was never opened to the air. Reduced pressures were determined with thermocouple gauges. A vacuum-pressure (50–0–50 in H_2O) brass bellows gauge monitored positive pressures.

All heatings in an air environment were performed in basically the same furnace outlined for the helium and argon studies. However, a confining bell jar and gas train were not employed to control the environment. The system was left free to achieve the atmospheric conditions prevalent in the surroundings. To inhibit oxidation during the early stages of the heat treatment, facilities were available to engulf the susceptor in a stream of helium. The helium flowed through an orifice located in the crucible mount directly below the susceptor. A blower aided in removing vapors from the optical path of the pyrometer. The forced air was directed across the top of the induction coil but did not impringe on any part of the furnace. The stream of air caused no noticeable detrimental effect.

[4] No attempt was made to remove nitrogen from either the helium or argon. The only impurities detected by mass spectrometric analysis were oxygen and nitrogen as air. The analyses were performed by the Analytical Chemistry Division, National Bureau of Standards.

c. Susceptor-Blackbody

Figures 4 and 5 illustrate the significant elements of the susceptor-blackbody assembly which was used in conjunction with each of the described furnaces. Table 3 lists the nominal dimensions of each of crucibles. With the exception of the brass support mount, all parts were machined from solid rods of either pure iridium or tungsten. The all-tungsten assembly was employed for heatings in vacuum, argon, and helium. The iridium susceptor-blackbody was utilized for environments of vacuum, helium, and exclusively for air applications.

The outer crucible served as the susceptor and was heated inductively. The inner crucible in turn was

TABLE 3. *Nominal dimensions of crucible assembly*

	Outer crucible "susceptor"	Inner crucible "blackbody"
	in	*in*
Outer diameter	0.75	0.50
Length	1.25	.75
Wall thickness	0.06	.06
Cover thickness	.06	.06
Cover diameter	.75	.50
Orifice diameter	.13	.03

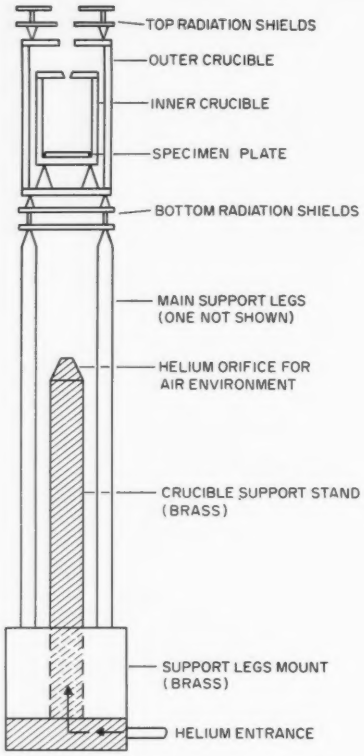

FIGURE 4. *Schematic drawing of susceptor-blackbody and related parts.*

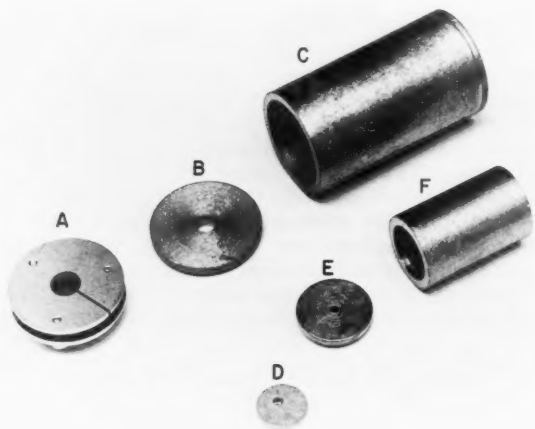

FIGURE 5. *Photograph of susceptor-blackbody disassembled.*
A = top radiation shields
B = outer crucible cover
C = outer crucible and base
D = inner crucible
E = inner crucible cover
F = specimen plate containing melted Al_2O_3 sample
G = bottom radiation shields not shown.

heated primarily by radiant energy emitted from the susceptor. In gaseous environments, energy transmitted by convection also influenced to a limited extent, the heating characteristics of the crucibles. The inner crucible performed a dual function, acting as both the specimen container and blackbody for temperature measurement. Each of the crucibles was supported on minimum contact pointed tungsten or iridium rods. This arrangement promoted temperature uniformity by minimizing heat flow to cooler areas. End losses were further reduced by radiation shields located at each end of the outer crucible. Each shield contained a 0.02 in wide slot to inhibit appreciable heating by induction. Successively larger holes in the outer crucible cover and top radiation shields permitted radiation emitted from the orifice in the inner crucible to pass through the glass window to the pyrometer. To insure diffuse reflections, all surfaces of the inner crucible and the internal surface of the outer crucible were grit blasted with Al_2O_3 powder. A removable specimen plate, 0.31 in diam, 0.04 in thick was located at the bottom of the inner crucible. A 0.03 in diam, 0.02 in deep depression in the plate, 0.05 in off center, provided a cavity for placement of the specimen.

3.2. Temperature Measurement

An automatic photoelectric pyrometer was used to monitor temperatures continuously during the course of each experiment. The photoelectric pyrometer is not a new innovation in temperature measurement, but only recently has it come of age as a precision piece of equipment. Since descriptions of this type of device are given elsewhere [11, 12], only pertinent details will be outlined here. Basically, the automatic pyrometer operates on the same general principle as the well-known visual optical pyrometer with a phototube performing the same function as the eye. The phototube detector, through a chopper arrangement, alternatively views images of the target and an internal calibrated standard lamp, each 90 times per second. A transitorized balancing mechanism automatically adjusts the emf to the lamp until the lamp brightness is equal to that of the target. The current drawn by the lamp can be then related directly to the brightness of the target. Once the current-temperature relationships of the internal lamp are established, the temperature of a blackbody target can be determined.

The photoelectric pyrometer, like the visual equipment, is a spectral instrument. A standard interference filter limits the band pass to a wavelength of 0.650 micrometers with a width at half height of about 0.020 micrometers. The pyrometer can respond in less than 1 sec to temperature changes of 0.2 °C at 1063 °C (gold point) and about 1 °C at 2000 °C. Target sizes can be as small as 0.030 in diam requiring an entrance angle of 0.006 steradians. Internally mounted absorbing screens are used to reduce the amount of radiation reaching the photomultiplier tube and provide four separate ranges of operation: 800 to 1200 °C (low), 1050 to 1700 °C (medium), 1350 to 2800 °C (high), and 2000 to 6100 °C (extra high).

The pyrometer was calibrated[5] on two separate occasions, at the beginning of the experimentation and after 300 hr of operation. Using a tungsten strip lamp as the temperature source and assuming a mean effective wavelength of 0.653 micrometers, the calibration related blackbody temperatures to corresponding currents of the internal pyrometer lamp. Table 4 gives selected low range values for each of the two calibrations. The data generally fit the equation:

$$T = a + bI + cI^2 + dI^3 + eI^4$$

where,

T = blackbody temperature, °C IPTS
I = pyrometer lamp current, milliamperes.

Overall there is a favorable comparison between the two sets of values, thus illustrating the stability of the pyrometer after extended use. Further tests indicated that moderate changes in ambient temperatures do not affect the calibrations.

Maximum uncertainties in the calibration are estimated to decrease from about ±3 °C at 800 °C to ±1.5 °C at 1063 °C, and then increase to about ±2 °C at 1225 °C for the low range. For the medium range, the uncertainties increase from ±2 °C at 1100 °C to ±3.5 °C at 1750 °C, and for the high range, increase from ±4 °C at 1500 °C to about ±4.5 °C at 2000 °C and to about ±6.5 °C at 2800 °C.

TABLE 4. *Automatic pyrometer calibrations (low range)*

Pyrometer lamp current	Blackbody temperature	
	Original	After 300 hours
Milliamperes	*°C, IPTS*	*°C, IPTS*
32.00	876	877
35.00	930	931
38.00	980	980
41.00	1027	1027
44.00	1072	1072
47.00	1115	1115
50.00	1156	1157
53.00	1197	1198
56.00	1237	1237

In the present work the pyrometer was mounted directly above the furnace, thereby eliminating the need for a prism and its additional source of error. The pyrometer was encased in an aluminum jacket which in turn was attached to a milling head-piston assembly. This arrangement allowed for vernier adjustment in the x, y, and z directions as well as providing for rotational movement. In all cases the pyrometer was alined normal to the top surface of the inner crucible. The aluminum jacket served as an electrical shield against rf pickup and in addition, protected the pyrometer somewhat against changes in ambient temperature.

[5] The calibration was performed by the Radiation Thermometry Section, Heat Division, National Bureau of Standards.

Both the power input and emf output of the pyrometer were filtered and shielded against electrical interference. The lamp current was measured by a high speed precision milliampere recorder-indicator. Frequent calibrations proved the reliability of the recorder.

3.3. Window Calibration

The absorption characteristics of the fused silica viewing window were determined routinely throughout the course of the investigation. To accomplish this, the automatic pyrometer was rigidly fastened to one end of a lathe bed which served as an optical bench. A type 30A/6V tungsten ribbon lamp, the temperature source, was mounted on the opposite end of the bench with a moveable window holder intermediate between the lamp and the pyrometer. The lamp carriage allowed for adjustments in the lamp position in the x, y, and z directions as well as providing for angular and rotational movement. The tungsten ribbon and the window were aligned normal to the optic axis of the pyrometer.

Power for lamp operation was furnished by a regulated solid state d-c power supply having a capacity of 0 to 18 V and 0 to 50 A. The power supply system was capable of maintaining a constant lamp current to within 0.02 percent, which is equivalent to less than 0.5 °C for a ribbon temperature of 2000 °C. Currents drawn by the lamp were determined by measuring with a precision potentiometer, the potential drop across a 0.001 Ω calibrated resistor in series with the lamp. Frequent spot checks on the accuracy and precision of the pyrometer were made possible through the use of a calibrated ribbon lamp. The lamp calibration[5] related the current drawn by the lamp to its brightness temperature at a wavelength of 0.653 micrometer.

4. Test Methods

4.1. Melting Point Determinations

Although numerous methods have been devised for determining the melting point of a material, none appeared completely suitable for establishing the Al_2O_3 point. The traditional method, thermal analysis, depends upon energy changes which occur during heating or cooling and is reliable only for materials having a relatively high thermal conductivity. Other procedures require an accurate knowledge of difficult to obtain properties, such as emissivity, to establish the melting temperatures.

Perhaps the greatest difficulty inherent with any method is the measurement of temperature. The method finally adopted in the present investigation concentrated on this facet of the problem, the attainment of accurate temperatures. To accomplish this a blackbody enclosure was built as an integral part of the system. Secondly, a specimen of sufficiently small

volume was utilized so as not to introduce unwanted thermal gradients and negate the attainment of blackbody conditions. In essence, the method simply consisted of the heating and cooling of a blackbody enclosure containing a specimen small enough not to disturb the blackness of the cavity. At all times during the heating or cooling cycle the specimen was invisible to the eye. A visible specimen would require a departure from blackbody conditions and thus defeat the purpose of enclosure. After each heating, it was necessary to classify the cooled specimen as either melted or not melted according to specified criteria. After a series of heatings the melting point could be established as that temperature midway between the maximum temperature at which no melting occurred and the minimum temperature where fusion was complete.

Quite obviously, the success of the method depends upon the ability to determine positively the degree of melting the specimen had undergone. Physical appearance of the specimen is a useful guide. A sample which had lost its original shape and flowed to surrounding regions can, of course, be considered completely melted. Unfortunately, the appearance can be deceptive at times due to plastic flow, creep and sintering which occur in the solid state. These difficulties were minimized to negligible problems by utilizing single crystals as test specimens. A single crystal will retain its identity, that is, remain single, unless melted. Upon melting, the liquid will solidify as a polycrystalline mass which is easily detected by microscopic techniques.

To insure the maximum degree of correlation between experiments performed in different environments, the same general procedure was followed for each individual test. A cylindrical-shaped single crystal (or polycrystalline specimen), about 0.03 in diam, 0.03 in long, was placed in the depression of the specimen plate located at the bottom of the inner crucible (blackbody). After assembly of the remainder of the susceptor-blackbody, the bell jar was positioned in place and the entire system evacuated by means of the mechanical pump. Using an auxiliary spotlight the pyrometer was alined and focused on the hole in the cover of the inner crucible.

Depending upon the required environment, either the system was evacuated further to about 2×10^{-5} torr with the diffusion pump (fig. 1) or in cases of the atmosphere furnace (figs. 2 and 3), ourgassed by heating to 1000 °C at mechanical pump pressures. For argon or helium applications, after the preliminary heating in vacuum, the system was then filled with purified gas to a pressure of about 30 in H_2O (gauge). The system was again evacuated and refilled with the entire flushing procedure being repeated a total of four times. After the final filling, the system was vented to the air through the bubbler. Gas flow was maintained at about 0.5 ml per minute at a positive pressure of about 2 in H_2O. For heatings in air, the system was, of course, left open to the surrounding environment. To inhibit oxidation, a gentle flow of helium from the orifice below the susceptor did, however, engulf the crucible during the first 1200 deg. At this temperature the helium flow was terminated and the remainder of the heating cycle conducted in air. During the cooling cycle, the helium flow was reactivated.

The heating rates were the same regardless of the environment. After the preliminary processing was completed, the power to the generator was increased in a stepwise manner at about 10 °C per minute until the temperature was about 10 to 15 deg below the desired temperature. The pyrometer was then realined by traversing across the sight area until the output of the pyrometer indicated a maximum. This position was found to coincide with the center of the hole in the inner crucible. The traversing procedure was necessary inasmuch as the inner hole was almost invisible to the eye due to the near blackbody conditions which prevailed in the area surrounding the smaller crucible. After realinement, the temperature was increased slowly at about 0.75 °C per minute until the desired temperature was attained. This temperature, T_m, was maintained about 30 to 60 secs before all power was shut off. Upon cooling, the entire assembly was dismantled and the specimen examined for evidence of melting. Routine examination included detailed analyses with both a binocular and polarizing microscope and, when applicable, x-ray diffraction.

In order to determine accurately the temperature attained in the vacuum, argon, or helium experiments, it was absolutely necessary to establish the absorption characteristics of the viewing window and deposited vapors. Window calibration was carried out by first positioning the window between the pyrometer and ribbon lamp in a manner as to similate test conditions in the induction furnace. The pyrometer was sighted through the window and focused on the midportion of the ribbon located adjacent to the filament notch. The lamp, representing the blackbody enclosure, was raised in temperature until the pyrometer indicated an output approximating the maximum obtained in the melting point test. After proper stabilization, adjustments were made until the brightness temperature of the lamp was within 2 °C of the experimental run. With the temperature of the lamp held constant the window was removed from the optical path causing an increase in the output of the pyrometer. The absorption of radiation due to the window and deposited vapors could be accounted for through the calculation of the "A-value" obtained from the equation:

$$\frac{1}{T_t} - \frac{1}{T_a} = A$$

where,

T_t = temperature (°K) observed without the window in the optical path

T_a = temperature (°K) observed through the window.

Once A was determined, it could be applied to the melting point test by substituting T_m for T_a in the above equation. Solving for T_t a temperature is obtained which should be equivalent to the maximum temperature actually attained by the blackbody and specimen. This assumes, of course, that blackbody conditions prevailed during experimentation. It further assumes that no significant amount of vapors were deposited on the window during cooling and that no appreciable quantity of radiation was absorbed by vapors in the optical path of the pyrometer.

4.2. Arc-Image and Phase Equilibria Experiments

In order to determine what effect various environments have upon Al_2O_3, a number of experiments were performed using arc imaging techniques. The arc-image furnace has been described elsewhere [13] and therefore will not be outlined here. The procedure followed essentially consisted of purifying a polycrystalline rod of Al_2O_3 by melting for 1 hr in a vacuum of 5×10^{-6} torr. The temperature of the molten Al_2O_3 was estimated to be about 2150 °C. After the initial treatment, the specimen was remelted for 10 min at the same temperature in about 1 atm (770 to 780 mm Hg) of the desired gas. Environmental gas included: air, air plus water vapor, helium, helium plus water vapor, hydrogen, nitrogen, and oxygen. All specimens were then examined with the polarizing microscope using the immersion method (1.760 index liquid and 500X magnification).

In addition to the arc-image experiments, a limited study was conducted on the phase equilibrium relationships in the Al_2O_3-W and in the Al_2O_3-Ir systems in vacuum, helium, and where appropriate, air. The same equipment and general procedure previously described for the melting point determinations were employed in this auxiliary investigation. Heating schedules were modified slightly to allow for longer holding periods at the desired temperature. Evidence for melting was based solely upon the physical appearance of the cooled specimen. All specimens were examined by x-ray diffraction at room temperature using a high-angle recording Geiger-counter diffractometer and Ni-filtered Cu radiation.

5. Materials and Specimen Preparation

Four single crystals and one powdered sample of Al_2O_3 were used for all melting point determinations. Table 5 gives the general qualitative spectrochemical anslysis [6] of each material.

The single crystals, 0.03 in diam, 6 in long, were purchased from the same supplier in two different lots of 8 to 10 crystals each. The four single crystal samples were selected at random, three from one lot and one from the other. Specimens were prepared from individual rods by cutting them with a diamond saw into 0.03 in lengths. The cut specimens were washed in alcohol, boiled in HCl, washed in distilled water, and finally dried at 140 °C.

The powdered sample, as received, was in the form of a fine, apparently amorphous material. Upon heating, the amorphous powder readily converted to polycrystalline α-Al_2O_3. Specimens were prepared from the as received powder by pressing into 0.03 in diam, 0.03 in long, cylinders using a small pellet press. Distilled water was added to the Al_2O_3 to aid in the fabrication. Other than air-drying, the specimens received no additional treatment.

All specimens for the phase equilibria study were fabricated from 99.9 percent pure W or Ir powder and the same Al_2O_3 powder as used for the melting point tests. Compositions prepared for study were limited to: $90Al_2O_3$:10 metal, 66.7 Al_2O_3:33.3 metal and $50Al_2O_3$:50 metal (mole percent). Appropriate amounts of Al_2O_3 and either W or Ir were first mechanically mixed, then pressed into 0.03 or 0.06 in diam pellets and finally air dried.

[6] Analyses were performed by the Analytical Chemistry Division, National Bureau of Standards.

TABLE 5. *General qualitative spectrochemical analyses of various* Al_2O_3 samples [a]

Impurity element	Al_2O_3 #1a single crystal as received	Al_2O_3 #1a single crystal 2047 °C in vacuum (not melted)	Al_2O_3 #1a [b] single crystal 2054 °C in vacuum (melted)	Al_2O_3 #1b single crystal as received	Al_2O_3 #1c single crystal as received	Al_2O_3 #2a single crystal as received	Al_2O_3 #3a polycrystalline as received	Al_2O_3 rod arc image sample melted in vacuum
Ag	T	FT	FT	T	T	T	−?	—
B	—	—	—	T	T	T	FT	—
CA	FT	VW	VW	VW	VW	T	FT	T
Cr	FT	VW	VW	VW	VW	W	—	—
Cu	FT	T	T	T	T	T	T	FT
Fe	VW	VW	W	T	T	VW	−?	VW
Mg	T	VW	VW	VW	VW	W	T	VW
Mn	FT	FT	FT	T	T	T	VW	—
Mo	—	−?	−?	—	—	—	—	—
Ni	—	—	T	—	—	—	—	—
Pb	—	—	VW	T	T	T	—	—
Si	VW	W	W	W	W	W	VW	VW
Sn	—	T	VW	VW	VW	—	—	—
Ti	—	VW	VW	VW	VW	VW	−?	VW
W	—		VS	—	—	—	—	—

[a] VS = > 10%
W = 0.01–0.1%
VW = 0.001–0.01%
T = 0.0001–0.001%
FT = < 0.0001%

— = not detected
? = questionable

[b] The melted specimen wet the tungsten setter and therefore could not be completely separated from tungsten impurities.

Specimens for the arc-image experiments were purchased in the form of sintered polycrystalline rods, about 0.25 in in diam. The rods were purified by vacuum melting as previously described. They received no other treatment prior to the actual test. Table 5 lists the spectrochemical analyses of a rod after purification.

6. Results and Discussion

6.1. Temperature Measurement

In spectral radiation pyrometry, as employed in this investigation, the measuring instrument determines a brightness temperature, not the true temperature of an incandescent body. Using Wien's law,[7] the relationship between these two temperatures is given by the equation:

$$\frac{1}{T}-\frac{1}{T_B}=\frac{\lambda_e}{C_2}\ln E_\lambda$$

where,

T = true temperature (°K)
T_B = brightness temperature (°K)
λ_e = effective wavelength
E_λ = spectral emissivity
C_2 = second radiation constant.

Quite obviously, for a given effective wavelength the difference between T and T_B may be rather large, depending upon the magnitude of the spectral emissivity. Unfortunately, emissivity is a very difficult property to determine experimentally and consequently is known for but a few materials. The practical approach to the problem is to incorporate a a blackbody in the measuring system. Since a blackbody, by definition, has an emissivity of unity, the observed and true temperatures necessarily would be equal.

Fundamental to the present investigation is the assumption that near blackbody conditions were attained by the inner crucible enclosure during experimentation. A perfect blackbody would represent an ideal situation, but this unfortunately cannot be achieved experimentally. Estimates must be made of the extent of the deviation from perfection. The quality of the blackbody can be determined from a knowledge of the geometrical design, and the reflectivity and natural emissivity of the materials of construction [14, 15]. Using the equations of Gouffé [14], the effective emittances of the blackbody containers were calculated from the dimensions listed in table 3 and from published emissivity values of iridium and tungsten [5, 16, 17, 18, 19]. For the tungsten blackbody, the effective emittances were 0.999 at room temperature and 0.998 at 2700 °C. The deviations in emittance from unity will cause an error of less than 1 °C at 2700 °C. At room temperature the effective emittance of the iridium blackbody was calculated as 0.998. Values at other temperatures could not be estimated because of the lack of reliable high temperature emissivity data for iridium.

The calculations are estimates and only valid if (1) the blackbody enclosure is uniformly heated, and if (2) the internal reflections are completely diffuse rather than specular. Any deviation from these two requirements would lower the effective emittance and cause significant errors in the temperature measurements. An attempt was made to insure diffuse reflections by grit blasting the surfaces of the crucibles prior to each test. The effectiveness of this procedure is unknown. However, the tungsten surfaces always remained roughed and dull after each heating. The iridium surfaces on the other hand, always, upon heating in vacuum or inert atmospheres changed from the dull appearance caused by the grit blasting to a bright shiny surface. These observations suggest that the effective emittance calculations might be more appropriate for the tungsten blackbody than for the iridium.

Temperature uniformity is perhaps even more difficult to verify. The radiation shielding obviously helped to promote uniform temperatures not only by limiting the escape of emitted radiation, but also by acting as susceptors of the induction field and thus producing independent sources of heat. Care was taken during the initial positioning of the crucibles in the induction coils to see that at least the outer crucible surfaces were uniformly heated. Using a manual pyrometer to measure the brightness temperature of the vertical outer surfaces, the position of the crucible was adjusted until no gradients were indicated. The relatively high thermal conductivity of tungsten and iridium were perhaps the greatest aid in assuring temperature uniformity. Even gross misalinement of the crucibles in the induction field did not produce significant gradients. Further tests for temperature uniformity were conducted by heating simultaneously a number of Al_2O_3 single crystal specimens located on various parts of the specimen plate. In every test, all specimens behaved in a similar manner, that is, the same degree of melting was indicated for each.

A definite indication of the relative quality of the blackbody and associated temperature uniformity was obtained in a manner pointed out by Kostkowski and Lee [20]. With reference to figure 4 it is evident that the upper portion of the outer crucible (susceptor) represents another blackbody having an effective emittance for tungsten calculated to be 0.960 at room temperature and 0.958 at 2700 °C. If both the upper blackbody and the inner enclosure are at the same temperature, the brightness temperature of each would be different by an amount related to their respective emittances with the inner blackbody always appearing the brighter. Calculated differences between corresponding brightness temperatures varied between 3 °C at 1000 °C and 10.5 °C at 2100 °C.

[7] Ideally, the Planck equation should be utilized since Wien's radiation formula is not strictly valid at extremely high temperatures. However, if $\lambda(t+273)$ is less than 0.3 cm deg the resulting error is less than 1 °C.

These apparent differences in brightness were measured at various temperatures by alternately sighting the pyrometer first on the hole in the inner crucible and then on its top surface. Data were obtained for three sets of conditions: (1) Tungsten crucibles in vacuum, (2) tungsten crucibles in helium, and (3) iridium crucibles in helium. The results of these experiments are given in figure 6. The solid line represents the differences calculated from the effective emittances for the tungsten blackbodies. The circles and triangles indicate measured differences. The correlation was excellent considering that it was assumed that the two blackbodies were always at the same temperature. Maximum deviation from the calculated differences for tungsten was 2 °C both in vacuum and helium environments. The data for the iridium blackbodies were included strictly for comparative purposes since calculated differences (solid line) apply only to the tungsten enclosures.

Although these tests yielded generally favorable results, it was thought advisable to obtain more direct verification of the quality of the blackbodies and the temperature measuring system. The melting points of Au (1063 °C), Pt (1769 °C), and Rh (1960 °C) were determined selectively in a manner similar to that previously described for the Al_2O_3 determinations. At least one, generally two, metal melting points were investigated for all possible combinations of environments and container materials. To prevent direct reaction with the tungsten or iridium containers, the test specimen was placed in a shallow cavity in a 0.125 in diam, 0.125 in long Al_2O_3 single crystal which in turn rested on the specimen plate. The specimen consisted of a small metal fragment cut from 99.9 percent pure metal ribbon. Complete fusion was indicated by the formation of a spherical-shaped ball from the original platelike specimen.

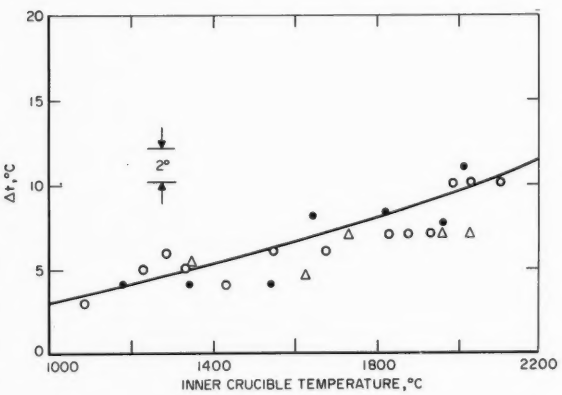

FIGURE 6. *Brightness Temperature Differences.*

Solid line = calculated differences in brightness temperatures for two tungsten blackbodies.
ΔT = temperature of inner crucible minus temperature of outer enclosure.
0 = measured differences for tungsten blackbodies in vacuum.
● = measured differences for tungsten blackbodies in helium.
Δ = measured differences for iridium blackbodies in helium.

Overall the standard metal study was of limited use in establishing the quality of the blackbodies. For the most part the results generally indicated the melting points of the metals as experimentally determined in this study agreed with the reported values to within the precision of the method, ±0.5 °C, ±1 °C, and ±1.5 °C for the Au, Pt, and Rh points, respectively.

The gold point tests proved to be the most reliable guide, checking out in every instance. At higher temperatures, depending upon the environment and container, the Pt and Rh determinations were not always conclusive. Notable discrepancies between reported and observed values occurred which in all probability can be attributed to causes other than the blackbody or temperature measuring system. Platinum for instance was found to melt in an inconsistent manner when heated in the tungsten crucible in vacuum. Platinum which had been previously melted invariably fused at temperatures lower than Pt receiving no prior treatment, perhaps indicating a possible reaction between the Al_2O_3 single crystal and the test specimen.

All attempts to determine the melting points of Pt and Rh utilizing the iridium crucible in air proved fruitless. In every test, both metals melted at temperatures considerably higher than expected. These metals were found to react with the Ir and/or Ir oxide vapor prevalent in the immediate surroundings to form Ir-Rh (or Ir-Pt) solid solutions which would have melting points higher than the Rh (or Pt). X-ray diffraction patterns of Pt or Rh strips heated for short times showed reflections identifiable with almost pure Ir. When the surfaces of strips were ground, the resulting x-ray pattern was indicative of a single solid solution phase having a composition containing considerable Ir.

Additional problems were encountered in checking the Rh point in argon or helium environments. The melting point of Rh as observed was approximately 5 °C lower than the reported value. The explanation for this phenomenon apparently is not as straightforward as a simple chemical reaction. X-ray patterns of Rh strips heated to just below melting showed no reflections whatsoever. Internal surfaces produced only broad ill-defined x-ray peaks of Rh. Upon heating, the crystalline starting material apparently became amorphous (to x-rays) as the result of helium or argon environments. An amorphous material, of course, can be expected to melt at a temperature lower than a crystalline material of the same composition. Similar experiments conducted on Pt indicated opposite results. The Pt remained crystalline throughout the heat treatment and was found to have a melting point in agreement with the accepted value.

Additional experiments are needed to elucidate more fully the basic principles behind each of the various discrepancies outlined. All would be complete investigations in their own right and therefore will not be pursued further at this time.

6.2. Phase Equilibria

Congruent melting indicates an equilibrium situation between a solid and liquid of the same chemical composition. Implicit is the requirement that both the solid and liquid represent the equilibrium phases defined only by the pressure-temperature relationships. Once the confining pressure is specified, the melting temperature is fixed and cannot change unless the equilibrium conditions are disrupted. Nevertheless, variations in the melting point are often observed experimentally. Pressure effects are normally small and generally can be disregarded for limited changes in pressure. The formation of metastable phases prior to melting may be a causative factor. The melting point of a nonequilibrium phase could not be expected to be equivalent to that of the stable modification. Major changes in the melting point of an oxide usually are associated with changes in composition induced through dissociation (or oxidation), or reaction with the container and environment.

Knowledge of the phase equilibrium relations of appropriate systems can give some insight as to the type of reaction or behavior which could be expected under specific conditions. In the present work a multicomponent system would be required for study if all the impurity elements in the Al_2O_3 specimens are considered. The impurities would cause a change in the melting point calculated to be less than a 1 °C depression for 0.2 mole percent contaminant. Neglecting these, however, the Al-W-O and Al-Ir-O ternary systems under appropriate environmental conditions would completely describe possible reactions. A complete study of each of these two systems would be difficult to accomplish experimentally: consequently, an investigation into only certain aspects must suffice.

Consider first the effect of dissociation of Al_2O_3 upon the melting point. In this situation the Al-O system becomes pertinent. Various compilations [21, 22] give only limited data on this system. Motzfeldt and Gitlesen [23] report preliminary data on the Al-Al_2O_3 system and indicate no reaction occurs between end members in the solid state. Hoch and Johnston [24] claim the existence of solid Al_2O and AlO, but their work cannot be verified. According to Motzfeldt and Gitlesen [23] the addition of Al to Al_2O_3 lowers the Al_2O_3 point a measurable amount. An eutectic was placed at about 7 mole percent Al. Figure 8a indicates the general configuration of the Al-Al_2O_3 system postulated from available information. In the figure A represents Al; and B, Al_2O_3. It is readily apparent from the diagram that gross dissociation of Al_2O_3 below melting would result in a two-phase assemblage, each probably detectable experimentally. Regardless of the total composition of the resultant mixture, melting occurs over a range of temperatures different from that of either end member. Although not indicated by the figure, oxygen deficient Al_2O_3 (Al_2O_3 solid solution) conceivably could exist. Here too, melting would occur over a range.

The arc-image experiments were conducted specifically to obtain information on the dissociation characteristics of Al_2O_3 under various environmental conditions. Microscopic examination of the various samples indicated quite definitely that some reduction of Al_2O_3 takes place upon heating in all the environments investigated. All samples contained vacuoles and occlusions of low indices (< 1.760). The vacuoles exhibited the shape of flowing droplets suggesting that they were originally composed of a second liquid phase consistent with the postulated Al-Al_2O_3 system. This liquid could have been formed by the melting of impurities but most probably was the result of dissociation. Quantitative estimates of extent of dissociation were difficult to obtain. It appears that melting in vacuum had the least deleterious effect. Environmental gases, however, affected the Al_2O_3 to a greater degree and as measured by the amount of occlusions, the extent of dissociation for a particular environment increased in the following order: (1) vacuum, (2) Ar, (3) N_2, (4) O_2, (5) He, (6) air, (7) He + water vapor, (8) air + water vapor, and (9) H_2. Surprisingly the presence of water vapor enhanced the detrimental effect. Normally water vapor would not be considered as a reducing agent. However, the effect could be accounted for if the water itself dissociated to hydrogen and oxygen with the hydrogen preferentially attacking the Al_2O_3. An alternative explanation would be a reaction between Al_2O_3 and H_2O in which AlOH gas is one of the prominent products.

Single crystal specimens heated in the iridium or tungsten crucibles during the melting point tests were also examined microscopically. Results comparable to the arc image tests were indicated with the vacuum treatments having the least effect and the air the greatest. No differences were detected between specimens heated in the same environment but using different container materials (W or Ir).

Originally it was believed that x-ray examination might have detected Al_2O_3 solid solution or perhaps the presence of the predicted second solid phase, Al. However, x-ray patterns of the specimens optically examined showed only reflections representing α-Al_2O_3. The unit cell dimensions, determined from back reflection measurements, were the same as those of the unheated starting materials. Apparently the dissociation process follows the equation generally postulated in vapor pressure studies [25]:

$$Al_2O_{3(s,\,l)} \rightarrow 2Al_{(g)} + 3O_{(g)}{}^{8}$$

Optical evidence supports this conclusion in that the vacuoles indicated vaporized regions. Even though dissociation is prevalent, the only condensed phase present during melting is stoichiometric Al_2O_3, solid or liquid. Consequently, the total composition probably would remain relatively constant and an experimentally determined melting point should be indicative of that of pure Al_2O_3 providing extraneous factors do not alter the equilibrium conditions.

[8] Other vapor species have been identified and include: AlO, Al_2O, Al_2O_2. The concentration of these are minor in comparison with the major phases.

Consideration should also be given to the effect of container materials upon the melting point of Al_2O_3. Any combination of materials, when in equilibrium, must undergo some type of reaction upon melting. The reaction will result in a change in the liquidus curve regardless of the extent of combination in the solid state. For dissimilar materials such as Al_2O_3 and W, and Al_2O_3 and Ir, one can expect large regions of liquid immiscibility and no compound formation. The phase equilibrium relations of the Al_2O_3-W and the Al_2O_3-Ir condensed systems probably can be represented by figure 7a with A indicating Al_2O_3 and B, the metallic constituent, W or Ir.

The validity of these predicted diagrams was tested by limited experimental studies of the Al_2O_3-W and Al_2O_3-Ir systems utilizing both helium and vacuum environments. In essence, the data indicated that as expected, solid state reaction between Al_2O_3 and the metals did not occur to any measurable degree. X-ray patterns of intimate mixtures heated to within 15 °C of melting showed the presence of only α-Al_2O_3 and W or Ir. The formation of intermediate compounds or solid solutions were not evident. Melting point experiments conducted on the mixtures indicated that the solidus temperatures were not significantly different from that of 100 percent Al_2O_3. Within the precision of the method the necessary change in liquidus temperatures could not be detected. Evidently the melting point of Al_2O_3 (T_A) and the solidus temperature (T_L) are approximately equal and the phase diagram illustrated by figure 7b is more indicative of actual relationships found in the Al_2O_3-W and Al_2O_3-Ir systems.

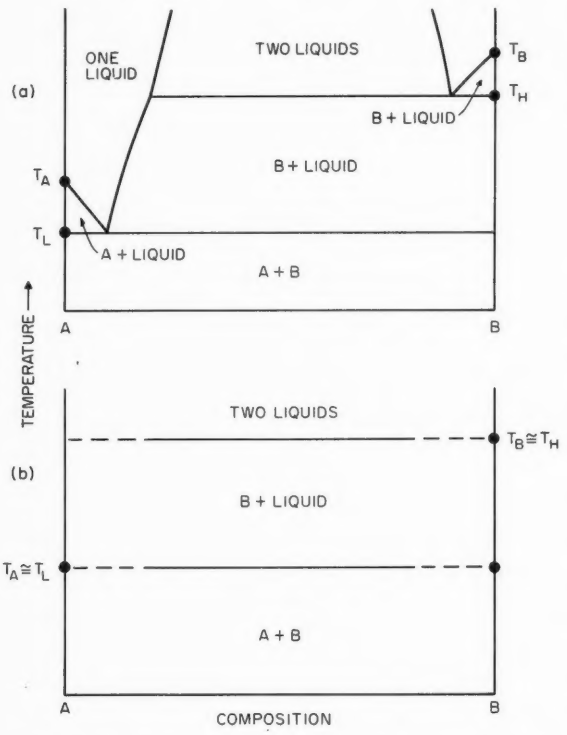

FIGURE 7. *Hypothetical phase diagrams for two dissimilar materials.*

A and *B* = condensed phases having different chemical compositions
T_A = melting point of phase A
T_B = melting point of phase B
T_L and T_H = solidus temperatures.

The melting point data for the Al_2O_3-W system presented here and in the preliminary report [8] are in apparent contradiction with the work of Grossman [26] who states that the solidus temperature (T_L) is 1997 ±20 °C. Grossman based his conclusions on cooling curve data of Al_2O_3 sealed in a tungsten container. Metallographic examination of the thermal analysis capsules indicated primary tungsten (< 1%) in the Al_2O_3 near the bottom of the containers. Although Grossman attributes the disagreement in results to the kinetics of the reaction, that is, nonequilibrium in the present work, it is postulated that his data pertains to systems other than the Al_2O_3-W binary, perhaps the Al-W system. From the previous discussion it is evident that Al_2O_3 itself dissociates to Al and oxygen. The vapor in a sealed system could then unite with the W to form one or more of a number of phases having a lower melting point. Further evidence for vapor-solid reactions is presented by Grossman who points out that the greatest dissolution of W occurs near the top of the capsule. In an open system as utilized in this investigation, a dynamic situation occurs in which any Al vapor is carried away. More data is needed before this question can be fully resolved. X-ray data on the included tungsten would be extremely useful.

The phase relationships would, of course, represent the extreme situation where chemical equilibrium has been attained between the container materials and Al_2O_3. This was not necessarily the case in the melting point experiments. Minimum contact between the Al_2O_3 specimen and the W or Ir setter plate considerably reduced the possibility of significant reaction. Spectrochemical analyses of Al_2O_3 specimens heated in vacuum, helium, or argon to temperatures just below the melting point supported the no reaction hypothesis. The analysis for Al_2O_3 heated in tungsten in vacuum, table 5, shows no assimilation of the metal by the oxide whatsoever, as would be required for reaction. Although not given in the table, similar analyses were obtained for samples heated in helium and argon utilizing both the tungsten and iridium crucibles. Analyses of specimens heated in air in iridium were not performed due to heavy deposits of IrO_2 which always coated the sample during cooling. Any analysis would always indicate the presence of Ir irregardless of the degree of interaction.

Thus far the discussion has been limited to the influence of chemical factors, dissociation and reaction, have upon the melting point of Al_2O_3. In recent years the phenomena commonly termed "premelting" has been related to observed variation in the melting temperature. Ubbelohde in his book "Melting and Crystal Structure" [27] gives an excellent description of "premelting." In essence, premelting refers,

not to the melting of impurity components, but to an anomaly occurring in the solid which causes lower melting temperatures. The extent of the anomaly determines the melting temperature with gross effects graphically illustrated by enhanced curvature in thermal curves near the melting arrest. These anomalies normally are associated with vibrational disorders or with defects of various types and result in the formation of lower melting quasi-crystalline materials distinctly different from their more crystalline counterparts. In addition to premelting, other properties including thermal expansion and heat capacity should show abnormal behavior indicative of a defect nature.

The rhodium melting point studies conducted in this investigation perhaps provide an excellent example of the premelting phenomenon. Here the Rh surface reverted to a noncrystalline state and in effect produced a lower melting material. The exact causes for the amorphous nature of the Rh are difficult to determine; however, they are apparently related to the high temperature gaseous environments of helium or argon. The mechanism whereby the gas destroys the crystallinity of the Rh is unknown. It may be that the bombardment of the metal by high velocity gas atoms or ions produced the quasi-crystalline material needed for premelting. Darken and Gurry [28], however, point out that the polarization power of gaseous environments, including the inert gases, may have a profound affect upon certain thermodynamic properties. In this context helium would be expected to have greater effect than argon. Vacuum treatment, of course, would be ineffectual.

Evidence for premelting of Al_2O_3 has been given by Gitlesen and Motzfeldt [29] who noted irregularities in heating curves 20 to 30 °C below the observed melting point. Kozlovskii and Shlyakova [30] suggest a partial destruction of the structure at high temperatures. Supporting heat capacity data is offered by Kantor et al., [31]. Barber and Tighe [32] showed that Al_2O_3 (sapphire) heated at 1900 °C in a mixture of argon and nitrogen produces surface effects different from that obtained by vacuum treatment. The gas treated surfaces were coated with porous material concluded to be Al_2O_3 but not necessarily the α form.

Under normal circumstances premelting originates at the surface and for large volumes, the bulk of the material remains predominantly unaffected. Depending upon the permeability of the solid Al_2O_3 the environmental gas could be expected to penetrate to certain depths and as the outer layer is premelted, permeate even further until eventually the entire sample is molten. It is apparent that the extent of premelting is governed by, among other factors, the surface area to bulk volume of the sample. Gitlesen and Motzfeldt [29] utilized a relatively large mass of Al_2O_3 in their experiments and had only minor indications of premelting. If the mass of the sample is considerably reduced as in the present work the premelting phenomenon is accentuated to such a degree that it is the predominate effect. Consequently, differences in the melting point should be observed for different environments, as is the case.

6.3. Melting Point of Al_2O_3

Table 6 gives the experimental results obtained in the determination of the melting points of five samples of Al_2O_3. Each entry represents a single experiment conducted on a different test specimen. The listed temperatures have been adjusted to account for the necessary window corrections. The observed melting point for each sample is given below the separate listings. Table 7 summarizes the data tabulated in table 6 and indicates the melting point of Al_2O_3 appropriate to the container and environment specified.

TABLE 6. *Experimental data on the melting point of various Al_2O_3 samples*

Specimen type [a]	Container material	Environment	Pressure [b]	Temperature IPTS °C	Observation
Al_2O_3 #1a Single crystal	Tungsten	Vacuum	5.9×10^{-5} (Torr)	2019	Not melted
			6.4×10^{-5}	2040	Not melted
			5.6×10^{-5}	2047	Not melted
			4.7×10^{-5}	2049	Not melted
			8.1×10^{-5}	2050	Not melted
			6.4×10^{-5}	2052	Melted
			5.6×10^{-5}	2053	Melted
			5.9×10^{-5}	2054	Melted
			5.6×10^{-5}	2054	Melted
			6.8×10^{-5}	2055	Melted
				Melting point 2051	
	Tungsten	Helium	Atm	2040	Not melted
			Atm	2042	Melted
				Melting point 2041	
	Tungsten	Argon	Atm	2030	Not melted
			Atm	2038	Not melted
			Atm	2044	Not melted
			Atm	2046	Melted
				Melting point 2045	
Al_2O_3 #1b Single crystal	Tungsten	Helium	Atm	2037	Not melted
			Atm	2042	Melted
			Atm	2047	Melted
				Melting point 2039.5	
	Tungsten	Argon	Atm	2030	Not melted
			Atm	2038	Not melted
			Atm	2044	Not melted
			Atm	2046	Melted
				Melting point 2045	
	Iridium	Air	Atm	2015	Partially melted
			Atm	2021	Partially melted
			Atm	2023	Partially melted
			Atm	2026	Partially melted
			Atm	2027	Partially melted
			Atm	2030	Partially melted
			Atm	2032	Partially melted
			Atm	2036	Partially melted
			Atm	2040	Completely melted
				Melting point 2038 (liquidus)	
Al_2O_3 #1c single crystal	Tungsten	Helium	Atm	2034	Not melted
			Atm	2038	Not melted
			Atm	2040	Not melted
			Atm	2041	Melted
			Atm	2045	Melted
			Atm	2047	Melted
			Atm	2056	Melted
				Melting point 2040.5	

TABLE 6. *Experimental data on the melting point of various* Al_2O_3 *samples* – Continued

Specimen type [a]	Container material	Environment	Pressure [b]	Temperature IPTS °C	Observation
Al_2O_3 #2a, single crystal	Tungsten	Vacuum	7.6×10^{-5} (Torr)	2050	Not melted
			7.5×10^{-5}	2052	Melted
				Melting point 2051	
	Iridium	Vacuum	2.4×10^{-5} (Torr)	2039	Not melted
			4.4×10^{-5}	2043	Not melted
			2.8×10^{-5}	2044	Not melted
			3.9×10^{-5}	2047	Melted
			2.5×10^{-5}	2049	Melted
			1.4×10^{-5}	2054	Melted
				Melting point 2045.5	
	Tungsten	Helium	Atm	2040	Not melted
			Atm	2042	Melted
				Melting point 2041	
	Iridium	Helium	Atm	2030	Not melted
			Atm	2034	Not melted
			Atm	2038	Melted
				Melting point 2036	
	Tungsten	Argon	Atm	2037	Not melted
			Atm	2044	Not melted
			Atm	2046	Melted
			Atm	2050	Melted
			Atm	2055	Melted
			Atm	2061	Melted
				Melting point 2045	
Al_2O_3 #3a Polycrystalline	Tungsten	Vacuum	8.4×10^{-5} (Torr)	2048	Not melted
			6.2×10^{-5}	2050	Not melted
			7.6×10^{-5}	2051	Melted
			6.5×10^{-5}	2054	Melted
				Melting point 2050.5	
	Iridium	Air	Atm	2025	Not melted
			Atm	2026	Partially melted
			Atm	2034	Partially melted
			Atm	2040	Completely melted
				Melting point 2037 (liquidus)	

[a] Numerals (1, 2 or 3) indicate separate lots purchased at different times. Letters (a, b or c) represent individual samples selected from lots #1, 2, or 3.
[b] The symbol atm roughly signifies atmospheric pressure.

TABLE 7. *Summary of* Al_2O_3 *melting points*

Environment	Tungsten container	Iridium container
	°C, *IPTS*	°C, *IPTS*
Vacuum	2051	2046
Argon	2045	.....
Helium	2041	2036
Air	.....	2038 (liquidus)

It is difficult to assign exact limits of precision and accuracy to the melting point values. Each melting point was obtained through the use of an integral system of equipment and procedures and involves the personal judgment of the investigator. An estimate of the precision obtained by an intercomparison of the results for all possible conditions would not be appropriate because influencing factors differ in extent. In fact, one prime purpose of the investigation was to detect differences in melting temperature for varying experimental conditions. Considering only one specific set of data pertaining to a given container and environment, the precision can be relegated to the ability to distinguish one temperature from another. This measure of the precision is estimated to be less than ± 1.5 °C at the melting point of Al_2O_3.

Considering the estimated precision it is apparent that real differences exist between the melting points listed in table 7. As expected from previous discussions, the melting points of Al_2O_3 determined in vacuum utilizing tungsten or iridium containers are the higher values. Gaseous atmospheres yield lower melting points. It is impossible to ascribe exact causes to the lower melting temperatures because more than one process may be operative. Presumably the premelting phenomenon has greater significance than either container reaction or dissociation.

An environment of air affected the Al_2O_3 samples in a manner unlike the other gases or vacuum. Specimens in air appeared to melt over a range of temperatures whereas the Al_2O_3 under the other conditions exhibit sharp congruent type melting. Characteristically a ring of brownish-colored polycrystalline material formed on the outer surfaces of the Al_2O_3 single crystals when heated in air at temperatures higher than about 2020 °C. Companion slumping and minor flow were also evident. As the temperature was increased, the ring appeared to move inward until no portion of the sample was identifiable as a single crystal. At still higher temperatures the sample became more translucent losing its brownish hue. Polycrystalline samples behave in a similar manner, forming the outer ring with partial slumping at first and eventually becoming clear of glasslike in appearance. Since incongruent melting was clearly indicated, tables 6 and 7 list the melting point as the liquidus temperature. The explanation for the different behavior in air as opposed to helium or argon environments is unclear. The presence of nitrogen or Ir oxide and Ir vapors may be contributing factors although there is no discernible evidence for this. Water vapor, of course, was shown to produce accelerated dissociation.

Melting points determined in the Ir crucible were lower than corresponding values obtained utilizing the tungsten containers. The 5 °C lower values conceivably could be caused by the difference in the degree of reaction between Al_2O_3 and W and between Al_2O_3 and Ir. The phase equilibria study on each of these systems essentially discounted this theory although reaction still could account for part of the reduction. An alternate explanation concerns the effective emittance of the Ir blackbody. A 5 °C lowering would require the emittance to be about 0.978 instead of the 0.998 calculated value. If the reflectivity were largely specular rather than diffuse, a change in the emittance of this order of magnitude would be expected. DeVoss [15] gives relationships showing the effect reflectivity has on the quality of various configurations of tungsten blackbodies. Detailed reflectivity data would be required to make similar calculations for iridium enclosure and this unfortunately is not available. However, an indication

that the reflectivity of iridium does change adversely upon heating is the fact that it fails to maintain a dull roughed surface.

Ideally the limits of accuracy of the experimental melting points should be established through a comparison with the absolute or true value, but this is an unknown quantity. Intercomparison with literature values would not be meaningful because of the diversity of samples, techniques, temperature scales and other factors. At present an estimate of the maximum uncertainties must be obtained from a consideration of the associated experimental errors. At present the melting point obtained in vacuum with the tungsten container, 2051 °C, is considered to be that least influenced by extraneous factors and thus is the value which it is thought approaches closest to the true melting temperature of α-Al_2O_3. It is doubtful that the various source of error (purity, pyrometer, blackbody, etc.) would be of the same sign. Even so, the overall maximum uncertainties of the 2051 °C melting point were estimated to be within ± 6 °C.

The same limits of accuracy, ± 6 °C, can be assigned to the other melting points determined in tungsten only if it is stipulated that they apply to Al_2O_3 changed in some manner due to the environment. If these melting points are compared with the true value, the limits of uncertainties must be increased.

A still wider range of possible errors must be placed on the melting points determined using the Ir containers because of doubts concerning the quality of the blackbody. For the value obtained in vacuum, 2046 °C, maximum experimental errors are estimated to be no more than ± 10 °C. Again, the limits of error associated with the helium and air melting points should be increased when comparing these values with the true melting point of α-Al_2O_3. Similar to the tungsten experiments, the ± 10 °C limits apply to an altered Al_2O_3.

7. Al_2O_3 as a Standard

Proposals to establish the melting point of Al_2O_3 as a secondary temperature standard should be viewed with caution. The study conducted here showed conclusively that gas atmospheres have pronounced effects upon the observed melting point. Only investigations utilizing a vacuum environment yield a value which can be thought of as approaching the absolute melting point. Even the container material can significantly modify the results. These conclusions, however, also apply to materials other than Al_2O_3 as amply illustrated by the variations found for the Rh melting points.

It is probable that no material can be utilized as a universal standard suitable for even a majority of possible conditions. The presently accepted metal secondary reference standards should be reviewed and evaluated, perhaps placing more stringent limiting conditions on their use. In this context Al_2O_3 conceivably could be used as a reference material provided the environmental conditions are specified. A cooperative Al_2O_3 melting point program among several laboratories is needed to establish the full potentialities of Al_2O_3. To this end the Commission on High Temperature and Refractories, International Union of Pure and Applied Chemistry is sponsoring such a program. Until the results of this joint effort are available it is recommended that investigators refrain from indiscriminate use of Al_2O_3 for references purposes and give consideration to environmental conditions.

Many thanks are due to E. M. Levin for the petrographic analyses and to A. L. Dragoo for preparation of the arc-image samples.

8. References

[1] H. F. Stimson, J. Res. NBS **65A** (Phys. and Chem.) No. 3, 139–149 (1961).
[2] H. T. Wensel and W. F. Roeser, BS J. Research **5,** 1309–1318 (1930). RP 258.
[3] W. F. Roeser and H. T. Wensel, BS J. Res. **12,** 519–526 (1934). RP 676.
[4] W. F. Roeser, F. R. Caldwell, and H. T. Wensel, BS J. Res. **6,** 1119–1129 (1931). RP 326.
[5] F. Henning and H. T. Wensel, BS J. Res. **10,** 809–827 (1933). RP568.
[6] S. J. Schneider, NBS Mono. 68, 31 pp. (1963).
[7] P. D. Foote, C. O. Fairchild, and T. R. Harrison, Tech. Papers B. S. No. 170 **14,** 1–325 (1921).
[8] S. J. Schneider and C. L. McDaniel, Rev. Hautes Tempér. et Réfract. **3,** 351–61 (1966).
[9] C. W. Kanolt, Bull. B. S. **10,** 295–313 (1914).
[10] S. J. Schneider, J. Am. Ceram. Soc. **43,** 354–355 (1963).
[11] H. N. Frock and W. T. Shreve, Instrum. Soc. Amer. Preprint No. 29.5. 1963, 1–6 (1963).
[12] R. D. Lee, Metrologia **2** [4], 150–162 (1966).
[13] J. J. Diamond and A. L. Dragoo, Rev. Hautes Tempér. et Réfract. **3,** 273–279 (1966).
[14] A. Gouffé, Rev. Opt. **24,** 1–10 (1945).
[15] J. C. DeVoss, Physica **20,** 669–689 (1954).
[16] W. Gutt, J. Sci. Instrum. **41,** 393–394 (1964).
[17] R. L. Weber, Heat and Temperature Measurement, 400–406 (Prentice-Hall Inc., New York, 1950).
[18] A. G. Worthing, J. Applied Phys. **11,** 421–437 (1940).
[19] J. C. DeVoss, Physica **20,** 690–714 (1954).
[20] H. J. Kostkowski and R. D. Lee, NBS Mono. **41,** 28 pp. (1962).
[21] M. Hansen, Constitution of Binary Alloys, 2d edition, 1305 pp. (McGraw-Hill Book Co., New York, N.Y., 1958).
[22] R. P. Elliott, Constitution of Binary Alloys, 1st Supplement, 877 pp. (McGraw-Hill Book Co., New York, N.Y., 1965).
[23] K. Motzfeldt and G. Gitlesen, private communication (1965).
[24] M. Hoch and H. L. Johnston, J. Am. Chem. Soc. **76,** 2560–2561 (1954).
[25] J. Drowart, G. DeMaria, R. P. Burns, and M. G. Inghram, J. Chem. Physics **32,** 1366–1372 (1960).
[26] L. N. Grossman, Bull. Am. Ceram. Soc. **45,** 371 (1966) (Abstract); preprint, High Temperature Thermal Analysis of Ceramic Systems.
[27] A. R. Ubbelohde, Melting and Crystal Structure, pp. 218–242 (Clarendon Press, Oxford, 1965).
[28] L. S. Darken and R. W. Gurry, Physical Chemistry of Metals, pp. 90–92 (McGraw-Hill Book Co., New York, N.Y., 1953).
[29] G. Gitlesen and K. Motzfeldt, Acta Chem. Scand. **19,** 661–669 (1965),
[30] A. L. Kozlovskii and K. S. Shlyakova, Tr. Vses. Nauch.-Issled. Inst. Autogen Obrabotki Metal. **6,** 136–139 (1960); Chem. Abstr. **55,** 16062 (1961).
[31] P. B. Kantor, L. S. Lazareva, V. V. Kandyba, and E. M. Fomichov, Ukr. Fiz. Zh. **7,** 205 (1962).
[32] D. J. Barber and N. J. Tighe, J. Res. NBS **69A** (Phys. and Chem.) No. 3, 271–280 (1965).
[33] O. Ruff and O. Goecke, Z. Angew. Chem. **24,** 1459–1465 (1911).
[34] O. Ruff, Z. Anorg. Allgem. Chem. **82,** 373–400 (1913).

[35] E. Tiede and E. Birnbrauer, Z. Anorg. Chem. **87,** 129–168 (1914).
[36] O. Ruff and G. Lauschke, Z. Anorg. Chem. **97,** 73–113 (1916).
[37] H. v. Wartenberg, H. Linde, and R. Jung, Z. Anorg. Allgem. Chem. **176,** 349–362 (1928).
[38] E. N. Bunting, J. Res. NBS **6,** 947–949 (1931) RP317.
[39] O. Weigel and F. Kaysser, Neues Jahrb. Mineral Geol. **64,** 321–396 (1931).
[40] R. F. Geller and E. N. Bunting, J. Res. NBS **31,** 255–270 (1943) RP1564.
[41] R. F. Geller and P. J. Yavorsky, J. Res. NBS **34,** 395–401 (1945) RP1649.
[42] W. A. Lambertson and F. H. Gunzel, Jr., A.N.L., U.S. AEC Publ. AECD–3465, 1–4 (1952).
[43] S. M. Lang. F. P. Knudsen, C. L. Filmore, and R. S. Roth, NBS Circ. 568, 1–32 (1956).
[44] F. H. Aldred and H. E. S. White, Trans. Brit. Ceram. Soc. **58,** 199–223 (1959).
[45] S. D. Mark, Jr., J. Am. Ceram. Soc. **42,** 208 (1959).
[46] J. J. Diamond and S. J. Schneider, J. Am. Ceram. Soc. **43,** 1–3 (1960).
[47] R. N. McNally, F. I. Peters, and P. H. Ribbe, J. Am. Ceram. Soc. **44,** 491–493 (1961).
[48] V. Ya. Chekhovskoi and V. A. Petrov, Meas. Tech. **9,** 751–753 (1963) [English translation]; original article–Izmeritel'naya Teknika **9,** 26–28 (1963).
[49] W. Gutt, J. Sci. Instrum. **41,** 393–394 (1964).
[50] B. Riley, J. Sci. Instrum. **41,** 504–505 (1964).
[51] M. Foex, Solar Energy **9,** 61–67 (1965).
[52] P. B. Kantor, E. N. Fomichev, and V. V. Kandyba, Izmeritel'n. Tekhn. **5,** 27–29 (1966).
[53] T. Sata, Rev. Hautes Tempér. et Réfract. **3,** 337–341 (1966).
[54] G. Urbain and M. Rouannet, Rev. Hautes Temér. et Réfract. **3,** 363–369 (1966).
[55] G. K. Burgess, BS J. Res. **1,** 635–640 (1928).
[56] Chemical Abstracts **65,** 11371(d), (1966).

(Paper 71A4–463)

Publications of the National Bureau of Standards*

Selected Abstracts

An apparatus for measuring thermal expansion at elevated temperatures, B. D. Rothrock and R. K. Kirby, *J. Res. NBS* **71C2** (*Engr. and Instr.*), *No. 2, 85–91 (Apr.–June 1967).*
An apparatus has been developed for making precise measurements of the absolute thermal expansion of refractory materials at temperatures up to 1600 °C. This apparatus consists of an optical comparator and a controlled gradient vacuum furnace. Special care was taken on the techniques of measuring length and temperature and on the calibration of the microscopes and thermometers. The expansion data obtained with this apparatus on specimens of platinum and sapphire have a standard deviation of less than 30 ppm and are estimated to be accurate to within 50 ppm.

Key Words: Thermal expansion, elevated temperatures, controlled-gradient vacuum furnace, optical comparator.

A 2:1 ratio inductive voltage divider with less than 0.1 ppm error to 1 MHz, C. A. Hoer and W. L. Smith, *J. Res. NBS* **71C2** (*Engr. and Instr.*), *No. 2, 101–109 (Apr.–June 1967).*
A simple ratio transformer having a 2:1 ratio of input voltage to output voltage can be made with a ratio error less than 0.1 ppm from 1 kHz to above 1 MHz. Applications and sources of error are discussed. Experimental results leading to an optimum transformer design are given. A bridge to measure the ratio error to 0.025 ppm from 1 kHz to 1 MHz is also described.

Key Words: Attenuator, bridge, high frequency, inductive voltage divider, ratio transformer.

A dual-load flow calorimeter for rf power measurement to 4 GHz, M. L. Crawford and P. A. Hudson, *J. Res. NBS* **71C2** (*Engr. and Instr.*), *No. 2, 111–117 (Apr.–June 1967).*
A new dual-load flow-type coaxial calorimetric power meter has been constructed at the National Bureau of Standards, Boulder Laboratories. Designed for use as a reference standard, the frequency range of the calorimeter extends up to 4 GHz and beyond. The power range extends from 2 W to 100 W with an error limit of 0.35 percent.
Design details, error analysis and results of intercomparison with other standards are given.

Key Words: Radio frequency power, flow calorimeter, coaxial.

Polymeric materials for dielectric reference specimens, A. H. Scott and J. R. Kinard, Jr., *J. Res. NBS* **71C2** (*Engr. and Instr.*), *No. 2, 119–125 (Apr.–June 1967).*
The results from a study of the effects of aging and humidity change on certain polymer specimens indicate it is possible to establish stable dielectric reference specimens. Specimens of polyethylene, polystyrene, polycarbonate, poly(tetrafluoroethylene) (PTFE), fluorinated ethylene-propylene polymer (FEP), and poly(1,4-cyclohexylenedimethylene terephthalate) were used in the investigation. Slow changes in the dielectric properties were observed on some specimens over a period as long as three years. Very long timed humidity runs indicate PTFE, and FEP to only a slightly less degree, are best suited for dielectric reference specimen preparation.

Key Words: Dielectric constant, dissipation factor, frequency, fluorinated ethylene-propylene, humidity, polycarbonate, polyethylene, poly(1,4-cyclohexylenedimethylene terephthalate), polystyrene, poly(tetrafluoroethylene), time, reference specimens.

The sensitivity of the Dicke radiometer, D. F. Wait, *J. Res. NBS* **71C2** (*Engr. and Instr.*), *No. 2, 127–153 (Apr.–June 1967).*
The literature is reviewed concerning the sensitivity of the Dicke radiometer, excluding gain fluctuations. Discrepancies are pointed out and a new derivation of sensitivity using a Fourier transform method is used to resolve these discrepancies and to extend the results to radiometers with lossy switches.
Experimentally it is shown that radiometers using half-wave square-law, linear-law, or envelope detectors all have a sensitivity equal to the theoretical full-wave square-law detector (within the ±20% uncertainty of the experiment).

Key Words: Microwave, sensitivity, radiometer, Dicke, switching.

Sensivity of a correlation radiometer, J. J. Faris, *J. Res. NBS* **71C2** (*Engr. and Instr.*), *No. 2, 155–172 (Apr.-June 1967).*
The correlation radiometer is analyzed to determine the sensitivity that can be obtained under various operating conditions.
The radiometer using a sine wave comparison signal is analyzed and compared with the usual radiometer that employs a random noise for the comparison signal. It is found that the radiometer employing the sine wave comparison signal is the more sensitive of the two circuits, particularly in the case that the effective temperature of the input noise signal is greater than the effective input temperature of the amplifiers.
It is shown that if nonidentical amplifiers are used in the correlation circuit, the properties of the radiometer are determined by the portion of the amplifier response functions in the frequency interval that the two response functions overlap. The effect of amplifier gain fluctuations are considered, and although the correlation scheme reduces the effect of gain fluctuations, it is shown that they still do contribute to the output fluctuations of the radiometer.
Calculations are included showing that the effect of a differential phase shift between the two channels is a reduction in radiometer sensitivity. The same conclusion is reached concerning the effect of a differential time delay.
Finally, it is shown that if the comparison signal and the input signal have the same statistical properties, the requirements on the multiplier are less stringent than if the two signals have different statistical properties.

Key Words: Correlation radiometer, gain fluctuations, noise comparison signal, sine-wave comparison signal, differential time delay, imperfect multiplier, nonidentical amplifiers.

Tables of molecular vibrational frequencies Part 1, T. Shimanouchi, *NSRDS–NBS6 (Mar. 1, 1967), 40 cents.*
A compilation of vibrational frequency data for selected molecules is being conducted at the University of Tokyo in cooperation with the National Standard Reference Data Program of the National Bureau of Standards as a part of an international effort to compile and evaluate physical and chemical data. This report, first of a series of annual reports, contains fundamental vibrational frequencies of 59 molecules together with vibrational assignments, sources of data, brief comments, and citations of references. The fundamental frequencies are obtained mainly from the infrared and Raman spectra. When these are not available, other experimental data such as microwave results are taken into account. The selection of vibrational fundamentals from observed spectral data is based upon careful studies of the spectral data and comprehensive mathematical analyses. These tables were designed to provide a concise summary needed for the computation of ideal gas thermodynamic properties. They may also provide a convenient source of information to those who require vibrational energy levels and related properties in molecular spectroscopy, analytical chemistry, and other fields of physics and chemistry.

Key Words: Molecular, vibrational, frequencies, data, tables, force, constants, spectral.

Scanning electron probe microanalysis, K. F. J. Heinrich, *Tech. Note 278 (Feb. 3, 1967), 30 cents.*
The combination of electron microprobe x-ray emission spectrometry with the scanning techniques first developed for the scanning electron microscope permits using the scanning electron probe as a microscope sensitive to elemental composition. This technique is particularly useful in the many applications in which spatial distribution of one or more elements in a specimen is more important than local composition. Although oscilloscope representation of probe scanning is usually obtained by the simple technique of producing a dot of light for each arriving photon, more sophisticated scanning techniques such as expanded contrast registration and concentration mapping can provide more quantitative information. Signals other than x-rays, such as target current, electron backscatter, or cathodoluminescence may be used for image formation. Electron beam scanning can also be performed in a discontinuous fashion, so that the electron beam irradiates in succession a number of spots arranged in a square or rectangular pattern, and the number of photons registered in each position is retained in the memory of a multichannel analyzer. The application of these diverse scanning techniques is illustrated.

Key Words: Electron probe, microanalysis, x-ray spectrometry, scanning electron microscopy, electron backscatter, cathodoluminescence.

Procedures for precise determination of thermal radiation properties, November 1964 to October 1965, J. C. Richmond, G. J. Kneissl, D. L. Kelley, and F. J. Kelly, *Tech. Note 292 (Feb. 10, 1967), 50 cents.*
An error analysis of the shallow cavity technique for measuring total normal emittance of ceramic materials at very high temperatures showed that there was an error due to the translucency of the specimens that was as much as +60% for alumina, and a second error due to thermal gradients in the specimen that was on the order of −10%. Two new techniques were devised in the hope of greatly reducing the translucency error. Progress was made in developing codes to compute and correct for the thermal gradients present in the specimen. The laser-source integrating sphere reflectometer for measuring reflectance of specimens at very high temperatures was extensively redesigned to eliminate errors due to flux reaching the detector on the first reflection, and to convert the reflectometer from the substitution to the comparison mode. A literature search was made of techniques for measuring thermal radiation properties of solids at temperatures above 2500 °K (4000 °F).

Key Words: Emissivity, emittance, high temperature reflectance, infrared reflectance, radiation properties, reflectance, spectral emittance, spectral reflectance, thermal radiation, total emittance.

Methods for performance-testing of electromechanical pressure transducers, P. S. Lederer, *Tech. Note 411 (Feb. 9, 1967), 25 cents.*
This publication describes methods in one particular program at NBS for the performance-testing of electro-mechanical pressure transducers (such as telemetering transducers used in aerospace testing). It covers static and dynamic calibration procedures in detail, delineates environmental and other tests, and describes the test equipment used. Examples of dynamic calibration results are interpreted.

Key Words: Electro-mechanical, pressure, transducer, calibration, performance, test method, dynamic calibration, and telemetering.

Exactly solvable nonlinear relaxation processes. Systems of coupled harmonic oscillators, K. E. Shuler and G. H. Weiss, *J. Chem. Phys.* **45,** *No. 4, 1105–1110 (Aug. 15, 1966).*
A class of nonlinear relaxation processes is discussed which involves the interaction of two finite systems characterized by special forms of the transition probabilities. For the particular set of transition probabilities it is possible to reduce the initial set of coupled nonlinear kinetic equations to a set of linear equations with time dependent coefficients which are amenable to exact analytical solutions. This reduction is effected through the use of summational invariants expressed in terms of the appropriate combinations of the moments of the distribution functions of the two systems. The vibrational-vibrational relaxation of two interacting systems of harmonic oscillators A and B has been worked out as a specific example. For the type of relaxation processes discussed here it is found that the relaxation of system A is independent of the form of the initial distribution of system B (and thus of its time history) and vice versa.

Flash photolysis of methane in the vacuum ultraviolet. I. End-product analysis, W. Braun, K. H. Welge, and J. R. McNesby, *J. Chem. Phys.* **45,** *No. 7, 1650–1656 (Oct. 1, 1966).*
Flash photolysis combined with matrix isolation spectroscopy has been employed to investigate the decomposition of a cyanogen azide-nitrogen solid at 20.4 °K. Two primary processes have been observed leading to the formation of NCN radicals either in an electronically excited $^1\Delta_g$ level or in the $^3\Sigma_g^-$ ground state. The first order decay of NCN ($^1\Delta_g$) has been studied and the mean lifetime in the solid found to be approximately 500 microseconds.

Key Words: Decay, flash photolysis, lifetime, matrix isolation, primary process

Galvanic pitting in metallic coatings, F. Ogburn and M. Schlissel, *Plating* **54,** *No. 1, 54–62 (Jan. 1967).*
An electrolytic cell is described which simulates a corrosion pit extending through a metal coating and permits measurement of the cell currents. Such cells were used to investigate the galvanic currents between coatings of chromium, copper, and nickel and substrates of zinc, iron, nickel, and copper. The investigation included outdoor, salt spray, and Corrodkote exposures; and determinations of the effects of anode size, depth of electrolyte, and proximity of a second anode on cell currents.
An equation for the cell current as a function of the cell parameters is discussed and compared with experiments.

Ion-molecule reactions in the condensed phase radiolysis of hydrocarbon mixtures. I. 2-methylbutane and 3-methylpentane, *J. Am. Chem. Soc.* **88,** *No. 24, 5701–5707 (Dec. 20, 1966).*
In the condensed phase, parent ions of 2-methylbutane and 3-methylpentane transfer an H_2-molecule to cyclopropane as well as to smaller unsaturated hydrocarbons according to the reaction:

$$C_nH_{2n+2}^+ + C_{m'}H_{m''} \rightarrow C_nH_{2n}^+ \qquad C_{m'}H_{m''+2}$$

The relative probabilities for the transfer of an H_2-molecule from $C_5H_{12}^+$ to cyclopropane, ethylene, propylene, 1-butene, acetylene, and 2-butene are, respectively, 2.4, 1.4, 1.0, 0.9, 0.77, and < 0.1. When cyclopropane-d_6 is added to iso-C_5H_{12}, $CD_2HCD_2CD_2H$ is formed as a product with a yield which increases as the square root of the cyclopropane-d_6 concentration from a G-value of 0.117 at 0.03 mole percent additive to 1.53 at 20 mole percent additive, while all lower perprotonated hydrocarbon products diminish proportionately. Similarly, addition of electron scavengers such as CCl_4 to an i-$C_5H_{12}-(CD_2)_3$ (1:0.03) mixture increases $G(CD_2HCD_2CD_2H)$ to a value as high as 2.85 while the G-value of products such as C_2H_3, C_2H_4, or C_2H_8 drop by factor of five. The importance of the H_2-transfer reaction to our understanding of the condensed phase radiolysis of alkanes is discussed.

Key Words: 2-methylbutane and 3-methylpentane, ion-molecule reaction, liquid phase photolysis, liquid phase radiolysis

Radiation-induced polymerization of hexafluoropropylene at high temperature and pressure, R. E. Lowry, D. W. Brown, and L. A. Wall, *J. Polymer Sci.* **4,** *Pt. A-1, No. 9, 2229–2239 (Sept. 1966).*
The radiation-induced polymerization of hexafluoropropylene was studied in the pressure and temperature ranges of 4,500–15,000 atm. and 100–230 °C., respectively. Retardation was a serious problem; data thought to apply to the unretarded polymerization are summarized below. At 1,500 rad/hr. the polymerization rate was 15%/hr. at 230 °C. and 15,000 atm. The activation enthalpy and volume are 9.5 kcal./mole and −10 cc./mole, respectively. The rate varies as the square root of the radiation intensity. The largest intrinsic viscosity of the polymer is 2.0 dl./g.; values increase with temperature and pressure. At 130 °C. and 10,000 atm. the intrinsic viscosity was the same at two radiation intensities.

Vibrational spectrum of $ClNF_2$, J. J. Comeford, *J. Chem. Phys.* **45,** *No. 9, 3463–3465 (Nov. 1, 1966).*
The vibration spectra of the hydrides and deuterides of yttrium and uranium have been investigated by the energy-gain scattering of cold neutrons. The measured spectra are all split into two bands, one at higher energies, due to the optical hydrogen modes, and another due to metal-atom vibrations at lower energies. Values have been obtained for the peaks and widths of the single optical hydrogen bands in YH_2, YD_2, UH_3 and UD_3 by the calculation of approximate frequency distributions from the observed neutron time-of-flight spectra. The derived peak frequencies (and widths at half-maximum) in cm^{-1} are: YH_2, -1030 ± 40; UH_3, -970 ± 60; UD_3, -710 ± 40. The relative width at half-maximum $\left(\frac{\Delta\hbar\omega}{\hbar\omega}\right)$ for the hydrogen band in UH_3 is double that for YH_2. The distribution of hydrogen vibrations in hexagonal YH_3 and YD_3 is considerably broader, and exhibits several maxima, due to hydrogens at different sites in the lattice. The hydrogen modes in all the compounds can be correlated reasonably well with the known crystal structures. The results are in satisfactory agreement with hydrogen frequencies calculated previously from heat capacity data.

Key Words: Metal hydrides, vibration spectrum, optical vibration, frequency distribution, neutron (scattering), inelastic scattering, cold neutrons.

Atomic standard of frequency and time, J. M. Richardson and J. F. Brockman, *Phys. Teacher* **4,** *No. 6, 247–256 (Sept. 1966).*
The National Bureau of Standards scale of time is provided by an atomic frequency standard. Thus, for the first time in our civilization, the basis of our measurement of time is atomic instead of astronomical. The major reasons for this change are that modern science can measure the resonance of an atom more accurately than it can measure the motions of stars and planets, all of the factors affecting atoms are better understood, and the atomic resonance appears to be more stable than planetary motions. This change has improved our accuracy of measurement by three orders of magnitude.
Presently, the best atomic clocks are based on atomic cesium beams such as the three at NBS. Further research, however, may reveal a better choice of atom or method. NBS is using four radio stations to distribute time (and its reciprocal, frequency) to the nation and over much of the globe, but again, research is being conducted on newer techniques that offer higher accuracies.
The change from astronomical to atomic time will have little effect on our daily living habits, but it will permit our technology to accomplish things we couldn't do before and to do the same things more economically.

Electrical standards and measurement, F. K. Harris, I. L. Cooter, B. L. Dunfee, W. P. Harris, F. L. Hermach, and C. Peterson, *Electro-Technol.* **97,** *55–70 (Jan. 1967).*
The basis of the electrical units and their derivation from the mechanical units is briefly reviewed. Methods used by the Electricity Division of the National Bureau of Standards for the establishment of measurement reference standards are discussed together with the techniques employed in extending the range of measurement from the reference standard to higher and lower values.

Key Words: Absolute measurements, electrical units, electrical reference standards, precise electrical measurements.

Acoustical thermometer and the National Bureau of Standards provisional temperature scale 2–20 (1965), H. Plumb and G. Cataland, *Metrologia* **2.** *No. 4, 127–139 (Oct. 1966).*
An acoustical thermometer has been developed at the National Bureau of Standards to determine values of temperature that approximate the Thermodynamic Temperature Scale. The instrument, called an ultrasonic interferometer in acoustical literature, has been used to determine isotherms of the speed of sound in helium gas as a function of pressure. Each isotherm has been extrapolated to zero pressure to approximate the condition of an ideal gas; from the resulting intercepts, values of temperature were calculated.
The instrument and its operation are described and the data isotherms, which have been determined at approximately every degree from 2°–20 °K, are listed. The isotherm data have been treated both graphically and by electronic computer analysis (by the method of least squares) to yield values of temperature that are the basis for a new temperature scale—NBS Provisional Scale 2–20 (1965). When the scale is compared with other existing scales, T_{58} and NBS (1955), in regions of overlap, the agreement with NBS (1955) is excellent but noticeable departures from T_{58}—the helium-4 vapor pressure scale—are indicated.

Chlorine K x-ray emission spectra from several chlorinated hydrocarbon and fluorocarbon molecular gases, R. E. LaVilla and R. D. Deslattes, *J. Chem. Phys.* **45,** *No. 9, 3446–3448 (Nov. 1, 1966).*
Emission profiles have been obtained in x-ray fluorescence for the four chlorinated derivatives of methane (CH_3Cl, CH_2Cl_2, $CHCl_3$, CCl_4), and five chlorinated fluoromethanes (CF_3Cl, CF_2Cl_2, $CFCl_3$, $CHFCl_2$, CHF_2Cl) in the gas phase. The chloromethanes contain two prominent lines whereas the chlorofluoromethanes have multiplet structures of up to four lines. These structures are interpreted in terms of the molecular orbital determined final state hole energies.

Key Words: Chlorine, Kβ x-ray emission, chlorinated molecular gases.

Radiance temperature at 6500 Å of the graphite arc, R. D. Lee and E. Lewis, *Appl. Opt.* **5,** *No. 11, 1858 (Nov. 1966).*
The radiance temperatures of over twenty positive electrodes in a graphite arc were measured with the NBS photoelectric pyrometer and were found to range from 3786 °K to 3808 °K. The radiance temperatures were measured to an accuracy of 2 deg K (standard deviation uncertainty) with a pyrometer sensitivity of 0.2 deg K.

Key Words: Graphite arc, pyrometry, standard, temperature.

Spectral radiance of a low current graphite arc, A. T. Hattenburg, *Appl. Opt.* **6,** *95–99 (Jan. 1967).*
The spectral radiance of the anode of a low current graphite arc has been determined throughout most of the 850–210 nm region by utilizing a recently developed high accuracy spectroradiometer. The estimated standard deviation uncertainty varies from about 1.5% at the longer wavelengths to about 5% at the shorter. Results are given at twenty wavelength points in the region and also as a continuous function of wavelength throughout most of the region, excluding some areas of high molecular band radiation originating in the arc stream.

Static theory of the giant quadrupole resonance in deformed nuclei, M. Danos, W. Greiner, and B. C. Kohr, *Phys. Rev.* **151,** *No. 3, 761–772 (Nov. 18, 1966).*
The modes and frequencies of the giant quadrupole resonance of heavy deformed nuclei have been calculated. The quadrupole operator is computed and the absorption cross section is derived. The quadrupole sum rule is discussed and the relevant oscillator strengths have been evaluated for various orientations of the nucleus. The giant quadrupole resonances have energies between 20 and 25 MeV. The total absorption cross section is about 20% of the giant dipole absorption cross section. Of particular interest is the occurrence of the quadrupole mode in a direction of approximately $\theta = 1/4^{\pi}$ from the symmetry axis. This may give information on the details of the nuclear shape.

Key Words: Deformed nuclei, giant resonance, nuclear hydrodynamics, octupole deformation, photon absorption, quadrupole resonance.

Superconductivity in semiconducting $SrTiO_3$, J. F. Schooley and W. R. Thurber (*Pro. Intern. Conf. Phys. of Semiconductors, Kyoto, Japan, Sept. 8–11, 1966*), *J. Phys. Soc. Japan* **21,** *Paper XVI–2, 639–642 (Suppl. 1966).*
Superconductivity that occurs in a substance which is semiconducting at higher temperatures possesses features which are different from ordinary metallic superconductivity. The occurrence of superconductivity in a material of relatively low charge carrier concentration n_c is due largely to an unusually high density of states at the Fermi surface N(0); heat capacity and superconducting critical field experiments, among others, show the presence of the large N(0). The variability in n_c within an essentially constant electronic energy band structure leads to a corresponding variation in the

superconducting transition temperature T_c. The presence of anisotropic Fermi surfaces in multi-valley semiconductors can result in unusually large and anisotropic pressure effects. The relatively low carrier concentrations in semiconductors leads to unusually deep penetration of static magnetic fields in the superconducting state. Finally, the static dielectric constant, which can be quite large in semiconductors, can be varied by combining similar semiconductors into mixed crystals; to the extent that the superconducting properties depend upon the dielectric properties, variation in T_c results.

Key Words: Superconductivity, semiconductors, strontium titanate.

The NBS photoelectric pyrometer and its use in realizing the international practical temperature scale above 1063 °C, R. D. Lee, *Metrologia* **2,** *No. 4, 150–162 (Oct. 1966).*
A photoelectric pyrometer has been developed with which the International Practical Temperature Scale (IPTS) above the gold point, 1063 °C, is realized about 5 times more accurately than with the prevalently used disappearing filament visual pyrometer. Estimated standard deviation uncertainties of realizing the IPTS with the photoelectric instrument are 0.06 deg C at 1063 °C, 0.12 deg C at 1256 °C, 0.27 deg C at 1650 °C, 0.7 deg C at 2330 °C, and 2 deg C at 3525 °C. The design, evaluation, and calibration to realize the IPTS are discussed.

The photodetachment cross section, electron affinity, and structure of the negative hydroxyl ion, L. M. Branscomb, *Phys. Rev.* **148,** *11 (1966).*
Experimental data on the cross section for photodetachment of OH^- and OD^- ions are given and used to argue that $r_e(OH^-) = r_e(OH) \pm 0.0002$ Å, that $\omega_e(OH^-) = 3700 \pm 560$ cm^{-1} and that the OH electron affinity E.A. (OH) $= 1.83 \pm 0.04$ eV. Thus, the structure of OH^- and OH are remarkably similar, which is consistent with the theoretical predictions of Cade.

Key Words: Photodetachment, OH^- ions, OD^- ions, cross section, electron affinity, negative hydroxyl ion, molecular structure.

Thermal energy-ion-neutral rates. I. Some reactions of helium ions, F. C. Fehsenfeld, A. L. Schmeltekopf, P. D. Goldan, H. I. Schiff, and E. E. Ferguson, *J. Chem. Phys.* **44,** *No. 11, 4087–4094 (June 1, 1966).*
A flowing, steady state afterglow system has been utilized to measure room temperature ion-neutral reaction rates. A description of the apparatus and technique is given. Measured rate constants for He^+ reactions with O_2, N_2, CO, NO, and CO_2 are reported, as well as upper limits for the reactions of He^+ with H_2, Ne, and Ar, and an estimate for the reaction of He_2^+ with He.
The reactions of He^+ with O_2, N_2, CO, NO, and CO_2 are all rapid the rate constants all being $\sim 10^{-9}$ cm^3 sec^{-1}, implying essentially a reaction per collision. It is suggested that the reactions may be dissociative charge-transfer processes and are not ion-atom interchange reactions.

Vibration spectra of yttrium and uranium hydrides by the inelastic scattering of cold neutrons, J. J. Rush, H. E. Flotow, D. W. Connor, and C. L. Thaper, *J. Chem. Phys.* **45,** *No. 10, 3817–3825 (Nov. 15, 1966).*
The infrared spectrum of chlorodifluoramine has been examined for the region of the fundamentals in both the gas-phase and in an argon matrix at 20 °K. The previously unassigned fundamental, ν_6, has been observed, completing the vibrational assignment.

Key Words: Chlorodifluoramine, infrared spectra, matrix-isolation, spectra, vibrational assignment, vibrational fundamentals.

Dielectric constants of imperfect gases. III. Atomic gases, hydrogen, and nitrogen, R. H. Orcutt and R. H. Cole, *J. Chem. Phys.* **46,** *No. 2, 697–702 (Jan. 15, 1967).*
A modified cyclic-expansion method has been used to determine dielectric constants as a function of relative density with a precision of less than 1 ppm for He, Ne, Ar, Kr, H_2, and N_2 at 49 °C and pressures below 150 atm, which with data at measured pressures below 7 atm determine the first and second dielectric virial coefficients, and can also be used to determine pressure second virial coefficients.
Dielectric second virial coefficients are for all six gases less than values predicted by present theories of fluctuations and pair polarizabilities, an effect believed to result from overlap interactions at short range. The low-density values of the Clausius-Mossotti function are in good agreement with other recent determinations.

Ellipsometric-potentiostatic studies of iron passivity. I. Anodic film growth in slightly basic solutions, J. Kruger and J. P. Calvert, *J. Electrochem. Soc.* **114,** *No. 1, 43–49 (Jan. 1967).*
Cathodically reduced iron was anodically oxidized to potentials in the passive region of the anodic polarization curve at passive potentials in nearly neutral sodium borate-boric acid solutions by means of a potentiostat. The kinetics of film growth were studied using an ellipsometer coupled with a high speed recording technique, which enabled a determination of the rate of film formation for times less than one second. This study of the kinetics of film growth using a non-electrochemical technique agreed with kinetic results based on total charge measurements.
Three states of growth were detected: (1) *First Stage*—growth limited by the diffusion of oxidizing species thru solution. (2) *Second Stage*—start of limitation of growth of film. A combination of several processes difficult to characterize by any rate law. (3) *Third Stage*—growth obeying either a direct or indirect logarithmic rate law. The latter was found to imply that the passive film consisted of an outer layer poorly conductive for electrons.

Key Words: Ellipsometry, potentiostat, anodic oxidation, kinetics, iron oxide films, iron and passivity.

The ionization constant of deuterium oxide from 5 to 50 °, A. K. Covington, R. A. Robinson, and R. G. Bates, *J. Phys. Chem.* **70,** *3820–3824 (1966).*
Electromotive force measurements of a cell without liquid junction have been used to determine the ionization constant of deuterium oxide from 5 to 50 °C. A value of $pK = 14.955$ has been found at 25 °C, the concentrations being expressed in terms of molalities. Enthalpy, entropy, and heat capacity changes for the dissociation process have been evaluated.

Key Words: Deuterium oxide, heavy water, isotope effects, ionization constant.

The national standard reference data system, E. L. Brady, *J. Chem. Doc.* **7,** *No. 1, 6–9 (Feb. 1967).*
The National Standard Reference Data System is a government-wide effort to give to the technical community of the United States optimum access to quantitative data on the physical and chemical properties of substances and their interactions, critically evaluated and compiled for convenience. The general functions of the System are to coordinate and integrate existing data evaluation and compilation activities into a systematic, comprehensive program, supplementing and expanding technical coverage when necessary, establishing and maintaining standards for the output of the participating groups, and providing mechanisms for the dissemination of the output as required. This program was established as a Federal policy in 1963 upon the recommendation of the Federal Council for Science and Technology. The National Bureau of Standards of the Department of Commerce has accepted responsibility for administering the effort. The plan of operation and the general status of activities initiated by the National Bureau of Standards will be described.

Key Words: National Standard Reference Data System, NSRDS, Information Centers, physical properties, data, properties.

Time-dependent behavior of activated molecules. High pressure unimolecular rate constant and mass spectra, F. H. Mies and M. Krauss, *J. Chem. Phys.* **45,** *No. 12, 4455–4468 (Dec. 15, 1966).*
A quantum mechanical theory of the unimolecular decay of metastable, or activated molecules is developed using Fano's treatment of resonance scattering. A resonance state is synonymous with the so-called activated molecule in unimolecular kinetics, and a set of widths are associated with each state which is a measure of

the coupling to the various dissociation continuum channels (each channel designates an "activated complex"). If the widths are small compared to the spacings between those neighboring states which are coupled to the same continua, then an ensemble of molecules prepared in a given activated state will decay exponentially in time, as does a radiating or autoionizing excited atomic state. However, unimolecular decay is fundamentally a problem in "overlapping" resonances widths, and is best considered using Fano's theory, which incorporated proper treatment of the overlap. This paper is particularly concerned with the implications of overlapping widths on the high pressure rate constant, and on mass spectra.

There are two effects of overlapping which are most striking. First, the time decay of a metastable molecule is no longer a pure exponential, but for the special cases considered is represented by a sum of exponential, oscillatory, and or linear terms, which certainly effects the interpretation of mass spectra. Second, the high pressure rate constant is related to the initial rate of decay of a canonical ensemble of activated molecules, and proper consideration of overlap imposes an upper bound on the rate of dissociation without any artificially imposed restrictions on the widths. This bound yields the "universal rate constant" kT/h times a transmission coefficient which is a function of the widths and *spacings* of the activated molecules, and has an upper limit of one.

Key Words: Dissociation, unimolecular dissociation, theoretical, quantum mechanics, lifetime, activated molecules, unimolecular rate, mass spectra, resonance scattering, predissociation, kinetics, high pressure rate constant, activated state, activated complex, metastable molecules, decay.

Approximate normal emissivity spectra in the infrared at elevated temperatures of single-crystal and polycrystalline calcium fluoride, W. B. Fussell and J. C. Geist, *Appl. Opt.* **6,** *No. 1, 119–124 (Jan. 1967).*

A single-beam infrared spectroradiometric system has been used to measure the normal spectral emissivity of specimens of single-crystal and polycrystalline calcium fluoride in the infrared at elevated temperatures. The wavelength range was 2 to 12 microns and data were taken at sample temperatures of 500 and 600 °C.

Room temperature data on the index of refraction of single crystal calcium fluoride, and its rate of change with temperature, were extrapolated to 500 and 600 °C, and the normal spectral reflectivities were computed from the extrapolated indices at these temperatures. The computed reflectivities were then used to extract normal spectral absorption coefficients from the emissivity data. It was possible to compute absorption coefficients with reasonable accuracy at wavelengths of 6, 8, and 10 microns; the smallest estimated error was about 2% at 8 microns. The absorption coefficients increased markedly with temperature at these three wavelengths. The absorption coefficients of the polycrystalline material were consistently higher than the corresponding values for the single-crystal calcium fluoride.

It was found that the spectral absorption coefficients at 8 and 10 microns varied approximately as the 2.1 and 1.6 power of the absolute temperature, respectively, between room temperature and 600 °C. These exponents lie within the range predicted by theory.

Key Words: Calcium fluoride, infrared absorption coefficients, elevated-temperature emissivity, infrared emissivity, polycrystalline CaF_2, single-crystal CaF_2.

Electrodynamic vibration standard with a ceramic moving element, T. Dimoff, *J. Acoust. Soc. Am.* **40,** *No. 3, 671–676 (Sept. 1966).*

This report describes a new rectilinear vibration exciter specifically developed for accurate calibration of piezoelectric accelerometers. It is an electrodynamic shaker using a permanent magnet with a ceramic moving element guided by an air bearing system. The moving element has a simple circular cross section and the driving coil is wound directly onto it. Its first axial resonance is near 25,000 Hz. The working range of the shaker extends from 5000 Hz to less than 5 Hz.

The moving element includes a means of mounting an internal accelerometer which can be used as a secondary standard. Alternatively, the moving element-accelerometer assembly can be calibrated by a reciprocity method and used as an absolute standard. The results of measurements of transverse motion and harmonic distortion are presented as well as an example of pickup calibration.

Key Words: Vibration standard, piezoelectric accelerometers, electrodynamic shaker, ceramic moving element, air bearing, reciprocity, secondary standard, piezoelectric acceleration transducer, vibration pickup.

Interface kinetics and the stability of the shape of a solid sphere growing from the melt, S. R. Coriell and R. L. Parker (*Proc. Intern. Conf. Crystal Growth, Boston, Mass., June 20–24, 1966*), *Crystal Growth, A Suppl. to J. Phys. Chem. Solids, J–3, pp. 703–708 (Pergamon Press, Inc., New York, N.Y., 1967).*

The effects of linear interface kinetics and of square law interface kinetics on the stability of the shape of a sphere growing in a diffusion field are investigated theoretically. Sluggish interface kinetics can greatly enhance the stability, by a factor of more than 3,000 in certain cases. The sphere can be stable even if its surface energy is zero. Numerical estimates are made for salol and for tin.

Key Words: Crystal growth, diffusion, heat flow, interface, kinetics, morphology, sphere, stability.

Mechanical properties of chemically strengthened glasses at high temperatures, M. J. Kerper and T. G. Scuderi, *J. Am. Ceramic Soc.* **40,** *No. 11, 613–618 (Nov. 1966).*

Young's modulus, shear modulus, and modulus of rupture of two chemically strengthened glasses were determined at elevated temperatures. The results showed that the Young's modulus and shear modulus decrease with increasing temperature with a sharp inflection present slightly above room temperature.

The modulus of rupture is not affected by short exposure to temperatures up to 260 °C, but drops appreciably when exposed to temperatures above 204 °C for 200 hours or more.

Measurement of deflection at room temperature showed the two chemically strengthened glasses to exhibit about five times as much delayed elasticity as did thermally tempered soda-lime-silica glass.

Key Words: Chemically strengthened glass, elevated temperature, glass, strength, Young's modulus.

On the solution of the Stefan problem for whisker growth, J. A. Simmons, H. Oser, and S. R. Coriell (*Proc. Intern. Conf. Crystal Growth, Boston, Mass., June 20–24, 1966*), *Crystal Growth, A Suppl. to J. Phys. Chem. Solids C–8, pp. 255–264 (Pergamon Press Inc., New York, N.Y., 1967).*

An integral equation which describes whisker length as a function of time is derived from the implicit exact solution of Simmons, Howard and Parker using a conservation principle. A convergent iterative method is employed to obtain numerically the exact growth curves and concentration profiles. Utilizing a dimensionless formulation, growth curves are shown to comprise (except for a short transient period) a one-parameter family dependent only on a dimensionless evaporation parameter. The Dittmar-Neumann and Curtis approximations are compared with the exact solution and are found to deviate significantly in some parts of the growth range; however, in those parts of the growth range where physical limits on the surface concentration are satisfied, both approximations are in good agreement with the exact solution. Methods and limitations are discussed for calculating the coefficient of surface self-diffusion and mean stay time from whisker growth data.

Key Words: Whisker growth, Stefan problem, Dittmar-Neumann approximation, surface concentration, surface self diffusion, Curtis approximation, Mean stay time.

Physiological optics at the National Bureau of Standards, D. B. Judd, *Appl. Opt.* **6,** *No. 1, 13–26 (Jan. 1967).*

Published work in physiological optics at the National Bureau of Standards is summarized under the headings: evaluation of light-dark patterns, light measurement, color measurement, color differences, and color perception. The bearing of this work on standard methods of the American Society of Testing and Materials, of the Illuminating Engineering Society, and of the American Standards Association, and on recommendations of the International Commission on Illumination is indicated. The purposes and methods of current work are briefly described.

Key Words: Color, gloss, light, perception of color, photometry, physiological optics, psychophysics, scaling of color.

The new tungsten-filament lamp standards of total irradiance, R. Stair, W. E. Schneider, and W. B. Fussell, *Appl. Opt.* **6,** *No. 1, 101–105 (Jan. 1967).*
The NBS standard of total irradiance as presently issued in the form of a 50-watt carbon filament lamp was originally calibrated more than 50 years ago. Recently needs for higher accuracy and wider ranges of total irradiance have necessitated the setting up of three sizes (100-, 500-, and 1000-watt) of tungsten-filament lamp standards of total irradiance. These standards operate at a higher temperature than was possible with the carbon-filament lamps, and are shielded, except for a narrow area of the bulb in front of the filament, so that the reception of long-wavelength flux from the lamps is reduced to a minimum. The new lamps were calibrated by the use of a blackbody at a known temperature together with a quartz plate whose spectral transmittance was accurately determined. The quartz plate limits the flux received from the blackbody to the spectral region below about 4.5 microns and thus reduces errors resulting from water vapor absorption at 6 microns and longer wavelengths. Comparisons show the new standards to be in close agreement with the carbon-filament lamp standard.

Key Words: Blackbody, total irradiance, and lamp standard.

Analysis of the α, β, and γ relaxations in polychlorotrifluoroethylene and polyethylene: dielectric and mechanical properties, J. D. Hoffman, G. Williams, and E. Passaglia, *J. Polymer Sci. Pt. C, No. 14, 173–235 (1966).*
Theoretical models for the α_c and γ_c relaxation effects found in chain-folded polymer crystals (single crystal mats and bulk) are presented, and compared with the available dielectric and mechanical loss data for polyethylene and polychlorotrifluoroethylene. Details of morphology and crystal structure that can be varied by crystallization and annealing procedures, e.g., roughness of chain-folded surfaces, number of intercrystalline links and cilia, number of chain-end defects and dislocations, and the existence of the extended-chain phase, are brought into the discussion. The α_c process, which consists of two overlapping mechanisms, is a result of motions of chain folds, and reorientation (with translation) of chains in the interior. (Chain twisting also occurs for long chains.) the theory connects the data on the *n*-paraffins and their polar derivatives (*n*-ketones, esters, ethers) with the results on polymers: the common feature is the chain reorientation and twisting process. A new theory of chain twisting is introduced. The γ_c relaxation is a result of reorientation of chains in a "loose" chain-end induced defect (a vacancy row) in the polymer crystal. When the effect of chain twisting is included, the theory successfully predicts the unusually broad and asymmetric loss curve found in the polymer, and is consistent with the experimental activation energies. The β relaxation arising in the amorphous component of PCTFE is analyzed, and its upward shift in temperature with increasing crystallinity discussed in terms of the Adam-Gibbs theory of relaxation in the glassy state. The γ_a amorphous relaxation, and the δ relaxation which is found at cryogenic temperatures, are also discussed.

Key Words: Polymer, semicrystalline, polyethylene, polychlorotrifluoroethylene, dielectric relaxation, mechanical relaxation, defect, vacancy, chain fold, chain rotation, chain twisting, annealing.

Calculated heats of dilute solid solution among the alkali halides other than cesium salts, T. B. Douglas, *J. Chem. Phys.* **45,** *No. 12, 4571–4585 (Dec. 15, 1966).*
Limiting high-temperature heats (energies) of dilute solid solution are calculated for all 96 cases of one NaCl-type alkali halide (except Cs salts) dissolving in another having a common ion. The direct-summation shell treatment used is based on a slightly modified Born-Mayer potential function and on the polarization energy up to terms square in the ion polarizabilities. Preliminary general expansion of the energy in positive powers (up to cubic) of the lattice-relaxation (ion-displacement) parameters of the first eight shells (98 neighbors) facilitated application to specific cases. In the linear solution for the minimum-potential lattice relaxation, one or two iterations for the first two shells sufficed. The convergence of the energy expansions and the sensitivity of the calculated energies to arbitrary variations in the semi-empirical parameters were extensively investigated. Comparison is made with calorimetric heats of solution in 16 cases, the agreement (averaging ± 10 percent) lying within the experimental and computative errors.

Key Words: Alkali halides, heats of solution, ion substitution, lattice relaxation, polarization energy, shell calculations, solid solutions.

Concepts, terminology, and notation for optical modulation, C. S. McCamy, *Photo. Sci. Eng.* **10,** *No. 6, 314–325 (Nov.–Dec. 1966).*
Reflectance, transmittance, and optical density are regarded as kinds of flux modulation factors. Transmittance is defined as the ratio of transmitted flux to the incident flux, while transmittance factor is here defined for an optical system as the ratio of the emergent flux with the sample in the system to the emergent flux with the the sample removed. Transmission density is defined as the negative logarithm of transmittance factor. This is essentially a new definition to accord with an old practice. Reflection, transmission, and fluorescence are considered generically as propagation and generalized modulation terms are proposed. A coordinate system and functional notation are adopted to systematize the description of optical systems which use or measure modulation. Simplified notation of the form D(g;S:g′:S′) describes most cases. Terms, symbols, and notation are proposed for standardization.

Key Words: Modulation, reflectance, transmittance, reflectance factor, transmittance factor, propagance, absorptance, optical density, contrast, symbols, and notation.

Elastic properties of NiTi as a function of temperature, S. Spinner and A. G. Rozner, *J. Acoust. Soc. Am.* **40,** *No. 5, 1009–1015 (Nov. 1966).*
Young's modulus, shear modulus, and internal friction of the intermetallic compound, N Ti, have been measured as a function of temperature from about −180 °C to 600 °C, in the kilocycle range. Annealed and cold-worked specimens were used.
All the specimens showed the same general pattern with a minimum in elastic moduli occurring about 70 °C to 140 °C, depending upon the particular specimen, and a maximum in internal friction occurring some 50 °C below the minimum in elastic modulus.
Young's modulus was the same for all the specimens (694 kilobars) within experimental error but the shear modulus of the cold-worked specimens was more than 10% higher than that for the annealed specimens.

Key Words: Nickel-titanium alloy, elastic moduli, internal friction, temperature dependence, cold-worked and annealed specimens.

Glass research at the National Bureau of Standards, G. W. Cleek, *Glass Ind.* **47,** *No. 12, 663–669 (Dec. 1966).*
A general account of the research and development in glass technology at the National Bureau of Standards is presented. A brief history of the Bureau's interest in glass is given, followed by a description of the present effort on specific projects in the Inorganic Glass Section.

Key Words: Glass research, glass technology, properties of glass.

Instrumental aspects of synchrotron CUV spectroscopy, R. P. Madden, D. L. Ederer, and K. Codling, *Appl. Opt.* **6,** *No. 1, 31–38 (Jan. 1967).*
Electron synchrotrons are becoming increasingly important as sources of extreme uv radiation for physical experiments. The NBS 180 MeV machine has been utilized for gas absorption studies over a four-year period, during which a 3-meter grazing incidence spectrograph and monochromator have been designed, constructed and put into operation. The instruments are extremely stable to vibration and temperature variation, and are operating with a slit limited resolution of the order of 0.06 Å. The design principles and features of these instruments are described, and a highly-successful pre-alignment procedure for grazing-incidence spectrometers is outlined. The effect of the unusual characteristics of this light source on the illumination and performance of the spectroscopic instruments is discussed.

Key Words: 3-Meter, grazing-incidence, spectrograph, monochromator alignment, 0.006 Å resolution, synchrotron light.

Measurement and calculation of Cu II, Ge II, Si II, and C I vacuum-ultraviolet lines, V. Kaufman and J. F. Ward, *J. Opt. Soc. Am.* **56,** *No. 11, 1591–1597 (Nov. 1966).*
The discharge in a water-cooled copper hollow-cathode containing germanium and silicon was photographed with the NBS 10.6 meter Eagle vacuum spectrograph to investigate a portion of the vacuum ultraviolet spectrum of singly ionized copper in first, second and third orders. 32 of the 33 Cu II lines of the $4p$-$6s$ transitions for which Ritz calculations have been made were investigated as to their suitability as standards. 104 other lines of Cu II in the interval 861–1623 Å were observed and measured in the second and/or third orders with estimated wavelength uncertainties of 0.0006 Å. Included in this group are two previously unobserved lines of the $4p$-$6s$ transitions, four members of the calculable $4s$-$5p$ transitions, and the three ground state transitions ($a\ ^1S_0 - 4p\ ^1P_1, {}^3P_1, {}^3D_1$). This latter group of three lines allows the calculation of shorter wavelength lines.
Some vacuum ultraviolet multiplets of C I, Si II, and Ge II in the wavelength range 1492–1602 Å, were also measured in second order. These lead to an extension, modification or confirmation of the present lists of calculated wavelengths of these spectra. A precise measurement of the Lyman Beta line of hydrogen in third order is an added confirmation of the presence of the Lamb shift of the $1\ ^2S$ state of hydrogen.

Key Words: Spectrum, copper, germanium, silicon, carbon, vacuum, ultraviolet, wavelengths, standards, Ritz.

Measurements of relative oscillator strengths of some C II multiplets, J. R. Roberts and K. L. Eckerle, *Phys. Rev.* **153,** *No. 1, 87–90 (Jan. 1967).*
An electric shock tube (T-tube) filled with a mixture of 95 percent He and 5 percent CO_2 at 0.5 Torr initial pressure was the source for spectroscopic measurements of some C II oscillator strengths. The absorption oscillator strengths of the C II 2512Å, 2837Å, 3920Å, and 3876Å multiplets were measured relative to the 4267Å C II multiplet. The plasma electron temperature was determined by the relative line intensities of the 4254Å and 4642Å O II lines.

Key Words: Oscillator strength (f-value), Carbon II, T-tube, equivalent electrons, Oxygen II, plasma, local thermal equilibrium, optical depth, electron temperature, Coulomb approximation, electron density.

Moisture permeation of leather and plastics used in shoes, J. R. Kanagy, *J. Am. Leather Chemists' Assoc. Tech. Note* **LXII,** *No. 2, 115–122 (Feb. 1967).*
Data are given on moisture permeation of leather and plastics exposed both to water and water vapor. The rate of moisture permeation of some plastics is equivalent to that of some leather now used. The permeation of moisture through leather depends upon the tannage, and by adopting the proper tannage could be greatly increased. However, leathers that are highly permeable to water are not practical for use in shoes, and in this respect man-made materials will undoubtedly be able to compete with leather. Other properties, such as insulation and ability to mold to the feet, are characteristics which will continue to make leather a preferred material for shoes.

Key Words: Absorption, water, adsorption, water vapor, leather, permeation, water vapor permeability.

The forbidden $I\ ^1\Sigma^- - X\ ^1\Sigma^+$ absorption bands of carbon monoxide, G. Herzberg, J. D. Simmons, A. M. Bass, and S. G. Tilford, *Can. J. Phys.* **44,** *3039–3045 (1966).*
The forbidden $I\ ^1\Sigma^- - X\ ^1\Sigma^+$ transition of CO has been observed at high resolution in the vacuum ultraviolet region. Eight bands have been analyzed to determine rotational and vibrational constants for the $I\ ^1\Sigma^-$ state. The bands consist of a single Q-branch which gains intensity through a rotational mixing of the $I\ ^1\Sigma^-$ and $A\ ^1\pi$ states. The local perturbations between the I and A states are summarized and discussed. Also an apparent "vibrational" perturbation in the $v=4$ and 5 energy levels of the I state is described. Indirect evidence suggests the perturbing state is a $^3\pi$.

Key Words: Carbon monoxide, absorption, vacuum ultraviolet, spectrum, forbidden transition, high-resolution.

Two-quantum photoionization of Cs and I^-, J. L. Hall, *IEEE J. Quantum Electron.* **QE-2,** *No. 9, 361–363 (Sept. 1966).*
This paper will review briefly a recent experiment which measured the photodetachment probability for I^- ions due to simultaneous absorption of two ruby quanta. We have calculated the two-quantum photoionization rate for atomic cesium as a function of wavelength. The "transition" from the initial state to the bound intermediate state is expressed in terms of oscillator strengths. The second "transition," from these excited valence states into the Coulomb continuum is expressed as a cross section. We have observed what appear to be genuine two-photon ionization signals in three cases: 1) near resonance in the $10P_{3/2}$ state using the second-harmonic of Q-switched ruby, 2) away from resonances, using the 5300 Å second-harmonic of Q-switched neodymium laser, and 3) away from resonances using the first anti-Stokes line at 5750 Å from ruby-pumped D_2 gas. Present experiments aim at scanning the interesting range near resonance, e.g., by thermally tuning the ruby.

Influence of paramagnetic resonance on the static susceptibility. The lattice-bath relaxation time of neodymium ethylsulfate, G. A. Candela and R. E. Mundy, *J. Chem. Phys.* **46,** *No. 1, 47–54 (Jan. 1, 1967).*
The spin-lattice-bath relaxation process of neodymium ethylsulfate was investigated by measuring simultaneously the change in the static susceptibility and the microwave power absorbed at electron spin resonance. This technique can be used at constant temperature to distinguish the spin-lattice process from the lattice-bath process. The relaxation time of neodymium ethylsulfate was studied at a microwave frequency of 14.5 G Hz as a function of temperature, helium exchange gas pressure, microwave power absorbed, two crystal orientations, and crystal size. At this microwave frequency the energy transfer from the lattice to the bath appears to be the rate determining process. The dominant lattice-bath relaxation time, τ_p, is inversely proportional to the square of the bath temperature $\tau_p T^2 = 0.20$ sec °K² but is apparently independent of the crystal size, the helium exchange gas pressure, and crystal orientation. The experimental data are in essential agreement with the data obtained by other researchers using different methods.

Key Words: Lattice-bath, relaxation time, neodymium ethylsulfate, electron static susceptibility, spin saturation.

Measurement of optical constants: optical constants of liquid mercury at 5461 Å, L. E. Smith and R. R. Stromberg, *J. Opt. Soc. Am.* **56,** *No. 11, 1539–1542 (Nov. 1966).*
The optical constants of liquid mercury have been measured by ellipsometry at a wavelength of 5461 Å. Discrepancies among values from the literature are discussed and the magnitude of the important sources of error are evaluated. The effects on the measured index of several different types of surface films between the mercury and several contact media have been calculated and compared. Errors in alignment are shown to cause large changes in the measured refractive index as well as an apparent dependence upon the angle of incidence.

Key Words: Ellipsometry, optical constants, mercury, refractive index, surface films, complex refractive index.

Nitrogen on rhenium observed with the field emission microscope, R. Klein and J. W. Little, *Surface Sci.* **6,** *No. 2, 193–207 (Feb. 1967).*
The adsorption of nitrogen on rhenium was observed with a field emission microscope. Nitrogen decreases the work function of rhenium but also decreases the pre-exponential term of the Fowler-Nordheim expression. The result is a small decrease in emission with nitrogen adsorption. Surface migration could not be directly observed because description precedes it. There are two chemisorbed binding states associated with nitrogen on rhenium. The first is little stronger than physisorbed but accounts for most of the nitrogen in a saturated layer at 50 °K. The second is inferred from small pattern changes above 750 °K. The weakly bound state

probably consists of a number of states with a distribution of desorption energies.

Key Words: Nitrogen, rhenium, chemisorption, field emission.

Nitrogen sorption measurements and surface areas of hardened cement pastes, C. M. Hunt, *Highway Research Board Symposium on Structure of Portland Cement Paste, Washington, D.C. January 1956, Highway Research Board Special Report 90, 112–122 (1966).*
Surface area by nitrogen adsorption and also nonevaporable water were determined on hardened cement pastes of four water cement ratios, ranging from 0.251 to 0.501, and four ages, ranging from 1 day to 180 days.
Water-cement ratio made very little difference in the surface area of hardened pastes at 1-day but with pastes at later ages, evidence suggests that surface area may reach a limiting value which is a function of the original water-cement ratio. The ratio of surface area by nitrogen adsorption to nonevaporable water was not constant but increased with increasing hydration in paste of water-cement ratio 0.501 and changed very little or even decreased slightly in paste of water-cement ratio 0.251.
The degree of subdivision of the past during drying exerted a significant effect on the measured surface area except for specimens of high water-cement ratio measured early in the hydration process. In most cases pastes which were dried as cylinders, ½-inch in diameter and ½-inch long, had lower surface areas than specimens of the same pastes which were crushed to smaller particle sizes below 1-mm before drying. The sorption isotherm and calculated pore size distribution of a past after different drying treatment were also determined.

Production and reaction of atomic fluorine in solids. Vibrational and electronic spectra of the free radical HNF, M. E. Jacox and D. E. Milligan, *J. Chem. Phys.* **46,** *No. 1, 184–191 (Jan. 1, 1967).*
The species $H^{14}NF$, $H^{15}NF$, and $D^{14}NF$ have been produced in an argon matrix at 14 °K by the reaction of photolytically produced atomic fluorine with NH. Sufficient concentrations of these species have been obtained for direct detection of two vibrational fundamentals, appearing at 1000 and 1432 cm^{-1} for $H^{14}NF$, as well as of an electronic transition between 3900 and 5000Å involving a progression in the upper state bending frequency. Force constants and thermodynamic properties have been derived for HNF. Other species observed in these experiments include NF, NF_2, and HNF_2. Evidence is presented indicating that the hydrogen atom can be abstracted from HN_3 by atomic fluorine.

Key Words: F atom reactions, force constants, HNF, HNF_2, infrared spectrum, matrix isolation, NF, NF_2, thermodynamic properties, visible-ultraviolet spectrum.

Proposal for the practical measurement of pH in amphiprotic and mixed solvents, R. G. Bates, *Intern. Union Pure Appl. Chem. Info. Bull. No. 26, 50–54 (Aug. 1966).*
Procedures analogous to those on which a practical *p*H scale has been based can be used profitably to establish operational acidity scales in certain other amphiprotic and mixed solvent media. A universal *p*H scale relating proton activity uniformly to the aqueous standard reference state is not yet a practical possibility, but separate scales for each medium can be achieved and will fulfill most of the requirements. The best choice of unit appears to be pa_H^* or $-\log(m_H \cdot s\gamma_H)$, where $a\gamma_H$ is referred to the standard state in each particular medium *a*. Data for reference solutions in 50 wt. percent methanol and in deuterium oxide are given.

A study of the angular and energy distributions of radiation at small distances from a point source of gamma rays or neutrons, C. Eisenhauer, *Nucl. Sci. Eng.* **27,** *240–251 (1967).*
The theoretical expression for the singly scattered angular and energy flux of radiation from a point source is studied in the limit of very small source-detector separation distances, ($\mu_0 r \ll 1$). It is shown that both the angular and energy distributions are related in a simple way to the scattering kernel. Examples are given for gamma and neutron point sources in air. The applicability of the distributions at separation distances of the order of a mean free path ($\mu_0 r \approx 1$) is discussed.

Key Words: Shielding, gamma rays, neutrons, air-scatter, single scatter, point source, angular distribution, energy spectrum.

A survey of second breakdown, H. A. Schafft and J. C. French, *IEEE Trans. Electron. Devices* **ED-13,** *No. 8–9, 613–618 (Aug–Sept. 1966).*
The existence of a "new high current mode of transistor operation" now generally known as second breakdown, was first reported by Thornton and Simmons in 1958 and was used to explain the mysterious failures that were observed to occur under certain operating conditions. Since then, with the production of higher power and higher frequency transistors, the problems resulting from the existence of second breakdown have proliferated. Interest in the phenomenon has grown concurrently and many papers about second breakdown can be found in the literature. These papers cover a range of interest that extends from theoretical studies of the basic mechanisms involved to interpretations of specifications for transistor operation free of second breakdown. A complete understanding of second breakdown has not yet been achieved and several concepts of second breakdown prevail. The purpose of this paper is to review historically the work that has been reported in order to present a coherent and comprehensive picture of the present status of second breakdown.

Key Words: Transistors, reliability, second breakdown, diodes, thermal instability, breakdown.

Cerous magnesium nitrate: a magnetic temperature scale 0.002–2 °K, R. P. Hudson and R. S. Kaeser, *Physics* **3,** *No. 2, 95–113 (1967).*
Isentropic demagnetizations from known starting conditions yielded a determination of the entropy-magnetic susceptibility, or S-χ, relation for single-crystal spheroids of the paramagnetic salt cerous magnesium nitrate, CMN. Enthalpy differences, ΔQ, between the low temperature end-points thus reached and a (arbitrary) reference temperature near 1 °K [determined by gamma ray heating] yielded a corresponding Q-S curve, whence one obtained S-T and χ-T, T being the thermodynamic temperature. The salt exhibits a broad maximum in χ centered on S/R = 0.32, for which region the absolute temperature is determined to be 0.001_5 °K. Our results disagree significantly with those of other workers (even S-χ, which is not subject to large experimental error) save for the observation that CMN obeys the Curie law at least down to 0.006 °K.
At high temperatures ($T > 0.006$ °K), all specimens show a heat capacity $C/R = bT^{-2}$ with $b = 5.76 \times 10^{-6}$. Superimposed upon this is a small "anomaly" first appearing at approximately 0.015 °K and reaching a maximum near 0.025 °K. The attribution of such an effect to small concentrations of magnetic impurities cannot be reconciled with the results of chemical analysis. Other evidence, moreover, supports the idea of a non-magnetic origin for this anomaly.

Key Words: Cerous magnesium nitrate; magnetic thermometer; low temperature scale.

Definition of temperature in the kinetic theory of dense gases, L. S. Garcia-Colin and M. S. Green, *Phys. Rev.* **150,** *No. 1, 153–158 (Oct. 7, 1966).*
The question of the appropriate definition of temperature in the kinetic theory of dense gases is discussed. An apparent contradiction in the value of the bulk viscosity between two methods of making the transition from the kinetic to the hydrodynamic stage is resolved. It is shown that the definitions of temperature through the kinetic energy and through the total energy are equivalent. The general question of the appropriate choice of macroscopic variables in non-equilibrium statistical mechanics is discussed.

Key Words: Temperature, non-equilibrium kinetic energy, total energy, bulk viscosity, macroscopic variable, macroscopic equations of motion.

Effective charge carrier lifetime in silicon *p-i-n* junction detectors, J. A. Coleman and L. J. Swartzendruber, (*Proc. 10th Scintillation and Semiconductor Counter Symp., Washington, D. C. Mar. 23–24, 1966*), *IEEE Trans. Nucl. Sci.* **NS-13,** *No. 3, 240–244 (June 1966).*

An estimate of the effective charge carrier lifetime can be obtained from a determination of the collection efficiency as a function of the transit time for charge carriers produced by incident short-range radiation in a *p-i-n* junction detector. The results of this method have the advantage of being independent of both the charge carrier mobility and the depletion depth of the detector. Effective lifetimes as low as a few microseconds (τ_e) for electrons produced by natural alpha particles have been observed in several 2-mm thick lithium-compensated silicon detectors operating at room temperature. No significant bias dependent windows which might cause misleading interpretation of the results were observed. Window effects were investigated by measuring the changes in pulse height of detector output signals initiated by natural alpha particles incident on the detectors at angles up to 45 degrees. The electron lifetimes were observed to decrease when the detector was operated at liquid nitrogen temperature. The short effective lifetimes that can occur in lithium-compensated silicon set a lower limit on the field strengths that must be maintained for effcient charge collection in thick *p-i-n* junction detectors. Effective hole lifetimes can also be obtained using this technique but with the present geometry of lithium-compensated silicon detectors this measurement is more difficult if short-range particles are used. The effects of charge carrier lifetime and amplifier pulse rise and fall times on the observed radiation-induced pulse shapes are discussed.

Key Words: Semiconductor nuclear radiation detectors, charge carrier lifetime, lithium-compensated silicon.

Fermi controlled recombination as a junction design factor in GaAs laser diodes, N. N. Winogradoff and H. K. Kessler, *Int. J. Electronics* **21,** *No. 4, 329–335 (1966).*
Since our first observation of the enhancement of radiative recombination rates in GaAs *p-n* junctions produced by the incorporation of shallow donors in the *p*-type side of the junction, the effect has been found to be quite general and has also been observed in GaP. Although several models for the radiative process have been proposed they do not provide a satisfactory explanation of the role of compensation. A new model based on Shockley and Read's statistics of recombination through an impurity center is described. It provides agreement with the experimentally observed differences in the light output of diffused, graded, and narrow, abrupt *p-n* junctions with and without compensation in the *p*-type side, and with the difference in the time delay between the leading edge of the current pulse and the commencement of lasing in diffused and epitaxial GaAs lasers at room temperature.

Key Words: Radiative recombination, compensated GaAs, epitaxial GaAs lasers, Fermi levels.

Kinetics of growth of multicomponent chains, J. I. Lauritzen, Jr., E. A. DiMarzio, and E. Passaglia, *J. Chem. Phys.* **45,** *No. 12, 4444–4454 (Dec. 15, 1966).*
A theory is presented by which the rate of growth and composition (including all pair and higher distributions) of a chain growing in a multi-component system may be calculated. Each position in the chain may be occupied by any of the components of the system. Only nearest neighbor interactions are assumed and the rate constants α^{ij} for addition of species j to a chain ending in species i, and β^{ij}, for the removal of species j from a chain ending in i, j are assumed known and independent of chain length, except for those referring to the first step of the chain, which are distinct. The full kinetic equations for the growth of such chains are formulated and a solution obtained for steady-state conditions. It is shown that when the matrix of α^{ij}/β^{ij} is indecomposable and primitive a solution of the equations which is independent of chain length always exists for sufficiently long chains and computational methods for obtaining this solution for a relatively large number of components (of the order of ten) are presented. In addition, the relationship of α^{ij}/β^{ij} to the energetics of the system is derived.

Key Words: Kinetics, multi-component, growth rate, composition, steady-state.

Lack of uniqueness in the international practical temperature scale above the gold point, H. J. Kostowski, *Metrologia* **3,** *No. 1, 28–29 (Jan. 1967).*
The International Practical Temperature Scale (IPTS) above the gold point is shown to vary with wavelength. Although the extent of this variation is barely significant relative to the present uncertainty of realizing the scale, the IPTS should be unique; and to achieve this a wavelength must be specified in the definition.

Key Words: International Practical Temperature Scale, temperature, standards, radiation thermometry, optical pyrometer, infrared pyrometer.

Mechanical relaxation in polychlorotrifluoroethylene, J. M. Crissman and E. Passaglia, *J. Polymer Sci. Pt. C, No. 12, 237–245 (1966).*
Measurements of the viscoelastic functions Δ, G', G'', J' and J'' as functions of temperature from $-180°$ to $+180$ °C have been obtained, using a torsion pendulum apparatus, for several samples of poly(chlorotrifluoroethylene) having widely different crystallinities as determined by density. The low crystallinity samples show two relaxations: a very broad one (γ) centered at about -35 °C which appears to be split into two processes, and one (β) at 84 °C. In the higher crystallinity samples, a third process (α) appears at about 137 °C, and the high temperature side of the γ relaxation peak is lower in magnitude as compared to the lower crystallinity specimens. For the β peak, which is assumed to be associated with the glass transition, the peak value for G'' is essentially independent of crystallinity, while both Δ and J'' show decreases in magnitude with increasing crystallinity. The relationship between the magnitude of the relaxation peak and crystallinity, and dependence of this relationship upon the viscoelastic function chosen to characterize the relaxation are discussed.

Key Words: Mechanical relaxation, torsion pendulum apparatus, poly(chlorotrifluoroethylene), varying crystallinities, quenched sample, isothermally crystallized sample, loss modulus, loss compliance, storage modulus, tan δ.

Nuclear hexadecapole interactions, R. J. Mahler, *Phys. Rev.* **152,** *No. 1, 325–330 (Dec. 2, 1966).*
The nuclear hexadecapole matrix elements for the static and the one phonon-nuclear interactions are developed and are evaluated for $\delta m = \pm 3$ and $\delta m = \pm 4$ nuclear transitions involving a spin 9/2 nucleus in a crystal with $\bar{4}$ 3m symmetry. An expression for the saturation factor for a general interaction which gives rise to nuclear spin transitions involving the change in the z-component of the spin by any amount $\delta m = \pm n$ is developed and is used to derive the angular variation of the one-phonon, $\delta m = \pm 3$ and $\delta m = \pm 4$ nuclear hexadecapole interaction. Finally a method to end the speculation about the observation of the hexadecapole interaction is presented.

Key Words: Hexadecapole, phonon interactions, angular dependence, saturation factor, $\bar{4}$ 3m symmetry, hexadecapole transitions.

Optical power increase in GaAs laser diodes coated with reflecting aluminum silicone mixture, H. K. Kessler, *Proc. IEEE Letter* **55,** *No. 1, 99–100 (Jan. 1967).*
GaAs laser output power has been increased by using the reflectance of an aluminum-silicone mixture coated on a laser diode. After such application, the light output increased from one side by 50%, and better heat dissipation from the diode was observed.

Key Words: GaAs lasers, optical power, aluminum-silicone compound, heat sink.

Other NBS Publications

J. Res. NBS 71C2 (Engr. and Instr.), No. 2 (Apr.–June 1967), 75 cents.

An apparatus for measuring thermal expansion at elevated temperatures. B. D. Rothrock and R. K. Kirby. (See above abstracts.)
Determination and smoothing of Fourier coefficients representing piecewise continuous functions. B. A. Peavy.
A 2:1 ratio inductive voltage divider with less than 0.1 ppm error to 1 MHz. C. A. Hoer and W. L. Smith. (See above abstracts.)
A dual-load flow calorimeter for rf power measurement to 4 GHz. M. L. Crawford and P. A. Hudson. (See above abstracts.)

Polymeric materials for dielectric reference specimens. A. H. Scott and J. R. Kinard, Jr. (See above abstracts.)

The sensitivity of the Dicke radiometer. D. F. Wait. (See above abstracts.)

Sensitivity of a correlation radiometer. J. J. Faris. (See above abstracts.)

Microwave attenuation measurements and standards, R. W. Beatty, Mono. 97 (Apr. 3, 1967), 25 cents.

Abscissas and weights for Gaussian Quadrature for $N=2$ to 100, and $N=125$, 150, 175, 200, C. H. Love, Mono. 98 (Dec. 28, 1966), 55 cents.

ASTM metric practice guide, Handb. 102 (Mar. 10, 1967), 40 cents.

Legibility of alphanumeric characters and other symbols. II. A reference handbook, D. Y. Cornog and F. C. Rose, Misc. Publ. 262–2 (Feb. 10, 1967), $4.25.

Bibliography on flame spectroscopy. Analytical applications 1800 to 1966, R. Mavrodineanu, Misc. Publ. 281 (Feb. 23, 1967), $2.00.

Bibliography of low energy electron collision cross section data, L. J. Kieffer, Misc. Publ. 289 (Mar. 10, 1967), 50 cents.

Cast-iron radiators, R174–65 (Dec. 31, 1965), 10 cents. Supersedes R174–47.

Standard sizes of blackboard slate, PS2–66 (May 15, 1966), 10 cents. Supersedes SPR15–35.

TFE-Fluorocarbon (polytetrafluoroethylene) resin skived tape, PS3–66 (Sept. 1, 1966), 10 cents.

Porcelain enameled formed steel plumbing fixtures, PS5–66 (Nov. 1, 1966), 15 cents. Supersedes CS144–47.

Trim for water-closet bowls, tanks and urinals (dimensional standards), PS6–66 (Nov. 1, 1966), 10 cents. Supersedes CS172–50.

Wire bar supports for reinforced concrete construction, PS7–66 (Aug. 1, 1966), 10 cents.

A survey of ionization vacuum gages and their performance characteristics, W. G. Brombacher, Tech. Note 298 (Feb. 3, 1967) 40 cents.

A broad-line proton magnetic resonance study of cobalt tetracarbonyl hydride, T. C. Farrar, F. E. Brinckman, T. D. Coyle, A. Davision, and J. W. Faller, Inorg. Chem. **6,** 161–163 (1967).

A pycnometer for small volumes of liquids, S. Marantz and G. T. Armstrong, Chem.-Anal. **55,** 114–115 (Oct. 1966).

Measurement of the surface area and the heats of wetting of dentin powders, G. M. Brauer (Proc. Second Workshop on Adhesive Restorative Materials, Charlottesville, Va., December 1965), Book, Adhesive Restorative Dental Materials II, 203–223 (Department of Health, Education, and Welfare, Public Health Service, Washington, D.C. 1966).

Relaxation of moments derived from a master equation, K. E. Shuler and G. H. Weiss, J. Chem. Phys. **45,** No. 4, 1110–1112 (Aug. 15, 1966).

The battle against corrosion, S. Lichtenstein, Compressed Air Mag. **71,** No. 12, 12–13 (Dec. 1966).

A new contribution—NBS and engineering standards, G. S. Gordon, Safety Standards **XVI,** No. 1, 3, 4, 24 and 25 (Jan.-Feb. 1967).

Additional thoughts on precision calibration of accelerometers, S. Edelman, Test Engineering and Management **XVI,** No. 5, 17, 18, 38, and 39 (Nov. 1966).

Air bath thermostat for use with absorption spectrophotometer, J. H. Gould, Rev. Sci. Instr. **37,** No. 9, 1229–1231 (Sept. 1966).

Combination RF radiation and fluid pressure seal, M. B. Hall, N. T. Larsen, and W. E. Little, Proc. IEEE **54,** No. 11, 1585–1586 (Nov. 1966).

Comparison of mass limiting two-phase flow in a straight tube and in a nozzle, D. K. Edmonds and R. V. Smith, Proc. Symp. Two-phase Flow, University of Exeter, Devon, England, June 21–23, 1965, 1, 401–414 (University of Exeter, Devon, England, 1966).

Forces shaping the role of the architect, J. P. Eberhard, Proc. Second Architectural Center Conf., May 13–14, 1966, Boston, Mass., pp. 12 (Boston Architectural Center, Boston, Mass., May 1966).

Galvanic corrosion of metals in cementing materials, J. W. Pitts, Military Engr. **59,** No. 387, 40–41 (Jan.–Feb. 1967).

Mass flowmeters in cryogenic service, W. J. Alspach, C. E. Miller, and T. M. Flynn, Proc. ASME Flow Measurement Conf., Pittsburgh, Pa., September 26–28, 1966, pp. 34–56 (1966).

Technology for the city, J. P. Eberhard, Intern. Sci. Technol. **57,** 18–29 (Sept. 1966).

The stress corrosion of metals, H. L. Logan, Book (John Wiley & Sons, Inc., New York, N. Y., Nov. 1966).

A modified Monte-Carlo quadrature, S. Haber, Math. Compt. **20,** No. 95, 361–368 (July 1966).

Electronic data processing in urban transportation planning, B. M. Levin and R. E. Schoefer (Proc. Second Annual Conference on Applications of E.D.P. Systems for State and Local Government, Apr. 1–2, 1966, New York, N. Y.), Book, The Larger-Scale Public E.D.P. System: Its Problems and Prospects, pp. 169–177 (University of New York, N. Y., 1966).

Time standards, J. M. Richardson, Book, Encyclopaedic Dictionary of Physics Supplementary **1,** 351–355 (Pergamon Press Inc., New York, N. Y., 1966).

A new radiometric equation and its application, H. J. Kostkowski, Appl. Opt. **5,** No. 12, 1959 (Dec. 1966).

An improved design for vacuum ultraviolet resonance lamps, A. M. Bass, Appl. Opt. **5,** No. 12, 1967 (Dec. 1966).

Accommodation faulting in Fe-Ni martensitic transformation, R. P. Reed, Acta Met. **14,** 1392–1394 (1966).

Anomaly in Young's modulus and internal friction of $5SrTiO_3$ $3La_{2/3}TiO_3$ below 100 °C, R. W. Dickson, J. Am. Ceramic Soc. **49,** No. 11, 628 (Nov. 1966).

Brownian motion models, R. J. Rubin, Summer Institute on Spectral Theory and Statistical Mechanics, Brookhaven National Laboratory, Upton, L. I., New York, July–Aug. (1965), Brookhaven Natl. Lab. Publ. PNL993 (T422) (Clearinghouse for Federal Scientific and Technical Information, Springfield, Va. 22151, 1966).

Comparison Langmuir probe and spectrometric electron temperature measurements, R. S. Powers, Jr., J. Appl. Phys. **37,** No. 10, 3821–3826 (Sept. 1966).

Coriolis zeta constants and force field for osmium tetraoxide, I. W. Levin and S. Abramowitz, Inorg. Chem. **5,** 2024–2026 (1966).

Correcting for astigmatism in the Czerny-Turner spectrometer and spectrograph, A. B. Shafer, Appl. Opt. **6,** 159 (Jan. 1967).

Effect of sample thickness and operating voltage on the contrast of Kossel transmission photographs, H. Yakowitz, J. Appl. Phys. **37,** No. 12, 4455–4458 (Nov. 1966).

Effects of a constant force on a Keplerian orbit, J. P. Vinti, Proc. Intern. Astronomical Union Symp. No. 25, Aug. 15–Sept. 3, 1964, Athens, Greece, pp. 355–362 (1966).

Erratum: Polycrystalline spin-wave theory of ferromagnetic resonance compared with the tilting experiment, A. S. Risley, E. G. Johnson, Jr., and H. E. Bussey, J. Appl. Phys. **37,** No. 9, 3646 (Aug. 1966).

Flash photolysis of matrix-isolated cyanogen azide in solid nitrogen, L. J. Schoen, J. Chem. Phys. **45,** No. 8, 2773–2776 (Oct. 15, 1966).

Molecular emission spectra in the soft x-ray region, R. D. Deslattes and R. E. LaVilla, Appl. Opt. **6,** 39–42 (Jan. 25, 1967).

Newly measured and calculated wavelengths in the vacuum ultraviolet spectrum of neutral nitrogen, V. Kaufman and J. F. Ward, Appl. Opt. **6,** No. 1, 43–46 (Jan. 1967).

Observation of the D $^1\Delta \rightarrow x\,^1\Sigma+$ transition of CO in the vacuum-ultraviolet region, J. D. Simmons and S. G. Tilford, J. Chem. Phys. **45,** No. 8, 2965–2968 (Oct. 15, 1966).

Observation of the superconducting energy gap in a semiconductor (GeTe), P. J. Stiles, L. Esaki, and J. F. Schooley, Physics Letters **23,** No. 3, 206–207 (Oct. 17, 1966).

Optical constants of germanium, R. E. LaVilla and H. Mendlowitz, Appl. Opt. **6,** No. 1, 61–68 (Jan. 1967).

Pyroelectric effect in bone and tendon, S. B. Lang, Nature **212,** 704–705 (Nov. 12, 1966).

Reflection of soft x-rays by organic fibers, S. B. Newman, J. Appl. Polymer Sci. **10,** 1929–1935 (1966).

Relation between refractive index and density of glasses resulting from annealing compared with corresponding relation resulting from compression, S. Spinner and R. M. Waxler, Appl. Opt. **5,** No. 12, 1887–1889 (Dec. 1966).

Resolving power predictions from lens design data, O. N. Stavroudis, Appl. Opt. **6,** No. 1, 129–135 (Jan. 1967).

Sodium-electron spin-exchange collisions, L. C. Balling, Phys. Rev. **151,** No. 1, 1–6 (Nov. 4, 1966).

Some approximations to the Planck function in the intermediate region with applications in optical pyrometry, D. E. Erminy, Appl. Opt. **6,** 107–117 (Jan. 1967).

Bonding adhesives and paints to treated concrete, W. C. Wolfe, CSI Monograph 9M1, Construction Specifier, pp. 1–8 (Aug. 1966).

Characteristics of the laser probe for spectrochemical analysis, S. D. Rasberry, B. F. Scribner, and M. Margoshes, Proc. XII Intern. Spectroscopy Colloquim, Exeter, England, 1965, pp. 336–339 (Hilger and Watts, London, England, 1966).

Chemiluminescence of CH in the $O+C_2H_2$ reaction; Rotational relaxation and quenching, W. Brennen and T. Carrington, J. Chem. Phys. **46,** No. 1, 7–18 (Jan. 1, 1967).

Corrosion's many faces, S. Lichtenstein, Southern Eng. **85,** No. 1, 44–47 (Jan. 1967).

Formation of $NH(c^1\Pi)$ and $NH(A^3\Pi_i)$ in the vacuum-uv photolysis of HN_3, K. H. Welge, J. Chem. Phys. **45,** No. 11, 4373–4374 (Dec. 1, 1966).

Growth of calcite crystals, P. M. Gruzensky, (Proc. Intern. Conf. Crystal Growth, Boston, Mass., June 20–24, 1966), Crystal Growth, A Suppl. to J. Phys. Chem. Solids D–3, pp. 365–367 (Pergamon Press Inc. New York, N.Y., 1967).

Growth of calcium molybdate crystals by a temperature-gradient zone-melting technique, H. S. Parker and W. S. Brower (Proc. Intern. Conf. Crystal Growth, Boston, Mass., June 20–24, 1966), Crystal Growth, A Suppl. to J. Phys. Chem. Solids E–12, pp. 489–491 (Pergamon Press Inc., New York, N.Y., 1967).

Introduction of the Acheson medalist, R. G. Bates, J. Electrochem. Soc. **113,** No. 12, 1–7 (Dec. 1966).

The crystal structure of twinned low-temperature lithium phosphate, C. Keffer, A. Mighell, F. Mauer, H. Swanson and S. Block, Inorg. Chem. **6,** No. 1, 119–125 (Jan. 1967).

The optical and magnetic spectra of copper doped dichloro(1-10-phenanthroline) zinc, G. F. Kokoszka, C. W. Reimann, and H. C. Allen, Jr., J. Phys. Chem. **71,** No. 1, 121–126 (Jan. 1967).

Procedures for precise determination of thermal radiation properties, J. C. Richmond, G. J. Kneissl, D. L. Kelley, and F. J. Kelly, Tech. Report AFML–TR–66–302 (Air Force Materials Laboratory, Air Force Systems Command, Wright-Patterson Air Force Base, Ohio, Aug. 1966).

Relation of fracture stress to the fracture pattern for glass rods of various diameters, M. J. Kerper and T. G. Scuderi, Am. Ceramic Soc. Bull. **45,** No. 12, 1065–1066 (Dec. 7, 1966).

The nucleation of Hg on W as observed by field-emission microscopy, S. C. Hardy (Proc. Intern. Conf. Crystal Growth, Boston, Mass., June 20–24, 1966), Crystal Growth, A Suppl. to J. Phys. Chem. Solids **C–13,** pp. 287–293 (Pergamon Press Inc., New York, N.Y., 1967).

Thermal correction and crystal growth in horizontal boats, flow pattern, velocity measurement, and solute distribution, H. P. Utech, W. S. Brower, and J. G. Early (Proc. Intern. Conf. Crystal Growth, Boston, Mass., June 20–24, 1966), Crystal Growth, A Suppl. to J. Phys. Chem. Solids **B–29,** pp. 201–205 (Pergamon Press Inc., New York, N.Y., 1967).

Wind effect on pre-existing waves, G. Kulin, Proc. 1965 ASCE Conf. Coastal Engineering, Santa Barbara, California, October 1965, ch. 16, pp. 369–389 (American Society of Civil Engineers, 1966).

A functional inequality, S. Haber, Am. Math. Mo. **73,** No. 10, 1103–1104 (Dec. 1966).

The role of the National Bureau of Standards in the establishment of measurement capability at the state level, T. M. Stabler, Instr. Soc. Am. Preprint 16.1–3–66, pp. 1–3 (Oct. 24–27, 1966).

A vacuum ultraviolet flash photolysis apparatus, W. Braun, A. M. Bass, and A. E. Ledford, Jr., Appl. Opt. **6,** No. 1, 47–49 (Feb. 2, 1967).

Condensation of dry air on a liquid hydrogen cooled surface in the pressure range 10^{-3} to 10 torr (Knudsen number of 10^{-4} to 1), J. Hord, Cryogenics **6,** No. 5, 285–293 (Oct. 1966).

Inversion temperatures and pressures for cryogenic gases and their mixtures, R. D. Gunn, P. L. Chueh, and J. M. Prausnitz, Cryogenics **6,** No. 6, 324–329 (Dec. 1966).

Matrix elements of general potentials in the harmonic-oscillator representation, R. M. Wilcox, J. Chem. Phys. **45,** No. 9, 3312–3316 (Nov. 1, 1966).

Note on the variation of the results of the Mullen burst test over the area of a hide, J. R. Kanagy, J. Am. Leather Chemists' Assoc. Tech. Note **LXII,** No. 1, 63–67 (Jan. 1967).

Recent advances in excitation of atomic spectra, M. Margoshes, Proc. XII Intern. Spectroscopy Colloquim, Exeter, England, 1965, pp. 26–42 (Hilger and Watts, London, England, 1966).

The dispersion of distributions derived from folding simple distributions, R. A. Schrack, Nucl. Instr. Methods **45,** No. 2, 319–321 (1966).

The effect of a two-dimensional roughness element on boundary-layer transition, P. S. Klebanoff (Proc. Eleventh Intern. Congress Applied Mechanics, Munich, Germany, 1964), Book, Applied Mechanics, ed. H. Gotler, pp. 803–805 (Springer-Verlag, Berlin, Germany, 1966).

The National Bureau of Standards and its contributions to geophysics, D. Baker, Trans. Am. Geophys. Union **17,** No. 4, 563–568 (Dec. 1966).

Determination of the composition of complexes and their instability constant by calorimetry. II. The complex in fused potassium chloride and cadmium chloride, W. H. Metzger, Jr., A. Brenner, and H. I. Salmon, J. Electrochem. Soc. **114,** No. 2, 131–138 (Feb. 1967).

Nonstoichiometric A15-type phases in the systems Cr-Pt and Cr-Os, R. M. Waterstrat and E. C. van Reuth, Trans. Met. Soc. AIME **236,** No. 8, 1232–1233 (Aug. 1966).

Pressures exerted on complete dentures during swallowing, M. Ohashi, J. B. Woelfel, and G. C. Paffenbarger, J. Am. Dental Assoc. **73,** No. 3, 625–630 (Sept. 1966).

Recent advances in U.S.A. research on dental amalgams and possible applications, G. C. Paffenbarger, Intern. Dental J. **16,** No. 4, 450–465 (Dec. 1966).

Structural interpretation of immiscibility in oxide systems: IV, Occurrence, extent, and temperature of the monotectic, E. M. Levin, J. Am. Ceram. Soc. **50,** No. 1, 29–38 (Jan. 1967).

The system $Sc_2O_3-B_2O_3$, E. M. Levin, J. Am. Ceramic Soc. **50,** No. 1, 53–54 (Jan. 1967).

Analysis and computer simulation of the production and distribution systems of a tufted carpet mill, J. A. Yurow, J. End. Eng. **XVIII,** No. 1, 135–140 (Jan. 1967).

Building code viewpoints, A. A. Bates, (Building Research Institute Fall Conf., Codes Session, Washington, D.C., Nov. 16, 1966), J. Bldg. Res. Inst. **4,** No. 1, 48–49 (Jan.–Feb. 1967).

Earth temperature and thermal diffusivity at selected stations in the United States, T. Kusuda and P. R. Achenbach, ASHRAE Trans. **71,** Pt. 1, 61–75 (Jan. 25–28, 1965).

Micrometer u-tube manometers for medium-vacuum measurements, A. W. Thomas and J. L. Cross, J. Vacuum Sci. Technol. 4, No. 1, 1–5 (Jan.–Feb. 1967).

Outdoor air psychrometric criteria for summer ventilation of protective shelters, T. Kusuda and P. R. Achenbach, ASHRAE Trans. **71,** Pt. 1, 76–87 (Jan. 25–28, 1965).

The city as a system, J. P. Eberhard, Proc. Mid-American Conf. Design, Kansas City, Mo., March 30–31, 1966, pp. 25–30 (Midwest Research Institute, Kansas City, Mo., 1966).

The RF connector, R. C. Powell, Microwave J. **10,** No. 3, 8 (Feb. 1967).

Processing of numerical test data, J. Mandel and T. W. Lashof, Book, Testing of Polymers, ed. J. V. Schmitz, 2, ch 2, 33–82 (Interscience Publ. New York, N.Y., 1966).

The design of a federal statistical data center, E. Glaser, D. Rosenblatt, and M. K. Wood, Am. Stat. **21,** No. 1, 12–20 (Feb. 1967).

Time-dependent behavior of an incompressible elastic fluid. Some homogeneous deformation histories, B. Bernstein, Acta Mechanica **II,** No. 4, 329–254 (1966).

Optimum allocation of calibration errors, E. L. Crow, Ind. Quality Control **23,** No. 5, 215–219 (Nov. 1966).

Adsorption of polymers, R. R. Stromberg, Book, Treatise of Adhesives and Adhesion, Vol. **1.** Theory, ch. 3, 69–118 (Marcel Dekkers Inc., New York, N.Y., 1967).

Avalanche radiation from the bulk of long, thin, forward-biased p^+-p-n^+silicon diodes, G. G. Harman, Appl. Phys. Letters **9,** No. 5, 207–209 (Sept. 1, 1966).

Baffled piston radiator: expansion of potential in far, paraxial field, M. Greenspan, J. Acoust. Soc. Am. **40,** No. 1, 251–252 (July 1966).

Divergence in the density expansion of the transport coefficients of a two-dimensional gas, J. V. Sengers, Phys. Fluids **9,** No. 9, 1685–1696 (Sept. 1966).

Elastic constants of single crystal UO_2 at 25 °C, J. B. Wachtman, Jr., M. L. Wheat, H. J. Anderson, and J. L. Bates, J. Nuclear Mater. **16,** 39–41 (1965).

Ferrimagnetic resonance low-field effects in rod samples, L. B. Schmidt, R. D. Harrington, and W. E. Case, Proc. IEEE **55,** No. 1, 120–121 (Jan. 1967).

Magnetization of iron from magnetometer calibrations, W. E. Case and R. S. Harrington, Proc. IEEE **54,** No. 12, 2004–2005 (Dec. 1966).

Radiative recombination within a space-charge region in a semiconductor, N. N. Winogradoff, J. Appl. Phys. **37,** No. 10, 3916–3917 (Sept. 1966).

Solid-vapour equilibrium in the system neon-methane, M. J. Hiza and A. J. Kidnay, Crogenics **6,** No. 6, 348–354 (Dec. 1966).

Spin-relaxation effects on the EPR spectrum of gaseous S-state atoms, R. L. Brown and W. Brennen, J. Chem. Phys. **46,** No. 1, 385–386 (Jan. 1, 1967).

Surface aspects of the thermal degradation of GaAs $p-n$ junction lasers and tunnel diodes, H. Kessler and N. N. Winogradoff, IEEE Trans. Electron. Devices **ED-13,** No. 10, 688–691 (Oct. 1966).

** Publications for which a price is indicated are available by purchase from the Superintendent of Documents, U. S. Government Printing Office, Washington, D.C. 20402 (foreign postage, one-fourth additional). The NBS non-periodical series are also available from the Clearinghouse for Federal Scientific and Technical Information, Springfield, Va. 22151. Reprints from outside journals and the NBS Journal of Research may often be obtained directly from the authors.*

U.S. GOVERNMENT PRINTING OFFICE : 1967 OL—263–637

UNIVERSITY MICROFILMS INC
ATTN SERIALS SECTION
300 NORTH ZEEB RD
ANN ARBOR MICH 48106

UNITED
GOVERNMENT PRINTING OFFICE
DIVISION OF PUBLIC DOCUMENTS
WASHINGTON, D.C. 20402
OFFICIAL BUSINESS

POSTAGE AND FEES PAID
U.S. GOVERNMENT PRINTING OFFICE

JOURNAL OF RESEARCH of the National Bureau of Standards
A. Physics and Chemistry

Vol. 71A, No. 4 July–August 1967

Contents

Page

Kinetics of crystallization in multicomponent systems: I. Binary mixtures of *n*-paraffins. John I. Lauritzen, Jr., Elio Passaglia, and E. A. DiMarzio. 245

Kinetics of crystallization in multicomponent systems: II. Chain-folded polymer crystals. John I. Lauritzen, Jr., and Elio Passaglia. 261

Infrared absorption spectra of 2-oxo-1,3-bis(phenylhydrazono) derivatives and related bis- and tris-phenylhydrazones. Alexander J. Fatiadi. 277

Dielectric constant of *n*-hexane as a function of temperature, pressure, and density. Frederick I. Mopsik. 287

Heat capacities and related thermal data for diethyl phthalate crystal, glass, and liquid to 360 °K. S. S. Chang, J. A. Horman, and A. B. Bestul. 293

Heats of formation of aluminum diboride and α-aluminum dodecaboride. Eugene S. Domalski and George T. Armstrong. 307

Effect of environment upon the melting point of Al_2O_3. S. J. Schneider and C. L. McDaniel. 317

Publications of the National Bureau of Standards. 335

Library of Congress Catalog Card Number: 62–37059

For sale by the Superintendent of Documents, U.S. Government Printing Office, Washington, D.C. 20402. Price $1 (single copy).
Subscription price: $5 a year; $1 additional for foreign mailing.
UNITED STATES GOVERNMENT PRINTING OFFICE, WASHINGTON : 1967